



The
University
Of
Sheffield.

**PERIODICALLY ARRANGED NONLINEAR PASSIVE PARTICLE DAMPERS
UNDER LOW-AMPLITUDE EXCITATION**

Sifa Gul DEMIRYUREK

A thesis submitted in partial fulfilment of the requirements for the degree of
Doctor of Philosophy

The University of Sheffield
Faculty of Engineering
Department/School of Mechanical Engineering

Submission Date

31/08/2022

"Kûn Fe Yekûn"

"Ol der ve oluverir"

"Be! And it is!"

(Surah Ya-Sin 36:77-83)

Dedicated to my parents...

who supported me at all steps I have taken.

I wouldn't accomplish all these things without your presence and prayers.

Abstract

Passive and active damping methods are two main techniques of overcoming the structural vibration issues. Compared to the active dampers, passive dampers are economic and requires less maintenance. One example of passive dampers is particle damper. It constitutes of a cavity containing granular structures. These dampers can suppress the structural vibration over broad range of frequencies, which make them attractive in comparison to many other passive damping technologies. In addition, since the particle dampers do not require regular maintenance and have long lifespan [1], particle dampers found wide application in engineering. Energy dissipation from the particle dampers is achieved through the interactions between the particles and between the particle-cavity walls based on momentum changes and kinetic energy level changes. The dissipation depends on the physical parameters, as well, filling ratio, cavity size, diameter of the granules, shape of the granules, etc. The performance of the particle dampers depends on the excitation amplitude and, to lesser extent, the frequency level of the excitation. Since, the granular structures are experiencing fluidisation in the higher level of amplitudes/vibration frequencies, this research is limited to the structural vibration at low amplitude levels.

Alternative treatment of the structural vibration considered in this research is periodic array of attachments to the host structure. When these attachments have definite properties such as locally resonating properties and subwavelength size they can be referred to as metamaterials. This research focuses on the energy dissipation at the low excitation amplitudes using a periodic arrangement of light weight cavities which have resonant properties and are partially filled with spherical granular material.

In order to find the resonating properties and estimate the effect of the granular material in the meta-damper design, damper casings have been analysed using the Finite Element Method (FEM). Granular structure parameters and equivalent material property definitions have been calculated using the Discrete Element Method (DEM) and iteration-based FEM-DEM coupled methodology. Once the equivalent material properties and resonator structure properties have been defined using analytical methodology, a system with and without meta dampers have been analysed both experimentally and

numerically. Periodic arrangement of resonator filled with granules have been studied numerically using Bloch-Floquet theory. The methodology used in this research infers the modelling of granular structure dynamics using FEM more computationally efficient manner. Findings of this research on periodic arrangements of the particle dampers impact the resonant properties of the main structure and reduce the amplitude of structural vibration where the granular structure interacts with the damper body and is used as a tuning mechanism. This study can offer a state-of-the-art passive damping technology with the improved damping approach in the form of periodically arranged resonators in aerostructures, machinery and civil structures where vibration needs to be treated.

Key Words: Particle Dampers, Passive Damping, Nonlinearity, Periodic Structures, Metamaterials, DEM, FEM, Equivalent Material Modelling

Acknowledgement

First, I would like to express my sincere gratitude to Dr Anton Krynkina for this long journey and for guiding me through my MSc and PhD studentships at the University of Sheffield. Dr Krynkina's knowledge, patience, precious time, and technical help with lots of encouragement surrounded me through the long path we have taken together. Without their supervision and mentoring, this thesis would not have been completed. Dr Krynkina had told me "Think critically!" at almost all times when I struggled to find solutions or options in my PhD life. I hope that I have learned how to be a successful researcher and wise academic while being a good listener from you. In addition to every detail, Dr Krynkina deserves a huge thank for being a great help in the revision and correction process of my PhD thesis.

Secondly, I would like to express my sincere thanks to my other supervisor, Dr Jem Rongong, who has guided me from the 2nd year of my PhD life. The laboratory opportunities, technical guidance and helpful directions from Dr Rongong helped shape my research. I feel myself as a lucky student to have research experience with Dr Rongong. I hope that I can be a good director as you are in the future.

I would also like to thank the University of Sheffield for providing research opportunities, social areas, Graduate Teaching Assistant experiences and a great opportunity to be a student in one of the top universities. The time I spent in Sheffield, around the Peak District, and the experiences I gained are unforgettable.

Mathew and Rob are the precious technicians of the Dynamics Lab at the University of Sheffield. I would like to thank them for helping me when I struggled with the lab experiments. Mathew, the experimental rig you prepared for me with details I couldn't think about helped me gain much data and technical experience. When I lost my smile because of the depressive research atmosphere, you drew a smiley face on the whiteboard and showed that to me. That was hilarious and really helpful. I appreciate your presence and your help a lot. Rob, you helped me to finish my experiments by adding really small but valuable technical attachments as you developed lids to the resonators I used in the experiments. That was a lifesaver in my experiments, and I am thankful to have the opportunity to work with you.

One of the huge sincere thanks to Mustafa Kemal Atatürk, the founder of the Republic of Türkiye (Turkey). Once Atatürk said, "I am sending you out as sparks. You will return as torches." when the selected group of students was sent to Europe for higher education in the first few years of the newly founded poor but proud country. Since I am one of the selected students in my higher education journey, I owe you and this nation a lot. I hope to be a successful scientist in my field to make my country prouder. Despite all my effort, I can't pay my heartfelt debt. I would like to thank to the Republic of Türkiye (Turkey) Ministry of National Education for funding and supporting my MSc and PhD with a once in a lifetime opportunity.

I also would like to show my appreciation to all of my teachers, starting from my mother as my first teacher to the lecturers at Firat University in Türkiye (Turkey) to the lecturers at the University of Sheffield. Specifically, I sincerely thank Prof Dr Yasin Varol for letting me learn a lot from their experiences and their guidance in applying for the scholarship, which is one of the precious opportunities in my life. He is one of the greatest examples for me to become a great academic, supervisor and scientist. I also would like to thank Prof Dr Cengiz Oner for being a great lecturer, another greatest example for me and a good listener and sharer as they had memories around Sheffield once they were a researcher. I hope to show you how grateful I am as your student through the success I gained through my journey and academic life. I cannot forget any of the efforts you made for me.

Now, I thank my loving family, my grandmother *Durdu Özden*, my mother *Gülümser*, and my father, *Eyüp*. Thank you for every support, unconditional love and limitless prayers you gave me while raising me until this point of my life. I am who I am because of your presence. My brothers and my sister (*Ensar, Ömer Faruk and Dürdane*), I know I left you alone when I left home at 17 for higher education. We spent a long time apart, but I hope to have more time with you and share many memories in the rest of our lives. Thank you for being light in my life; I hope this will last forever.

One last thank you to my cat, *MissCat*, for being part of my life for the last one year. She is one of the light and joy in the thesis writing process. She came to the table whenever she felt I needed to take a break. Even today, while almost writing this letter, she jumped in front of the screen. I pray to have your purrs and meows all my life.

Last but not least, a huge thanks is to me. I spent such a long time without my family, and I had the opportunity to visit them only for small times as holidays. Please, be a nice person to yourself, you know that you have faith for yourself, and you fought for overcoming any hardship in your life. Remember these days, how hard and stressful they were in that time. But you managed, you stood by yourself and for yourself because you were the only source of your future. You have been by yourself since you were 17. People came and left but you stayed all the time. Please, remember that you succeeded when you were surrounded with lots of tears, stresses, hardships, and a little joy. All the tears, loneliness, depression, hard work, and all experiences... Countless things you went through those made you the woman, researcher, and scientist you are now. Always be grateful for what you have and be proud of yourself since you made this journey with your power. Remember to walk pass through the mountains, great places from all over the world, be with people, know them, learn from them, and find joy from any moment you have, because you deserve all of the joy. Do not forget you are a human and be a good example for the future girls in society, always show them what they can achieve when they work hard and when they really want. I would like to write here that I desperately desire to be a great teacher, lecturer, researcher and academic for the world where I am remembered for long time with my works and produced research after I left this world. But I also would like to be great person in the society to be a precious example for people around me. I hope that they can remember me not only with my professional achievements but also with my personality and as a good member of society.

I would like to finish with a verse:

``Moses prayed, My Lord! Uplift my heart for me, and make my task easy, and remove the impediment from my tongue so people may understand my speech.`` in Surah Taha (25-28). I hope to inform and reach to my audience throughout my personal and professional life.

Şifa Gül DEMİRYÜREK

23/12/2022

Adana

List of Publications

- 1- S. G. Demiryurek, A. Krynkin, and J. Rongong, "Non-linear metamaterial structures: Array of particle dampers," *Proc. Int. Congr. Acoust.*, vol. 2019-Septe, no. September, pp. 4878–4884, 2019.
DOI: 10.18154/RWTH-CONV-239301
<https://publications.rwth-aachen.de/record/769712>
- 2- S. G. Demiryurek, A. Krynkin, and J. Rongong, "Modelling of Nonlinear Dampers Under Low-Amplitude Vibration," in *ACOUSTICS 2020*, 2020, vol. 42.
<https://www.ioa.org.uk/catalogue/paper/modelling-nonlinear-dampers-under-low-amplitude-vibration>
DOI: 10.25144/13356
- 3- S. G. Demiryurek and A. Krynkin, "Low-Frequency Broadband Vibration Dampers from Nonlinear Structures with Metamaterial Properties," in *Proceedings of the Institute of Acoustics*, 2021, vol. 43.
<https://www.ioa.org.uk/catalogue/paper/low-frequency-broadband-vibration-dampers-nonlinear-structures-metamaterial>
DOI: 10.25144/13760
ISBN: 9781713841500
ISSN: 14786095
- 4- S. G. Demiryurek and A. Krynkin, "Low-Frequency Broadband Vibration Damping Using the Nonlinear Damper with Metamaterial Properties," in *DAGA 2021*, 2021, pp. 94–96.
ISBN: 978-3-939296-18-8
https://pub.dega-akustik.de/DAGA_2021/data/daga21_proceedings.pdf

Declaration

I, the author, Sifa Gul Demiryurek confirm that the Thesis is my own work. I am aware of the University's Guidance on the Use of Unfair Means (www.sheffield.ac.uk/ssid/unfair-means).

This work has not previously been presented for an award at this, or any other, University.

Table of Contents

Abstract.....	iii
Acknowledgement	v
List of Publications	viii
Declaration.....	ix
Table of Contents.....	x
List of Tables	xv
List of Figures	xvii
Nomenclature	xxiii
Symbols	xxiii
Acronyms	xxvi
Chapter 1: Introduction	1
1.1- Aims	5
1.2- Objectives	6
1.3- Thesis Outline and Brief Summary of Chapters.....	6
Chapter 2: Literature Review	9
2.1- Vibration and Mechanical Systems.....	10
2.2- Damping Schemes.....	11
Evaluation of Passive Dampers	12
2.3- Granular Structure-Based Dampers: Impact Dampers to Particle Dampers	13
Experimental and Analytical Approaches to the Granule-Based Dampers	19
Numerical and Analytical Approaches to the Granule-Based Dampers	23
Amplitude Dependent Character of Granular Packing	26
Application Areas of the Impact Dampers	29
Application Areas of the Particle Dampers	30
2.4- Periodic Structures.....	31
Analytical Expression of Periodicity	34
Mass-spring-damper Systems and Coupled Resonators	40
Bragg Scattering	44
Negative Effective Material Properties.....	45
2.5- Metamaterials.....	49
Vibro-acoustic Applications of Metamaterials.....	53

2.6- Knowledge Gap and Significance of This Research.....	54
Chapter 3: Granular Structures and Analysis Methods	56
3.1- Classification of Granular Structures	57
3.2- Interactions Between the Granules in a Packing	58
Coefficient of Friction and Force Interactions Between Granules.....	58
Coefficient of Restitution	61
Gliding	64
Packing of Multiple Granular Structures: Segregation	65
Packing of Multiple Granular Structures: Coordination Number	66
Packing of Multiple Granular Structures: Wave Propagation.....	67
Phases in the Dynamics of the Granular Materials.....	68
Fluidisation.....	69
Stick and Slip Motion	70
Collision and Deformation	72
3.3- Design and Study Options for Granular Structures	74
DEM (Discrete Element Model)	74
3.4- Modelling of Contact Mechanisms Between Granules	75
Hertz-Mindlin Contact Theory	77
Linear Spring Contact Theory.....	78
Evaluation of Contact Analysis. Model selection	79
3.5- Excitation Conditions and Granular Structure Behaviour.....	81
3.6- Discrete Element Modelling of the Spherical Particles Using EDEM	85
Modelling in EDEM.....	85
3.7- Impact of Granular Structure Size.....	89
3.8- Impact of the Friction Coefficient in Granular Contact	93
3.9- Equivalent Solid Medium Characterisation of Granules in a Packing.....	95
3.10- Derivations for the Granular Packing.....	97
Step-by-Step Calculation Procedure for the Equivalent Isotropic Solid Structure	100
Metal Granules Equivalent Material Properties	101
Viscoelastic Granules Equivalent Material Properties.....	105
Iteration-based Analysis of Isotropic Equivalent Structure Calculation	110
3.11- Conclusion of the Chapter	113
Chapter 4: Specification of the Resonator	115
4.1- Broadband Absorption Using Resonators.....	115

4.2- Numerical Simulation with COMSOL Multiphysics.....	119
4.3- Numerical Model of the Host Structure	120
4.4- DMTA Testing of 3D-Printed Samples of the Resonator Material.....	122
4.5- Geometry of the Resonator. Particle Damper	125
4.6- Numerical Model of the Resonator	126
4.7- Investigation of Resonator Properties	131
4.8- Conclusion of the Chapter	133
Chapter 5: Periodically Arranged Locally Resonating Structures.....	135
Metamaterials and Subunits.....	135
Dynamic Vibration Absorption and Periodically Arranged Resonators	137
5.1- 1D Periodic Array of Resonators.....	138
1D Periodic Array of Unit Cells.....	138
Periodically Arranged Resonators.....	145
5.2- 1D Periodic Arrangement of Beam with Resonators.....	150
Periodically Arranged Single Resonator on Beam.....	152
Periodically Arranged Multiple Resonator on Beam	154
5.3- Conclusion of the Chapter	163
Chapter 6: Dynamic Absorption Using Locally Resonating Structures	165
6.1- Vibration Absorption Using Locally Resonating Structures	165
6.2- Numerical Analysis of Finite Structure Modelling	166
Single Resonator Impact on the Base Structure	166
Multiple Resonators Impact on the Base Structure.....	168
6.3- Generating a Frequency Gap Using Resonators	173
6.4- Validation of Base Structure Analysis	176
6.5- Experimental Analysis of Resonating Structures	181
Individual Resonator Testing and Variation of Resonance Properties	181
Response of Single Resonator Attachment on the Beam	186
Response of Multiple Resonators Arrangement on the Beam	188
6.6- Numerical Investigation of Modified Resonators.....	192
6.7- Conclusion of the Chapter	196
Chapter 7: Dynamic Absorption Using Particle Filled Resonators	198
7.1- Equivalent Material Properties.....	199
Equivalent Material Properties for Metallic Granules	200
Equivalent Material Properties for Viscoelastic Granules	202

Loss Properties of the Granules	205
7.2- Periodically Arranged Nonlinear Dampers	208
Single Resonator Impact on the Base Structure	209
Multiple Resonators Impact on the Base Structure.....	215
7.3- Numerical Analysis of Finite Beam and Resonator Filled with Metal Particles.....	223
Single Resonator Impact On the Base Structure.....	223
Multiple Resonators Impact on the Base Structure.....	228
7.4- Numerically Analysed Plastic Granule Filling.....	232
Single Resonator Impact on the Base Structure	232
Multiple Resonators Impact on the Base Structure.....	236
7.5- Experimental Results for the Resonators Filled with Steel Granules	239
Single Resonator Impact on the Base Structure	239
Multiple Resonators Impact on the Base Structure.....	244
7.6- Experimental Results for the Resonators Filled with Plastic Granules.....	248
Single Resonator Impact on the Base Structure	249
Multiple Resonators Impact on the Base Structure.....	254
7.7- Frequency Response of Resonators with Mixed Granule Attached Beam.....	256
Single Resonator Impact on The Base Structure.....	257
Multiple Resonators Impact on the Base Structure.....	259
7.8- Conclusion of the Chapter	262
Chapter 8: Conclusion.....	265
8.1- Main Conclusion of the Thesis.....	266
8.2- Future Research Ideas	268
References	270
Appendices.....	283
Chapter 3-Appendix.....	283
Appendix 3.1	283
Appendix 3.2	284
Chapter 4-Appendix.....	285
Appendix 4.1	285
Appendix 4.2	286
Appendix 4.3	287
Appendix 4.4: Height Calculation-MATLAB Code	288
Appendix 4.5: Contact Fit Calculation-MATLAB Code.....	288

Appendix 4.6	289
Polynomial Fit Data of D=11 mm	289
Polynomial Fit Data of D=22 mm	289
Polynomial Fit Data of D=50 mm	289
Polynomial Fit Data of D=66 mm	289
Chapter 5-Appendix	290
Appendix 5.1	290
Appendix 5.2	291
Appendix 5.3	291
Chapter 7-Appendix	292
Appendix 7.1	292
Appendix 7.2	293
Appendix 7.3: Loss Factor Calculation Methodology-MATLAB Code	294

List of Tables

Table 3. 1: Coefficient of Friction (static and rolling) values from a variety of sources.....	60
Table 3. 2: Coefficient of Restitution values from a variety of sources for spheres	64
Table 3. 3: Material and geometrical properties of the tube and the granules	79
Table 3. 4: Amplitude levels over the case numbers and granular structure materials	83
Table 3. 5: Variety of granular size for particles placed in the spherical cavity	87
Table 3. 6: Variety of granular sized for particles placed in the spherical cavity	90
Table 3. 7: Friction coefficient varieties over the case numbers.....	94
Table 4. 1: DMTA resulted ABS material properties.....	125
Table 4. 2: Corresponding eigenfrequency and mode shape details for the area ratio of 0.1	130
Table 5. 1: Unit cell eigenfrequency data at the first mode shape for $k=0.975$	139
Table 5. 2: Resonator attached unit cell eigenfrequency data at the first two mode shapes for $k=0.975$	145
Table 7. 1: Isotropic solid structure material properties for 62% steel-filled granular packing	201
Table 7. 2: Isotropic solid structure material properties for 47.5% acrylic plastic filled granular packing	203
Table 7. 3: Isotropic solid structure material properties for 7.5% POM-filled granular packing	204
Table A4. 1: Mesh details of the solid geometries	285
Table A4. 2: Material properties of the solid geometries	285
Table A4. 3: DMTA test results for ABS at 25°C	286
Table A4. 4: DMTA test results for PLA at 25°C	286
Table A4. 5: Mesh Properties of the Resonator	287
Table A4. 6: Material Properties of the Resonator	287
Table A4. 7: Polynomial Fit Calculated Values	289
Table A5. 1: Mesh properties of the unit cell (L=170 mm).....	290
Table A5. 2: Material Properties of the Unit Cell (L=170 mm).....	291
Table A7. 1: 10% Steel filling equivalent isotropic solid medium Young's Modulus.....	292

Table A7. 2: 25% Steel filling equivalent isotropic solid medium Young's Modulus	292
Table A7. 3: 35% Steel filling equivalent isotropic solid medium Young's Modulus.....	292
Table A7. 4: 45% Steel filling equivalent isotropic solid medium Young's Modulus	293
Table A7. 5: 10% AP filling equivalent isotropic solid medium Young's Modulus.....	293
Table A7. 6: 25% AP filling equivalent isotropic solid medium Young's Modulus.....	293
Table A7. 7: 35% AP filling equivalent isotropic solid medium Young's Modulus	294
Table A7. 8: 45% AP filling equivalent isotropic solid medium Young's Modulus.....	294

List of Figures

Figure 1.1: Impact dampers [4]	2
Figure 1.2: Particle dampers [4].....	2
Figure 2. 1: Particle Dampers (a) Impact Damper, (b) Multi-unit Impact Damper, (c) Particle Damper and (d) Multi-unit Particle Damper [4]	16
Figure 2. 2: Designed damper geometry with movable brackets [20]	21
Figure 2. 3: Categorisation of periodically arranged structures [72]	32
Figure 2. 4: 1D array with periodic placements, d is unit cell length, a is thickness [75].....	35
Figure 2. 5: Dispersion relation [75]	36
Figure 2. 6: Formation of bandgaps on a unit cell of Timoshenko beam; (a) shows simply supported beam without periodicity, (b) shows periodic masses on the unit cell, (c, d) shows periodic resonators [80].....	39
Figure 2. 7: Undamped mass-spring system	41
Figure 2. 8: Damped mass-spring system	41
Figure 2. 9: Forced-damped mass-spring system	42
Figure 2. 10: Coupled mass-spring system example for tuned resonators	43
Figure 2. 11: 2-DOF systems with (a) mass-in-mass and (b) mass-in-spring representations, similar to the figure in [90]	46
Figure 2. 12: Example of metamaterial [95].....	50
Figure 3. 1: An illustration of colliding structures	61
Figure 3. 2: Motion of the granules regarding the friction laws [103].....	64
Figure 3. 3: Oyama’s Cylindrical Drum (Segregation in Granules) [125]	65
Figure 3. 4: Travelling waves on the surface of granules at low amplitude [45]	67
Figure 3. 5: Travelling waves on the surface of granules at high amplitude [45]	68
Figure 3. 6: An illustration of stick and slip motion in granular packing [131]	71
Figure 3. 7: Stick-slip motion in granular packing	71
Figure 3. 8: Stick-slip motion in contour plot	72
Figure 3. 9: Ideal collision between two grains	73
Figure 3. 10: Overlap, displacement at the contact area	76
Figure 3. 11: Granular arrangement in the tube.....	80
Figure 3. 12: Granular structure behaviour for amplitude level changes [37].....	83
Figure 3. 13: Granular behaviour at different amplitude levels: (a) Velocity change over time, (b) Dimensionless energy distribution over time for packed granules	84
Figure 3. 14: The filled geometry for time precision analysis	87

Figure 3. 15: The time precision analysis of velocity	88
Figure 3. 16: The time precision analysis of dimensionless energy	89
Figure 3. 17: Various granular size filling details: (a) Dimensionless energy, (b) Velocity trends for a variety of granular size filling	91
Figure 3. 18: Coordination number distribution for R_1 -sized granular packing: (a) before the excitation, (b) steady state part	92
Figure 3. 19: Coordination number distribution for R_3 -sized granular packing	93
Figure 3. 20: Particle velocity (a) and number of granular collisions (b) at various friction coefficients	95
Figure 3. 21: Two spheres in contact, similar to Walton's case [56]	96
Figure 3. 22: Steel filling amounts: (a) is 10%, (b) 25%, (c) 35%, (d) is 45% and (e) is 62% filling amounts	102
Figure 3. 23: Steel filling at filling fraction of 10% in the cavity: (a) equivalent isotropic structure Young's Modulus and (b) average coordination number	103
Figure 3. 24: Steel filling at filling fraction of 25% in the cavity: (a) equivalent isotropic structure Young's Modulus and (b) average coordination number	104
Figure 3. 25: Steel filling at filling fraction of 62% in the cavity: (a) equivalent isotropic structure Young's Modulus and average (b) coordination number	104
Figure 3. 26: Acrylic plastic filling amounts: Figure (a) is 10%, Figure (b) 25%, Figure (c) 35%, Figure (d) is 45% and Figure (e) is 47.5% filling amounts	106
Figure 3. 27: Acrylic plastic filling at filling fraction of 10% in the cavity: (a) equivalent isotropic structure Young's Modulus and (b) average coordination number	107
Figure 3. 28: Acrylic plastic filling at filling fraction of 25% in the cavity: (a) equivalent isotropic structure Young's Modulus and (b) average coordination number	107
Figure 3. 29: Acrylic plastic filling at filling fraction of 47.5% in the cavity: (a) equivalent isotropic structure Young's Modulus and (b) average coordination number	108
Figure 3. 30: 7.5% POM particles filling amount	108
Figure 3. 31: POM filling at filling fraction of 7.5% in the cavity: equivalent isotropic structure Young's Modulus (a) and average coordination number (b)	109
Figure 3. 32: Equivalent Young's Modulus change trend for amplitude level-1 (a) and amplitude level-2 (b) for tubular structure	112
Figure 3. 33: Equivalent Young's Modulus change trend at amplitude level-1 for spherical structure	112
Figure 3. 34: Coordination number change trend for all cases	113
Figure 4. 1: Metamaterial formation using a mass-spring attachment on a beam [4]	117
Figure 4. 2: FRF of various situations: (a) increased DOF using equal absorbers, (b) additional damping on resonators, (c) varied eigenfrequency impact on FRF [157]	118
Figure 4. 3: Beam model in [mm] dimensions using COMSOL Multiphysics	120

Figure 4. 4: Bending modes of the beam; (a) the first mode, (b) the fifth mode	121
Figure 4. 5: 3D-printed test sample.....	123
Figure 4. 6: DMTA test machine (a and b) and 3D test sample mounted to the machine (a)	123
Figure 4. 7: Young's Modulus range of ABS and PLA from DMTA test at 25°C	124
Figure 4. 8: Spherical cavity eigenfrequency at interested mode shape, sizes in mm	127
Figure 4. 9: Geometry used for the analysis of quantifying the contact area	129
Figure 4. 10: Contact area and corresponding eigenfrequency for the geometries: (a) supportive base diameter 1 (11 mm), (b) supportive base diameter 1 (22 mm), (c) supportive base diameter 1 (25 mm), (d) supportive base diameter 1 (66 mm)	129
Figure 4. 11: The resonating damper geometry modelled in COMSOL Multiphysics	132
Figure 4. 12: Resonator mode shapes at various eigenfrequency levels (a-f)	133
Figure 5. 1: Boundary conditions of the unit cell: (a) periodic boundaries applied layers, (b) prescribed displacement applied layers	139
Figure 5. 2: Dispersion relations of unit cell sizes (a) 60 mm, (b) 70 mm, (c) 90 mm and (d) 110 mm	140
Figure 5. 3: Dispersion relations of unit cell sizes (a) 130 mm, (b) 150 mm and (c) 170 mm	141
Figure 5. 4: Conversion points through the first dispersion line for L=130 mm	142
Figure 5. 5: Evaluation of wave number (k) 0.05 on the dispersion relations with the mode shapes	143
Figure 5. 6: Bending mode transition through the Bloch wave numbers for L=130 mm	144
Figure 5. 7: Resonance of the inclusion on the unit cell size (L) (a) 130 mm, (b) 150 mm, and (c) 170 mm	147
Figure 5. 8: Dispersion relations of resonator attached unit cell (a) 60 mm, (b) 70 mm, (c) 90 mm and (d) 110 mm	147
Figure 5. 9: Dispersion relations of resonator attached unit cell (a) 130 mm, (b) 150 mm, (c) 170 mm	148
Figure 5. 10: Resonating inclusion impact on the unit cell (L=130 mm) at $k=0.05$	149
Figure 5. 11: Dispersion relations of bare beam unit cell modelling	151
Figure 5. 12: Representation of mode shape corresponding to the diagonal line on dispersion relations.....	152
Figure 5. 13: Dispersion relations of single resonator attachment on bare beam unit cell modelling	153
Figure 5. 14: Corresponding mode shape in the diagonal line on the dispersion relation	154
Figure 5. 15: Dispersion relations of double-resonator attachment on bare beam unit cell modelling (d=30 mm)	155
Figure 5. 16: Dispersion relations of double-resonator attachment on bare beam unit cell modelling: (a) d=90 mm and (b) 130 mm	156
Figure 5. 17: Dispersion relations of three-resonator attachment on bare beam unit cell modelling: (a) d=90 mm and (b) 130 mm	158
Figure 5. 18: Dispersion relations of four-resonator attachment on bare beam unit cell modelling: (a) d=70 mm and (b) 90 mm.....	160

Figure 5. 19: Dispersion relations of five-resonator attachment on bare beam unit cell modelling: (a) $d=70$ mm and (b) 90 mm.....	162
Figure 6. 1: Frequency response of empty single resonator attachment on the beam	167
Figure 6. 2: 70 mm attachment resonator impact on the beam	168
Figure 6. 3: Frequency response of two empty resonators attachment on the beam	169
Figure 6. 4: Frequency response of three empty resonators attachment on the beam	170
Figure 6. 5: Frequency response of four empty resonators attachment on the beam	171
Figure 6. 6: Frequency response of five empty resonators attachment on the beam	173
Figure 6. 7: Comparison of various cases by reading the acceleration away from the centre of the beam	174
Figure 6. 8: Experimental rig diagram	178
Figure 6. 9: Beam model for production	178
Figure 6. 10: Bare beam horizontal and vertical test results	180
Figure 6. 11: 3D-printed and maintained resonators	181
Figure 6. 12: Shaker-Beam-Individual resonator setup	182
Figure 6. 13: Frequency response of each resonator (a) 0.05 - 1.2 kHz, (b) close-up looking	184
Figure 6. 14: Small-scaled beam dynamic test results	185
Figure 6. 15: Single resonator attachment on the beam frequency response analysis	187
Figure 6. 16: Two-resonator attachment on the beam frequency response analysis	188
Figure 6. 17: Three-resonator attached beam frequency response analysis	189
Figure 6. 18: Four-resonator attachment on the beam frequency response	190
Figure 6. 19: Five-resonator attachment on the beam frequency response	191
Figure 6. 20: Two-resonator placement on the beam with individual eigenfrequencies	194
Figure 6. 21: Three-resonator placement on the beam with individual eigenfrequencies	194
Figure 6. 22: Five-resonator placement on the beam with individual eigenfrequencies	196
Figure 7. 1: Steel filled (62%) resonator in (a) EDEM, (b) COMSOL modellings	201
Figure 7. 2: Acrylic plastic filled (47.5%) resonator in (a) EDEM, (b) COMSOL modellings	203
Figure 7. 3: POM filled (7.5%) resonator in (a) EDEM, (b) COMSOL modellings	204
Figure 7. 4: Hysteresis loop for the granular packing.....	208
Figure 7. 5: Equivalent structure added single resonator placed unit cell analysis: (a) 10% steel filling, (b) 35% steel filling, (c) 62% steel filling	210
Figure 7. 6: Interested mode shapes of the unit cell with steel-filled single resonator: (a-b) 10%, (c-d) 35%, and (e-f) 62% filled cases	211
Figure 7. 7: Equivalent structure added single resonator placed unit cell analysis: (a) 10% acrylic plastic filling, (b) 35% acrylic plastic filling, (c) 47.5% acrylic plastic filling	213

Figure 7. 8: Interested mode shapes of the unit cell with acrylic plastic filled single resonator: (a-b) 10%, (c-d) 35%, and (e-f) 62% filled cases	214
Figure 7. 9: The 10% steel-filled multiple resonators in array with 70 mm distance: (a) two resonators, (b) four resonators, (c) five resonators	215
Figure 7. 10: Mode shapes of the unit cell with five resonators filled with 10% steel particles. Bloch wave number $k=0.2$	216
Figure 7. 11: The 62% steel-filled multiple resonators in array with 70 mm distance: (a) two resonators, (b) four resonators, (c) five resonators	217
Figure 7. 12: Interested mode shapes of the unit cell with 62% steel-filled five-resonator modes.....	218
Figure 7. 13: The 10% acrylic plastic filled multiple resonators in an array with 70 mm distance: (a) two resonators, (b) 4 resonators, (c) five resonators.....	219
Figure 7. 14: Interested mode shapes of the unit cell with 10% acrylic plastic filled five-resonator modes	220
Figure 7. 15: The 47.5% acrylic plastic filled multiple resonators in an array with 70 mm distance: (a) two resonators, (b) 4 resonators, (c) five resonators	221
Figure 7. 16: Interested mode shapes of the unit cell with 47.5% acrylic plastic filled five-resonator modes ..	222
Figure 7. 17: 10% steel granule-filled single resonator placement cases	224
Figure 7. 18: 25% steel granule-filled single resonator placement cases.....	225
Figure 7. 19: 35% steel granule-filled single resonator placement cases	226
Figure 7. 20: 45% steel granule-filled single resonator placement cases	227
Figure 7. 21: 62% steel granule-filled single resonator placement cases	228
Figure 7. 22: Steel granule-filled two-resonator placement cases	229
Figure 7. 23: Steel granule-filled three-resonator placement cases	230
Figure 7. 24: Steel granule-filled four-resonator placement cases.....	230
Figure 7. 25: Steel granule-filled five-resonator placement cases.....	231
Figure 7. 26: 10% acrylic plastic granule filled single resonator placement cases.....	232
Figure 7. 27: 25% acrylic plastic granule filled single resonator placement cases.....	233
Figure 7. 28: 35% acrylic plastic granule-filled single resonator placement cases	234
Figure 7. 29: 45% acrylic plastic granule-filled single resonator placement cases	234
Figure 7. 30: 47.5% acrylic plastic granule filled single resonator placement cases	235
Figure 7. 31: 7.5% POM granule filled single resonator placement cases	236
Figure 7. 32: Acrylic plastic granule-filled two-resonator placement cases.....	237
Figure 7. 33: Acrylic plastic granule-filled three-resonator placement cases.....	237
Figure 7. 34: Acrylic plastic granule filled four- and five-resonator placement cases.....	238
Figure 7. 35: 10% steel granule-filled single resonator placement cases	240
Figure 7. 36: 25% steel granule-filled single resonator placement cases.....	241
Figure 7. 37: 35% steel granule-filled single resonator placement cases	241
Figure 7. 38: 45% steel granule-filled single resonator placement cases.....	242

Figure 7. 39: 62% steel granule-filled single resonator placement cases	243
Figure 7. 40: Steel granule-filled two-resonator placement cases	244
Figure 7. 41: Steel granule-filled three-resonator placement cases	245
Figure 7. 42: Steel granule-filled four-resonator placement cases.....	246
Figure 7. 43: Steel granule-filled five-resonator placement cases.....	247
Figure 7. 44: Steel granule (130 gr) filled single resonator and five-empty-resonator placement cases.....	248
Figure 7. 45: 10% acrylic plastic granule filled single resonator placement cases	250
Figure 7. 46: 25% acrylic plastic granule filled single resonator placement cases	250
Figure 7. 47: 35% acrylic plastic granule-filled single resonator placement cases	251
Figure 7. 48: 45% acrylic plastic granule-filled single resonator placement cases	252
Figure 7. 49: 47.5% acrylic plastic granule-filled single resonator placement cases	252
Figure 7. 50: 7.5% POM granule filled single resonator placement cases.....	253
Figure 7. 51: Acrylic plastic granule-filled two-resonator placement cases	254
Figure 7. 52: Acrylic plastic granule-filled three-resonator placement cases	255
Figure 7. 53: Acrylic plastic granule filled four- and five-resonator placement cases.....	256
Figure 7. 54: Mixed granule-filled resonator placement cases.....	257
Figure 7. 55: Mixed granule-filled resonator placement cases	258
Figure 7. 56: Mixed granule-filled resonator placement cases.....	259
Figure 7. 57: Mixed granule-filled two-resonator placement cases.....	260
Figure 7. 58: Mixed granule-filled three-resonator placement cases	261
Figure 7. 59: Mixed granule-filled four- and five-resonator placement cases.....	262
Figure A3. 1: Equivalent Young's Modulus vs Coordination Number Evaluation for Metal Particle Filling	283
Figure A3. 2: Equivalent Young's Modulus vs Coordination Number Evaluation for Viscoelastic Particle Filling	284
Figure A4. 1: Meshed solid structures	285
Figure A4. 2: Meshed Resonator	287
Figure A5. 1: Meshed unit cell (L=170 mm)	290
Figure A5. 2: Multiple resonator arrangement (L=90 mm) in the thickness mode : (a) two-resonator, (b) three-resonator, (c) four-resonator, (d) five-resonator arrangement.....	291

Nomenclature

Symbols

e	coefficient of restitution
L	unit cell length, m
f	frequency, 1/s
ω	angular frequency, rad
Λ	wavelength, m
ρ	density
u	displacement through x-axis, m
t	time, s
φ	phase change of the wave
v_φ	phase velocity, m/s
α	logarithmic decay rate
β	phase difference
μ	wave propagation constant
Λ	period length of wave
c	wave speed in solid structure, m/s
f_e, F	external force, N
F_n	normal force, N
F_t	tangential force, N
V	velocity, m/s
δ	overlapping amount, m
δ_n	normal overlapping amount, m
δ_t	tangential overlapping amount, m
R, R^*	radius of the granular contact, m
t_R	Rayleigh time step, s
D_1, D_2, D_3	particle diameter, m
μ, ν	Lamé Moduli

C_N	coordination number
Φ_F	filling fraction
Φ_P	packing fraction
k	wave number
K	stiffness matrix
M	mass matrix
C	damping matrix
$\Gamma X M \Gamma$	Brillouin Zone limits
$q(t)$	displacement change over time
k_c	coupled stiffness
μ_s, μ	friction coefficient
H_{ij}	frequency response function
A_1, A_2	amplitude
Γ	normalised acceleration
g	gravity acceleration, m/s^2
$ K $	wave vector
β	structural coefficient given by Rao
η	loss factor
Hz	Hertz, $1/s$
kHz	kilohertz, $1/s$
E	elasticity modulus, Pa
G	shear modulus, Pa
m	mass, kg
k_{eff}	effective stiffness
m_{eff}	effective mass
ν	Poisson's Ratio
P	pressure
K	bulk modulus
K^*	effective bulk modulus
N	number of granules in a packing

V	volume of an enclosed geometry
V_P	volume of a particle
E'	storage modulus
E''	loss modulus
E^*	equivalent Young's Modulus
ρ^*	equivalent density
ν^*	equivalent Poisson's Ratio
I	second moment of area
Dw	energy dissipated per cycle
U_{max}	peak strain energy
μm	micrometre
mm	millimetre
θ	Coulomb's angle
mV	millivolt
dB	decibel
$3D$	three-dimensional
J	Joules
$d.../dt$	time derivative of ...

Acronyms

DEM	Discrete Element Method
FEM	Finite Element Method
DMTA	Dynamic Mechanical And Thermal Analysis
MPC	Model Predictive Methods
TLD	Tuned Liquid Dampers
TMD	Tuned Mass Dampers
SDOF	Single Degree Of Freedom
MDOF	Multi-Degree Of Freedom
MD	Molecular Dynamics
NES	Nonlinear Energy Sink
NOPD	Non-Obstructive Particle Dampers
FFT	Fast Fourier Transform
DARPA	Defence Advanced Research Projects Agency
PMMA	Polymethyl Methacrylate
PTFE	Polytetrafluoroethylene
POM	Polyoxymethylene
ABS	Acrylonitrile Butadiene Styrene
PLA	Polylactic Acid

Chapter 1: Introduction

Mechanical oscillations are not desired situations on solid structures in general since they affect structural health and, as a result, reduce the lifespan. Free and forced vibrations are two primary structural oscillations classified due to their attenuation sources. Free vibration is related to the disturbance from outside which initiates the oscillation of a structure. Self-sustained oscillation might induce resonance of the structures. On the other hand, forced vibration is related to the continuous external force which impacts the structure. Vibrational issues are typical disaster causes, as happened at the Tacoma Narrows Bridge, the most famous one in free vibration caused failures [1]. In order to mitigate undesired consequences, dynamic responses to the structure must be understood and analysed carefully. Then, vibration dissipation techniques may be required to be applied to the structures in both free and forced vibration cases. For example, forced vibration has been successfully treated by the application of the particle dampers [2] which are of main interest in this research. Vibrational issues are typical disaster causes, as happened at the Tacoma Narrows Bridge, the most famous one in free vibration caused failures [3]. In order to mitigate undesired consequences, dynamic responses to the structure must be understood and analysed carefully. Then, vibration dissipation techniques may be required to be applied to the structures.

Structural vibration has been an interestingly not well-understood issue attempted to overcome for many years. For instance, it is explained using the definitions of dynamic processes like impact interactions in the bodies as a part of Vibro-impact dynamics [4]. Vibro-impact dynamics suggest that all structures are made of tiny granules that interact in the event of oscillation and dissipate the excitation energy through the structural body. These interactions are used to identify the reasons for the excitation-induced situations to develop damping solutions to reduce their outcomes. Depending on the applicability, the damping methods are classified into two groups with their energy requirement mechanisms: Active and passive damping methods [5].

Passive damping methods are the primary energy mitigation option that does not require additional/external energy for the damping mission. They are designed for particular

conditions like frequency range or certain excitation amplitude. When the structure is under the minimum required external conditions in the damper's primarily defined certain levels, the passive damper automatically absorbs the undesired energy. However, the passive dampers' effective working width (frequency range or amplitude barrier) is limited to the resonant frequencies or their designated frequencies [1]. Therefore, the passive damping methods, with their ease of usage and implementation, inexpensive and accountable aspects, attract the attention of the researchers on these types of dampers [1].

A passive damping method was developed by placing a single granule in a cavity that compromises the impact (particle) damper, as shown in Figure 1.1. Damping was succeeded with the motion of that single granule through its impact relations with the cavity walls.

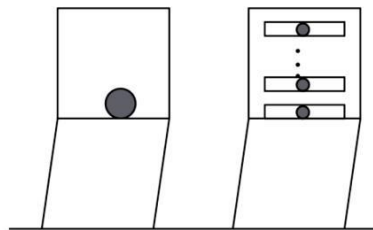


Figure 1.1: Impact dampers [4]

Multiple granules (Figure 1.2) were placed in a cavity (or cavities) to manage the passive damping in the further developed version of the impact dampers. The damping is succeeded through inelastic collisions and momentum exchanges between collided bodies [1]. The granules in the cavity might have the same material properties as the cavity, but it is not necessarily a situation; they might be in different materials too. When the particles have the same properties as their substrate material, they can be counted as a block of that material. For instance, granules made of glass have the same properties as glass blocks.

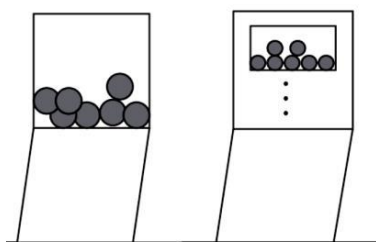


Figure 1.2: Particle dampers [4]

However, the particle dampers achieve improved damping effectivity in a limited range of excitation amplitudes (or lesser extent, frequency levels). Therefore, variability of the effective damping properties depends on environmental conditions like the excitation amplitude or the frequency range of excitation. This undesired situation is called the nonlinearity of the particle dampers. The nonlinearity of the granular structures is a complicated phenomenon for the particle dampers, which has been stated as changing the state of packed granules from solid-state to gas-state depending on the external conditions [6], [7]. This aspect of particle dampers raises various issues besides damping effectivity. Additionally, when these dampers are added to the structures, they add weight to that structure which is not a desired situation compared to their effective working ranges.

In addition to the particle damping, resonating substructure attachments on the structure provide extraordinary energy dissipation behaviour. When the main structure is under dynamic excitation or free vibration conditions, the attachments as resonating substructures help dissipate the structural energy by taking the energy on their body to resonate. Therefore, the primary structure energy is dissipated. The critical phenomena are the attachment structures as dampers and their resonating properties.

Further development of the resonating structure usage is to model them in a periodic arrangement. When these structures are arranged periodically, they tend to reduce the structural energy by accomplishing coupling between the resonators. This way, depending on the periodic arrangement, they absorb more energy from the main structure. Periodically arranged resonators have shown reasonably beneficial and applicable character, such as sound transmission, wave retarding, acoustic liners, energy dissipation, and damping abilities are among them. When these structures are designed in less than the wavelength for the main structure or illustrating similar eigenfrequencies to where they are attached, they are called metamaterials [8]. Metamaterials introduce effective material properties and structural behaviours when using a primary structure.

A particular study related to metamaterials has dealt with acoustic wave propagations. This particular metamaterials group is called elastic wave absorbers (elastic metamaterials) [9]. In the application, an acoustic metamaterial beam is included with small isotropic subsystems, which are elementary (or unit) cells within the periodic arrangement of the local

resonators. The ideal modelling techniques illustrate the dispersion properties as the inertial forces act against the external forces, and the elastic wave propagation is prevented forward [10]. The solution for these subsystems (unit cells) formulates the frequency bands, including pass and stop bands. While the metamaterial beam performs as a vibration absorber, it also shows negative effective material properties corresponding to the bandgap (stopband). As a result, the structure behaves like it has a reduced mass at particular frequency levels.

Their knowledge shows that particle dampers and metamaterials have been developed to dissipate structural vibration efficiently. Therefore, this research project aims to defect the structural vibration to a broader extent using the granular structures placed with nonlinear resonating dampers. Both fully and partially filled resonating dampers are periodically arranged to research the broader range of capabilities in damping. This study introduces the possibility of using particle dampers as a metamaterial building block to affect more comprehensive frequency dissipation ranges. According to that, analytical and numerical studying methods are developed to define an equivalent material from the properties of the granular structures placed in a cavity. The equivalent medium characterisation is included with numerical analysis and analytical calculations on top of the data received from that numerical analysis. The numerical step of the material characterisation includes the Discrete Element Method (DEM) to apply this continuum structure to the Finite Element Method (FEM) analysis procedure. Modelling the granular structures and studying the cavity's distinct behaviour and the particles' physical interactions are modelled and analysed using EDEM V2021.1, a DEM-based commercial software. The qualified data from EDEM is processed according to the developed methodology, and equivalent structure material properties are calculated using the analytical calculations deriving the granular structure's nature. To sum up, from the individual granular structure to an isotropic solid medium, the physical and mechanical properties of the granules are used in the procedure.

COMSOL Multiphysics V5.0, a Finite Element Method-based commercial software, has been used for continuum structure modelling of the granules as equivalent isotropic material. Since the studying methods using DEM for granular structures require a great deal of computational cost, modelling these structures as an equivalent medium and providing a studying method using FEM is believed and proved to be more convenient [6]. FEM is also

used for the finite beam-damper arrangements to illustrate the pass, stop band properties, and model the motivated particle damper-resonators. The dynamic structure model is achieved within FEM software using the unique unit cell modelling methodology Bloch-Floquet Method. The effect of the vibration absorbing mechanism of the periodically arranged particle damper-resonators is illustrated in dispersion figures to evaluate and compare the filling types, variability of the periodic arrangement, and filling fractions. In order to validate this methodology and results, an experimental rig has been designed and produced, which contains a fixed-fixed end conditioned beam with a periodic arrangement of particle dampers modelled with the same procedure in the numerical studies. Different granular structures have investigated a wide frequency range and amplitude levels to evaluate their energy dissipation character. Therefore, this research study has shown the abilities of application for a derived and progressed methodology to study nonlinear damping phenomena.

Overall, the research question for thesis to be scientifically studied is

"If particle dampers were evolved into the metamaterial, how this novel arrangement would affect the overall behaviour of the vibratory structure and how the nonlinear behaviour would contribute to the metamaterial performance?".

1.1- Aims

According to the introductory information, this research project aims to investigate the capabilities of the granular structure-based nonlinear damper in a broader range of frequencies by developing these structures as metamaterials.

The particle damper cavity is produced as resonating structures while aiming to improve the main structure's stability properties under low amplitude excitation levels. Various granules in different sizes and materials are aimed to question how much they widen the tuned frequency range and increase the energy dissipation from the primary structure. Since the research has been completed over the years is not enough to answer the vibration dissipation, and particle dampers are not a perfect solution to this issue; this novel research is a proposed option to the gap in the literature. The researcher (Sifa Gul Demiryurek) prepares the gap by considering the particle damper and metamaterial applications as a

coupled phenomenon that would be a beneficial solution to vibration-related situations. This research aims to achieve an effective and applicable damper solution using metamaterial understanding by proving the proposed idea in numerical, analytical, and experimental approaches.

The list of objectives was reduced and clarified to improve the link with the main aim of the project which is given before the list of objectives in the main text.

1.2- Objectives

- Understanding of the states of the particle behaviour starting from the theoretical view and proving their states in numerical and experimental studies,
- Developing a method for the equivalent model of granular packing by working on the theory of particle interactions analytically,
- Introducing a numerical method to model the granules and an equivalent isotropic solid structure, which corresponds to the granules, using numerical (DEM-FEM) and analytical method,
- Investigating the particle damping phenomena and the nonlinearity using numerical and experimental methods with various materials of particles,
- Modelling and investigating the effect of periodically arranged resonators in the low amplitude excitation using the numerical approach,
- Modelling and investigating the effect of periodically arranged resonating particle dampers in the low amplitude excitation using the numerical approach,
- Studying different diameters of metallic and viscoelastic granules in the resonating dampers to compare their benefits in the vibration damping and energy dissipation using numerical and experimental approaches.

1.3- Thesis Outline and Brief Summary of Chapters

The research study is conducted in the light of aims through the followed objectives. The research completed over time is divided into chapters to be analysed wisely.

Chapter 1 is prepared to introduce the particle dampers, local resonators, and metamaterials. This chapter explains the research statement, research aims, and objectives. The outline for the thesis is placed at the end of this chapter.

Chapter 2 acknowledges the reader about the literature behind the proposed research, the Vibro-impact theory and impact dampers with industrial applications. Vibration and dissipation techniques are introduced to divide the particle damper's place in the vibration defeating options. Then, periodicity and periodically arranged structures are explained with research examples. Bloch-Floquet Theory applications, Brillouin Zone and locally resonant structures are mentioned in addition to metamaterials and their vibro-acoustic applications.

Chapter 3 is designed to give the readers theoretical information about the granular structures. According to the knowledge given in this part, the granular structures have interactions in their enclosing cavity under the external source oscillations. Considering this, analytical and theoretical information on the granular interaction in packing is defined in this chapter. From the single-particle state to the multiple particle interactions and their relationship with the surrounding volume elements are explained with the derivations of mathematical understanding using Hertz's Contact Theory in EDEM V2021.1. The data extracted from the numerical simulations are post-processed to calculate the isotropic solid medium properties.

Chapter 4 informs about the locally resonant structures and resonators. Theoretical information leads to the resonating damper casing, a 3D printed structure. 3D-printed structures tend to behave differently than their original material properties. Therefore, a sample is printed out from the Ultimate Cura 3D printing structure to test the sample. The material properties of the printed structure are revealed using the DMTA (Dynamic Mechanical Thermal Analysis) testing option. This chapter defines the procedure of the material characterisation of the locally resonant damper casing.

Chapter 5 informs the dispersion analysis of periodically arranged resonator impacts on the beam. Floquet-Bloch Theory is the method of the chapter, and the resonators are studied without the granular structure attachment within this chapter.

Chapter 6 introduces the numerical (based on COMSOL Multiphysics V5.0) and experimental analysis of a locally resonating damper as an empty structure in the frequency range of 0.05-

1.2 kHz. Eigenfrequency analysis is introduced for the main structure (the beam) and the resonator in this chapter.

Chapter 7 is designed for the numerical and experimental frequency sweep analysis of the particle damper attachment on the beam at various filling fractions while the periodically arranged particle damper dispersion analysis. Since the experimental setup is small enough to consider a finite rather than an infinite structure, numerical modelling of the periodically arranged particle dampers on the finite beam is explained.

Conclusion **Chapter 8** has information on the conclusion of this research study. The research outcomes are evaluated overall, and some interesting points about the research methodology and findings are discussed. Additionally, future research suggestions are given in this chapter.

Chapter 2: Literature Review

The research study has been designed around the particle dampers and the locally resonant structures. Therefore, the particle dampers have been introduced in this chapter after evaluating the passive damping techniques. Theories on granular structures and specific relations between granular structures in a pack are studied both in this chapter and in the further chapters. The literature review presents research options for the granular structures in the following subsection. A locally resonating structure that used to be filled with granules to treat the vibration amplitude in the further chapter has been introduced here. As given in this chapter, these structures are studied as finite or periodically arranged infinite structures in the literature. In this research study, the locally resonating structure has been used to dampen the excitation energy, and its tunability has been performed. Thus, specific literature examples on how to treat vibration issues using the locally resonating structures have a special place in this thesis.

Particle dampers are the structures that provide a cavity/cavities enclosure and multiple granular structures; with this understanding, the review of the particle dampers and the variety of granular structures involving dampers are given in this chapter. The research of the particle dampers through the previous studies is given to engage the topic by starting from design methodologies to dissipative properties of these dampers.

Periodicity in the structures and periodic arrangement properties with their physical and mechanical penetration with other structures are reviewed in this chapter to give insightful background to the recent research study. In addition, a specific term is used here: Metamaterials are the structures that have properties of modelling by humans that cannot be found in nature. Background for metamaterials and their properties for mechanical excitation issues are given with provisional information in the following subchapters, both in the literature review and in the following chapters in the thesis.

Most of the background related to the thesis is given with theoretical information in the literature review. Revealing and increasing the understanding and knowledge are aimed in this thesis chapter.

2.1- Vibration and Mechanical Systems

In order to understand the damping phenomena, the structural properties and vibration-related behaviour should be analysed first. A mechanical system consists of three main parts: input, process, and output: The *input* information is the motion, force, or power sources of the system, which are inclusions. The *output* of a mechanical system is relatively achieved change upon the input of the system. The *process* is the proceeding mechanism between the system's input and output. These definitions can be exemplified with a combustion engine. The fuel ignites the gas mixture, and there is an expansion of the burnt gas. The expansion force moves the piston down. Under the effect of this motion, the crank and the sliders move rotationally. This example shapes and images a mechanical system as the ignited fuel is the input; conversion in the force and motion are the process, and the rotational motion is the output for the system.

Structural vibration is an undesired *input* issue aimed at defeating using various techniques through vibration damping applications. The hypothesis has been set to define the relationship between vibration input and impact outcomes on the structures. In order to approach structural vibration, the vibro-impact theory has been introduced as a step.

The vibro-impact theory was defined as a nonlinear phenomenon depending on the frictional and contact impacts between the elements; since then, it has been defined using the nonlinear differential equations. Interactions between the bodies are defined in the impact events [11]. An assumed system in the vibro-impact theory works with the energy losses through the impact interactions, characterised by the measurement using the coefficient of restitution (e). Therefore, in many cases, this theory has been used in order to reveal the energy dissipation of the systems. Several examples of the applications can be accounted with the vibro-impact theory: blood flow modelling in the veins, turbomachinery system developments, heat exchanger tubes with aerodynamic excitation, impacted ships by floated ice, rubbing effects between stator and rotor blades in the machinery, especially in the turbomachinery, etc. [12].

One of the most successful vibro-impact interaction processes has been defined in the vibration suppressing method, specifically in the passive damping method [11]. Therefore,

the most relevant application using the vibro-impact theory has been the particle damping systems where the granular structures maintain the structural damping issues. In particular, it is claimed that impact dampers are accepted as an effective method of passive damping [12].

2.2- Damping Schemes

Structural vibration has an important place in engineering applications. In order to eliminate undesired impacts of structural vibration, various damping mechanisms are developed. Active, hybrid and passive dampers are the main classes of these damping varieties; however, active and hybrid damping options are briefly mentioned, while only the passive damping options are explained in more detail.

Active damping methods are equipped with sensors and electrical connections that link the external energy to the damper, aiming to initiate the damping solution to absorb undesired structural oscillations. Active damping methods need to be designed according to the system's requirements due to its complexity with the electrical elements. In addition to the active dampers, semi-active and hybrid dampers are classified under the active damping methods since their working mechanism is designed with the same philosophy as active dampers; they are designed to activate when the system requires damping. As a result, effective and desired damping properties can be achieved using active dampers. However, these dampers require regular maintenance in order to keep the system healthy; also, the equipment on these dampers makes the application costly besides the external energy requirement [5].

Hybrid dampers are developed to be an option for the active dampers' unfavourable concepts. They are activated when the system requires an active damping performance; otherwise, it works as a passive damper [13]. However, similar to the active dampers, they are also sensitive to environmental conditions and require regular maintenance.

On the other hand, passive dampers are non-external energy-required structural vibration damping methods. Because of this property of the passive dampers, they are often economically feasible applications. Their less/no maintenance required nature increases the

attractivity of the passive dampers used in the structural vibration isolation. The following parts of the subchapter detail these options with a few literature examples.

Evaluation of Passive Dampers

Introduced information regarding the damping options and their properties has shown that each damping method has specific, characterised, and favourable impacts on their cooperation systems. In line with this, passive damping treatments are more attractive applications. Numerous varieties include viscoelastic dampers, tuned mass dampers, friction dampers, etc. In addition to their favourable properties, these dampers are not perfect options; there are limitations for these applications, such as leakage issues, temperature intolerance, excessive wear, and many similar situations related to the total operation time. Some passive dampers are seismic isolation techniques, viscous and viscoelastic dampers, friction dampers, tuned liquid dampers, and tuned mass dampers. These exemplary applications can be detailed in the following lines to understand their principles and issues.

- The seismic isolation techniques are one of the passive damping options, and they tend to lose their efficacy under the huge dynamic load. Since they are mostly produced using rubbery materials, these damping varieties have a small lifetime as a structure. Laminated rubber bearings are the type of example [13].
- Other examples of passive damping options are viscous dampers and viscoelastic dampers. Since these dampers are made of polymeric-based materials, their effectivity depends on the time of the operation. These materials are sensitive to temperature changes since their working conditions increase the system's temperature. They lose their strength and reduce the effectivity since shear forces are changed by heating [12]. The temperature degrades the method's efficacy under very low and very cold conditions; also, these dampers' environmental temperature is increased [12].
- Friction dampers are another useful example of passive damping techniques where the damping is established through two different parts of dampers in connection, which results in friction. Their effectivity is reduced while the surface degradation and

wear issues increase. The wear is caused by changes in surface conditions and degrades the strength of the material properties in time [14].

- Tuned liquid dampers (TLD) has own advantageous properties; however, they are filled with liquid, and the liquids change their viscosity while the temperature level changes. Even though this damping method is an applicable option, the damper usage is limited since the leakage issues. Leakage and reduced effectivity arose at high-temperature levels [15].
- Tuned Mass Dampers (TMD) are applicable and effective methods in the linear passive damper options. The effectivity of the damper depends on the design criteria. Other than their designed effectivity ranges, they lose the effectivity on the structural vibration event. Their performance is quite sensitive to the main structure and external excitation conditions [16].

2.3- Granular Structure-Based Dampers: Impact Dampers to Particle Dampers

Following the evaluation through the knowledge and examples given in the active and passive dampers in the previous subchapter, there is a required option to balance these undesired situations, specifically for the passive dampers. In order to eliminate these weaknesses of passive damping varieties and make a relationship between the vibro-impact theory and the damping application, impact dampers are developed as an alternative damping option. These dampers, also known as acceleration dampers in the literature, are used to reduce the vibration effects in SDOF (Single Degree of Freedom) and MDOF (Multi-Degree of freedom) systems. The first developed variety of particle damper has been the impact dampers, constituting a single granule in a cavity enclosure. The movement of granules is generally defined as *rolling* and *hitting* the walls of the container. In principle, the impact damper absorbs the vibratory energy from the primary structure under excitation impact [4].

The impact dampers are designed with a cavity and a single particle that placed into the cavity, which can be embedded into the main structure, or the damper casing is attached to the main structure externally. Therefore, the container can be a part of the vibratory system, which is generally a drilled hole in the main structure, or even an external additional part of

the system [17]. The damper casing might have a single room or multiple rooms inside for placing a single granule in each room. Representation of possible impact damper variations is given in further pages.

After the initial studies showed successful results, the second variety of impact damper, a multi-unit impact damper, was developed as an advanced version of the single unit impact dampers. The application was simple: many impact damper bodies were attached or mounted to the main structure. Studies showed that multi-unit impact dampers are more effective than impact dampers in reducing the undesired vibration effects [18]. According to the research example conducted to lighten the impact damper's physical situation, reduced acceleration and displacement levels were observed even for a small mass ratio of the attached impact dampers compared to the main structures. Further, the viscous attachment to the impact damper promoted the effectivity of the damper [19].

Simple SDOF system representation and the impact damper usage to reduce the structural vibration and to illustrate the effectivity of the impact dampers is studied earlier. The impact damper usage on the system helps to reduce the excitation level and increases the structure's stability under excitation impacts. Effectivity has been characterised by the duration of impacts when the direction of the particle is reversed to the direction of the damper. However, according to the study, the effectivity of the impact damper depends on the system's several properties. These properties are stated mainly as the particle's mass and size, the gap between the single particle and the cavity wall, which is also the size of the room where a single particle is placed [17]. In addition to this information, the study has been a good example for analytical modelling of the impact damper.

The advantages of using impact damper on (or within) a system were given as

- available application for a range of acceleration and frequency levels,
- resistant to high or very low-temperature levels,
- relatively available to use for a longer time than the other passive damping methods [20].

Following the evolved options of the impact damper and increased efficiency, efforts have been put into improving the impact damper's design by changing the geometrical shape of

the cavities. In addition to the design improvements, the effectivity of the impact dampers was further improved by increasing the number of cavities, which included more than one unit to place the single granules in each unit. The next step in the improvements of the impact damper designs had been placing multiple granules rather than a single granule into the enclosing cavity of the impact damper. The impact damper's novel approach was called *multi-particle damper or particle damper*, a variety of granular-based dampers [21].

One of the earliest examples of the study of replacing multiple particles indicated the idea of replacing a single particle with multiple ones which were smaller in size and equal in mass [22]. Even with the changeable impact forces between the particles during the steady-state physical impact from the main structure, the peak level of the accelerometer reading was subsequently reduced comparing the single particle damper's case [22].

Similar to the previous example, another earliest example was studied by replacing the single particle damper with a bed of granules to control the SDOF system behaviour. The primary properties of the multiple granules placed damper, such as the clearance and mass ratios, were studied using experimental and theoretical approaches. It was aimed to evaluate the effectivity and impact of the multiple granules in this research [23]. A multiple particle damper arrangement was shown to have effective amplitude reduction at the resonances of the main structure in a similar analysis based on the analytical evaluation [2].

Numerically and experimentally analysed particle damper comparison-based study has shown the frequency shift observations with amplitude reduction at the resonance area. Momentum changes and kinetic energy level differences between the granular structure placed damper casings have been noted as the damping process. In addition, using auxiliary mass performance has shown a similar impact with added mass effect on the frequency response. [24].

As a result of developments in the traditional granular structure-based damper varieties, there has been a classification of four main categories in these dampers: the impact damper, the multi-unit impact damper, the multiple particle damper (also known as the particle dampers) and the multi-unit particle damper [25]. Depending on their configurations, materials involved in the damping process and their combinations, the particle dampers

were divided into various groups. These different classifications all support the robustness, and the effectivity of the particle dampers, which can be controlled via granular materials, combinations, and mechanisms. Figure 2.1 below shows this classification and varieties in a nutshell representation [1].

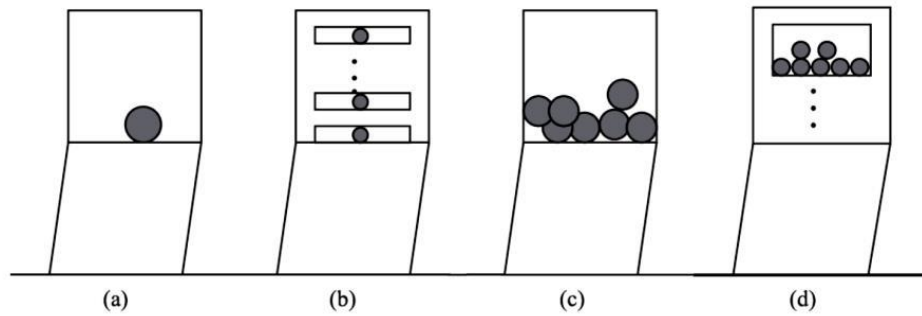


Figure 2. 1: Particle Dampers (a) Impact Damper, (b) Multi-unit Impact Damper, (c) Particle Damper and (d) Multi-unit Particle Damper [4]

According to Figure 2.1, the impact damper can be designed using multiple cavity holes with single particles placed in each block. This design method has been evaluated since an increased number of impact dampers on the substrate was thought to be more efficient in the dispersion aims [1]. An increased number of impact dampers attached to the same main structure means increased collisions; since then, it means increasing the momentum changes and further promoting energy dissipation quality.

Single granules in the cavity might have ceramic, metallic or viscoelastic material properties, which show dissipative energy behaviour under dynamic excitation and damp the primary structure at various quality levels [15]. The damped (main) system can be designed as a Single Degree of Freedom (SDOF) or Multi Degree of Freedom (MDOF) system. Energy dissipation is characterised by the interactions between the single particle and the cavity walls through structural excitation. The dissipative property of the single particle interactions influences the main structure through the collisional mechanism between the granule and the walls of the container. Each collisional behaviour leads to the momentum changes between the colliding bodies.

The collisions with large impacts and restricted area of the container made the impact dampers less favourable. Undesired situations on the SDOF system were studied analytically

and experimentally; it was mentioned that using multi-units with an auxiliary mass of the particle from a single-unit impact damper reduced the vibration amplitude level at the same range. However, the impact force and noise levels were recorded lower than in the single-unit damper case. It was quoted that the container-particle collisions would be twice per cycle, corresponding to a half-period of time for each collision, in different directions of the container walls in the steady-state excitation process. This was used to explain the symmetric motion of the particles easily. The study showed that individual units did not show identical behaviour in terms of motion, even though they were placed on the same vibratory system. The motions of each unit were described out of phase in the system [26], [27].

In the earlier works of Masri [27], the vibrational system and damper were assumed to be SDOF systems; however, later, the system was assumed to be a 2DOF system after aiming to develop the modelling of the particle dampers. Thus, the nonlinearity of the particle damper was obtained by the relative velocity and the displacement terms. It was shown there, assuming the MDOF system behaviour in the study showed more realistic results, which were taken from experimental studies.

Different impact dampers have been developed to work in different frequency ranges. However, there are studies to define the strategy to define a geometry for the impact dampers and to find a damper geometry which would be applied in a broader range of frequencies. For instance, Papalou and Masri [20] worked on an experimental study to explain the damper's complex physics. The complex behaviour came from the nonlinearity of the damper. An analytical approximation was developed from the experimental results. However, their study was only an assumption of the theory. The effectivity and applicability of impact dampers were defined by empirical methods such as the experimental trial and error method [28].

Multi-unit impact dampers, as mentioned, evolved from single unit impact dampers since single unit impact dampers showed less coupling effect, higher deformation, and a higher level of dry friction [29]. Experimental and numerical methods have been studied since the multi-unit impact damper's undesired situations. The system's total mass was equal to the impact damper for multi-unit impact dampers cases. Therefore, the comparison was made,

and multi-unit impact dampers were found more efficient and less noisy than the impact damper case in Masri's study [21].

According to the studies, few benefits of impact damper usage for energy dissipation have been found. These dampers are available for harsh working conditions while providing a considerably small weight impact on the overall structure [30]. Impact dampers are available to be effectively used for higher working temperature levels. Due to the simplicity and efficiency of the impact dampers, there is an increasing interest in developing these types of dampers.

Research studies are mainly focused on 'How to cancel the side effects of the vibration on a structure?' throughout vibration-related studies since the vibration is not desirable for safety and effectivity reasons. The studies about particle dampers started with the first idea of impact dampers in research history. The next improvement on the impact dampers was to replace the single particles in the cavities with multiple particles. This idea was developed by examining the multiple particles with equal mass to that single particle in the impact damper in the same cavity volume [28]. In order to eliminate ineffective properties and improve the impact dampers' damping abilities, a single granule in the cavity was thought to be replaced with a smaller-sized and equal mass of granular particles. It was found that particle dampers were more efficient than the previous two methods: impact damper and multi-unit impact damper.

One of the first examples of particle dampers was studied using the main structure as the bed of particles. Therefore, the small diameter of cavities in the main structures was filled with particles. The aim was to increase the damping effect in this research study [21]. Thanks to the later works of two-particle placed single damper under the sinusoidal load impact, it was understood that the effectivity of dampers depends on the volume of the cavity [26].

In a later study, one cycle and types of collisions in one cycle were defined to understand the mechanism of the granules in the same cavity for proposing an analytical methodology based on the previous work [31]. The first type of collision was between the container walls and the particles; likewise, the previous collision assumptions were made for the impact damper. The second type of collision was the newly assumed type defined between the

particles as particle-particle collision. These collisions were explained as four impacts in one cycle; a collision between the left side of the container and particle-1, a collision between particles, a collision between the right side of the container and particle-2 and the last impact of the cycle was the second collision between particles under sinusoidal excitation conditions. The efficiency of the two-particle impact damper was almost two times better than the single-particle impact damper by using the analytical approximations [32]. This study enlightened the literature to work on multiple particles in the same cavity.

In addition to the facts about the particle dampers, their performance is affected by other system parameters, as well. Material properties, size, amount and shape of particles and cavity are in these parameters since the contact mechanism, and all these inclusions of the system change force-displacement relations. A term was defined to express empty volume of the cavity after filling with particles as *the clearance ratio* (also mentioned as *the filing ratio* [26]), which is used to evaluate the effectivity of the particle damper [27]. It was realised that the cavity's clearance should be at the optimum level for collisions of particles in the cavity. Also, controlling the cavity's clearance might help increase the damping abilities [23]. For instance, Saeki questioned the number of cavity effects on the particle damper behaviour. The increased number of cavities provided comparatively better damping. It was also stated that increasing the number of cavities allowed to reduce the optimum size of the cavity [33]. Several attempts have been made to reveal the portion of these parameters in working particle dampers using analytical, numerical, and experimental methods.

In the next subchapter, evaluation of the particle damper (in some cases, the impact damper) studies are given as their studying methodology, specific phenomena of particles and the application areas with the particle damper functions on the specific engineering applications.

Experimental and Analytical Approaches to the Granule-Based Dampers

Researchers studied the impact dampers in the experimental studies for several reasons, like exemplifying the exact applications or validation purposes of the numerically/analytically studied cases. For example, an important part of the damping was revealed from the particle interactions and their shear-friction relations in an experimental-a and numerical-based study [34]. The second variety of experimental approaches aimed to validate the numerical

study findings and reveal the damping mechanism through the experimental studies by using piston and extension springs [35]. In these studies, the amplitude dependency of the granular structures, excitation condition-related effectivity changes and the damper-like clearance ratio's physical properties have been studied.

Experimental studies greatly impact finalising the real application of analytical and numerical approaches of the particle dampers. However, experimenting vast variety of parameters has been quite expensive. Therefore, a systematic understanding of particle dampers has been tried using numerical methods, mostly. According to these literature examples and information, numerical studies are the most convenient approach to understanding the particle dampers' dynamic process whereas, the numerical studies have required computational capabilities and high memory of usage [36], [37].

The geometry of the enclosing cavity has been studied as major impacting property on the damping effectivity in addition to several other criteria. These are mainly amplitude, frequency range, the mass ratio between the particle damper and the primary structure, lid clearance ratio, damping ratio, coefficients of restitution, etc. [20]. Acceleration level and noise were mentioned as very high in the impact damper collision process. It was stated that the reasons for reduction in the effectivity were not only because of the surface deflections but also the variety of parameters of the impact damper. To reduce the disadvantageous effects of a single particle damper, a study based on experimental and analytical approaches was conducted by changing the particle with multiple particles as an auxiliary mass under a stochastic process, as given in Figure 2.2 [20]. Optimum design parameters and working conditions were offered by completing the study. Also, it was asserted that the noise level was reduced, and the dependency on the amplitude level was shown. Analytical calculations were used to address the specification of the optimal damper parameters in addition to the experimental interpretations [20].

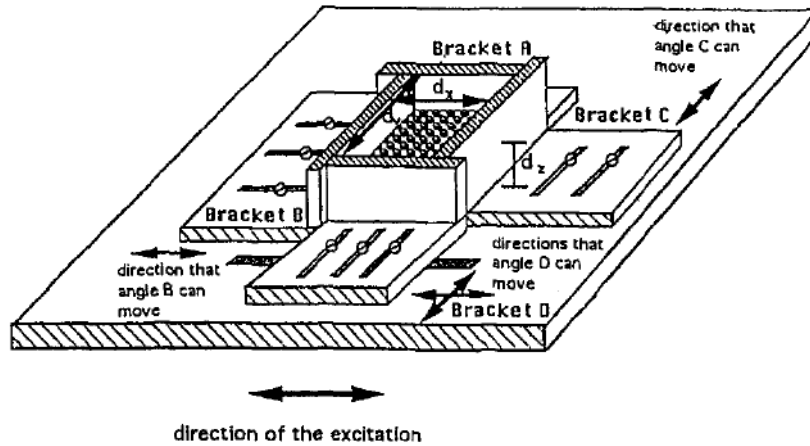


Figure 2. 2: Designed damper geometry with movable brackets [20]

Improved understanding of particle-based dampers has given thoughts on the damper's physical properties and the particles' damping abilities. These studies showed that energy dissipation depends on the inelastic collisions and sliding over the particles. Inelastic collisions have controlled the momentum changes and kinetic energy conversions to heat energy through the particles. In addition to this process, it has been thought that the particle-particle interactions control frictional losses of the whole system [17]. In the later studies, frictional losses because of the granular interactions have been related to the material properties of the granules in contact. Metal granules with stiff material specifications show higher frictional loss character, while viscoelastic materials show higher viscous losses with granular interactions [6], [38].

The damping effect combines loss mechanisms through the vibrating process, such as friction and elastic/plastic losses from the collision of particle-wall interactions [39]. The particles freely moved around the container/cavity; the movement of the particles was relative to the dynamically excited structure, which resulted in impacts between the particle and the container. Thus, the impact occurred when the particles reached the enclosure cavity wall level in the vibratory effect process. The interactions between the wall and the particles dissipated energy and momentum changes through the vibratory system. These dampers are used to define their applicability and effectivity, generally used with empirical methods such as experimental trial and error [39].

Another damping process explanation depends on the particle interactions with the cavity and their immediate neighbouring particles; internal particle resonance was found as the way of excitation damping in the structural vibration [23].

The impact process is given in this section, as well. Acceleration level and noise were mentioned as very high in the impact damper collision process. It was stated that the reasons for reducing the effectivity were not only the surface deflections but also a variety of parameters of the impact damper. However, understanding of particle behaviour and physics of the particle dampers are strict with experimental studies. According to the studies, impact dampers produced noise because of the collisions between particles and the cavity. Their damping behaviour is less influenced by the temperature differences and requires less maintenance than other types of damping treatments. The studies showed that it is possible to optimise the damper performance by changing its volume and particle size [39], [40].

Traditional damping mechanisms on the industrial systems, such as turbine blades, could be insufficient and ineffective for some applications under extreme centrifugal loads and high-temperature conditions. Viscous damping is not available after high temperatures, and friction damping is not applicable at some time of usage because of wear and life issues. However, particle dampers are found to be effective in harsh environments. Even though their damping behaviour is highly nonlinear; the combined energy dissipation mechanism, including the plastic deformations, frictional effects and momentum exchanges, are the reason for the damping effects. After comparing the traditional passive dampers, the SDOF (Single Degree of Freedom) system was used in Olson and Drake's paper [28] for analytical approximation to the particle damper system, which has friction forces. Momentum transfer between primary and secondary structures was defined in the equations. The fourth order Runge-Kutta algorithm was used for analytical solutions and gained applicable and understandable results.

Fixed-free end condition beam was experimented to validate the analytical approach method random excitation was applied in the frequency range of 0-5000 Hz. Mass ratio, cavity size and excitation levels were changed as parameters included with SiC (silicon carbide) particles in the experiments [28]. Regular shaped and irregular-shaped particles were compared, and regular shaped particles were found to have better packing properties

which was a superfluous situation to increase the damping effectivity. The acceleration level was asserted to be high enough to excite the particles and change the particles' positions; thus, external friction effects and better momentum transfer will be obtained. Even though this study was found to have [41] good approximation with the first-order analytical solution for internal friction and momentum transfer effects, it was not accurate enough due to the lack of external friction effect. It needs to be improved in the sense of external friction effects.

The impact dampers can either be a cavity embedded in a structure or a casing attached to a structure. The cavity/casing contains one particle made of metal or ceramic material, which dampens the primary structure's response [42]. The energy dissipation in this type of damper is characterised by interaction (collision) between particle and cavity/casing wall when the primary structure is under dynamic load. According to the structural momentum conversion rules, while the collision happens in the system, the momentum on the individual bodies change variation can be observed with produced noise because of the collisions between particle and cavity [43], [44].

Numerical and Analytical Approaches to the Granule-Based Dampers

Analytical methods have been the earliest approaches for understanding the attitude of the granular structures, and these methods were used to find better approximations for the related studies. Even though the analytical methods helped in the aiming approaches, they were not inclusive in terms of reflecting the physical arrangements and contact properties. Therefore, numerical attempts were produced using these analytical assumptions and were further developed to show the parameters of the particle dampers [26].

Most of the recent studies have approximations through numerical and analytical methods to illustrate the damping mechanisms. The damping is explained through the SDOF system relations between the colliding structures by defining the mass of the interacting structures, damping constants and spring stiffness of the structures under the excitation force impacts. This definition has been expressed as the piecewise linear relationship since the interaction between the structures in the collision is in relatively small duration, and there are several examples of this approximation in defining the damping of the particle dampers [7], [14], [23].

The earlier numerical and analytical studies have been prepared by considering one collision impact per half-cycle on an SDOF system [45]. This work was extended and evolved considering two impacts per loading cycle. N-impacts per cycle were required to develop a new, nonlinear theoretical approach in the later works including the multiple particles [46]. Studies aiming to understand the physics of particle dampers showed that there are criteria which affect the damper's effectivity. The effect of the clearance ratio, the effect of the excitation method and its direction, the effect of the mass ratio, etc., were the research criteria for many cases related to the impact dampers.

Numerical method varieties depend on the application area since the particle properties; several provided approaches like Molecular Dynamics (MD), Discrete Element Method (DEM), etc. The contact relations are different in each numerical application method. For instance, DEM is generally used as a method of numerical studies of granular structures, including particle dampers for engineering applications. Pleasant damper design and development require numerical modelling techniques for an economical approach to the research. For this reason, particle damper applications should be modelled numerically to check many parameters and understand their parameter-dependent mechanism. There are developed several methods of numerical studies including granular structure interactions [27]. Discrete Element Method (DEM) uses individual granule definitions using Newton's Second Law of Motion for the particles and contact force-displacements. For the simplicity of contact conditions, Coulomb's friction is used for the normal and tangential contacts. Also, damping terms are defined using linear spring and dashpot mechanisms [47]. Many research studies to understand the damping with particles, segregation and damage investigations were conducted using three-dimensional DEM with several commercial software such as EDEM [48].

Several examples of literature include the numerical modelling of granule-based dampers. Modelling the granular structures in the numerical studies requires contact interactions of the granules in the definitions of the numerical analysis setup. Depending on the nature of the contacting structures, particles and cavity walls, there are soft and hard particle identifications [49]. Also, the direction of the contact, either tangential or normal, has been another distributed term to model the granular structure interactions [50]. Several contact

mechanism definitions have been developed in terms of defining the contact. Hertz-Mindlin is one of the contact models to define the interaction between contacting bodies, which has been used mostly in the analysis. There are developed options to the contact models in case of the additional physics involving the interaction, for instance, the rolling conditions or the heat transfer involvement [36].

Event Driven Method is another method which uses a hard sphere model with a coefficient of restitution for the particle modelling. It also requires the mass and size of the granules. The contact mechanism is only related to the coefficient of restitution for this case which makes the modelling simple. This method's successive collision time is short since there is only one contact between particles. This method is cost-effective in terms of computational effort; however, it can be useful only for isolated instantaneous collision types [51].

Numerical studies of particle dampers include design of particles and cavity geometry, modelling the physical interaction between the system elements and kinematic definitions of the dynamic process. Since the system elements are a number of particles and cavity, each system element should be considered, and related equations should be solved for the interaction between these system elements. The Finite Element Method (FEM) is a modelling and simulation option for continuous structures. However, structures' granular states are discrete systems that should be solved by individual modelling and tracing. Therefore, there are numerous ways of discrete system approaches. The Discrete Element Method (DEM) is one type of modelling and simulating option for this type of interaction. In this method, granular structures are designated individually and modelled the physical interaction for each element. The contact mechanism between the granular structures and the host structure is also defined in this method. Each step in the analysis consists of force-displacement relationship calculations. The next step is modelled and calculated according to the data processed in the former step. The individual steps consist of iterations that process the calculation close to the theoretical point. All these details of the DEM conclude that this method is computationally expensive since it requires high memory capacity and capability of the workstation. For simplicity and inexpensive analysis, there is a new simulation method to study granular structures rather than an expensive DEM solution. There is an interesting coupling between the methods of FEM and DEM, which has been

developed to save the process from undesired sides of DEM analysis. The coupled algorithm can be modelled using the calculations from the DEM studies and used to model the interactions in the FEM. In general FEM-DEM coupling, the traced force and displacement interactions are transferred to the FEM software after a successful calculation in the DEM software. The design procedure, for instance, has been studied using this coupling method to find a design procedure and effective working process for a particle damper attached gear pair under centrifugal loads. Therefore, depending on the particle size and cavities, the damping properties have been available for modelling and evaluation in DEM-FEM coupled methodology [30].

Amplitude Dependent Character of Granular Packing

An interesting phenomenon has been observed in granular impact dampers; depending on the volume capacity of the surrounding cavity, they can show behaviours similar to solid, fluid or gas states of the materials. A densely packing glass beads may show solid glass block behaviour since they resist the external force. Whereas tilting the cavity might change the granules' state and granules behave like a fluid. Moreover, shaking with higher amplitude (or higher frequency levels), the glass granules might jump around and hit the cavity wall; therefore, they might be counted as gas [52]. Since granular structures have properties to act into the three physical states of the materials depending on the excitation conditions, they can be used for various applications in industry. Granular structures are placed in a cavity to constitute particle damper from the vibration damping perspective. These granules in the cavity are expected to resist the external force and follow physical and mechanical steps. At a minimum excitation level for them to start vibrating, they also slide through each other; they even experience collision with each other and the cavity wall, as well. Dissipation of the external energy is succeeded through these physical and mechanical changes. Therefore, these particles placed in the damper might be helpful in a variety of materials [39].

In the earlier works of Masri, the vibrational system and damper were assumed to be SDOF systems [53]; however, later, the system was assumed to be a 2DOF system after aiming to develop the modelling of the particle dampers. Thus, the nonlinearity of the particle damper was obtained by the relative velocity and the displacement terms [32]. Also, an increased

amplitude level of excitation was expressed to increase the effectiveness in the control level until a level of amplitude. If that amplitude level kept increasing, the control level was reduced [6]. This behaviour was noted to turn back to the previous behaviour after a certain amplitude level, affecting an increase in the control mechanism [54]. Therefore, it can be said that in addition to all other uncertain mechanisms, granule-based dampers were found to illustrate nonlinear dynamic mechanisms.

Friend and Kinra (2000) studied the particle dampers' nonlinearity within the analytical and experimental studies by using a cantilever beam in the vertical direction with the effects of lead particles. Properties of particle dampers such as gravity effects, filling ratio, and vibration amplitude have been questioned by using the Bernoulli-Euler Beam Theory. In that study, types of movements of particles have been modelled in the equation form. Even though each particle has different velocities after each collision, the particle was assumed as a single particle in the theoretical studies. They showed that each movement depends on the previous time step's movement. The dissipation mechanism was explained between the particle-wall and particle-particle collisions. The amplitude dependency was studied in different cases (a totally of 25 different amplitude levels) by changing the amplitude level and checking the energy dissipation level for each case. It was shown that the behaviour of the damper was not stable for different cases. It showed that particle dampers are highly nonlinear damping applications [17].

The applicability of the particle damper was explained in the gas turbines and rocket motors since they are durable under harsh environmental conditions. When particles are metallic, they tend to increase the friction forces in the cavity; thus, the amount of movement and collisions are reduced, and the dissipated energy level is degraded. The sticking behaviour of granules might be experienced in the lower levels of amplitudes. While the excitation amplitude increased, the particles had more active behaviour in the enclosure. They tended to slip over each other and had more contact with the cavity walls. The particles had smaller volumes when the amplitude level was at higher levels. The behaviour was noted as flying in the cavity, which was explained in a 'gas-like manner'. The transition of the movement, which depends on the amplitude level, was mentioned as '*between solid-like and liquid-like*' in the vibratory system. The excitation direction was also found as a parameter which affects

the applicability of the particle dampers [6], [18], [55]. The nonlinearity was also described by the discontinuity and randomness of collisions and velocity of the particles [6]. Also, the nonlinear behaviour of the granule-based dampers was studied in various numbers of damper geometry at different time steps of analysis [33].

The excitation level changes the position of the particles in the damper, which, in total, shapes the damping. Firstly, gravity affects the particles when the system is either at a resting position or under small excitation. Static forces are mentioned as *hydrostatic pressure* [56] between the particles, keeping them stable like a solid structure. The first case is called *the solid phase* of the particles, where a small amount of energy is reduced from the main structure. Secondly, with the increased dynamic load, the particles have inner dynamic forces and friction forces acting on them to move and vibrate. Positions of the particles are changed, and contact surfaces are redefined because of the changed state of the excitation amplitude. While amplitude is being elevated, contact forces are derived to another level, and friction force between the contacts is reduced. At this level of excitation amplitude, there is *fluid-like* convection in the particle motion. Associated with the excitation level, the contact forces can lock the particles, or a *slipping-sliding* motion may occur between the particles. The transition between the solid-like behaviour to fluid-like behaviour is noted as the maximum damping efficiency range for the particle damper application since there is maximum contact and interaction in the inner structures of the damper; in fact, this statement does not have actual proof yet. When excitation is increased to exceed the gravitational force and beyond the friction forces between the particles, they start moving around in the cavity with a *gas-like* motion, at which the particles occupy a very small volume in the damper cavity. This range of excitation is the lowest damping efficiency observation range [7].

Nonlinear Energy Sink (NES) is a particle damper characterised by the granular structures' amplitude-dependent properties. NES has quite powerful energy dissipative behaviour; however, the benefits depend on the excitation conditions and the system properties. Similar to the nonlinearity of the particle dampers, they changed the behaviour to the nonlinear properties with the increased excitation amplitudes. However, these systems have

shown great applicability in low excitation amplitudes. Therefore, the energy dissipation was utilised with the changed amplitude levels [57].

Studies show that the behaviour of the damper is very sensitive to amplitude changes [33], [58], [59], [60]. Controlling the vibrations on the buildings, structures under earthquake motion and machine tool vibrations may be stabilised by using impact dampers [4]. According to these statements, the particle dampers' damping effectivity and excitation amplitude dependency can be explained as the nonlinearity of these structures. The excitation range in which the granular system can dissipate the maximum energy from the main structure is conducted in this study. There are numerous studies have been performed to reveal the efficiency of the particle dampers in the literature [37], [61], [62]. They showed that particle dampers have illustrated effective way of usage compared to the other passive damping methods. However, there are disadvantages to the particle damper systems, as well. Since the system is highly nonlinear, it is better to apply in the given frequency ranges; the fluidization depends on the frequency level and the excitation amplitude [63], [6], [64]. The size of the particles, their volume and the packing ratio, the direction of the excitation, material properties of the particles, etc., many parameters affect the functionality of the particle dampers. As stated in this context, even though particle damper was found to be a very effective method to reduce structural vibration, the effectivity of the particle damper depends on several different parameters. The studies should continue to have viable parameters under various conditions.

Application Areas of the Impact Dampers

One of the first applications of impact damper was to control the flutter on the aeroelastic structure studied in NASA [57]. The following applications were on turbine blades, aircraft wings, etc. Since the method was sensitive to changes in the system parameters, it was proposed to replace the single particle with multiple ones with the same mass as the single particle in the same cavity [57]. Controlling the vibrations on the buildings, structures under earthquake motion and machine tool vibrations were thought to be stabilised by using impact dampers, according to the addressing from earlier studies [1]. Impact dampers are applicable in industrial options such as turbine blades, cutting tools, and shafts [7]. The

performance of impact dampers depends on many different properties related to the model, material, size of the damper itself and particle itself. Therefore, the dynamic of the impact damper is one of the main research topics for the fanciers.

Simonian studied the impact damper actions aiming to reduce the structural vibration effects from the space structures. Molecular Dynamics (MD) options were mentioned, and Discrete Element Method (DEM) options have been used in the study in order to model the granular structure-based damper and to define the impact interactions [43]. A single particle is placed in the impact damper cavity to reduce the undesired vibration level of the space structures. Since the damping is elevated using the acceleration amplitudes, the damper type has been called the acceleration damper in the study. The beam-type space structure has been used with the acceleration dampers. According to the study, effect of the particle-damper system has been classified with the excitation amplitude effects in the particle, such as solid-like, fluid-like, and gas-like behaviours, as detailed earlier [43], [65].

Noise measurements at the collision states in the impact dampers showed that the impact dampers are noisy applications while they are easily influenced by the attenuation level [66]. Therefore, considerable developments have been attempted in the impact dampers to reduce inefficiency and increase the effectiveness of these dampers. These optimisations have been mainly change in the particle size and the cavity geometry volume [67]. According to this information, the effectiveness of the impact damper depends on several system-related parameters, and the following improvement has been tried to defeat these sides.

Application Areas of the Particle Dampers

The particle dampers' applications in the studies mainly focused on the applications of structural vibration on planes, aerostructures (such as space crafts), civil structures, engine systems and gas turbines. For instance, the background noise and vibration were found to reduce the efficiency of the combustion from a research based in Rolls-Royce [40]. The hot gasses from the combustion chamber leave the system through the transition ducts and then the annular transmission chamber to drive the gas turbine. In this process, the noise is found to be at very high levels. Also, since the machinery motion and milling are on the turbine, there is chatter on parts of the turbine body. This is not a desirable situation since it reduces

the lifetime of the turbine parts. To solve these problems, it was thought that a non-rotating, external damper mechanism should be a necessary additive part of the turbine. Therefore, studies are developed on the particle damper for applying gas turbines. This idea is questioned within the variety of shaped dampers under different conditions. The study, which has two different filling ratios as 95% and 100%, shows the different results for each parameter. Solid-like to gas-like motion in the damper cavity has been observed and explained with the addition of the increased effectivity of the combustion process in this research study [40].

The applications needed to be neutralised, and particle damper variations have been studied recently. For instance, bean bag particle dampers were developed and used to reduce the particle collisions' noise side effects [46]. On the other hand, in terms of increasing the damping effectivity, the Non-obstructive Particle Dampers (NOPD) have been designed at the appropriate locations of the main exciting structures to place the granules for the damping [68], [69].

2.4- Periodic Structures

A periodic array means several identical structures are regularly placed in a meaningful arrangement to form a whole structural system [70]. Periodically arranging the solid structures on/in the main substrate differentiate the way of the solid waves/excitation impact travel through the substrate structures. Scatterers, which means the solid structures placed on the front side of the travelling wave, meet with the coming wave and are excited with the energy/amplitude of the incident wave. Then the incident wave might be absorbed, radiated, diffracted, distorted, dissipated, refracted, transmitted or reflected because of the presence of the scatterer (damper). The relationship between the impacted wave and the incident wave experiments *the phase difference* (time lag). This happens when a wave incident interacts with a scatterer. Since the impedance and wave speed properties change from one structure to another (or from one material to another), the phase difference is experienced [71] naturally.

Various periodic structures can be classified according to their refractive index, the periodic structure presence volumetric ratio, etc.; Figure 2.3 illustrates the variations. Volume

periodic structures and surface periodic structures have been distinguished from each other by the properties of the periodicity of the structure [72]. The impact of periodic structures can be evaluated through the transfer (or transmission) function between the source and destination fields. The transfer function always corresponds to a value in the periodic array, while it provides a zero value outside the periodic array.

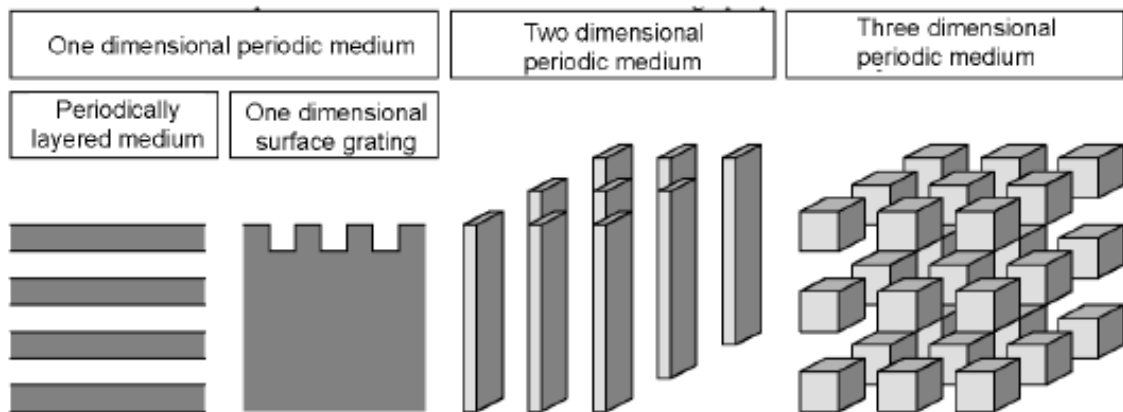


Figure 2. 3: Categorisation of periodically arranged structures [72]

According to the figure, a periodic structure can be a one-dimensional, two-dimensional, or three-dimensional periodic medium; also, without showing the example in the figure, the periodic structures might be layered to provide a periodic layered medium. Even though the periodic structure definition is related to the infinite structure perception, the realistic structures would provide vaguely different outcomes than an infinite structure expectation. Periodic structures are associated with the \mathbf{K} -vector ($|\mathbf{K}|$), which has the length of the period in the arranged structures or the wave number of the wavelength per element size. There are always reciprocal relationships within a finite length of period. The period length or the wavelength (λ) is given in Equation (2.1) below.

$$|\mathbf{K}| = \frac{2\pi}{\lambda} \quad (\text{Eq. 2.1})$$

Periodically arranged structures exhibit band properties according to either their spatial arrangement or the local resonating properties, or both of them. As stated by Bragg in his study using the emergence of the spatially arranged gratings, the light wave propagates through these gratings and opens up a window which no waves can propagate through. Due to the periodic arrangement's presence, destructive and constructive interference occurs.

The impedance mismatching between the periodically arranged structure and the incident wave results in destructive interference, and *the bandgap* appears. Specifically, when the two scatterers are placed at a distance at the half wavelength size, there is the strongest destructive interference for the wave propagation. This event is known as “Bragg Scattering” for the periodically arranged structures. According to this knowledge, when the propagation condition (i.e., the frequency, *f* or ω) and the distance between the periodically arranged structures (ΔL) meet the criteria of the Bragg scattering condition (in Equation 2.2), there is naturally possible availability of the cancellation for the wave propagation. This wave cancellation results in the bandgaps for the interested frequency level and presents an option to change the wave propagation by the distance between the scatterer arrays.

$$\Delta L = \frac{\lambda}{2} = \frac{c}{2f} = \frac{\pi c}{\omega} \quad (\text{Eq. 2.2})$$

As stated, the local resonance properties are the second option to affect the wave propagation. This option has a similar effect without seeking large separations between the arrays. In this case, coupling phenomena is an important parameter. Coupling between mechanical modes elevates several applications' efficiency, such as amplification, cooling, phonon lasing, and many varieties of applications [73]. For instance, coupling between acoustic resonators like speakers or exhaust systems can be modelled analytically using Helmholtz resonators to calculate the acoustic impedance and reflection impedance values for various arrangements [74].

For this reason, a simple explanation for the coupled structures assumes two identical oscillators with closely related resonance frequencies. These discrete systems can be combined. As a result of this combination, the common frequency for the system can be found in eigenvalue solutions. According to the knowledge of local resonances and the wave propagation through the coupled structures, there is a destructed and degenerated wave propagation. This results in the cancellation of the wave, a similar effect in the Bragg scattering case. However, in this case, locally resonant structures are coupled in their eigenfrequencies and change the way of wave propagation.

The periodic arrangement is a useful wave manipulation option using either the Bragg scattering or the locally resonant coupled structures. Therefore, periodically arranged structures can be used in prohibitively large spatial arrangements to destruct the low-frequency attenuations or long wavelengths. Wave propagation is altered using periodically arranged structures, and these structures are eligible to modify the wave propagation accordingly to their spatial organisation. The bandgaps are the resulting situations of these periodic structures.

Analytical Expression of Periodicity

Literature sources have experimental, numerical, and analytical studies about metamaterials and periodic structures. There are examples of studies comparing added mass, periodically arranged structures and metamaterial applications. Snell's Law is transmitted when an incident wave travels through the periodically arranged structures and reflected waves occur. Infinite structure modelling is one of the top ideas about the periodic arrangement; therefore, there is an effort to model these structures in numerical assumptions. Since the arrangement is prepared to follow identical sections, studying the behaviour of one of these identical sections to determine the whole structure's behaviour is a proper approach for periodically arranged structures. Also, the infinite structure approach increases the computational cost, and there is a lack of ability to model these structures as their substrates. Therefore, unit cell assumption is developed. As mentioned earlier, the unit cell, modelled concerning the identical sections on the main structure, is the smallest part to display the periodic arrangement. The distance between two inclusions is known as the lattice constant, which is used as a constant of the element size of the unit cell to define the identical individual components [75]. Then, the unit cell can be used by giving certain periodic boundary conditions to the related edges. Therefore, a composed unit cell shows the entire periodic arrangement structural behaviour under the system conditions. Bloch-Floquet theory sets these boundary conditions to one edge and then re-applies them to the other; however, there is an additional effect from one edge to another. In order to observe more realistic situations and to apply the same order solution to both edges, the complex-valued phase correction is added to the boundary condition. Therefore, the unit cell approach

reduces the computational expenses since the periodic boundaries behave like a finite size of an infinite structure.

Unit Cell is a specific term to define the smallest portion of the whole periodically arranged system. A unit cell includes all the parameters of the periodic arrangement as an exemplary concept. Figure 2.4 illustrates the example of the periodic structure, and the length d in the figure corresponds to the periodic arrangement's unit cell.

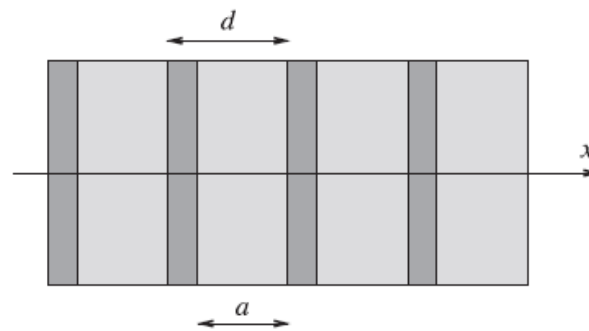


Figure 2. 4: 1D array with periodic placements, d is unit cell length, a is thickness [75]

Waves travel through any medium to which they are introduced. Modes of the waves are evaluated for a solid structure specified in this thesis. Stiffer materials with larger Young's Modulus provide faster wave speed, whereas the lighter (softer) materials with lower material density [76]. When the mode of the wave is evaluated, the mode shape, the wave speed (c) and the wavenumber (k) are evaluated. Equation (2.3) given below represents a general form of wave equation which depends on the frequency of interest (ω) in addition to the information given in the previous sentence. From this equation, the relationship between the wavenumber (k) and angular frequency (ω) has a relationship as ($\omega(k)=c|k|$) with $c^2=E/\rho$, which indicates the speed of the wave is the square root of the ratio of the Young's Modulus to the material density of the solid structure. The exponential in the equation provides the solution for the wave propagation.

$$u(x, t) = e^{i\varphi(x,t)} = e^{i(kx-\omega t)} \quad (\text{Eq. 2.3})$$

Moreover, the wavenumber (k) controls the wavelength ($\lambda=2\pi/k$) and the wave's phase. The relationship between the wave number and the angular frequency Figure 2.5 is prepared.

This figure explains that the wave number and frequency relationship provides dispersion relations. Also, for any integer n , the wave number and lattice constant have a relationship of $kLn=2\pi$ and $kLn=0$ simultaneously. Therefore, the wave number takes values between $[-\pi/L, \pi/L]$ as it is the first Brillouin Zone.

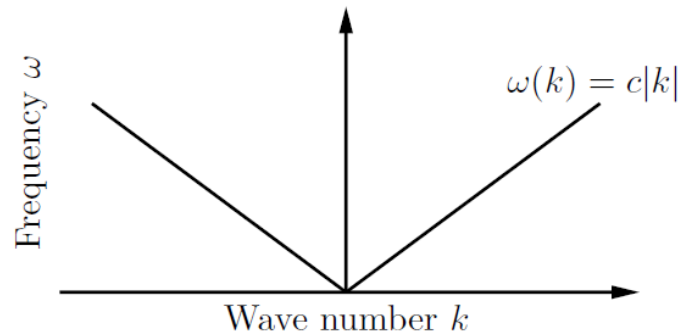


Figure 2. 5: Dispersion relation [75]

The phase velocity is another major information regarding the wave phenomena in solid structures. Evaluating the generalised wave equation for a point in space, which has a constant phase, is moving in time provides the phase velocity (v_ϕ) of the moving point as $(\omega(k)/k)$ given in the series of equations (Equation (2.4) and Equation (2.5)).

$$0 = \varphi_0(x, t) = kx - \omega(k)t \quad (\text{Eq. 2.4})$$

$$x_0 = (\omega(k)/k)t \quad (\text{Eq. 2.5})$$

Wave propagation in periodically arranged inclusions has been studied both numerically and analytically. The theories enable to model and analyse the waveguides within the uniform cross-sectional boundaries or along the wave propagation where periodic conditions are applied on the parallel faces. The most common way to calculate and determine the dispersion relations of waveguides in a specific elementary cell is Bloch-Floquet Boundary Condition [77],[78] within the first Brillouin Zone analysis. The definition of Bloch-Floquet Boundary Condition in a 2D lattice [79] is given by

$$u_{dst} = \underline{u}_{src} e^{-ik(\underline{r}_{dst} - \underline{r}_{src})}, \quad (\text{Eq. 2.6})$$

where \underline{r} is the spatial coordinates. The index "dst" and "src" define the destination and the source boundary Equation 2.6 [79]. This equation has been taken from the COMSOL analysis

setup since this has been studied in Chapter 5. Equation (2.6) was derived from modelling propagation surfaces by solving the wave propagation problem as an eigenvalue problem through x and y directions. The effect of boundary conditions was ignored to model the infinite structure; the band frequencies were plotted in propagation surface plots. However, the finite structure results are comparable with the infinite structure results, which means the infinite structure analysis results have slightly different results.

The structure with periodic cells presents particular interest in this research. The numerical interpretation of the eigenvalue problem associated with stop band frequencies in these plates and derivation of Floquet-Bloch conditions is given in Equation (2.7). This theory (Floquet-Bloch) has the properties of approaching the infinite structural behaviour using finite structures. Then given boundary conditions help to understand the infinite structures.

$$[K(\mu_x, \mu_y)] - f^2[M(\mu_x, \mu_y)] = 0 \quad (\text{Eq. 2.7})$$

K and M are stiffness and mass matrices, respectively. f is the excitation frequency, and μ is the propagation constant for x and y. The frequency levels that give solution to this equation are known as "*propagation surfaces*" in the two-dimensional form. The gaps between these surfaces were defined as stopbands where the propagation was not allowed through the medium [80].

Finite structure modelling has restrictions on understanding the infinite structural behaviour. Therefore, the studies should be modelled as infinite structures; however, this is not convenient because of the computational cost. Therefore, modelling a unit cell to represent the infinite structure and applying the proper boundary conditions to modify the unit cell are possible steps using the Floquet-Bloch Theorem. In this literature study, infinite study approximation is modelled using Floquet-Bloch Theory. There were implications in periodic structures theory in the modelling of infinite structure. It was shown in many studies that the periodic structures demonstrated unique dynamic effects for filtering the wave propagation [80]. In the previously studied experimental and numerical research, it was shown that the simple clamped-free end condition of plate-shaker study with four different arrangements have illustrated different results to be able to use as a mechanical filter in a wide range of frequencies [81]. Equation (2.8) illustrates the complex wave equation, which consists of two

constituents of the propagation constant. The real number (α) expresses the exponential decay rate of the wave propagation, which is the attenuation of the wave. In contrast, imaginary number (β) is the definition of the phase difference between two neighbouring cells, also called phase change [80].

$$\mu = \alpha + \beta i \quad (\text{Eq. 2.8})$$

If the real number (logarithmic decay rate, α) is different from zero, it is in the wave propagation's stop band or attenuation levels. If it has a zero value, which means if the wave has only an imaginary number (phase difference, β), then the wave characteristics show pass band behaviour where there is no attenuation through the propagation. The wave propagation constant varies in the 2π range to complete one full cycle [80].

An applied arbitrary field distribution is evaluated on some discrete points in the unit cell where the wave propagation or frequency sweep is applied. The sweeping parameter option is available to find the optimum values for the entire system and certain parameters' sensitivity. This is approachable by running a series of simulations described in the sweep parameters. Band structure analysis is a parameter sweep study over the wave vector (\mathbf{k}) and searching for strong frequency resonances. The system which contains layers (or periodic arrangements) is evaluated in terms of the wave modes acting in the field. Evaluated modes are definable with a nonlinear equation of time-frequency and wavenumber. The connection between these defined terms is shown using dispersion curves. *Dispersion curves* are a source of recorded patterns of extinguished and persisted propagations. Extinguished propagation consisting of frequencies that do not match the periodic boundaries is not allowed to affect the structure. At the same time, only the persisted modes are allowed to propagate on the structure. Tracing the frequencies and k-space scanning are options to observe the persisting modes as they deliver the band structure via FFT applied spectra ($\omega a / 2\pi c$ vs *FFT*) or band structure computation (*ΓXMF* vs $\omega a / 2\pi c$). As reported by the performed unit cell would give an insight into the infinite structural behaviour over the given system conditions.

Periodic structure analysis allows the researchers to identify the frequency bands (stop and pass). As explained here, these band frequencies showed the behaviour of the structure as a

damped structure and at which level of frequencies they show this behaviour. It was noted that if the structure is applied extra viscoelastic, loss properties of the viscoelastic structure can improve the ability to control the wave attenuation which is expected to be better than absence of the viscoelastic material case [80].

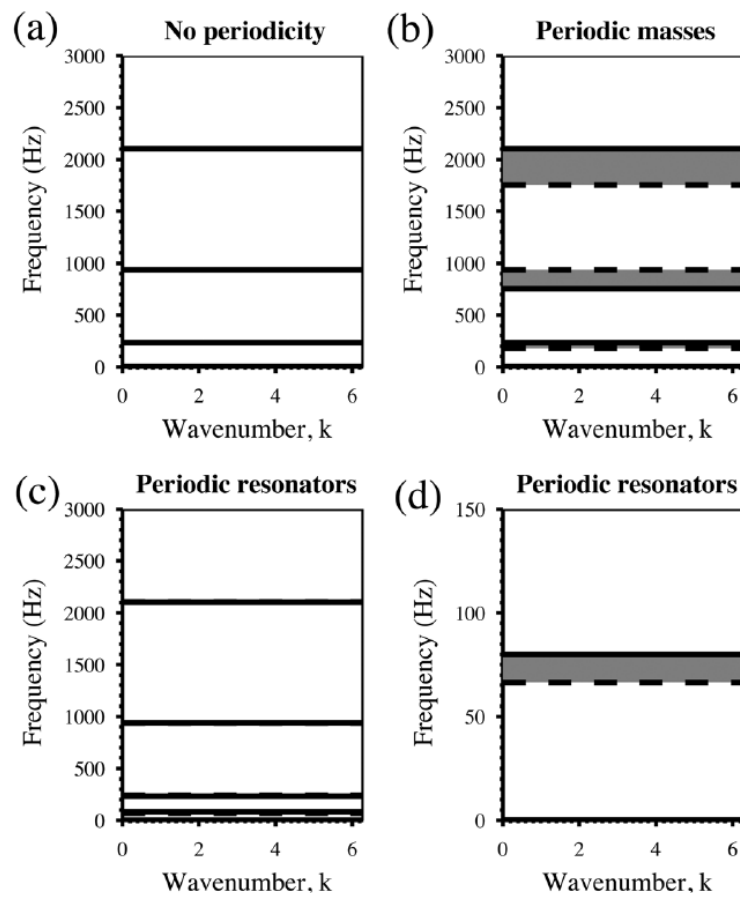


Figure 2. 6: Formation of bandgaps on a unit cell of Timoshenko beam; (a) shows simply supported beam without periodicity, (b) shows periodic masses on the unit cell, (c, d) shows periodic resonators [80]

It was noted earlier in the previous paragraph that the bandgaps depend on the properties of the periodic structures. Bandgaps can be formed due to local resonators or Bragg resonance. The unit cell size and the scatterer should have small sizes in the case of Bragg resonance. Local resonators might have similar properties except the reduced unit cell size. Aperiodic structures require a larger unit cell size to show bandgaps on the system for attenuation of the larger wavelengths; however, bandgaps can be shown better in the periodically arranged cell mechanism. Figure 2.6 shows a similar understanding from research based on various periodic arrangement analysis results [82].

Overall, using periodic structures at the resonant frequency ranges on the structure helps to obtain bandgaps better than the aperiodic arrangements and without resonator cases, as shown in Figure 4.8 [82]. This figure shows the natural frequencies of a supported beam with a continuous line (there is no periodicity). Subfigure b shows the natural frequencies of the supported beam (continuous line) and guided beam (dashed line) with added periodic masses. Subfigures c (0-3000 Hz) and d (0-150 Hz) show the natural frequencies of periodic resonators on the unit cell for the supported beam (continuous line) and guided beam (dashed line). Subfigure-a shows the condition without periodicity, which means that the eigenfrequencies will be the same for guided (free end) and supported beams. Adding periodic masses to the unit cell reduced the natural frequencies. Subfigures-c and -d illustrate the bandgaps due to the periodic resonators on the structure. These figures show that while eigenfrequencies of modes on the guided beam are increased, the frequencies of modes on the supported beam are reduced. Therefore, the bandgap between these two levels was increased. Acceptance functions were used to express the modes of the structure (unit size of beam in that case) by using periodicity conditions of the Bloch Wave [82].

Mass-spring-damper Systems and Coupled Resonators

Structures such as in mechanical systems are analysed through simplified models, which include mass, spring, and damping properties. Depending on the external force inclusion, the system model is controlled by the external force. Lumped mass systems to define structures have been found useful and reliable in working on properties such as the natural frequency [83]. The number of masses in the system is evaluated within the predetermined time steps. In other words, the mass matrix of the system is evaluated at the pre-processing step for one time in one spatial direction, and then this matrix is used for each step in the overall calculation process [84]. The representation of a lumped mass system of a single degree of freedom system (SDOF) is given in the following figures [14].

Figure 2.7 represents the undamped mass-spring system; Figure 2.8 represents the damped mass-spring system, and Figure 2.9 represents the forced-damped mass-spring system.

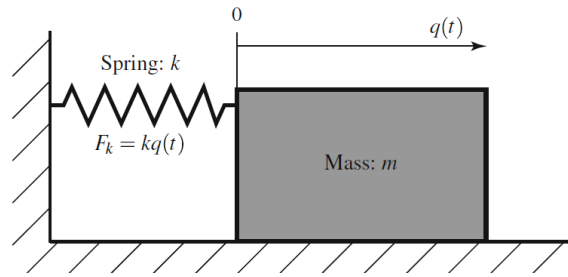


Figure 2. 7: Undamped mass-spring system

$$m \frac{d^2 q}{dt^2} + kq(t) = 0 \quad (\text{Eq. 2.9})$$

The figures are mass bonded with a linear spring on a frictionless surface. According to the Ordinary Differential Equations, the relevant equations to equate the relationship in the system elements are given in the mathematical expressions below the figure. Equation (2.9) expresses the undamped SDOF system where m is mass, k is spring constant, and q is the displacement due to the inertial forces. As mentioned, the system depends on the time; however, the mass does not change with time intervals. The second-order time derivation of the system displacement changes the state of the mass on the substrate with a free motion, which means the system is free from external motions and forces in Figure 2.8.

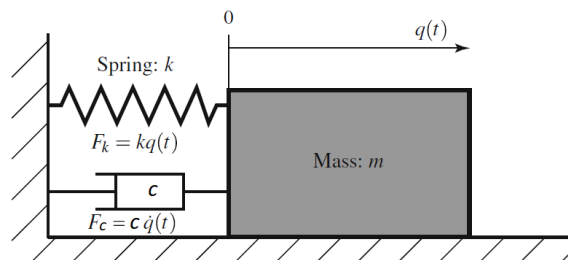


Figure 2. 8: Damped mass-spring system

$$m \frac{d^2 q}{dt^2} + c \frac{dq}{dt} + kq(t) = 0 \quad (\text{Eq. 2.10})$$

Equation (2.10) represents an SDOF system with damping applied to it. The system has the same properties as the previous system mechanism; however, there is a dissipative energy element in addition to the conventional system. This additional element, called the damper mechanism, leads to energy losses in the oscillatory system [14]. The damping constant of

the damped SDOF system, c , is given in Equation 2.10 with the multiplication of the first-order time derivation of the displacement, which equals the velocity of the system.

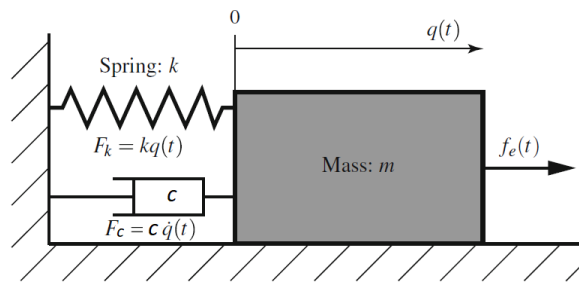


Figure 2. 9: Forced-damped mass-spring system

$$m \frac{d^2q}{dt^2} + c \frac{dq}{dt} + kq(t) = f_e(t) \quad (\text{Eq. 2.11})$$

The lumped systems may have external force attached, which is also an additional energy supplement on the SDOF system, as shown in Figure 2.9. In that case, the system is called the forced vibration system. The force can be internally generated, externally attached or excitation might be induced from the environment. Equation (2.11) represents the damped mass-spring system with an external force ($f_e(t)$) attached to it; as seen from the notation, the external force also depends on the time intervals. The external force of the oscillatory system [14] includes a force amplitude (f_a) and angular frequency ($\omega = 2\pi ft$) as in Equation (2.12) below.

$$f_e(t) = f_a \sin \omega t \quad (\text{Eq. 2.12})$$

The mechanical systems are not always under SDOF system classification; when they have more than one variable for each type of system element, the system is often called a multi-degree of freedom (MDOF) system. The representative equation (Equation (2.13)) consists of each element's matrix forms. These matrices are M for mass, C for damping constants, K for spring constants and F_e for the external force, whereas q for the displacement of the system with its second derivative in time.

$$[M]\{\ddot{q}\} + [C]\{\dot{q}\} + [K]\{q\} = \{F_e\} \quad (\text{Eq. 2.13})$$

Examples of lumped mass systems are mass-spring-dashpot systems, pendulums, rotating machines, plates and heat exchangers, and impact and crash analysis.



Figure 2. 10: Coupled mass-spring system example for tuned resonators

Mass-spring systems are oscillating structures; they are called resonators or oscillators. In the physical systems, multiple oscillators might be attached and constitute complex systems rather than a single degree of freedom. Individual oscillators can also show their resonating properties, as they might be coupled to transfer the energy through each other. Their motion is not necessarily to be periodic. In terms of assessing the coupled mass systems, Figure 2.10 is exemplified. The masses m are connected to the spring (k), and their connected spring constant is k_c which is the interaction force between them.

When the masses are in an equilibrium position, the springs, k , are also in equilibrium. In this system, each mass and its force equilibriums are evaluated individually. Therefore, the equilibrium force which controls the mass on the left side is in Equation (2.14) given below. Also, the mass on the right side is controlled with force in Equation (2.15). Displacements in the equations are given with notation of q_1 and q_2 .

$$F_1 = -kq_1 + k_c(q_1 - q_2) = -(k + k_c)q_1 + k_cq_2 = M\ddot{q}_1 \quad \text{Eq. (2.14)}$$

$$F_2 = -kq_2 + k_c(q_1 - q_2) = -(k + k_c)q_2 + k_cq_1 = M\ddot{q}_2 \quad \text{Eq. (2.15)}$$

The equations of motions are given in the following equations (Equation (2.16) and Equation (2.17)).

$$M\ddot{q}_1 + (k + k_c)q_1 - k_cq_2 = 0 \quad \text{Eq. (2.16)}$$

$$M\ddot{q}_2 + (k + k_c)q_2 - k_cq_1 = 0 \quad \text{Eq. (2.17)}$$

The solution of these equations gives harmonic oscillations of $q_1(t)=A_1e^{i\omega t}$ and $q_2(t)=A_2e^{i\omega t}$ as trivial solutions. These solutions are substituted into the earlier equation to model the matrix form of the coupled mass-spring system. As a result, the determinant of the system inclusions is as in the equation below (Equation (2.18)).

$$\begin{vmatrix} k + k_c - M\omega^2 & -k_c \\ k_c & k + k_c - M\omega^2 \end{vmatrix} = 0 \quad \text{Eq. (2.18)}$$

Solving this determinant means eigenfrequencies for the coupled system are found as the system's normal (asymmetric and symmetric) modes. Symmetric masses are *considered in-phase* masses, while asymmetric masses are considered *out-of-phase*. The given solution is a general representation of equal mass and equal spring stiffness systems.

Bragg Scattering

The wave propagation in the periodic structures is usually studied through the dispersion relationship between wavenumber on the frequency of the propagating waves. The band gaps can be due to either Bragg scattering or the structural resonance of a periodic "scatterer". Bragg scattering was found in destructive interferences of the dispersion diagrams, defined as the difference between constructive and destructive interferences, which depends on the spacing of the structures and the wavelength, which the situation is called "*Bragg-resonance*" [85].

The Refractive index of the structures has periodic, constant, and random values in three spatial dimensions. The structure is called a homogenous space when the refractive index of the structure is constant in all directions. However, if the structure has a periodic arrangement in one direction, it is called a one-dimensional periodic medium. Two- or three-dimensional periodicity on the refractive index for a structure is called a two-dimensional or three-dimensional periodic medium. The three-dimensional periodic medium is a perfectly periodic structure with infinitely extended dimensions. The real applications have only finite properties; therefore, practically, the structures would have different properties than the theoretical approximations [72].

The wave propagation or the mechanical energy distribution in the periodic structures is studied through dispersion relations, which defines the relationship of the wavenumber of the propagating wave. As was mentioned earlier, mechanical energy on the structures can be manipulated through Bragg scattering and using the local resonance of the structures. Even though understanding and familiarisation of the wave propagation on the structures are important in manipulating the energy, building Bragg scatterers and local resonators might help achieve the aim without wave information. When vibrational energy hits the scatterer, the scatterer is excited with the coming energy [86]. This is similar to when wave propagation is an incident on a scatterer. The scatterer (or the damper, the absorber, the resonator, etc.) radiates the energy (wave propagation).

Bragg scatterers work in the principle of the Bragg condition. There might be a phase difference or a time lag because of the structural interactions. Depending on the phase changes, the wave's amplitude can be controlled. When the phase change equals π (out-of-phase), a destructive interference modulates the wave propagation using the scatterer. When the phase change is equal to zero (in-phase), there is a constructive interference that has no impact on wave propagation. Bragg's principle informs that for a one-dimensional periodic structure, the incident angle on the reflected and transmitted layers are the same for the excitation wave. A strong reflection would appear when the waves are in-phase, resulting in the Bragg condition ($m\lambda/2L$, m is the integer, and L is the periodicity of the structures) [72]. Bragg bandgap is found in the dispersion relations' destructive interferences, which is the division between the instructive and destructive interferences. As already noted, this relates to the spacing of the scatterers and the wavelength of the exciting propagation [85].

Negative Effective Material Properties

Coupled resonators illustrate effective material properties such as negative dynamic mass and negative dynamic stiffness, which are widely studied properties [87]–[91]. In order to exemplify these situations, 2-DOF systems are used here (Figure 2.11).

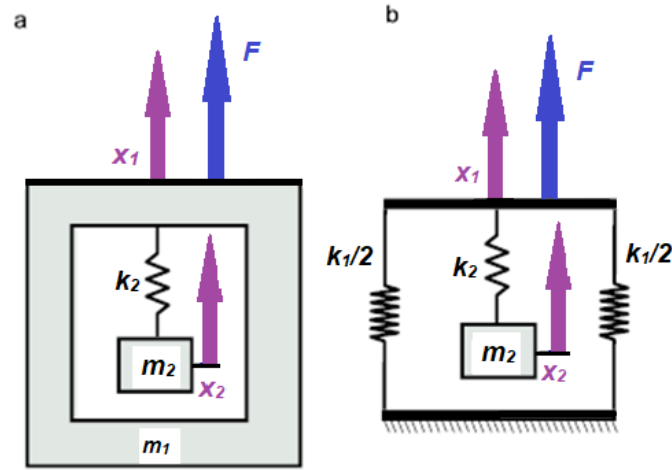


Figure 2. 11: 2-DOF systems with (a) mass-in-mass and (b) mass-in-spring representations, similar to the figure in [90]

The first example includes mass-in-mass elements, as shown in Figure 2.11-a, representing *the negative effective mass* properties. The equation of motion for this system has frequency response function $H_{j1}(f)$ ($j=1,2$), which is evaluated between the response of $x_1(t)$ and $x_2(t)$ under the applied force $F(t)$. $F(t)$ in this system depends on the applied frequency ($F(t)=F_0e^{ift}$). The effective mass for this system is $m_{eff}(f)$ is derived using the following equations (Equation 2.19-2.20).

$$\begin{bmatrix} m_1 & 0 \\ 0 & m_2 \end{bmatrix} \begin{Bmatrix} \ddot{x}_1 \\ \ddot{x}_2 \end{Bmatrix} + \begin{bmatrix} k_2 & -k_2 \\ -k_2 & k_2 \end{bmatrix} \begin{Bmatrix} x_1 \\ x_2 \end{Bmatrix} = \begin{Bmatrix} F \\ 0 \end{Bmatrix} \quad (\text{Eq. 2.19})$$

$$\begin{Bmatrix} x_1 \\ x_2 \end{Bmatrix} \equiv \begin{Bmatrix} A_1 \\ A_2 \end{Bmatrix} e^{ift} \quad (\text{Eq. 2.20})$$

The frequency response function (FRF) is widely used to describe the dynamic relations of the input and the output of the frequency-based system. According to the MDOF system frequency response function calculations, Equations (2.19) and (2.20) are transformed into Equations (2.21) and Equation (2.22) below.

$$H_{11} \equiv \frac{A_1}{F_0} = \frac{k_2 - m_2 f^2}{(k_2 - m_1 f^2)(k_2 - m_2 f^2) - k_2^2} \quad (\text{Eq. 2.21})$$

$$H_{21} \equiv \frac{A_2}{F_0} = \frac{k_2}{(k_2 - m_1 f^2)(k_2 - m_2 f^2) - k_2^2} \quad (\text{Eq. 2.22})$$

Using the given equations and Newton's 2nd Law of Motion by treating the absorber as unknown, the effective mass (m_{eff}) of the mass-in-mass system is given in Equation (2.23) below. In this equation, f_2 is the eigenfrequency of the additional mass (m_2) as the squared root of the ratio of stiffness of the spring-2 (k_2) to the mass-2 (m_2).

$$m_{eff} \equiv \frac{F}{\ddot{x}_1} = \frac{F_0}{-f^2 A_1} = \frac{m_2 f_2^2}{f_2^2 - f^2} \quad (\text{Eq. 2.23})$$

Equation m_{eff} might have resulted in an infinite number when the excitation frequency (f) equals the eigenfrequency of the absorber (f_2) because it results in the response of m_1 (H_{11}) and the displacement of m_1 (x_1) itself is equal to zero. According to this, the external force ($F(t)$) would not impact the total system since the mass absorber absorbs its impact. This explains *the mechanical vibration* absorber idea. In addition, when the excitation frequency (f) has higher amounts than the eigenfrequency of m_2 , the effective mass tends to see negative values that are not observed in the real application. However, for some situations like the higher excitation frequency, the effective mass tends to see negative values in the theoretical calculations around the eigenfrequency of the system. In reality, the coupled mass system only responds to the force (F) according to Newton's 2nd Law of Motion ($F=ma$, a is the acceleration value). In addition, at any excitation frequency with the same value as the mass absorbers eigenfrequency, the amplitude of the mass absorber (A_2) decreases when the mass of the absorber (m_2) increases.

In the second example, a mass-in-spring system, as given in Figure 2.11-b, is investigated to model *negative dynamic effective spring stiffness*. The equation of motion for this system has frequency response function $H_{j1}(f)$ ($j=1,2$), which is evaluated between the response of $x_1(t)$ and $x_2(t)$ under the applied force $F(t)$. The effective spring stiffness, $k_{eff}(f)$, is derived following the given strategy in Equation (2.24).

$$\begin{bmatrix} 0 & 0 \\ 0 & m_2 \end{bmatrix} \begin{Bmatrix} \ddot{x}_1 \\ \ddot{x}_2 \end{Bmatrix} + \begin{bmatrix} k_1 + k_2 & -k_2 \\ -k_2 & k_2 \end{bmatrix} \begin{Bmatrix} x_1 \\ x_2 \end{Bmatrix} = \begin{Bmatrix} F \\ 0 \end{Bmatrix} \quad (\text{Eq. 2.24})$$

$$\begin{Bmatrix} x_1 \\ x_2 \end{Bmatrix} \equiv \begin{Bmatrix} A_1 \\ A_2 \end{Bmatrix} e^{ift} \quad (\text{Eq. 2.25})$$

Following a similar strategy in FRF calculation provides the following equations (Equation (2.26) and Equation (2.27)).

$$H_{11} \equiv \frac{A_1}{F_0} = \frac{k_2 - m_2 f^2}{(k_1 + k_2)(k_2 - m_2 f^2) - k_2^2} \approx \frac{1}{k_{eff}} \quad (\text{Eq. 2.26})$$

$$H_{21} \equiv \frac{A_2}{F_0} = \frac{k_2}{(k_1 + k_2)(k_2 - m_2 f^2) - k_2^2} \quad (\text{Eq. 2.27})$$

Using the given equations and Newton's 2nd Law of Motion by treating the absorber as unknown, the effective spring stiffness (k_{eff}) of the mass-in-spring system is given in Equation (2.28) below.

$$k_{eff} \equiv \frac{F}{x_1} = k_1 + \frac{k_2 f^2}{f^2 - f_2^2} \quad (\text{Eq. 2.28})$$

When the excitation frequency of the system (f) equals the eigenfrequency of the absorber (f_2), the effective stiffness will receive an infinite value because the frequency response of the main system (H_{11}) and the displacement of the main system (x_1) will be zero. In contrast, the exciting force equals $-k_2 A_2$. According to this information, the external force, the exciting force, is cancelled out by the internal absorber dynamics through its spring stiffness (k_2). This example is another option for a *mechanical vibration absorber*. In addition, at any excitation frequency with the same value as the mass absorbers eigenfrequency, the amplitude of the mass absorber (A_2) decreases when the mass of the absorber (m_2) increases.

As a result of these mechanical vibration absorber examples, the effective mass of the system tends to receive negative values when the system is excited with a higher frequency level than the eigenfrequency of the absorber and the second part of Equation (2.21) is larger than m_1 . On the other hand, the effective stiffness tends to see negative values when the system is excited with a lower frequency level than the eigenfrequency of the absorber, and the second part of Equation (2.26) is larger than k_1 .

Mechanical vibration absorber modelling using the strategies given above examples provides several options:

- Suppose the excitation frequency (f) is smaller than the eigenfrequency of the absorber (f_2) since the effective stiffness (k_{eff}) is larger than zero and the FRF values of the elements (H_{11} and H_{21}) are lower than zero. In that case, the motions of the system elements (x_1 and x_2) are in phase, and this is an *acoustic mode*.
- Suppose the excitation frequency (f) is smaller than the eigenfrequency of the absorber (f_2) since the effective stiffness (k_{eff}) is smaller than zero and the FRF values of the elements (H_{11} and H_{21}) are larger than zero. In that case, the motions of the system elements (x_1 and x_2) are in phase, and this is an *acoustic mode*.
- If the excitation frequency (f) is higher than the eigenfrequency of the absorber (f_2) since the effective stiffness (k_{eff}) is larger than zero and H_{11} is lower than zero, but H_{21} is larger than zero, the motions are out of phase, which means it is an *optical mode*.

The phase difference is the resulting property from the relationship between the wave propagation and the absorber (scatterer) in addition to the properties of the absorber. When there is more than one scatterer in front of the wave propagation path, a special situation is observed in the identical scatterer's case, depending on the distance between the scatterers, the wave modulation and phase changes controlled by these scatterers. Since destructive interference is beneficial in wave propagation control, half of the wavelength for the distance between the scatterers is where the highest destructive effects are expected.

2.5- Metamaterials

The featured artificial structures have been used for over 50 years for many applications with the aim of new technologies breaking metamaterials' limits. Metamaterials were first studied in electromagnetics [85], then explained in vibration-related studies. They found effective ways of reducing the undesired attenuations on the structures [92]. In addition to electromagnetic studies, metamaterials have also found a place in acoustic studies. Metamaterials are characterised by the subwavelength performance that enables to control of waves much bigger than the characteristic size of the structure [93]. Metamaterial is a term that the Defence Advanced Research Projects Agency (DARPA) has started to define these unconventional composite structures that cannot be found in nature [94]. Metamaterials are not possible applications directly from nature; their effect comes from

design properties and periodicity. The periodicity effect of metamaterials comes from the array of multiple resonators. They show MDOF system behaviour, which the researchers found exciting [95]. A simple arrangement of resonators in metamaterial study is shared in Figure 2.12.

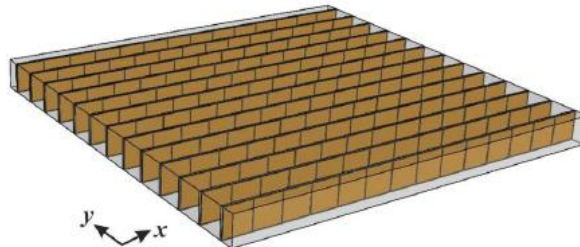


Figure 2. 12: Example of metamaterial [95]

Metamaterials were used to control the seismic wave propagations of their seismic invisibility cloaking properties. Seismic wave propagation is very strong through the soil and alluvial topographic medium. Therefore the dynamic effect is expected to be very high in ground motion attenuation, called "*side effects*" [96]. Therefore, the structures were aimed to be protected from seismic changes. The tree-like structures were applied in a study to show an example of geological scale application. Trees in a forest were accepted as sub-wavelength resonators since the researchers assumed that the wavelength was very high for seismic wave propagation. This study showed that the simple metamaterial example of trees could be used to define the bandgaps in the given frequency ranges and seismic wave propagations. The band frequencies (stop bands and pass bands) were found using Bloch-Floquet theory in the numerical studies. This was a geophysical scale study with soil-type medium and natural resonators (tree) interaction in the medium [96].

Metamaterials have built-in local resonance effects on the main structures, and they are possible solutions to reduce the challenging sides of the situations. In this case, the main structure was presented to increase the degrees of freedom for controlling the wave propagation [90], [97]. The properties of the newly adapted structures should be smaller than the shortest wavelength in the wave propagation if these structures have homogeneous properties. Thus, they can show effective properties under working conditions. This effect was so-called blocking the propagation [98] in the stop band frequencies [97]. These structures are eligible when they are designed by focusing on the "*stop band*" and "*pass*

bands” frequency ranges while focusing on frequency ranges with their unnatural properties. Examples of the application areas of the metamaterials,

- Absorption and dissipation (by using perforated covers on plates or quarter-wavelength resonators, etc.),
- Reflection is the other type of application rather than deflecting or blocking the wave propagation (i.e. by using corrugated beams or inclination on metamaterial walls aircraft engine [92]),
- Noise trapping is the most interesting for the researchers (using selective angles or surfaces to block the wave propagation, meaning that the surface is not allowed to propagate waves, such as acoustic liners). For instance, take-off and landing processes are always the noisiest processes on aerostructures. This is mainly found in propulsion systems-related situations. There were several applications to reduce the effects of these undesired situations on aircraft [92],
- Cloaking [92].

Metamaterial theory states that all the dimensions of the metamaterial structures should be smaller than the shortest wavelength if the material is homogeneous [97]. Moreover, the same paper had two different arguments about the metamaterial theory. One implied that within a known wave condition (direction and magnitude), the resonant frequency of the metamaterial structure should be smaller than the modes of the primary structure. This was required for the metamaterial to meet that wave first-hand. The other implication that if the wave properties were unknown, it was better to design the metamaterials in subgroups. Therefore, each subgroup's resonant frequency can cover a wider range of frequencies through the wave propagation on the beam [97].

Nonetheless, if the aim is absorption in a lower range of frequency waves (wider wavelength), then the design criteria should be around the eigenfrequencies and boundary conditions [97]. The writers offered that the metamaterial applications open the way for new properties on the structures and the materials to be effectively used [92]. Proper calculations for the design parameters [99] may help to widen the application of metamaterials in real applications [97].

Periodically arranged structures have benefited the band gap arrangement for both high- and low-frequency wave propagations. However, especially for the low-frequency propagation, the spatial arrangement in the periodic structures have to be large enough for large wavelengths to maintain the band gap. Therefore, this situation has been a type of limitation to overcome. Locally resonant structure attachments in the unit cells of the periodic arrangements change the way of wave propagation. In addition, with rapid advances in micro-production techniques, composite materials, and increased abilities in the modelling approaches, locally resonant structures attached small sized unit cells are produced in time. These small subunits illustrate unconventional structural properties which cannot be found in nature. The local resonance mechanism breaks the rules for the sound transmission in the structures and increases the effectivity of periodic structure usage in smaller-sized spatial arrangements. Increasing common interest in finding advanced technology options in the applications has directed the implication of unnatural novel solutions, periodically arranged inclusions on the host structure to show effective structural behaviours known as metamaterials [100].

In another research study, the effective properties of materials of the metamaterial were found to be negative (i.e. negative effective density, negative bulk modulus, etc.). Therefore, these properties affect the wave propagation inside the medium, and as a result, energy flow was directed unusually through the medium by using metamaterials. Acoustic super lenses are an example of this type of application in aeronautics [92]. Periodically arranged resonance structures around the local resonant frequencies were useful since they showed unique behaviour. However, periodically arranged metamaterials on the same mechanism were more efficient [80]. By checking these propagation plots, the range of band frequencies can be extracted; thus, the structure and the resonators can be used as mechanical wave filters for the vibratory system. The application of metamaterials and bandgaps is being explored in a recent research study.

Acoustic metamaterials deal with the mechanical wave propagation through the structures. Similar to electromagnetic metamaterials, acoustic metamaterials illustrate mechanical wave dispersion properties when designed as subunits on a structure to resonate under mechanical wave affection [101]. When these subunits of the acoustic metamaterials on the

structure show local mechanical resonant behaviour, they illustrate negative effective mass and spring properties.

Micro-structuring technologies in engineering and developments in the materials sciences increase the opportunity of developing smaller and more efficient metamaterials. Therefore, metamaterial applications have been attractive in many engineering areas in the last half-century [102].

The particle damper's main aims as other damping methods are reducing the structural vibration and decoupling the attenuation of the structures. In addition to these dampers, the periodic arrangement is also found interestingly effective on the exciting structure as they increase absorption and damping properties due to the increased number of freedoms of the attached structure [6]. Periodic structures are organised identical substructures which are merged in periodically repeated compartment. Properties of these structures are improved in terms of design and material properties, which constitute metamaterials. Therefore, metamaterials have their parameters as subwavelength size, periodic arrangement, impedance matching and resonating properties, which make these structures original and desired application elements.

According to the earlier research studies, when metamaterials are used in the structure, they show effective structure parameters like negative refraction, negative reflection, effective permittivity, and effective permeability. These effective parameters result from the spacing of metamaterials with the source structure. Their application and study areas are not only in vibration-damping-related issues but also in absorption, reflection, dissipation, and noise trapping areas where metamaterials can be applied.

Vibro-acoustic Applications of Metamaterials

Metamaterials have been useful applications to increase structural abilities like increasing the signal quality, noise reduction or altering the attenuation of the structures. Since the metamaterials have specific properties that cannot be found in nature, these properties are increased in their periodical arrangement. Similar to the other application areas of the

metamaterials, they have been useful and effective in modifying structural vibration. Modification means that these structures are used to attempt to stop or confine the undesired properties like disturbances in the main structures. The theory of periodically arranged substructures on the main bodies has been applied variety of formats as spring-mass systems, periodic beams, periodic plates, or continuous structures to be used in several applications like space structures, underwater types of machinery, aerostructures, etc. In addition, attaching additional elastic structures with damping abilities increases the effectivity of the external excitation. In order to increase the structural damping properties on an exciting beam, metamaterial application was explored using experimental and numerical approaches with plane beam, air holes placed beam, VEM (Viscoelastic Material) attached beam, and VEM-mass attached beam configurations within Kirchhoff Theory [80]. In this study, each subunit is prepared with a small mass which compromises as a resonator on the unit. Band properties with change in the propagation constant and the phase change were divided and shown individually.

2.6- Knowledge Gap and Significance of This Research

According to the literature, examples of the particle dampers and locally resonating structure application on the main structure, vibration absorption and energy dissipation require more attention. There have been several examples of both applications individually. However, compacting these two successful applications in one model and developing a locally resonating nonlinear damper is thought to be more beneficial and effective in controlling vibration attenuation.

In order to understand the energy dissipation mechanism of the granular structures, a prediction method is required. An equivalent solid structure method will be developed since DEM would require much computational effort. A whole vibratory system analysis based on the frequency-dependent solutions would not be available. Therefore, the Discrete Element Method (DEM) and the Finite Element Method (FEM) are required for modelling and analysing the granular structures and the equivalent structure. Multiple particle damper effectivities and periodic arrangement effect are studied using the equivalent isotropic solid structure approach. This study aims to provide understandable and trustworthy insight into

particle damper physics and its effectiveness. It also aims to show how to increase their effectiveness as a local resonator. In conclusion, extending the effectivity of the particle dampers by arranging them periodically on the main structure is one of the main objectives of this work. It is believed that this research is a new window to damping research which would be a helpful and informative source of granular matter studies and periodically arranged structures.

Chapter 3: Granular Structures and Analysis Methods

Granular structures have been of great interest since they were introduced as the primary elements of solid structures [103]. This idea arises from the deformation of a solid structure: interaction between the neighbouring granules, which are substrates of the solid structure, maintains reciprocal interactions through the other neighbouring granules in an impact event for a solid structure. These series of interactions between the granular structures result in the deformation of the solid structure.

The classification of the granular structures is based on the environmental conditions where they were placed, what conditions they are applied and the state of the granular structures [103]. Granules participate in many areas and processes in the industry. The nature of granular structures allows the applicability of the same principles for a few orders of magnitudes in the size of granules and can be used in identifying industrial applicability of the granular structure inclusions [103]. For instance, in the construction industry, granular structures have a massive implication from housing and hydraulic concrete to piping which are using granular structures.

Vibration damping is considered as one of the engineering applications of the granular structures due to their interaction with other packing members. The transition of energy and change in the momentum between members of granular structures while changing the total energy from the structural body has been studied in detail [17]. To understand the energy dissipation process caused by granules, the properties of these structures should be studied first.

This chapter is aimed to introduce the relations of granules in a packing and equivalent isotropic structure material modelling for further application. Therefore, the chapter includes necessary definitions regarding the granules and their mechanical interaction with neighbouring granules in the first part. Followed by numerical analysis based on the introduced relations. In addition, selections of granular structures, contact mechanics and relative contact information are integrated into numerical model. Lastly, equivalent isotropic solid structure model is introduced for metal and plastic granules.

3.1- Classification of Granular Structures

Knowing granular structures and understanding their physical and mechanical properties are essential since they constitute a significant portion of the physical assumptions imposed on solid structures. According to the definitions given in by Brown and Richard [104], granular structures have been divided depending on their size. This division assumes that granules stay in contact with each other at most of their resting position under the effect of gravitational forces. Since each granule illustrates its physical and mechanical properties, individual elements in a granular packing are generally assumed to be discrete solid structures. Loose packings and fluidised beds are exceptions to this specification because of the packing properties and less interaction between individual members. The classification between the granular structures according to sizes is as follows [104]:

- Powder defines the granular structures for a diameter of less than 100 μm . This classification has additional branches: *Granular powders* (10 to 100 μm), *Superfine powders* (1 to 10 μm), and *Hyperfine powders* (0.1 to 10 μm).
- Granules between 1000 to 3000 μm (equal to the size of 1-3 mm) that constitute *granular solid*.
- The granule diameter larger than three mm which are classified as *broken solid*.

A significant contribution was accomplished to the granular structure relations using different sizes and different material permutations for granules and enclosing volume in experimental-based research [105]. Study conducted by Güttler [105] provides fundamental information on how particles collide with each other and their enclosing cavity. It was stated that the size of the particle diameter has an essential impact on stress distribution in the granular pack. The contact was characterised as adhesive and plastic depending on collision velocities for the particular size of spherical granules. Distributed dynamic behaviours such as the velocity of the impacting bodies and contact engagement levels were different for each size of granules. Granules with smaller diameters were illustrated more active movement with higher velocities than the larger sized granules. Additionally, the material properties of the colliding structures impacted interaction quality and elasticity properties at

the contact event. Surface roughness and surface polishing were other critical parameters of the contact properties for the granules [105].

Granular size impact was investigated in a numerical-based study using steel spherical particles under various rolling conditions [106]. As a result, the interaction between different size of granules and their physical arrangement was identified as including various states. Also, the angular momentum of different sized granules was recorded as conserved throughout the collision event.

3.2- Interactions Between the Granules in a Packing

Granular structures have dynamically interacted with each other as stated previously. According to this statement, evaluating the force interactions and resulting impact deformations between the granules provides understanding of the granular dynamics. Dynamic interactions of granules in a pack depend on specific properties such as coefficient of restitution and friction coefficients. Therefore, these properties might change accordingly with the material of the granules in contact. In addition, granular structures behave in several ways, given in further subchapter, depending on the excitation impact on the enclosure cavity, and these properties are analysed in the following section.

Coefficient of Friction and Force Interactions Between Granules

In a packing, granular structures illustrate their micromechanical properties that define the granule to granule contact and the contact between the granules and the container walls. Depending on the directions of the contact between structures, static and dynamic frictions were introduced by Euler [103]. Euler's idea of friction model were used in Coulomb's article within normal and tangential forms, which, later, have been used to define the friction laws in granular structures [107].

The friction coefficient between the contacting bodies (μ_s) depends on the material properties. In addition to contacting two bodies within the position of temporary placement, plastic deformation at the contact is expected [103]. Contacting two structures might change the state of elastic and plastic interactions through the contact event. In terms of frictional contact, the granular structures change/eliminate the energy stability of their bodies, such

as momentum changes between the bodies which defines the dissipated energy in the overall system [108]. As stated in other sources, where the frictional motion and the plastic deformation exist, energy dissipation has been mentioned, as well [52].

The contact forces are divided into two directional contact interactions: the normal contact force and the shear contact force. The forces acting on a granular body are calculated using Equation (3.1) below. According to the equation, the slipping motion only depends on the normal force value. If the shear force acting on the granular body is larger than the maximum expected force, the granular structure tends to slip in the next movement/cycle of the granular system. This statement was supported by Mindlin and Deresiewicz's work and they were concluded the work using the Coulomb's law [109]. According to Mindlin and Deresiewicz's work, applying a predefined friction coefficient for the contacting structures and multiplying it with the normal contact force value equals the shear force between the contacting structures as in Equation (3.1). As a result of higher shear force than the normal force, sliding occurs during the contact. The friction coefficient (μ) between two contacting bodies is considered equal and uniform for all similar contacts.

$$F_{s,max} = \mu F_n \quad (\text{Eq. 3.1})$$

In addition to the previous information, in terms of energy dissipation, the granules with low loss properties, such as steel, tend to illustrate high frictional loss effects in the total energy dissipation of the systems. On the contrary, the granules with high loss properties dissipate lower frictional energy but higher viscous energy. The reason behind the various loss and energy dissipative properties is the material form of the structures. According to previous research that studying interaction forces between contacting two granules over various granular materials [36], the difference between contacting bodies' Young's Modulus impacts the contact forces. These parameters would not be crucial for a single granule; however, this is a significant concern in analysing the elastic relations between bodies in the multiple particle arrangement. Dynamical interactions and the kinetic behaviour of the packing were almost the same for the same type of materials [36]. The friction coefficient was argued to impact the bulk structure's elastic behaviour significantly. According to the discussion about friction coefficient changes, the stiffness of the entire system was changed in the higher

friction contacts [110][111]. Therefore, it can be acknowledged that the friction coefficient has a crucial impact on the granular packing's dynamic properties.

Table 3.1 identifies friction coefficients between certain materials. Specifically, the static friction coefficient significantly impacts this research since the granules are expected to stay in contact in the granules' solid phase, which will be explained later.

Table 3. 1: Coefficient of Friction (static and rolling) values from a variety of sources

Material - 1	Material - 2	Coefficient of Static Friction	Coefficient of Rolling Friction	Source Reference
Steel	Steel	0.5-0.8	0.15-0.42	[112]
Aluminium	Aluminium	1.05-1.35	n/a	[112]
Aluminium	Steel	0.45-.61	0.47	[112]
Brass	Steel	0.11-0.51	0.3-0.44	[112]
Tungsten Carbide	Steel	0.4-0.6	n/a	[112]
Iron	Steel	0.21-0.4	0.133-0.23	[112]
Plexiglass	Steel	0.4-0.5	n/a	[112]
Polyethylene	Steel	0.2	n/a	[112]
Polyethene	Polyethene	0.2	n/a	[112]
Polystyrene	Steel	0.3-0.35	n/a	[112]
Polystyrene	Polystyrene	0.5	n/a	[112]
PTFE	Steel	0.05-0.2	n/a	[112]
PTFE	PTFE	0.04	0.04	[113]
Acrylic Plastic	Acrylic Plastic	0.1	n/a	[114]
Nylon	Nylon	0.15-0.25	n/a	[112]
Nylon	Steel	n/a	0.027	[115]
PMMA	PMMA	0.54	n/a	[116]

As a result of contacting bodies, various motions are expected to be observed since the frictional force acted upon them. These motions are gliding without rolling, rolling without gliding, frustrated rotations, and transitions between the motions and stick-slip motion [103]. These motions define processes in industrial applications such as mining, construction, and pharmaceutical industries [52].

Coefficient of Restitution

The collision of two spherical structures consists of compressive energy, which results in plastic deformation. The restitution coefficient is a fundamental property for the granular structures to model their elastic behaviour according to the theory proposed by Hertz [105], [117]. This property measures the elasticity between the structures in contact, which can take values between 0 and 1. This applies to granule to granule and granule to cavity wall contacts. When the coefficient of restitution equals to zero, the collisions between the bodies or the structure wall are considered perfectly plastic. In contrast, the collision is perfectly elastic in the case of a restitution coefficient equals to 1 [118].

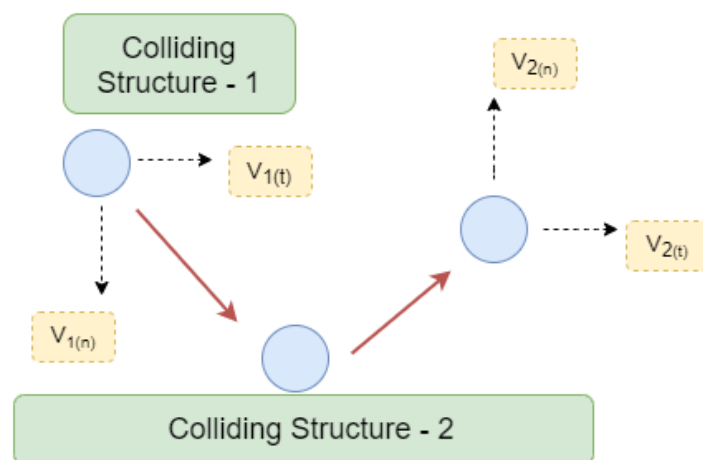


Figure 3. 1: An illustration of colliding structures

Figure 3.1 demonstrates the restitution coefficient elements including normal and tangential velocities before and after the collision. According to this, the restitution coefficient is defined using the value of the after-collision velocities. The restitution coefficient is presented in various methods, such as calculating the kinetic energy transformation and changes in the velocity level. The changes in the velocity levels of the granules are recorded

before and after collisional states. Equation (3.2) explains the restitution coefficient for impacting two granules [119]. The velocities for particle-1 (v_1) and particle-2 (v_2) are given for before $(t - \frac{dt}{2})$ and after $(t + \frac{dt}{2})$ impact collision events.

$$e = \frac{v_1^{t+\frac{dt}{2}} - v_2^{t+\frac{dt}{2}}}{v_1^{t-\frac{dt}{2}} - v_2^{t-\frac{dt}{2}}} \quad (\text{Eq. 3.2})$$

In the velocity level tracking method, the granular structure might be brought down from a height to the surface to illustrate an elastic collision between the granule and the cavity wall. This process is called *the drop test* in the literature [105]. In this case, the velocity of the wall is stationary and equals to zero for before and after collision events. Therefore, the coefficient of restitution is calculated through the velocity changes of the granule as in Equation (3.3). Experimental justification requires technical elements such as a high-speed camera, vacuum tweezers, and adjustable stand: One granule is brought from a height, and the camera is used to capture the velocity of the colliding structures for calculations [19].

$$e = \left| \frac{v_1^{t+\frac{dt}{2}}}{v_1^{t-\frac{dt}{2}}} \right| \quad (\text{Eq. 3.3})$$

Granular structure shape is an essential factor similar to the material properties. The regularly shaped granules (like spherical ones) have straightforward calculation options. In contrast, irregularly shaped particles, like oval-shaped granules, require much attention since they have normal and tangential velocity components in incoming and outgoing directions, separately. There are several studies of the restitution coefficient calculation for granules with irregular shape in the literature [118].

The restitution coefficient can also be defined through the kinetic energy changes. The system's kinetic energy magnitude are evaluated before and after the collision. The kinetic energy level after the collision equals to the difference between the kinetic energy level before the impact interaction and the absorbed (or dissipated) kinetic energy level during the impact event as given in Equation (3.4).

$$e = \sqrt{\frac{KE_{after}}{KE_{before}}} = \sqrt{\frac{KE_{before} - KE_{dissipated}}{KE_{before}}} \quad (\text{Eq. 3.4})$$

Various materials were studied to find their elasticity in the collision events [46]. For instance, softer the material, lower the restitution coefficient value, which means that for the softer material velocity changes less after the impact than in case of the stiffer material. Therefore, the coefficient of restitution might be smaller for plastic structures than in the metallic structures. For instance, particles made of rubber material have a lower value coefficient of restitution than steel particles [118]. The difference between the coefficient of restitution can also be explained with surface conditions (rough or smooth) as the rougher surface conditions would be expected to reduce the bouncing velocity of the granules after the first collision. Several experimental findings on the coefficient of restitution for various materials, material sizes and velocity regimes can be found in the paper written by Güttler et al. [105].

An analytical approach based on theoretical contact mechanics can also be used in acquiring the coefficient of restitution as shown by Thornton and Ning. In their study, the contact mechanics between the structures (granule-granule and granule-enclosure) were analytically modelled. The equation for equivalent restitution coefficient was resolved using velocity definitions for the impact. Impact velocity was divided into yield velocity and adhesive (sticking) velocity groups which were used to define a set of kinetic energy equations [120].

Previously evaluated certain granular materials and their coefficient of restitutions are given in Table 3.2. The properties of various material classes and the size of granules in the table are given for the same structural contact relations. As seen from the table, particles made of metal or plastic are represented by the range of values of coefficient of restitution. According to the table, coefficient of restitution gains various values depending on the material properties of the granules. However, the size of the granules do not have obvious impact on deciding the coefficient of restitution as seen from Table 3.2, examples of steel granules.

Table 3. 2: Coefficient of Restitution values from a variety of sources for spheres

Material	Diameter Size [mm]	Coefficient of Restitution	Source Reference
Steel	13	0.65-0.95	[105]
Steel	5	0.85-0.9	[121], [122]
Steel	1.29	0.7-1	[123]
Aluminium	5	0.55-0.85	[105]
Nylon	7	0.7-0.9	[105]
Acrylic Plastic	3.175	0.934+/-0.009	[114]
Silicon	1.25	0.6-0.8	[124]

According to the aims of this research, closely related values of the restitution coefficient for modelling metal and plastic particles were selected from the previous experimental studies for the granular size and cavity material used in this research.

Gliding

Motions between contacting bodies of two granules depend on their angular velocities of spinning and rotation. The spinning velocity is described as velocity of granule moving in the vertical direction and includes spinning's angular velocity. The rotation velocity is described similarly to the spinning velocity. The motion of granule through the in-plane direction is called rotation and velocity of this motion is the rotation velocity which includes the angular velocity of rolling [103].

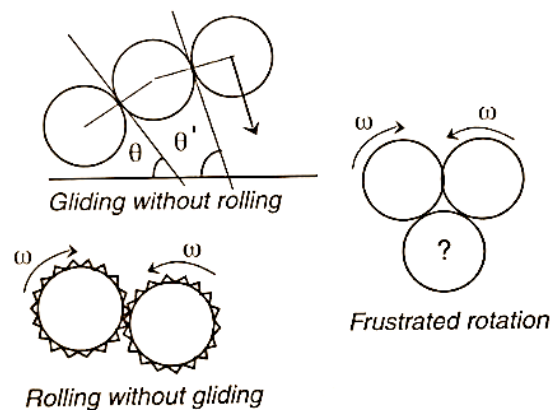


Figure 3. 2: Motion of the granules regarding the friction laws [103]

Gliding is the motion of a particular granular structure that does not change position while moving with preserved contacting angle, and its position depends on the relative velocity between the contacting other bodies of itself. Figure 3.2 demonstrates these motions between the particles [103]; gliding may occur between the perfectly smooth or frictionless granules. It might happen when two granules' contacting angle increases to less than Coulomb's angle ($\theta = \tan^{-1} \mu_s$) where μ_s is the shear friction coefficient. The structures might stay on their axis when rolling without gliding is experienced. The rotation is transferred to the neighbour, but they do not move from their position. This active process at the unchanged position might happen when the surface roughness is high. Also, in some cases, two granules might have a motion in reverse directions; however, their contacting third granule may have an undetermined position. In that case, the motion for the third granule is called the frustrated rotation [103].

Packing of Multiple Granular Structures: Segregation

A heterogeneous mixture is defined as placing granular structures, regardless of their size, shape, and mechanical properties. When these particles are in the shaking process, the collection of the particles is changed. Similar-sized granules are compacted at the same side in the packing. This phenomenon is called the granules' segregation behaviour [125].

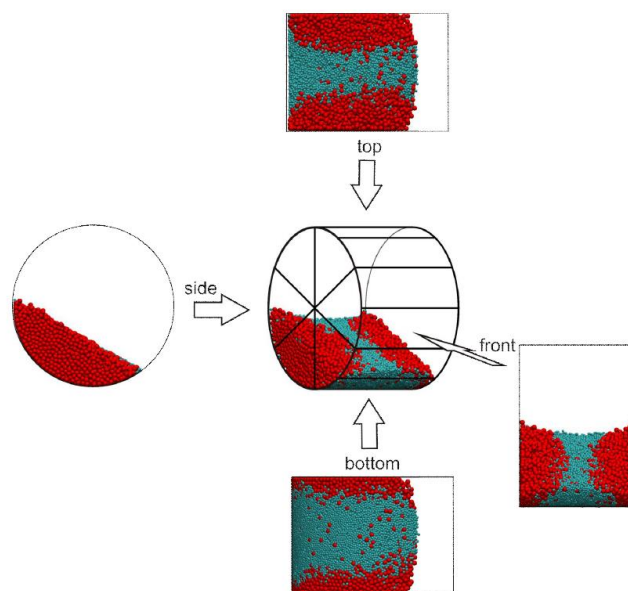


Figure 3. 3: Oyama's Cylindrical Drum (Segregation in Granules) [125]

Segregation was conducted in an experiment-based study using two different granules with different colours. Their cavity was horizontally excited, which resulted in grouping the granules according to their size in the vertical direction. Increasing the interval of the excitation process showed that grouping between the different granules was promoted. This phenomenon was explained as a general situation for granular mixing when the motion of the structures is relative to each other [30]. This experiment is called 'Oyama's Cylindrical Drum (Fig. 3.3). Segregated granules will be exemplified in the experimental analysis of mixed granules in Chapter 7.

Packing of Multiple Granular Structures: Coordination Number

The research conducted for several years showed that the amount of granules in a packing controls the filling fraction. There might be permanent change and diversity depend on the packing conditions, whether regular or a random arrangement for the granules [126], [127]. Also, it depends on the frictional impacts between the granules in contact [52].

The filling fraction is also the fraction of the total particles in the total volume of the enclosure. Kepler defined the maximum filling fraction with a regular arrangement as 0.74. Notably, under the same regular arrangement and hexagonal close pack conditions, the maximum filling fraction was calculated as 0.74 [52], concluding that the regularly arranged same sized granules would have a filling fraction with a maximum of 74% of the total volume of their placement cavity. This case was reconsidered when these hard granules were randomly placed in the same cavity. In this case, the filling fraction was identified as 0.64, indicating that they occupy 64% of the container volume [128]. However, the random close packing debate continues since there is uncertainty on the random arrangement definition. According to the random and regular arrangement ideas, there are additional definitions for the packing of granular structures. When randomly placed granules were carefully placed in the cavity, they occupied 64% of the volume. On the other hand, random loose packing was composed of randomly thrown and placed granules with a maximum capacity of 0.55 for the filling fraction [126].

Granular structure packing is defined by their filling fraction as well as with the coordination numbers. The coordination number is characterised according to the number of contacts of

a single particle in the packing with its neighbours. Nolan evaluated different granular arrangement types and fraction relationships [126]. This study showed that the mean coordination number depends on whether the filling orientation is loose or close and whether it has a random or regular arrangement.

Mean-field theory [128] means the average contact numbers for all packing elements. The packing is evaluated with the number of contacts, quantified with a non-zero force member of the packing. Experimental and numerical approaches describe the granular arrangement's lattices and coordination number. However, there are some restrictions on deciding the coordination number from experiments, such as differences in the packing technique, wall effects of the container, scale between the particles and the cavity volume. Therefore, a homogenous distribution of the granular structures and certain porosity levels can be considered for the consistent coordination number [127].

Packing of Multiple Granular Structures: Wave Propagation

Surface wave propagation has been recorded on the free surface of the vibrating granules [129]. The wave propagation is observed through the upper surface of the granular packings under specific excitation conditions. Figure 3.4 illustrates the travelling surface wave in the packed granules under low amplitude vibration conditions [45].

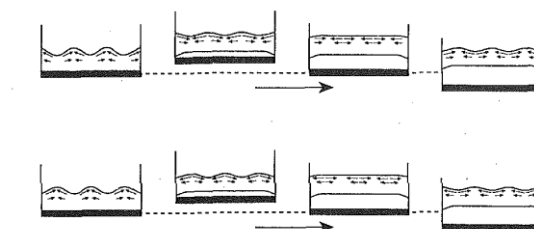


Figure 3. 4: Travelling waves on the surface of granules at low amplitude [45]

In addition, Figure 3.5 illustrates the surface wave in high amplitude vibration. These figures share similarities in wave propagation; however, increasing the vibration amplitude resulted in sharper peaks in the wave formation [45].

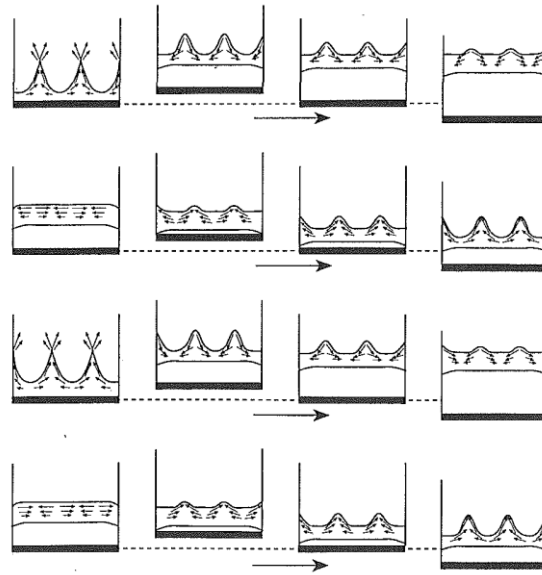


Figure 3. 5: Travelling waves on the surface of granules at high amplitude [45]

In the high vibration amplitudes, the surface wave ended in a standing wave and peaked at the edge of the container [45]. Granules experiencing standing wave motion and resonance properties at the surface placements [108]. Therefore, the material properties of the granules have a decisive effect on the surface wave definition. While rough sand and grass seed showed a well-defined and reproducible wave propagation, smooth sand and monodisperse glass bead showed a wave propagation which disappeared soon [130]. Therefore, observing surface wave propagation on the granular packing requires the granules to be in the solid phase (which will be explained in next section), which also depends on their material properties.

Phases in the Dynamics of the Granular Materials

The granular packing includes many individual granular bodies, which behave separately depending on the excitation amplitude or the excitation frequency. In the low amplitude excitation levels, the granular structures in the packing stay in contact permanently until the excitation conditions are changed. Granular structures are accepted in *the solid phase* since they behave like solid structures, and the solid phase is where the granules do not experience any rolling or jumping movement. In terms of energy dissipation, the solid phase of the granular structures is the most efficient since most of the contact is preserved here [131], which is related to the interaction between the granular structures in these amplitude levels.

The granular bodies experience changes in their state with the increasing excitation amplitude (or, lesser extent, increased frequency). This changeable form is defined using three states: (i) solid-like phase, (ii) fluid-like phase and (iii) gas-like phase [6], [62]. In the low excitation values, the behaviour of the granular structures is defined using their collisional and frictional properties. The granules primarily interact with each other and the cavity walls with negligible relative motion in the low amplitude range. Since granular particles move around their original state and preserve their contacts, this phase of the granules is known as *the solid-like phase*. Increasing the excitation amplitude changes the granules' state in the cavity from solid to *fluid-like phase*. The granules tend to move with stick-slip motion and roll on each other in further movement. The friction forces between the granular structures are lower than the excitation force; therefore, the motion of the granules is increased compared to the solid-like phase. In *the gas-like phase* of the granular structures, the convective motion of the granules is experienced, which means the granules behave like gas particles in the cavity. Their contact with other packing elements is reduced, resulting in less energy dissipation.

Fluidisation

Packed same sized granular structures under high acceleration levels experience fluid or gas state of the granular structures, which was explained in the subchapters '*Phases in the Dynamics of the Granular Materials*' and '*Stick and Slip Motion*'. Regarding the phases of the granules, the critical parameter is the normalised acceleration ($\Gamma=A\omega^2/g$); thus, the acceleration amplitude and the excitation frequency take a great place in the phase of granular packing.

Granules change their state with the reduced acceleration level; the contacts between granules increase, and granules take position to have a set of columns in the cavity volume. In these conditions, cavity and granules are locked to the excitation, which means they can save their position with infinitely low changes over some frequency and acceleration levels. Under low amplitude excitation, granules behave similarly to a single structure; therefore, their restitution coefficient is very low at that state, as can be expected from the inelastic single granular structure [132].

Increasing the harmonic excitation amplitude to surpass the gravitational acceleration, the granular particles leave stable position and start jumping. However, change starts from the top of the granules since excitation from below is transmitted through granular pack elements in time. Rest of the granules experience the same behaviour through the increased acceleration. When the granules change their stable state to fluid- or gas-like behaviour, they go through the *fluidisation* state [133]. This property can be controlled by changing the number of granules in the packing; for instance, the fluidisation starting time step can be postponed by adding more particles. This is because the transformation of the excitation acceleration through the packed granules requires more time in that case [63]. Most of the energy changes in the granular structures can be received through the solid state rather than the fluidised state. This particular property of the granular structures has been studied by many researchers in the literature [63], [134], [135].

Stick and Slip Motion

Stick-slip motion is frequently experienced in the dry granules packing when they are in contact under Coulomb-Euler friction laws, which force them to show elastic behaviour. The dynamic friction coefficient is less than the static one, and as a result, depending on the granules' velocity, the impact duration might be changed by this motion [120]. In an earlier explanation, material properties of the contacting bodies were linked to the rotation and rolling motions. Therefore, these properties affect individual granules' frictional contact and motion [105].

Also, to raise the energy dissipation by the frictional impact, the stick-slip motion was suggested to be kept at a minimal level since it introduced additional high-frequency excitation [136]. The dynamic characteristic properties constantly change while the particle velocity increases, affecting the frictional impact between the contact. Therefore, the friction mechanism between the granules strongly depends on the frequency level of the excitation [131].

Figure 3.6 illustrates the stick and slip motion phases using the points of A, B and C from an analysis of the increased excitation frequency. From point A to point B, particles do not show relative motion to each other until excitation frequency is increased to point B. The frequency

change is shown as around 5 Hz to reach behavioural change. Then the particles move and slip through their contact surfaces, and suddenly, the response level drops to point C. The stick-slip motion continues as the frequency of excitation increases since the difference in frequency level changes the contact of the granules [131].

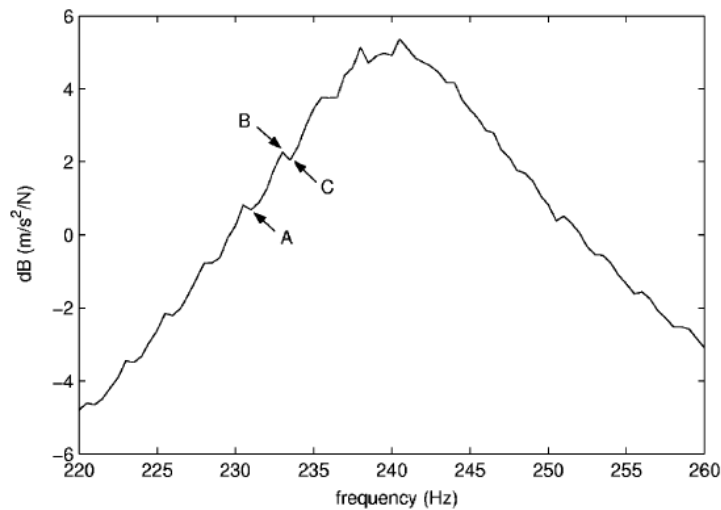


Figure 3. 6: An illustration of stick and slip motion in granular packing [131]

When a pack of granules stay still, individual granules might have some energy to move downwards from the top of the packing through the slope. So, the particle's arrangement is not a stable state. When the slope reaches and exceeds the angle of movement (ϑ), the frictional force is said to be equal to the $mg\cos(\vartheta)$.

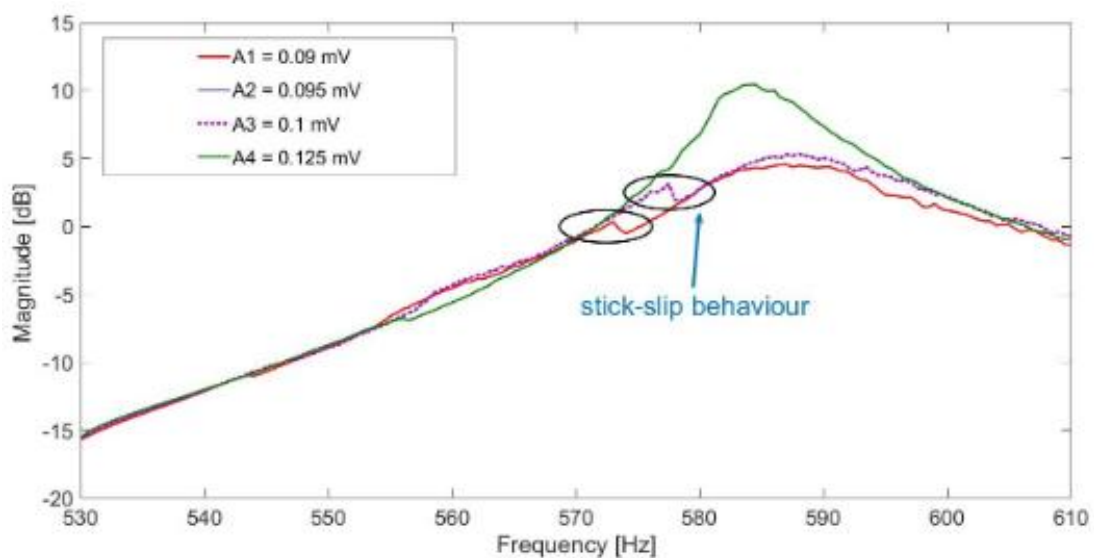


Figure 3. 7: Stick-slip motion in granular packing

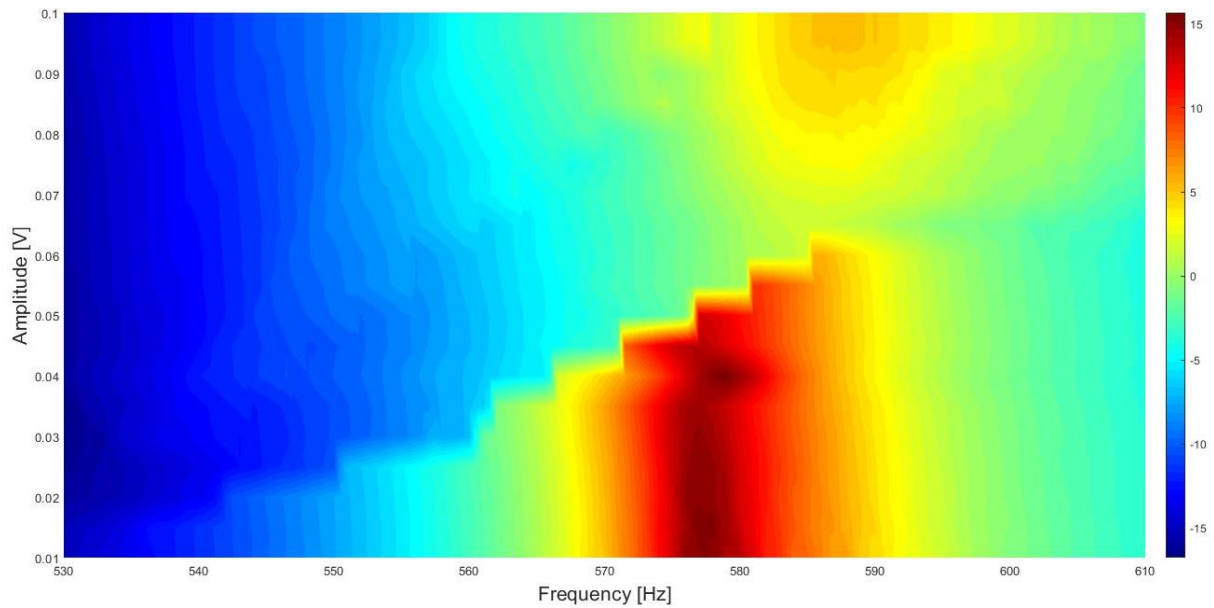


Figure 3. 8: Stick-slip motion in contour plot

In an earlier preliminary study of this project, filled geometry was vertically excited at various amplitudes. Figure 3.7 illustrates the granules' state change over the range of impact excitation frequency; voltage given in the figure refers to the excitation input for the controller/signal generator. Granules were in contact until around 570 Hz and around 575 Hz, and they experienced stick-slip motion under 0.09 mV amplitude. In addition, Figure 3.8 shows the same structure at various frequency and amplitude levels. According to the figure, phase of the granular material depends on both frequency and amplitude and changing the amplitude and frequency leads to the granules' gas-like phase.

The stick-slip motion is a nonlinear phenomenon on the physics of the granules. In this study, in order to minimize the nonlinear phenomena, the solid phase of the granule is considered. Therefore, the amplitude levels should be kept low. Since frequency sweep analysis is required in this research, range of the excitation frequency will be considered as given in Chapter 5, Chapter 6, and Chapter 7.

Collision and Deformation

The collision of two spherical particles illustrates their impact relations through their central axis, which has the collinear velocity for each of these colliding granules [103]. According to

the mechanics, conservation of the kinetic energy and momentum involves in an ideal collision as shown in Figure 3.9 below.

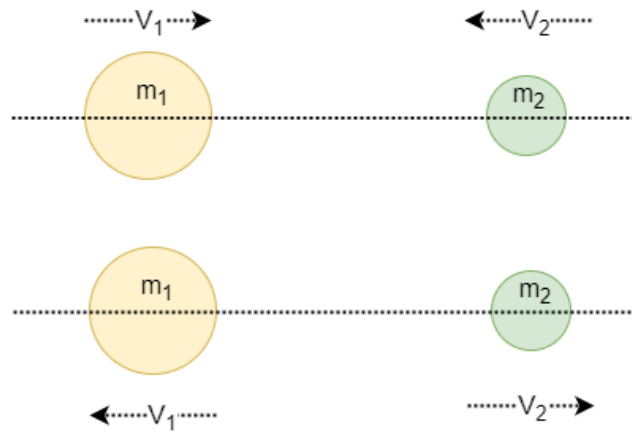


Figure 3. 9: Ideal collision between two grains

This activity is a more straightforward case when it is compared to the packed granular structures and their impacts. The complication in the granular structure interactions is that these grains behave like inelastic materials and experience collision at different angles, various pressures, and friction levels. Then the actual collision comes with changes in the kinetic energy and momentum levels. The coefficient of elastic restitution is defined in these collisions to equate changes in energy and momentum level before and after collisions.

$$\begin{bmatrix} v_{12} \\ v_{22} \end{bmatrix} = \begin{bmatrix} \frac{1-e}{2} & \frac{1+e}{2} \\ \frac{1+e}{2} & \frac{1-e}{2} \end{bmatrix} \begin{bmatrix} v_{11} \\ v_{21} \end{bmatrix} \quad (\text{Eq. 3.5})$$

Equation (3.5) gives information about how grain velocity can be changed through collisions. The effect of the coefficient of restitution (e) was investigated; when it is equal to zero, it means the collision is inelastic (or plastic), and since the collision, the kinetic energy of the granule is converted into other forms of energies like heat. On the other hand, when the coefficient of restitution equals 1, very little portion of the kinetic energy is transformed into other energies and is perfectly elastic [103], [137]. Additionally, according to the results from the experimental studies conducted by Duncan et. al. [46], higher restitution coefficient has shown significant impacts on the overall shape and amplitude of the damping.

3.3- Design and Study Options for Granular Structures

Granular structures are discrete elements that must be evaluated at each contact relation within each time step. Analytical and experimental methods are not sufficient to cover all contact properties and dynamical interaction of the granular structures. Numerical simulation techniques are thought to be a practical option for the advanced analysis. Various methods were developed to simulate the particle interactions and their behaviour in granular packing depending on the assumptions made for the interactions. *Particle Dynamics Simulation* [35] is a generalised title for all granular structure-based simulation techniques: Continuum Models, Cellular Automata, Monte Carlo, Hard Sphere (Event Driven), Soft Sphere, and Particle Dynamics Simulation options [138]. In addition, other particle dynamics simulation options were mentioned as Brownian Dynamics, Stokesian Dynamics and Multiparticle Dynamics [139].

Each simulation technique included specific properties for sophisticated simulation opportunities. Moreover, these particle dynamics simulation options work through the integrations of the force-displacement relationships and update the following contact relations using the latest contact information between the particle-wall and the particle-particle contact mechanisms [108].

DEM (Discrete Element Model)

The Discrete Element Model (DEM) was developed to study the dynamical properties of micro-sized granular structures such as rock dynamics. This dynamic simulation model has been developed to process the granular structure interactions of individual granular bodies while computing the dissipation properties of the total system under impact. This method is currently used within various industrial applications to address issues in granules or discrete structures [139].

DEM methodology calculates the force-displacement law in the contact area and Newton's Law of motion in regular time steps. A simple contact model in the DEM simulation method is modelled to divide the contact in two main directions: normal and tangential contact directions, including mass-spring-dashpot properties, to illustrate all dynamic behaviours

[140]. The method helps calculating the relative motion and force-displacement properties to inform the next step's physical arrangements. In addition to these properties, there is a frictional impact by a simple Coulomb friction member, and DEM might have complex contact interactions mentioned in the next section. DEM is used for various sized granules under various boundary conditions to analyse various phenomena and progress for various collisions and movements [139]. In this study EDEM V2021.1 commercial package [48] is used to model the contact mechanics between particles.

3.4- Modelling of Contact Mechanisms Between Granules

Contact mechanics of the granular packing include elastic behaviour and dynamic properties of the individual granular structures. Contact interactions were developed using analytical definition of the resultant force (F) by considering the normal (F_n) and tangential (F_t) direction of contact between the structures (Equation (3.6)), which is evaluated over the spherical area of two contacting bodies. Then developed contact relations were improved by considering the cohesiveness of the contact, either elastic or plastic contacts.

$$\vec{F} = \vec{F}_n + \vec{F}_t \quad (\text{Eq. 3.6})$$

As a result of the contact force, granules experience overlaps at the contact interface amount of which is dependent on elastic and specific contact relations such as the material properties, coefficients of restitution. Granular structure contact mechanics are calculated in the previously defined time steps (Δt). Normal and tangential force information are recorded before and after the collision. Overlap (Figure 3.10), the outcome displacement of the applied force between the granules, is updated according to the dynamic relations. As a result, each time step includes a force-displacement relationship for a particular granule and feeds the later time step with new state of the particles at the contact.

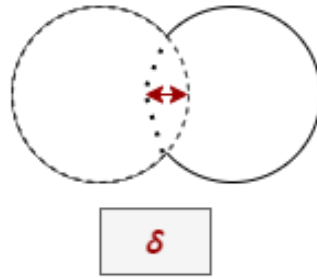


Figure 3. 10: Overlap, displacement at the contact area

There is a various contact modelling options in Discrete Element Methodology. Hertz-Mindlin Contact model, a widely used approach in contact theory, includes the fundamental properties of the contact definitions. The Hertz-Mindlin Contact theory can be evolved into new contact modelling theories by adding more conditions/constrains [48]:

- Hertz-Mindlin (No Slip, without slipping but with slider between the granules because of the friction coefficient)
- Hertz-Mindlin (No Slip) with RVD Rolling Friction
- Hertz-Mindlin with Archard Wear
- Hertz-Mindlin with Bonding
- Hertz-Mindlin with Heat Conduction
- Hertz-Mindlin with JKR Cohesion [141].

In addition to these contact models, for a specific commercial software EDEM, Linear Cohesion approach is implemented to model the cohesive contacts; Linear Spring for the spring contact force modelling; Hysteretic spring for the deformation included spring modelling and Moving Plane for the conveyor motion [48]. These contact models consider the contact radius between the structures is smaller than their geometrical radii of the granules. The radius of contact area between contacting bodies is called the overlap (δ). However, this option has been helpful for only specific geometries (for example spherical geometries) and specified behaviours. Other contact mechanics were developed according to structure contact properties and boundary conditions. The contact theories which can be used in this study have been investigated for their definitions in the next two sections.

Hertz-Mindlin Contact Theory

The contact model for the normal direction force-displacement relations was developed by Hertz in 1882. Mindlin improved the tangential force-displacement relationship in 1949, which was updated in 1953 as Mindlin-Deresiewicz's work included Coulomb friction to the model [48]. Damping properties of both contacts were applied since the restitution coefficient, in other words, elastic properties of the structures impact the contact. Normal force in the contacting granules includes the normal overlap (δ_n) and is evaluated using the following description (Equation (3.7)):

$$F_n = \frac{4}{3} E^* \sqrt{R^*} \delta_n^{\frac{3}{2}} \quad (\text{Eq. 3.7})$$

In this equation, E^* and R^* represent the equivalent Young's Modulus and equivalent radius of the contacting two granules. These properties can be evaluated using the following equations (Equation (3.8) and Equation (3.9)):

$$\frac{1}{E^*} = \frac{(1-\nu_1^2)}{E_1} + \frac{(1-\nu_2^2)}{E_2}, \quad (\text{Eq. 3.8})$$

$$\frac{1}{R^*} = \frac{1}{R_1} + \frac{1}{R_2}, \quad (\text{Eq. 3.9})$$

where $E_1, R_1, \nu_1, E_2, R_2,$ and ν_2 are Young's Modulus of the first granule, the radius of the first granule, the velocity of the first granule and Young's Modulus of the second granule, the radius of the second granule and the velocity of the second granule respectively. The tangential force between the contacting granules is calculated using Equation (3.10), which includes the tangential overlap (δ_t), equivalent Young's Modulus and equivalent radius.

$$F_t = -8G^* \sqrt{\delta_n R^*} \delta_t \quad (\text{Eq. 3.10})$$

where G^* is the equivalent shear modulus of the contact given by $G^* = \lambda^*(1 - 2\nu^*)/2\nu^*$.

Hertz-Mindlin contact theory is one of the most used contact models in granular structure analysis since the simplified calculation procedures while providing efficient and accurate approach in force-displacement calculations [142], [143].

Linear Spring Contact Theory

The physical statement of the contact model was first described by Cundall and Strack [144] using the definition of the distinct element method. In their work, the method was applied as a linear spring, and a damping dashpot parallels each other at the contact position. Calculations were made through contact tracing between the granules. The contact force, whether it is a normal or a tangential force, depends on the spring stiffness (k) and the dashpot coefficients (c) under the overlap constraints (δ) as given in Equation (3.11). δ is an overlapping amount and $\dot{\delta}$ is the overlapping velocity of the granules in the equation. This is similar to the Hertz-Mindlin Contact model implemented in EDEM [47], which is commercially developed software for the granular interactions, except for stiffness calculation in the first step to decide on the overlapping value. Contact duration, Equation (3.12) is limited to the material properties, and tangential force is similar to the normal force in this case.

$$F_n = k\delta + c\dot{\delta}, \quad (\text{Eq. 3.11})$$

where k is stiffness which is provided by the material properties. On the other hand, depending on the overlapping measure constraints, which are part of the elastic properties of the structures, the physical status of the granules can be controlled using the contact method applied in the numerical modelling. The contact time is usually defined with Equation 3.12.

$$t_c = \pi / \sqrt{\frac{k}{m^*} \left(\frac{\beta^2}{1+\beta^2} \right)} \quad (\text{Eq. 3.12})$$

Equation 3.12 limits the contact time in terms of the normal stiffness and mass of the contact area of the contacting structures in addition to the coefficient of restitution (e). β in this equation corresponds to the ratio of $\pi/\ln(e)$. The equivalent mass m^* in Equation (3.13) can be defined as

$$\frac{1}{m^*} = \frac{1}{m_1} + \frac{1}{m_2} \quad (\text{Eq. 3.13})$$

where m_1 and m_2 are the individual mass of the contacting granules. Duration of contact is a decisive parameter for analysis setup and valuable data. The time step should be a low percentage, which is given in Rayleigh Time Step section, of the contact duration (t_c) for an informative contact calculation. For instance, an evaluated form of linear spring contact model is the Hysteretic Spring Contact Model is a choice to model a compressible material [48]. A hysteretic spring is an example of these contact models that also allow plastic deformation at the contacting surfaces [48]. The contact model is an elastic model to the predefined stress value. When the maximum stress value is reached at the contact, particles experience plastic deformation at their contacting level, which does not have a memory to remember the deformation at the contact after the granules were separated.

Evaluation of Contact Analysis. Model selection

In order to differentiate the contact modelling methodologies, DEM-based analysis has been used. All of DEM-based software analysis is modelled in 3D geometry. Since Hertz-Mindlin (No Slip) and Linear Spring contact theories were mentioned to be closely related in terms of contact model approach, a simple case was modelled by applying these contacts in individual cases between the spherical grains in a packing to decide which model would be more appropriate to use in this study. Granules ($R=7.05$ mm) have been placed in a cylindrical tube with 20% of its volume, constituting 68 granules in the cavity. Table 3.3 gives the material and geometrical properties of the structures used in the analysis.

Table 3. 3: Material and geometrical properties of the tube and the granules

<i>Material Properties</i>	The Tube	The Granules
Young's Modulus [Pa]	8.5 E10	2.58 E6
Density [kg/m ³]	1600	1170
Poisson's Ratio	0.14	0.35
<i>Geometrical Properties</i>	The Tube	The Granules
Diameter [mm]	50	15.1
Height [mm]	300	-

Figure 3.11 shows the state of the tube and the granules at various time steps. As seen from the detailed time step representations, granules require 0.75 s to be packed in the enclosure cavity. Horizontally excited geometry was impacted with 0.05 mm amplitude at 655 Hz frequency for 0.2 s of total duration of the modelled process. The fixed time steps for Hertz-Mindlin were selected as 10^{-5} s, and data saving intervals have been set as 10^{-4} s, providing 10 iterations for each contact calculation. On the other hand, using Equation 3.12, t_c was found to be 0.002 s and using 5% of this number, the fixed time steps have been set at 10^{-4} s for the Linear Spring Contact Theory applied analysis. Since the applied force at the contact area depends on the overlapping amount and the stiffness values, Linear Spring Model provides lower force values that might be sensitive to these properties [48].

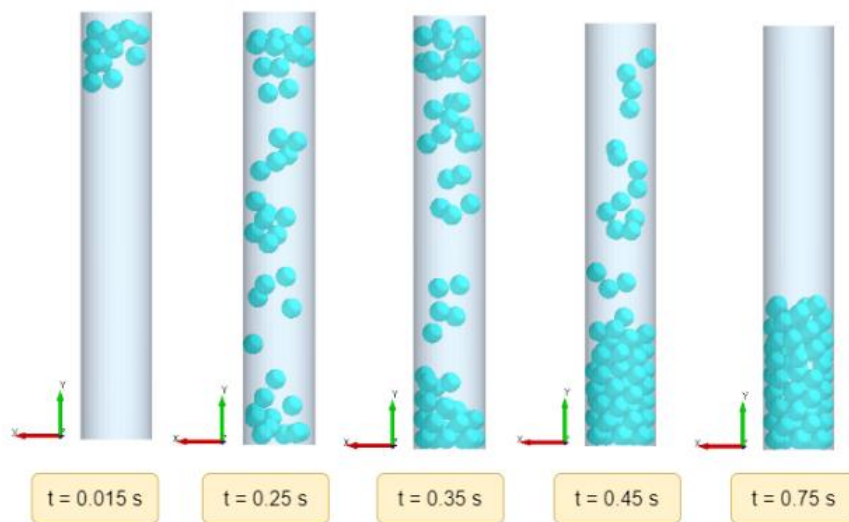


Figure 3. 11: Granular arrangement in the tube

Modelling the contact relations using these principled theories is typical practicality in calculating the normal and the shear contacts. However, in addition to the common sides of these contact models, their developed additional properties increase the differences. Especially the frictional impacts or the predefined overlap in the contact mechanism show a significant difference within these theories. Acknowledgement of the contact using the detailed contact theories increases the opportunity for an excellent evaluation of the mechanism. Therefore, knowledge of the granular material properties, contacting

structures' character and functioning of the environmental cavity are crucial details for an informative representation. Since Linear Spring Contact Theory strongly depends on the stiffness properties and illustrates continuously changing overlaps, it might not be appropriate to apply all types of analysis in this research because of the variety in the material types as metal particles and viscoelastic particles. As a result, applying the same contact properties for all of the granular types in this research, Hertz-Mindlin Contact Theory has been decided to be applied. This is an simplified option for the contact forces including the normal and tangential spring stiffness, the normal and tangential damping and the slider friction coefficient at the contact of the two granules [145].

3.5- Excitation Conditions and Granular Structure Behaviour

Many excitation-related analyses were about the granular structures' nonlinear behaviour [7], [19], [24] . In [64], a pack of granules under the gravitational forces were excited in the perpendicular direction to question the granules' nonlinear behaviour and energy dissipation effect. Granular structures were shown to exhibit an added mass effect in the cavity at both extremely low and high excitation amplitudes; however, in the middle range of the excitation amplitudes, they demonstrate increased energy dissipation effect [146]. In this excitation range, mass ratio and aspect ratio (the ratio between the cavity's length and diameter) were additional effects on the nonlinearity [147].

Vertically excited granular structure packings were studied in some examples [114]. The densification, which means the compressed granules in a smaller volume by the impact of the excitation and the gravity, was experienced and connected to the frequency level and the excitation amplitude. In a study aimed to increase the bulk solid fraction, the excitation frequency was kept between 25 Hz and 100 Hz, while the relative acceleration for the cavity was studied at $0.94 < \Gamma < 11.54$. The 'gas-like' behaviour was observed when the excitation amplitude was near the highest values [114]. Vertically excited granular packings have more complex relations than the horizontally excited granular packings since the gravitational force impacts the granular structures [129].

To resolve the complexity of particle behaviour additional compressions with a layer of foam on the granules in the packing was applied. The results showed that adding extra pressure to

the top of the packing which increases the effective region of the granular structures and helps the granules to be active in the higher frequency regions, as well [7].

Several studies include centrifugal excitation of the granular structures using the applications of turbine blades or fans as these dampers are attached to the targeted structure. While the structure is being impacted with the excitation, packed granules move with the excitation impact to suppress undesired response [5]. The nonlinear parameters were investigated using the experimental approaches, resulting in the granular structures changing their behaviour and energy dissipation effectivity changing with the centrifugal loading [148].

In this study, amplitude dependent properties of granules were studied using PMMA granules placed in a tubular cavity and excited horizontally at various amplitudes. Figure 3.12 is used to illustrate the activity level of granules at a variety of excitation levels. The excitation levels have been varied from 0.0001 m to 0.0009 m for the first 10 cases. Further cases have been set with 0.0005 m increments as 0.0010 m (Case-10), 0.0015 m (Case-11), 0.0020 m (Case-12) and 0.0025 m (Case-13). Case-3 which has 0.0003 m of displacement amplitude has not been included in Figure 3.12 since the trend representing the case has been similar to Case-2. As the excitation amplitude increased, the kinetic energy of the granules was also increased by the excitation amplitude [37]. Since the granules' kinetic energy is calculated through the velocity of the particles and total mass of the particles, the trends in the figure illustrate similar behaviour where the time dependent behaviour of the granules has resulted in various kinetic energy levels at each time step. The total kinetic energy of particles was calculated in accordance with the methodology implemented in EDEM which calculates the total velocity of the particles and their total mass [48]. The total kinetic energy calculation in EDEM is processed in 'Analyst' section of the software which proceeds the dynamic and static relations of the granules as analysed with the settings primarily prepared in 'Creator' and 'Simulator' sections in the software.

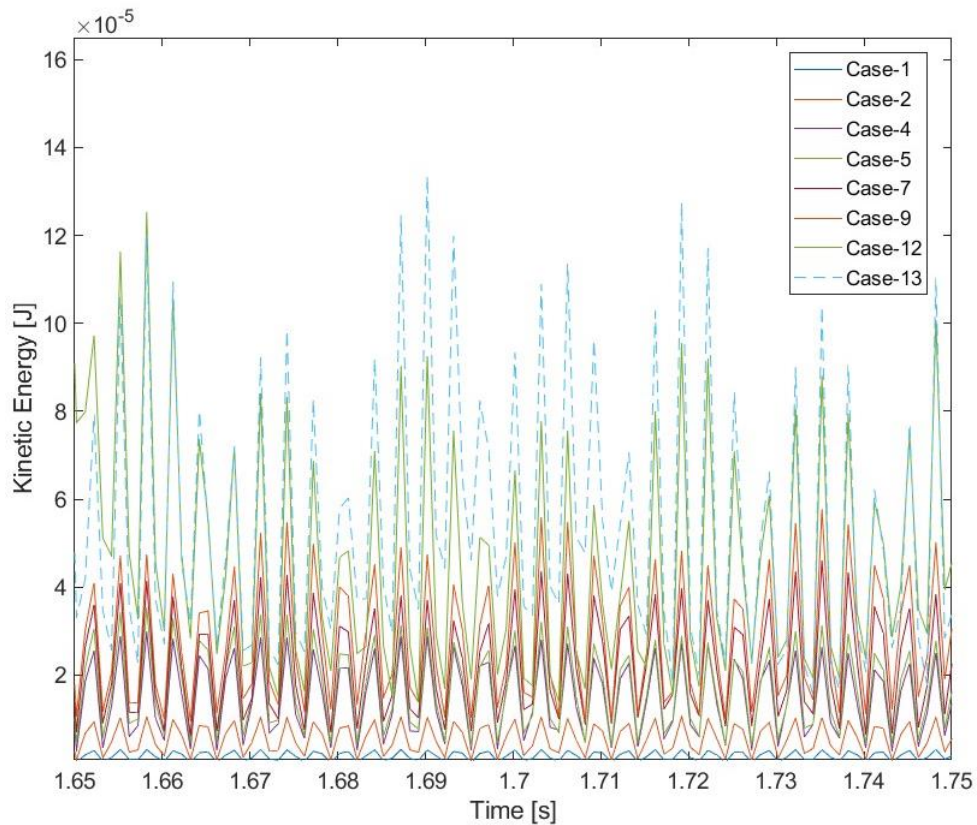


Figure 3. 12: Granular structure behaviour for amplitude level changes [37]

Excitation amplitude impact on the granular packing is studied in a series of analyses using the same enclosing cavity and granular structures as in the Hertz-Mindlin Contact Theory evaluation. The excitation conditions and duration are set at the same levels as in the previous case, and Hertz-Mindlin Contact Theory has been applied as the contact model. The table below details the amplitude levels applied in the analysis and the contact number of granules in the given analysis setup.

Table 3. 4: Amplitude levels over the case numbers and granular structure materials

Steel grains (D=1.58 mm)	Amplitude Level [mm]	Coordination Number (Average)
Case-1	0.01	3.88
Case-2	0.025	3.94
Case-3	0.05	3.94
Case-4	0.1	3.91

According to Table 3.4, excitation amplitude impacts the contact relations of a single granule. In the first case (Case-1), the granules are in random places with such small amplitude of excitation [62], while increasing the excitation amplitude, the coordination number has been increased which means the granules have had more contact with each other in the cavity. The change rate between the coordination numbers is around 1.52% which might increase by the change in applied amplitude level. However, as explained in the amplitude dependency of the granules, increased amplitude does not mean increased number of contacts within the packed granules. This is seen in Case-4, the increased amplitude level has reduced the mean coordination number of the granular packing.

Figure 3.13 has been prepared to evaluate the granular structure dynamic relation at various amplitude levels. The velocity of granules at different amplitudes is given in Figure 3.13-a. Dimensionless energy (Figure 3.13-b) has been calculated using kinetic energy and total energy ratio using the data traced. The first peaks in the figures show the response to the first excitation impact on the cavity; therefore, the magnitudes between 1.5-1.55 s were much higher than the rest of the time steps. As expected, granule velocity was higher at highest amplitude than other amplitude levels because it resulted in higher kinetic energy levels. The ratio of higher kinetic energy in the dimensionless energy formation gives a higher value.

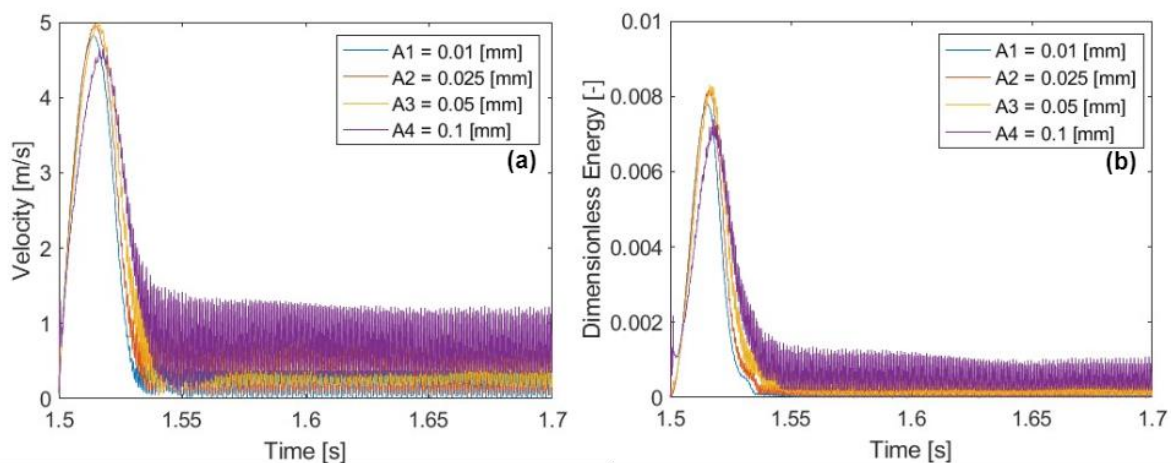


Figure 3. 13: Granular behaviour at different amplitude levels: (a) Velocity change over time, (b) Dimensionless energy distribution over time for packed granules

Overall, granular structure dynamics are sensitive to various properties, and excitation amplitude level is one of them since it impact instantaneous changes in the contact properties. The granular structures have been found more effective in damping when in their solid phase (as explained in the previous subchapters). Therefore, working on their efficiently processing regions depend on the excitation conditions while depending on the direction of the excitation. For this reason, horizontally applied excitation, which reduces the rapid changes in the coordination number, would be appropriate for the research aims in the future analysis. The amplitude level needs to be appropriately selected by considering the granular structure response to avoid the nonlinear behaviour.

3.6- Discrete Element Modelling of the Spherical Particles Using EDEM

Interactions within the granular packing between the grains and the enclosure cavity can be evaluated while tracking their dynamic relations in the step-by-step procedure, which is possible using EDEM V2021.1, a commercial software based on the Discrete Element Method. EDEM provides modelling, analysis and post-processing opportunity for powder behaviours, granular interactions, conveying kinematics, mixing and agglomeration analysis and many process simulation options [149]. Contact dynamics calculations for a given time step using the developed contact models in the numerical modelling are performed in EDEM.

Modelling in EDEM

EDEM divides the analysis preparation and structures into several steps. The first step in EDEM for modelling granular structures and their physical interactions are available in the *Creator Tree-Bulk Material* section. This part provides a modelling opportunity for the granular geometry and its material properties. To model more precise geometry for the granules, importing previously modelled geometry options is also available. Elastic properties of all packing elements, contact theories to be applied to the structures and boundary conditions of the analysis are defined in this part of the simulation setup.

The next step is '*Simulator Settings*' in the software, where the total time of the analysis, time steps of the analysis, and definition of the simulator meshing properties can be set. In addition to these features, the number of simulator engines can be selected from the

available CPU capacity. It should be noted that an increased number of engines use more computer storage during the analysis process. Also, the collisions during the analysis can be tracked using the *'Track Collision'* feature. Specifically, a time step decision is essential in analysis preparation since a well-defined, precise time step has two benefits in the analysis outcomes. These benefits prevent the excessive overlaps that result in higher predicted force values and avoid effects of the disturbance from the Rayleigh wave propagation over the far elements in the granular packing [48].

A single granule is affected by its closest neighbours and other granules staying at distant locations in the pack. Since their disturbance impacts, these neighbouring granules may affect each other over the Rayleigh wave propagations. Therefore, choosing a small-enough time step helps keep the impact of the disturbances around the immediate neighbours rather than far away particles. EDEM automatically calculates the Rayleigh time step as shown in Equation (3.14), which can be finalised by clicking on the *'Auto Time Step'* box in the simulation setup. In general, using the same fraction of time step calculated in the software prevents the numerical instabilities and guarantees acceptable force-displacement calculations over the granules [150].

$$t_R = \frac{\pi R \left(\frac{\rho}{G}\right)^{\frac{1}{2}}}{0.1631\nu + 0.8766} \quad (\text{Eq. 3.14})$$

In this equation, all properties are from the granules: G is the shear modulus, R is the radius, ρ is the granules' material density, and ν is the Poisson's ratio. The time step can be adjusted for individual analysis properties; however, a typical time step is set between 0.001 s and 10^{-6} s in EDEM.

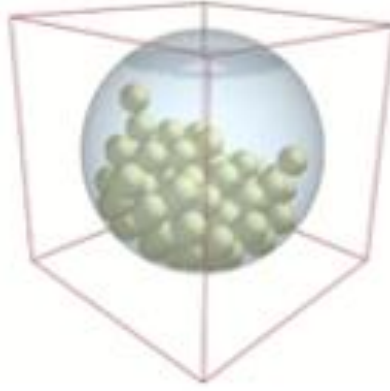


Figure 3. 14: The filled geometry for time precision analysis

In this study, a spherical cavity is partially filled with particles to analyse the time step accuracy impact on the granular structure-based system analysis (Figure 3.14). Granules in the cavity are set as steel particles ($E=2e+11$ Pa, $\nu=0.25$, $\rho=8027$ kg/m³) with a size of 1.58 mm in diameter. The spherical cavity properties are set to Acrylic Plastic properties ($E=1.45e+9$ Pa, $\nu=0.35$, $\rho=950$ kg/m³). Hertz-Mindlin (No Slip) contact mechanism has been defined as the particle-particle and particle-wall contacts. In the analysis, the only changing parameter is the time step which was changed to smaller and larger values than the automatically calculated Rayleigh time step.

Table 3. 5: Variety of granular size for particles placed in the spherical cavity

Rayleigh Time Step (%)	Time [s]	Coordination Number (Avg)
75	1.2273e-6	3.057
100	1.636e-6	3.071
125	2.0456e-6	3.079

According to Table 3.5, the coordination number value, which is related to the number of contacts between the granules, has been vaguely impacted by the time step precision. The change in the coordination number equals 0.71%, which is a reasonable level of contact between granules. Therefore, the contact number between the granules does not depend on the time precision; unless it was changed to a much smaller or higher time step for the analysis not to capture all related contact properties.

The total velocity distribution of the granules in the packing is shown in Figure 3.15. The analysis has been processed with the same setup properties for each analysis except time increment between the time steps. The time steps have been set at different incremental levels as given in Table 3.4. Since the same analysis environment was used, the velocity levels captured from each analysis were expected to be similar varied within 100% of the Rayleigh time step. However, the data captured from the analyses have slight changes in the first few cycles of the excitation according to Figure 3.15, given below.

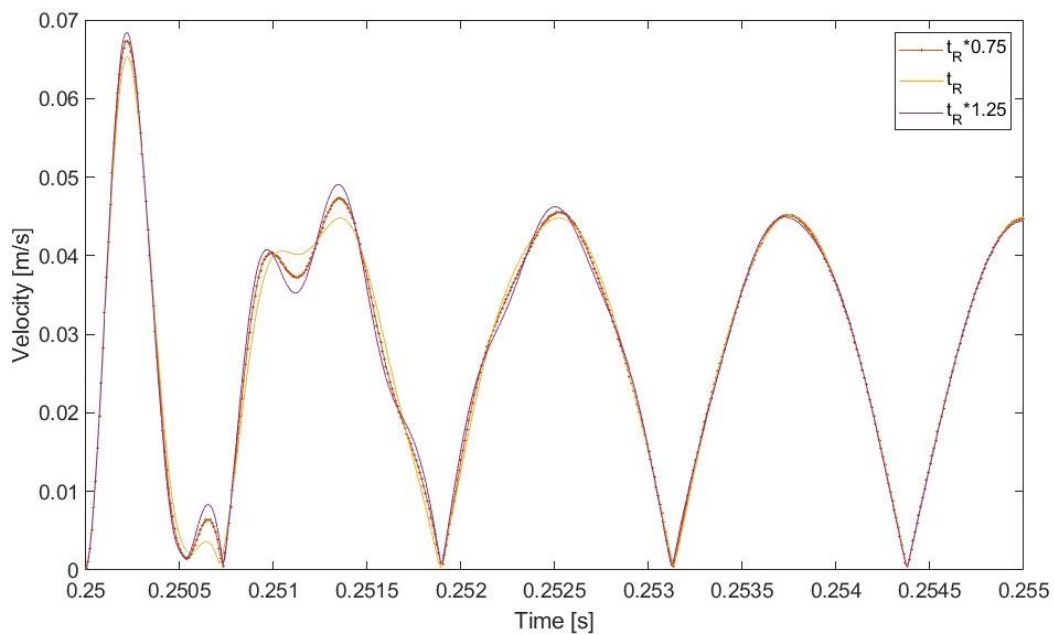


Figure 3. 15: The time precision analysis of velocity

The velocity and the dimensionless energy dependence over time on temporal resolution are illustrated in Figure 3.15 and Figure 3.16, respectively. In these figures, the time step is varied around Rayleigh time step within 25%. It can be seen that both velocity and energy oscillation over time have negligible changes because of the varied time step. Like the velocity data, energy distribution has inconsiderable changes because of the time step precision changes Dimensionless energy calculation has been given in the previous subchapter (subchapter 3.5).

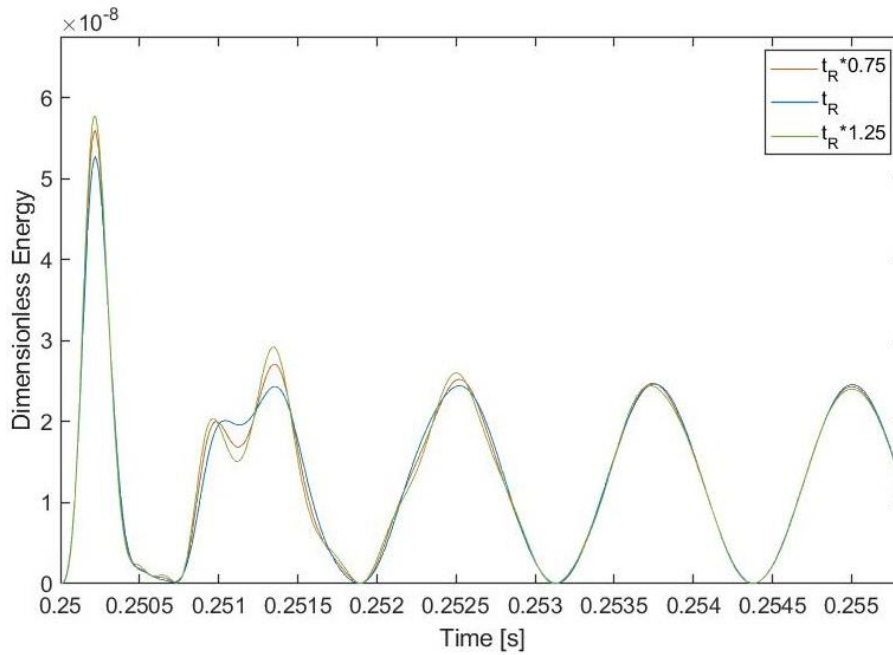



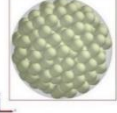
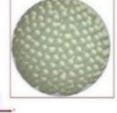
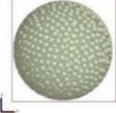

Figure 3.16: The time precision analysis of dimensionless energy

Overall, comparing all time steps, the Rayleigh time step precision showed that the automatically calculated value, t_R , is a sufficient and representative calculation in terms of the dynamic properties of the granules. Following the results, the time step in future research analysis is decided to be around its original value, which is the Rayleigh Time Step (t_R) in all types of analysis.

3.7- Impact of Granular Structure Size

Even though this matter has been widely studied in other literature sources, it has been aimed to investigate the dynamic properties of the several diameter sizes of the granules in packing. A spherical geometry was filled with four different sizes of granules in each case. Granules and the cavity material properties are set in the EDEM model setup as mentioned in Section 3.6 of this chapter. In addition, time step precision was kept equal for all analysis types at Rayleigh Time Step.

Table 3. 6: Variety of granular sized for particles placed in the spherical cavity

$R_1 = 3 \text{ mm}$	$R_2 = 1.5 \text{ mm}$	$R_3 = 1 \text{ mm}$	$R_4 = 0.75 \text{ mm}$	$R_5 = 0.5 \text{ mm}$
				
<i>Total Particle Number</i>	<i>Total Particle Number</i>	<i>Total Particle Number</i>	<i>Total Particle Number</i>	<i>Total Particle Number</i>
15	167	624	1500	5667
<i>Coordination Number (Avg)</i>	<i>Coordination Number (Avg)</i>	<i>Coordination Number (Avg)</i>	<i>Coordination Number (Avg)</i>	<i>Coordination Number (Avg)</i>
2.65	3.15	3.4	4.09	4.12

The spherical cavity is excited sinusoidally in the horizontal direction at frequency 400 Hz for 0.2 s. Since the aim is to keep all granules in the solid phase, excitation amplitude is set at a low level of 0.0002 mm for each analysis. According to the coordination number shown in Table 3.6, the average contact number for a single granule in the smallest sized granular packing is higher than the largest because of the higher filling fraction in R_5 -sized granular structure packing. Also, R_5 -sized granular structures increase the contact options with their neighbouring structures. As a result, the coordination number of the smallest sized granular packing R_5 changed by 55.5% compared to the largest sized granular packing R_1 .

Figure 3.17 illustrates the dimensionless energy and corresponding velocity change over time for different sizes of granules. Since the different sizes of granules needed different time to fill the cavity enclosure and rest in the geometry, the time of impact and the data collection start at different time for each analysis. R_1 -sized granules required the least duration to fill the cavity enclosure and in this case the cavity is impacted at 0.2 s, as seen from Figure 3.17. The largest granular structure packing R_5 showed a much lower velocity data trend as shown in Figure 3.17-b. As can be seen from Figure 3.17-a, the dimensionless energy depends on the granular size, meaning that the largest granules exhibit the lowest energy distribution over time. Since the granules have gravitational energy in the packing, their velocity and energy properties tend to zero over time [126].

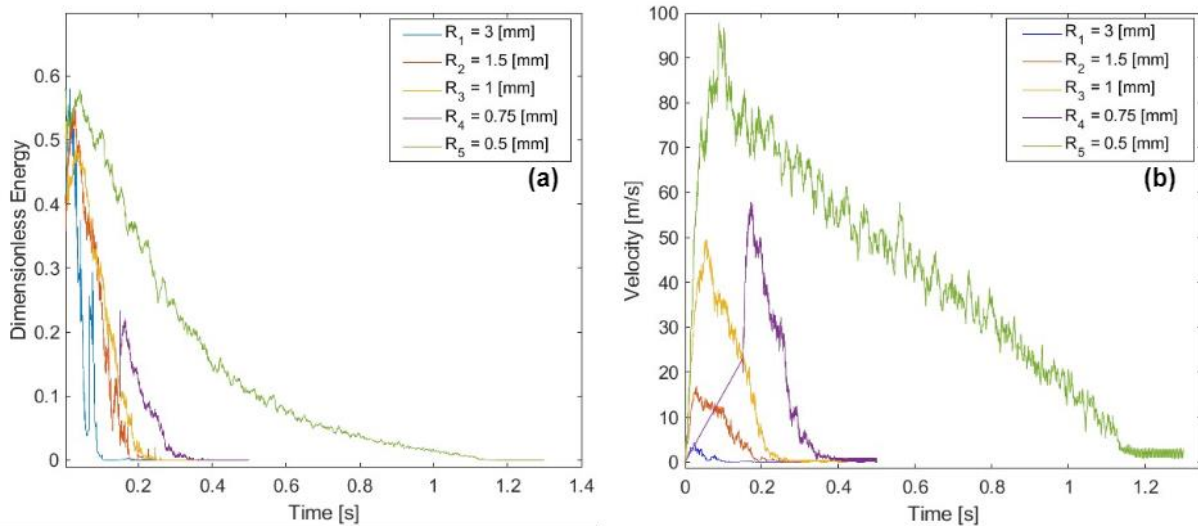


Figure 3.17: Various granular size filling details: (a) Dimensionless energy, (b) Velocity trends for a variety of granular size filling

The random arrangement of granular structures is thought to show various averaged coordination numbers. Therefore, investigation on the coordination number distribution has been conducted filling cavity multiple times in the numerical-based research. R_1 -sized granules have been selected for this study and filled in the same cavity for 25 times. All cases have been studied under sinusoidal excitation load at a specific frequency level and displacement amplitude which has been given in section of Evaluation of Contact Analysis. Model selection. Figure 3.18 shows the results of this analysis. Figure 3.18-a has been prepared using the data collected over the interval before the excitation impact hits the cavity. Figure 3.18-b has been prepared using the data from the excitation impact analysis, which contains the steady state part of the dynamic excitation. As expected, granules are randomly arranged in the cavity and their averaged coordination number varies in each filling attempt, as shown in Figure 3.18-b [126]. Therefore, in this study the average coordination number has been taken in the vicinity of its mean value of multiple filling attempts. Figure 3.18-a shows close to zero average coordination number dominating in 25 fillings which is caused by slow cavity filling process as a result of the minimal contact between the particles during this process. In case of random arrangement, the average coordination number might vary which would not be observed in the case of regular arrangement.

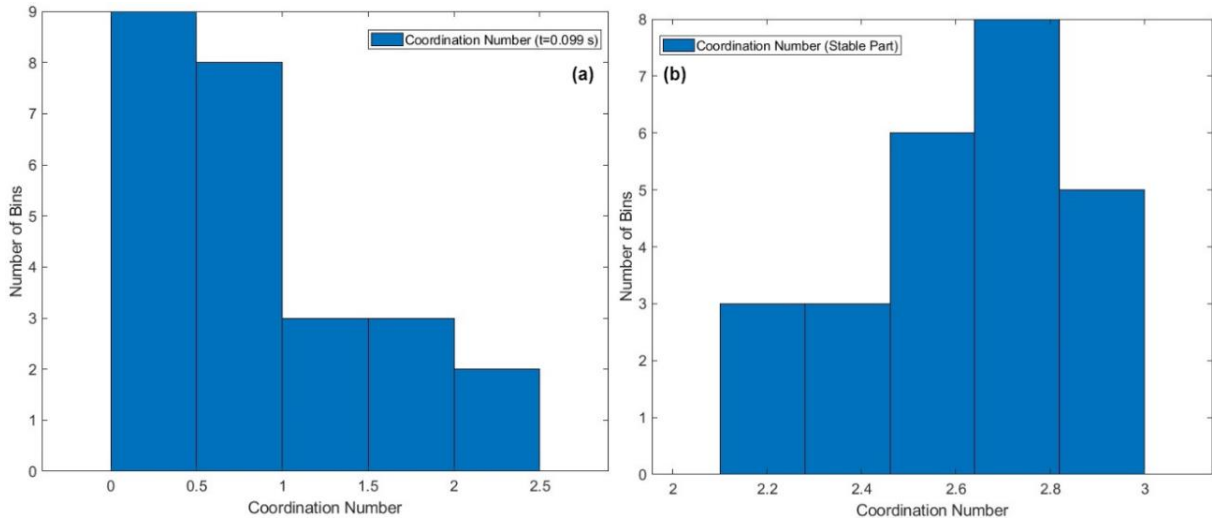


Figure 3. 18: Coordination number distribution for R_1 -sized granular packing: (a) before the excitation, (b) steady state part

Furthermore, granules in their dynamic steady state illustrate a Gaussian distribution in the coordination number changes over that 25-different calculation. Comparing the coordination number data given in Table 3.5, multiple attempts of filling showed similar contact properties distributed around mean value 7.60 with standard deviation 17.96. Interestingly, these data have shown wider range than the coordination number given by Nolan [126] at which proposed mean coordination number varied between 4.4 and 5.9. This might be related to the numerical simulation capturing more data than the analytical assumptions.

In addition to the coordination, number variety check analysis using R_1 -sized granules and R_3 -sized granules have been tried in the same analysis format to check the variation for smaller-sized granules. Even though the number of cases analysed using R_3 -sized granules, variation of coordination number is observed here, as well. Smaller sized granules illustrate more contact before the excitation implied to the geometry.

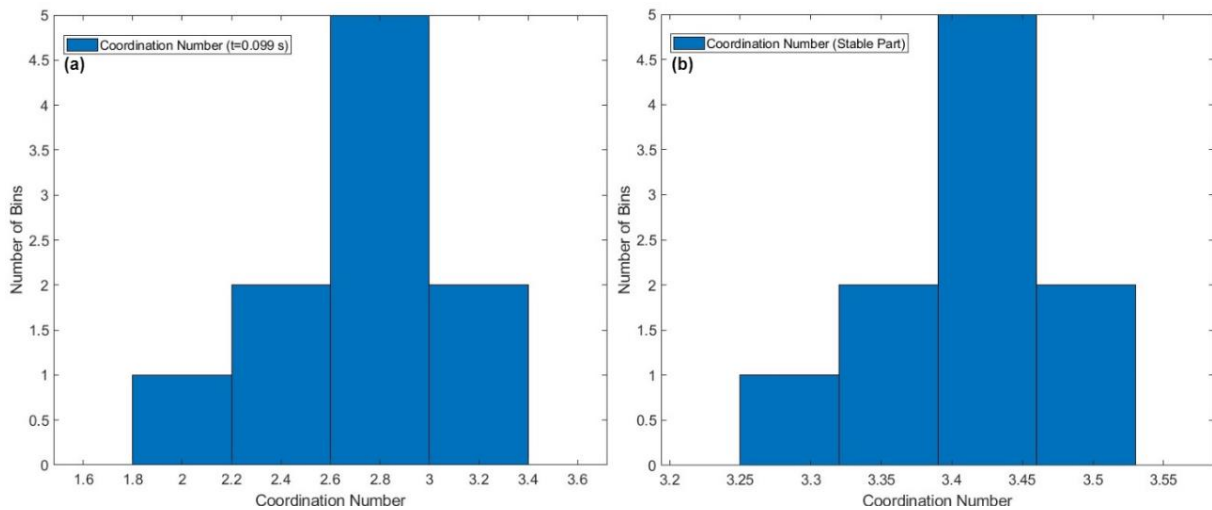


Figure 3.19: Coordination number distribution for R₃-sized granular packing

As a result of the chapter, different granular sizes show various behaviour in addition to their distributed energy properties. In addition, as there is a random arrangement in the granules to illustrate natural filling properties, granules might show various contact properties even though the filling and excitation properties are the same.

3.8- Impact of the Friction Coefficient in Granular Contact

Various levels of displacement amplitudes have been analysed through DEM-process to check the state of the granular structures. It has been aimed to keep the granules in the contact state. According to the evaluations made between the displacement amplitudes and behaviour of the granules, range of amplitude has been identified for the analysis in this chapter. Similar to the previous cases, a minimal amplitude has been applied at 400 Hz for all analyses to keep the granules in the solid phase for informative data capturing and more energy dissipative behaviours. The effect of the static friction coefficients were studied numerically in this subsection by giving polymeric material and various friction coefficient details. Representable analysis steps have been set to analyse the effect of friction coefficient on granular contact and general dynamic relations like the coordination number changes or the force-displacement relations of the granular impacts. The spherical cavity and granular structures were used in the Time Step Precision analysis by changing the static friction coefficient between the granules in each analysis, as shown in Table 3.7. The friction

coefficient which is noted as original in the table is the original friction coefficient of the material of the granular structures used in this analysis.

Table 3.7 introduced the average coordination number levels for each friction constant calculated with EDEM within the steady state regime. According to the coordination number change ratio, the granules' change between different friction levels is 29.09% between the highest and the lowest friction coefficients. Since the packing properties would differ over different granular interactions, average coordination numbers are changed due to this variation. The average coordination number has been getting smaller over the increased static friction coefficient. However, it has seen an equal number of contacts in the analysis of μ_{s3} and μ_{s4} because granules stuck together at high friction conditions for a given dynamic load.

Table 3. 7: Friction coefficient varieties over the case numbers

Static Friction Coefficient [μ_s]	Averaged Coordination Number
$\mu_{s1} = 0$	5.50
$\mu_{s(\text{original})} = 0.695$	4.09
$\mu_{s2} = 1$	4.08
$\mu_{s3} = 5$	3.90
$\mu_{s4} = 10$	3.90

Figure 3.20 (a) compares the analysed friction coefficient results regarding the particle velocity change over time. As evident in the figure, higher friction levels limit the particle activity (both rolling and sliding), and velocity ends at zero at an earlier time step. It was thought that the higher friction coefficient was a reason for the granules to stay stuck at their position. It is supported by the findings of spherical and non-spherical structure evaluation [151]. As the friction coefficient is a ratio of friction force to the normal force, a low friction coefficient is a reason for sliding motion. This motion would not occur at higher friction forces because of higher friction coefficients.

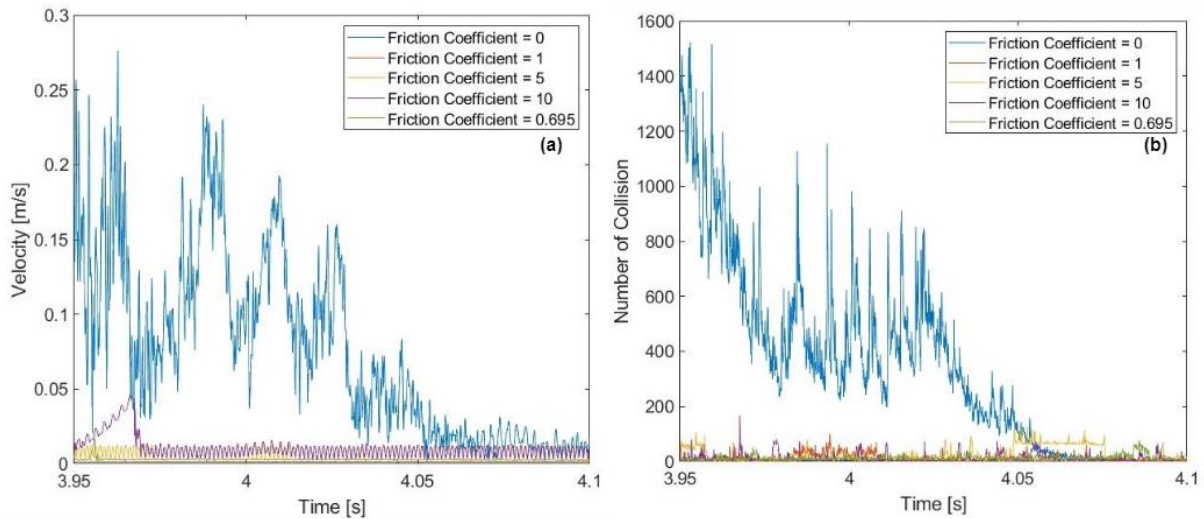


Figure 3. 20: Particle velocity (a) and number of granular collisions (b) at various friction coefficients

The relationship between the frequency of excitation and the friction coefficient is another property of the contact mechanism and packing of the granules that needs further investigation. However, this would be analysed over several frequency levels to calculate isotropic structure properties; therefore, will be found in the further Sections.

The friction coefficients for materials used in this research are overtaken from the previous studies [35], [110], [112], [148]. As a result of the analysis evaluated in this subsection, since the friction coefficient significantly impacts structural contacts and dynamic relations, the selected friction coefficient is decided to be 0.695 for metal particles as it was given in the literature source [112]. In addition to these information, it has been noted that the mechanical properties such as the rolling friction, the sliding friction and the coefficient of restitution within the contact of two granules have great importance in the modelling since they control and manipulate the nature of the collision and segregation [110].

3.9- Equivalent Solid Medium Characterisation of Granules in a Packing

Granular structure physical properties and their relationships with other structures in contact is based on the granular medium discrete nature requires and these properties tend to change over time between the collision events. Numerical calculations are expensive in computational efforts. An affordable and efficient method is required to replace discrete

structural modelling to understand the relations of the granular states in relation to their impact excitation.

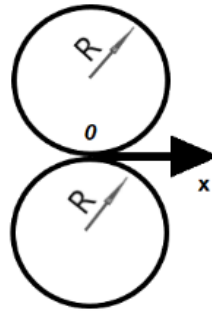


Figure 3. 21: Two spheres in contact, similar to Walton's case [56]

According to Walton's research idea [59], a granular packing in an enclosure cavity can be defined as a statistically isotropic effective medium using the dynamic properties of the granules in the packing [56]. In Walton's work, to characterise the isotropic medium, contacting bodies need to be analysed thoroughly. Therefore, two spherical granules were modelled (Figure 3.21) by the assumption of an initial stress-strain relationship between the granules at first. Then, their force-displacement status was investigated using analytical approaches. Changes in the pressure field through the incremental updates in strain (ϵ) because of the contact relations of the granules were identified using the contact area calculations. These were related to a simple stress equation in structural mechanics, which presumes that stress depends on force and the area where force is acting. The isotropic equivalent material bulk modulus and Lamé moduli were defined according to the stress-strain relationship between the granular packing elements (coordination number, packing fraction), the initial confining pressure knowledge and the initial material modulus.

Equivalent material bulk modulus were re-arranged using the relationship between classical Lamé Moduli and Bulk Modulus [56]. Then, the effective bulk modulus (K^*) of the equivalent material for packing rough particles can be calculated in Equation (3.15).

$$K^* = \lambda^* + \frac{2}{3}\mu^* = \frac{1}{6} \left(\frac{3E^2\Phi P^2 C_N^2 P}{\pi^2(1-\nu^{*2})^2} \right)^{1/3}, \quad (\text{Eq. 3.15})$$

where μ^* and λ^* are the equivalent Lamé Moduli, E is the Young's Modulus of the granules, Φ is the packing fraction, C_N is the average coordination number, P is the hydrostatic

pressure and ν is the Poisson's Ratio of the granules. It must be noted here that in this study equivalent parameter is dependent on variable coordination number which will be varied in accordance with the granular size, filling ratio and other geometrical and material properties of the studied problem.

The equivalent structure modelling approach was used in the study of Darabi et al. [60] by defining the granular packing of viscoelastic structures as an isotropic medium with fixed coordination number. In this study the granular pack were excited with low amplitudes [152] resulting in the granules staying in contact with negligibly low displacements and forming the solid phase. According to the knowledge of the granular structure's phases, the solid phase is where most granules stay in contact, and most energy dissipation is governed by the mechanics of the contacts in this phase [5], [6], [152]. Since the excitation impact is small in the cavity, the granules experience material-wise energy dissipation in the solid phase which also explained in the subsection of 'Phases in the Dynamics of the Granular Materials' of this chapter (Section 3.2). A further comparison-based study was conducted regarding the energy dissipation and assumption on damping properties using the experimental methods with granular structures [61]. In addition, they validated their understanding via numerical modelling using the isotropic structural modelling in FEM [37].

3.10- Derivations for the Granular Packing

Modelling individual granules as a solid structure, understanding the relation between granules, and working on a whole packing is a step-by-step approach in the analytical options. One can visit the source for the full step-by-step methodology of material prediction for the same sized granular structure packing [56].

The isotropic equivalent structure material properties are evaluated within the contact relations of the granules, which need to be tracked in a transient event. The process of calculations is initiated between the neighbouring granules in a packing and numerical simulation with the initial strain. It continues with the applied force, which results in displacement between the granules. This procedure is a reason for breaking one contact and making another one throughout the dynamic process.

The volume concentration for a granular packing is defined as a *filling fraction* (or filling ratio) which depends on the number of granules in the packing (N), the radius of the single granular structure (R) and the total volume of the cavity geometry (V) [19]. The equation below (Equation (3.16)) can be used for calculating the filling fraction of a granular packing (Φ_F) [56].

$$\Phi_F = \frac{4\pi R^3 N}{3V} \quad (\text{Eq. 3.16})$$

Another definition related to the filling fraction which is used in this study is *the packing fraction* (Φ_p) which is the occupied volume of the particles (V_p) in the partially filled cavity defined by Equation (3.17).

$$\Phi_p = \frac{4\pi R^3 N}{3V_p} \quad (\text{Eq. 3.17})$$

Literature sources have stated the filling fraction and the packing fraction as the same definitive information [19]; however, they should have been stated two different situations. Therefore, in this thesis, these definitions have been given opportunity to carry their own meanings. It should be noted that in this study, Equation (3.17) was applied for all calculations of the equivalent parameters. Equation (3.18) can be used for the calculation process of the density of the equivalent isotropic solid medium.

$$\rho^* = \rho\Phi_p \quad (\text{Eq. 3.18})$$

Considering granular packing in the static section (which is not excited yet), the total pressure on the granules in an enclosure cavity can be defined as its hydrostatic pressure, which is the simplified approach for stress definition. In this case, this terminology is the value of the initial confining pressure (P) which can be calculated analytically by using Equation (3.19). In this equation, ϵ is the initial strain field of the granular packing. Statistically homogeneous strain, that has a small value for linear elasticity theory to be valid, has been applied to the granules which are in contact. Using the linear elasticity relationship between the granules and applied strain, Walton [153] derived the initial stress.

$$P = \frac{4\phi_p C_N (-\epsilon)^{\frac{3}{2}}}{3\pi \left(\frac{1}{\mu} + \frac{1}{\mu + \lambda}\right)} \quad (\text{Eq. 3.19})$$

According to the equation for the initial pressure field in the packed granules, the average contact number between the granules has a direct impact on the pressure. As the knowledge given in this thesis, random or regular placement of the granular structures in the packing changes the average coordination number.

In comparison between the two cases, for the same level of filling fraction, the initial pressure value is expected to be larger in the regular arrangement of the granules in the packing. Therefore, another parameter for these calculations is the pressure mentioned as the granules' hydrostatic pressure. The first exemplary work for the pressure field using the relationship between the granular field and the enclosure structure was made by Janssen (1885), which noted that the confining pressure depends on the height of the filled cavity for a cylindrical geometry when the granules are induced by with the gravitational loading [153]. However, calculations are made in this research by keeping the confining pressure equal when the cavity was filled with a decided filling ratio. This decision provides simplicity and continuity in the dynamic and static levels of the calculation procedure. Keeping the confining pressure constant makes the coordination number the decisive parameter in the calculation procedure.

By recalling the relationship between Poisson's ratio and Lamé Moduli (Equation (3.20)), Poisson's ratio of the equivalent structure can be rearranged using Equation (3.21) below [56].

$$\nu = \frac{\lambda}{2(\lambda + \mu)} \quad (\text{Eq. 3.20})$$

$$\nu^* = \frac{\lambda^*}{2(\lambda^* + \mu^*)} = \frac{\nu}{2(5 - 3\nu)} \quad (\text{Eq. 3.21})$$

Similar to the derivation of Poisson's Ratio, the equivalent Young's Modulus of a granular packing can be evolved using the Lamé moduli and Young's modulus relationship. Equation (3.22) illustrates the general Young's Modulus calculation through the Lamé parameters. Then, using this equation in terms of the equivalent structure Lamé parameters, effective Young's Modulus for a given granular packing can be developed as in Equation (3.23) [37], [56].

$$E = \frac{\mu(3\lambda + 2\mu)}{\lambda + \mu} \quad (\text{Eq. 3.22})$$

$$E^* = \frac{\mu^*(3\lambda^*+2\mu^*)}{\mu^*+\lambda^*} = \frac{(1-2\nu^*)}{2} \left(\frac{3E_p^2 \phi_p^2 C_N^2 P}{\pi^2(1-\nu^{*2})} \right)^{\frac{1}{3}} \quad (\text{Eq. 3.23})$$

As noted before the coordination number is a parameter that depends on the dynamic state, the filling fraction and arrangement properties (random or regular) [127], [128]. To identify this parameter for the specific granular packing numerical simulations with the EDEM are used in this study.

Step-by-Step Calculation Procedure for the Equivalent Isotropic Solid Structure

These process details have been explained in the previous sections; however, the step-by-step calculation procedure has been given to explain and state this understanding of the isotropic structure modelling of the granules.

- Particle geometry and enclosure cavity volume are selected,
- Equation (3.17) is used to calculate the packing fraction,
- Equivalent density calculation using the packing fraction and the original mass density of the granular structures is calculated using Equation (3.18),
- The coordination number numerically identified using EDEM,
- The average confining pressure calculation is found using Equation (3.19) with the hydrostatic pressure assumption or numerical results.
- Equivalent structure Poisson's Ratio calculation using the original ratio value is found using Equation (3.21),
- Equivalent Young's Modulus calculation for the isotropic solid structure definition is identified using Equation (3.23).

This is the procedure for the isotropic equivalent structure definition of the granules in a pack. The shape of the granule affects the equivalent structure calculation outcomes since the spherical and multi-shaped granules are expected to have various coordination numbers. Also, the excitation amplitude and the excitation frequency change the level of contact between the granules; the coordination number would differ for various excitation conditions. Therefore, the equivalent Young's Modulus should be revisited in the calculation process of frequency sweep analysis. As a result, there needs to be a series of isotropic equivalent Young's Modulus depending on the frequency of excitation.

Viscoelastic and metallic granular structure dynamic contact relations are studied using numerical assessment. Isotropic equivalent solid structure properties are calculated using the data obtained from the Discrete Element Method (EDEM) by processing the granular interactions using the steps given above. Metal particles and viscoelastic particles are placed in an enclosing spherical cavity of 20 mm radius. Since the granules have a variety of dynamic behaviours over different frequency levels, these analyses have been run at different frequencies: 50 Hz, 150 Hz, 250 Hz, 350 Hz, 450 Hz, 550 Hz, 650 Hz, 750 Hz, 850 Hz, 950 Hz and 1050Hz. The isotropic equivalent structure properties are calculated for each filling fraction, and their relations are given below.

Metal Granules Equivalent Material Properties

Steel particles of 1.58 mm diameter have been selected to assess the dynamic properties of metallic structures. Various filling fractions Φ_F are studied, which are 0.1, 0.25, 0.35, 0.45, and 0.62 of the total volume of the enclosing cavity. The highest filling in the volume, 0.62, is the fully filled case. The amount of particles in the cavity is 26.3 g, 65.76 g, 92.06 g, 118.37 g, and 163.09 g respectively, as demonstrated in Figure 3.22. The amount of particles are calculated using Equation (3.24) by feeding the filling fraction, the granule's radius, and the cavity's volume where particles are placed.



Figure 3. 22: Steel filling amounts: (a) is 10%, (b) 25%, (c) 35%, (d) is 45% and (e) is 62% filling amounts

$$N = \frac{3V\Phi_F}{4\pi R^3} \quad (\text{Eq. 3.24})$$

Figure 3.23 shows variable equivalent material property over the frequency for 10% of the filling fraction of steel particles in the cavity, the data for the equivalent Young's Modulus have been calculated using the procedure explained in subsection Step-by-Step Calculation Procedure for the Equivalent Isotropic Solid Structure. According to Figure 3.23 (a), Young's Modulus reduces by 4.39% over the frequency range [50 Hz, 1050 Hz]. The coordination number changes with the excitation frequency level as shown in Figure 3.23-b. Since the granules change their state with the excitation frequency, the coordination number has been recorded at different levels.

Figure 3.23 (b) shows average coordination number levels at different frequency levels, and the change in the coordination number is 5.03% in the frequency change. Since the average coordination number reduces through the increasing excitation frequency, Young's Modulus also reduces at similar levels. According to the visual checks on each frequency analysis processed in EDEM, the granular structures in the cavity stay in contact as stated in the solid

phase. While the frequency level has been increased through different analysis, contact between the granules has been reduced because of the frequency impact. Therefore, coordination number is reduced through the increased frequency ranges. However, the excitation amplitude is small and do not impact the physical state of the particles.

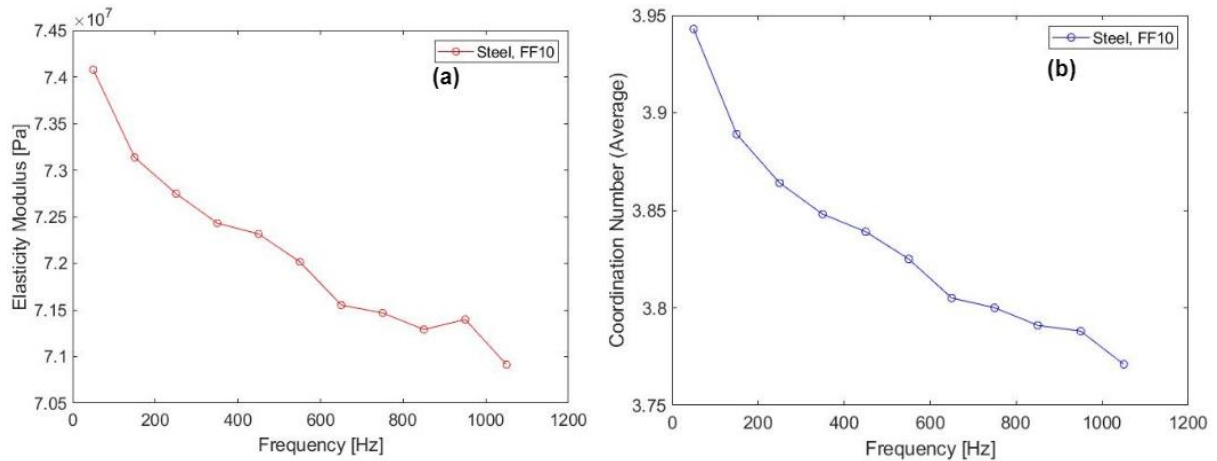


Figure 3. 23: Steel filling at filling fraction of 10% in the cavity: (a) equivalent isotropic structure Young's Modulus and (b) average coordination number

25% filling fraction is analysed in Figure 3.24-a. The new Φ_F changes the limits of coordination number since the number of granules in contact increases. However, this has been reduced while the excitation frequency increases (Figure 3.24-b) since contact is reduced between granules while increasing frequency level. The coordination number through the frequency level change by 2.78%, which is less than in the previous case since the granules are packed tighter in the cavity. Following this, the equivalent Young's Modulus is reduced over the increasing frequency by 2.19%.

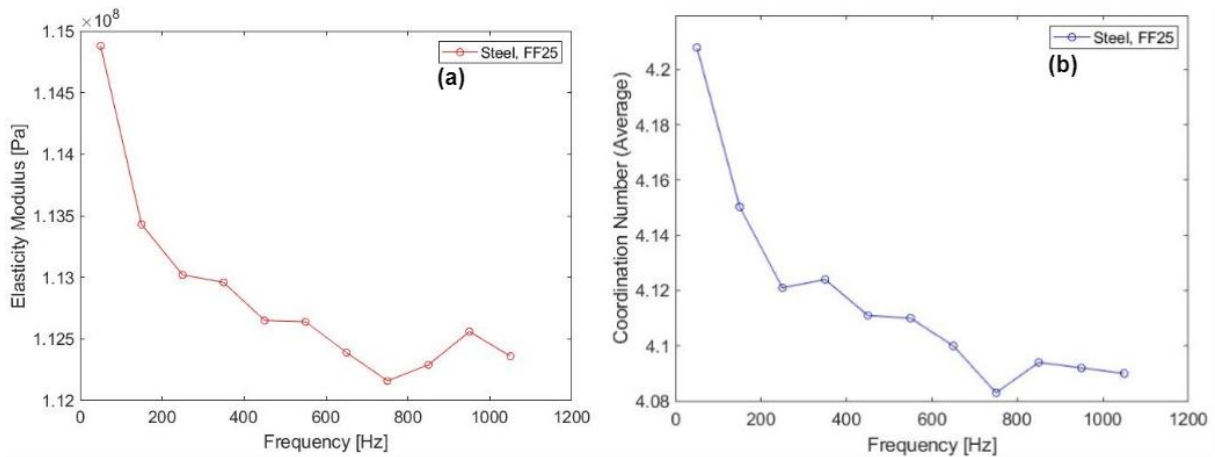


Figure 3. 24: Steel filling at filling fraction of 25% in the cavity: (a) equivalent isotropic structure Young's Modulus and (b) average coordination number

Figure 3.25 shows the average coordination number and equivalent Young's Modulus for a fully filled enclosing cavity with steel particles. Coordination number (Figure 3.25-b) and Elasticity Modulus (Figure 3.25-a) trends are similar through the frequency level increase. However, both of them are reduced while the excitation frequency increases. That is related to the relationship between the granular behaviour and excitation frequency level. The change in the equivalent material properties is 1.52%, while the change in the coordination number level is 2.28%.

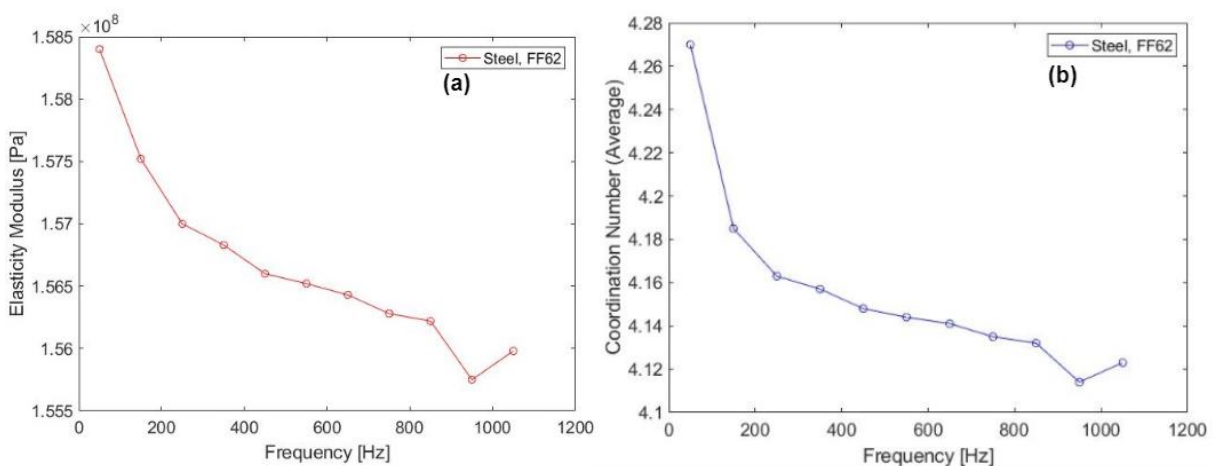


Figure 3. 25: Steel filling at filling fraction of 62% in the cavity: (a) equivalent isotropic structure Young's Modulus and average (b) coordination number

According to the analysis of metal particle arrangement in the cavity at various fillings, particles in the cavity control the contact between the neighbouring particles. This is obvious in the given results as the coordination number increases while the filling fraction increases because of the number of granule impacts. The relationship between the equivalent Young's Modulus and the coordination number at each filling fraction levels for steel particle fillings is given in Appendix 3.1 (Figure A3.1). Also, the equivalent Young's Modulus is increased with a constantly changed filling fraction. However, the change in these levels is not stable since the granules show their individual and unique behaviour, which is nonlinear as explained by various activation levels at different frequencies. However, in these results, granules stayed in contact in the solid phase due to the excitation of low amplitude.

Viscoelastic Granules Equivalent Material Properties

Viscoelastic granules have been analysed thoroughly to evaluate their dynamic relations. Therefore, acrylic plastic particles with a diameter of 3 mm and POM particles of 1.58 mm have been selected for these analyses setup. A variety of filling fractions are studied for acrylic plastic granules, which are 0.1, 0.25, 0.35, 0.45, and 0.475 of the total volume of the enclosing cavity. The highest packing in the volume, 0.475, is the total volume of the enclosing geometry fully filled with the particles. The total mass of acrylic plastic granules in the cavity is 3.98 g, 9.96 g, 14.05 g, 17.94 g, and 18.95 g respectively (see Figure 3.26 demonstrating weighting procedure). The number of particles is calculated using Equation (3.24), given in the previous section.



Figure 3. 26: Acrylic plastic filling amounts: Figure (a) is 10%, Figure (b) 25%, Figure (c) 35%, Figure (d) is 45% and Figure (e) is 47.5% filling amounts

Figure 3.27 shows acrylic plastic filling at a 10% impact on equivalent Young's Modulus and coordination number. According to the figure, increasing excitation frequency reduces the properties since it impacts the arrangement of granules in the packing. Young's Modulus is reduced by 5.10%, while the coordination number is reduced by 3.32% through the increased frequency level. These amounts are smaller compared to the metal particle case at the same filling fraction. Compared to the same amount of metal particle filling fraction, the total mass of viscoelastic particles is smaller. Regardless of the total mass in the packing, the particles showed similar contact behaviour observed through the similar average coordination numbers as shown in Figures 3.23-a and -b.

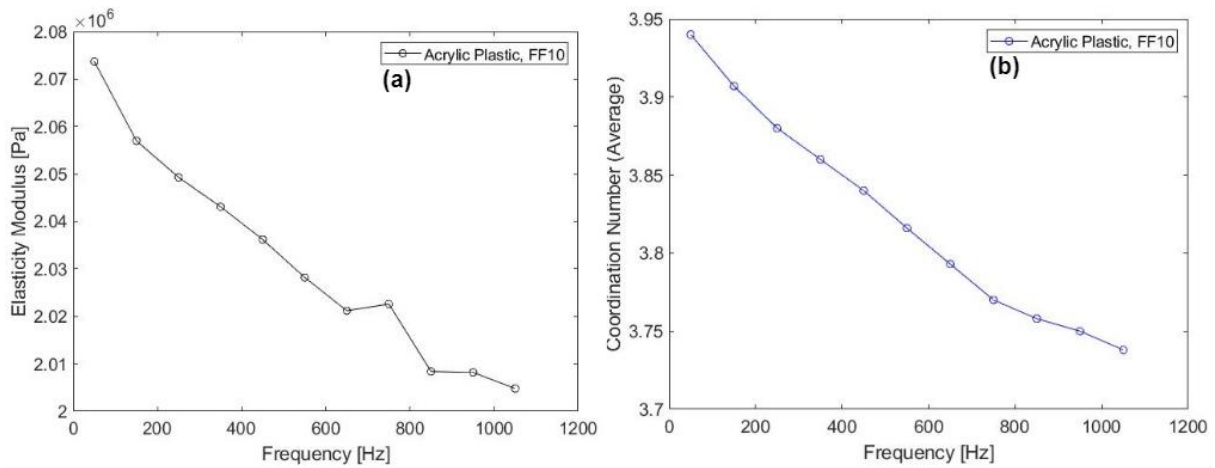


Figure 3.27: Acrylic plastic filling at filling fraction of 10% in the cavity: (a) equivalent isotropic structure Young's Modulus and (b) average coordination number

The granules showed a different behaviour in the case of 25% acrylic plastic filling in the cavity (Figure 3.28). The change rate in Young's Modulus is 12.7%. In comparison, the coordination number change rate is 13.5%, which might be about the coefficient of restitution changes in plastic granules in addition to increasing the number of particles which tends to increase the contact levels with the neighbouring particles.

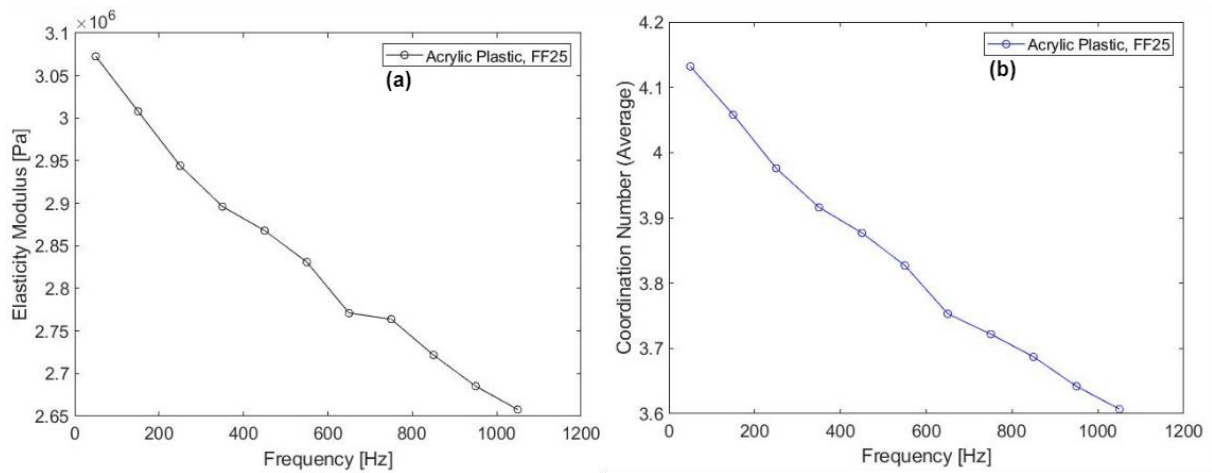


Figure 3.28: Acrylic plastic filling at filling fraction of 25% in the cavity: (a) equivalent isotropic structure Young's Modulus and (b) average coordination number

Similar to the metal particle case, increasing the filling level to the fully filled state of the cavity impacts the number of contacts for a single particle, which results in higher

coordination numbers (Figure 3.29-b). As a result of these higher contact numbers, equivalent Young's Modulus reached higher values (Figure 3.29-a). However, increased excitation frequency resulted in more minor levels for the coordination number and the equivalent Young's Modulus. The changes in these properties are calculated as 3.53% in Young's Modulus and 5.25% in the coordination number.

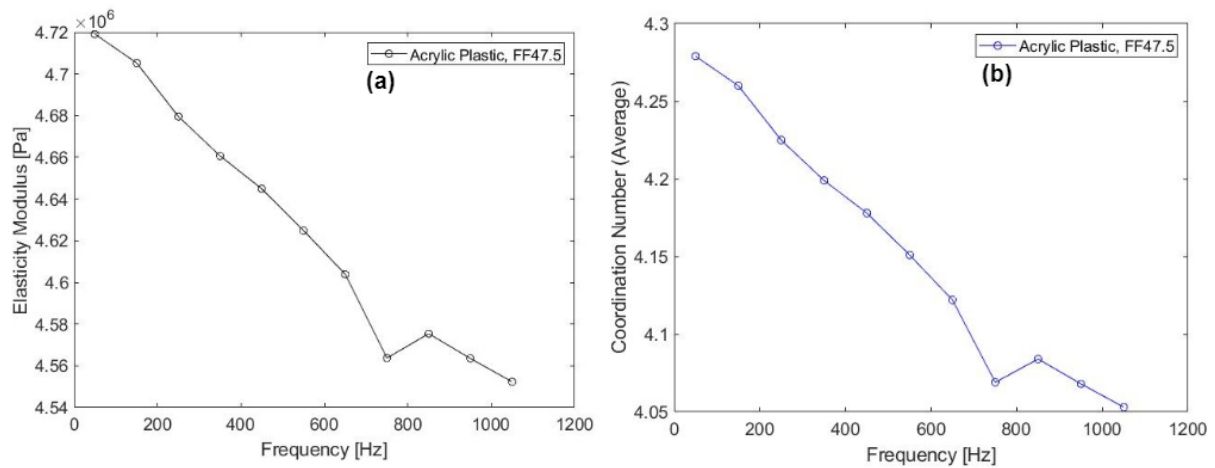


Figure 3. 29: Acrylic plastic filling at filling fraction of 47.5% in the cavity: (a) equivalent isotropic structure Young's Modulus and (b) average coordination number



Figure 3. 30: 7.5% POM particles filling amount

Figure 3.30 shows the amount of POM particles to fill 7.5 % of the enclosing cavity. Figure 3.31 shows the changing trend for the equivalent Young's Modulus and the average coordination number at various excitation frequencies. Even though increasing excitation frequency reduced the equivalent Young's Modulus (Figure 3.31 a) in general, it was not accurate in POM particle filling at low-frequency range. The reverse of the general expectation happened in this case. The change in the properties was 0.576% in the equivalent Young's Modulus and 1.57% in the coordination number (Figure 3.31 b), which informs that POM particles are more stable than the acrylic plastic ones since their change rate is much lower. Also, it might be related to the amount of the granules in the cavity, which is much lower than the other cases studied in this subchapter, so the granules do not have proper contacting opportunity.

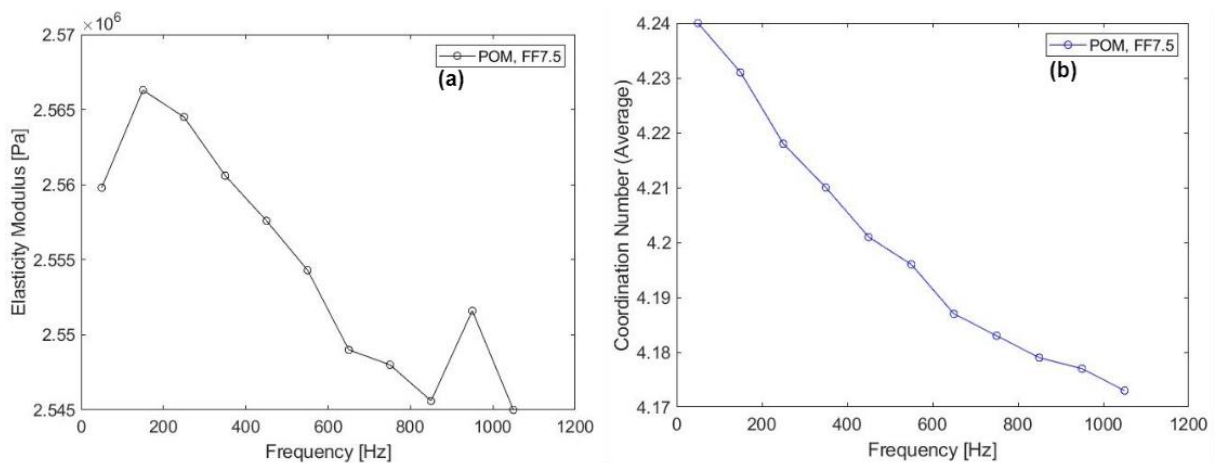


Figure 3. 31: POM filling at filling fraction of 7.5% in the cavity: equivalent isotropic structure Young's Modulus (a) and average coordination number (b)

Similar to the metal particles case, particles in the cavity control the contact between the neighbouring particles. This is obvious in the given results as the coordination number increases while the filling fraction increases because of the cavity's mass and the number of granule impacts. The relationship between the equivalent Young's Modulus and the coordination number at each filling fraction levels for viscoelastic particle fillings is given in Appendix 3.2 (Figure A3.2). Also, the equivalent Young's Modulus is increased with filling fraction. Even though acrylic plastic and POM particles have very similar material properties, they showed different properties (10% acrylic plastic filling and 7.5% POM filling were

compared). Usually, the comparison should be made between the same amount of the same sized granules; however, accounting for viscoelastic granules, these two materials can be compared regardless of their size and amount since similar behaviours have been observed according to the given figures. As the previous section explains, a higher coordination number would also be about the granule's size (Table 3.5). As a result, 7.5% of POM particles showed more contact than 25% filling of acrylic plastic. Since the original Young's Modulus of POM particles is less than acrylic plastic, the equivalent Young's Modulus was also smaller.

Metal and viscoelastic granular structure filling have been exemplified in this subchapter according to their filling fractions and corresponding equivalent material properties. As seen from the figures in this subchapter, the equivalent Young's Modulus trend has reached peak at around 600-800 Hz. The reason behind this phenomenon might be related to the filling fraction, material properties of the granules in the cavity and the associated eigenfrequency. The dynamic relations (contact relationship) between the granules and the cavity walls might also result in peak for each case. The resolution in time used in EDEM might also be cause of the small variations in the coordination number resulting in peaks observed in the figures.

Iteration-based Analysis of Isotropic Equivalent Structure Calculation

Since the granules tend to change their contact properties at each analysis setup in the random arrangement, it was decided to check the equivalent material property change in a series of iterative studies and observe convergence in material properties. In order to complete this study, a cylindrical tube was filled at 20% of its volume, and a spherical geometry was filled at 78% of its volume. Granules in these two structures are at identical amounts and have the same structures made of PMMA. However, changing the shape of the cavity changes the filling level in general. The excitation has been applied at the cavity's natural frequencies; 655.89 Hz for the cylindrical tube and 159.54 Hz for the spherical container. In order to validate and check the convergence of the equivalent medium properties, the natural frequencies of the whole structure (cavity and granular structure filling) have been used. The dissipation has been studied at two different levels for the tubular structure, $1e-5$ m, and $2e-5$ m, to question the impact of excitation amplitude on the change of equivalent material properties.

The first iteration has been set at the eigenfrequency of the enclosing cavity. Coordination number and pressure level have been recorded from this iteration, and isotropic equivalent structure material properties have been calculated. Then, whole structure's natural frequency is analysed in FEM-based computation. Each iteration step consists of the previous case's eigenfrequency of the whole structure (the granules and the cavity) at the same amplitude level. The isotropic equivalent structure material properties have been calculated with the data recorded from each iteration step. The density of the filled structure has not been included in the convergence analysis. According to Equation 3.18, the equivalent density for the granular material depends on the filling fraction and the granules' individual material density only. Therefore, it does not change with the coordination number and stay constant in the convergence analysis. Following this, equivalent material properties have been calculated, and these properties have been used in the Finite Element Analysis for the eigenfrequency search. After a considerable amount of iterations for example 5-10 iterations, the material properties and the natural frequencies have shown some level of convergence through the DEM-FEM iteration-based structural analysis.

Figure 3.32 shows the equivalent Young's Modulus levels at different iteration numbers for each excitation amplitude. According to the figures (Figure 3.32-a and -b), the equivalent Young's Modulus is bigger at the 1st iteration step for the lower amplitude excitation. With the increase in the number of iterations the value of the Young's Modulus become similar, and the higher amplitude of excitation showed slight increase. For instance, the ratio of the last iteration step for the amplitude level-1 to amplitude level-2 is equal to 0.995. Young's Modulus change ratio has been calculated using the data from iteration step two and the last iteration step. According to the calculation, the change ratios are 0.34% for amplitude level-1 and 6.6% for amplitude level-2 in the equivalent Young's Modulus properties. Comparing change ratios for both cases, higher excitation amplitude impacted the granular structure mechanism more. Even though there is a relatively small change, both cases showed immediate convergence in the results.

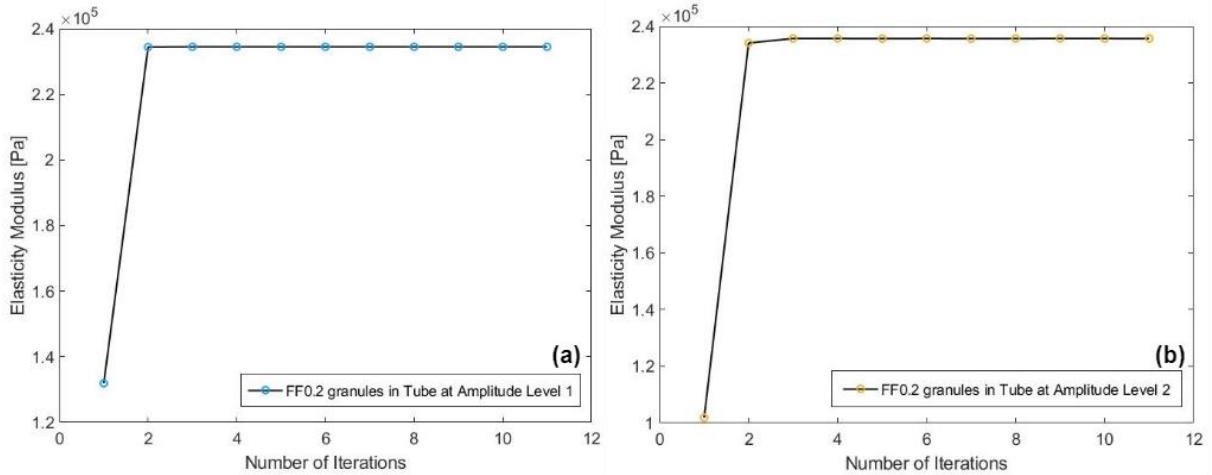


Figure 3. 32: Equivalent Young's Modulus change trend for amplitude level-1 (a) and amplitude level-2 (b) for tubular structure

According to the study on spherical structure filling, similar to the previous ones, the first step with equivalent Young's Modulus was smaller than other iterations (Figure 3.32). The convergence is slower compared to the previous cases. The change ratio between the second iteration and the last iteration steps for the equivalent Young's Modulus was equal to -3.5%.

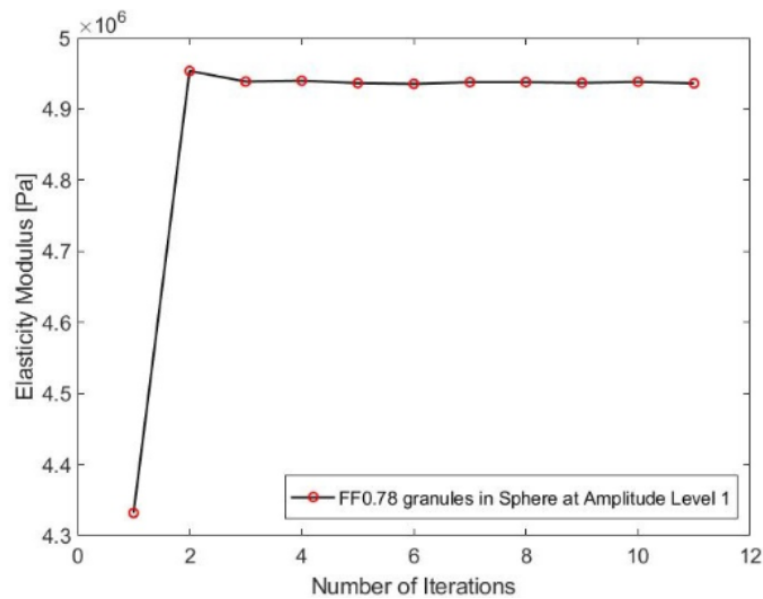


Figure 3. 33: Equivalent Young's Modulus change trend at amplitude level-1 for spherical structure

Since there are several structures and a couple of excitation amplitudes, the coordination number for each case should be considered for comparison. Figure 3.34 shows the coordination number levels for each case at different iteration steps. According to the results

shown in the figure, amplitude level-2 for the tubular structure showed higher numbers which means the contact between the structures was more in this case when compared to amplitude level-1 for the tubular structure. However, both cases had less contact than the spherical structure filling. This means that the enclosing cavity has an essential role in defining the contact numbers and, as a result, the equivalent Young's Modulus levels.

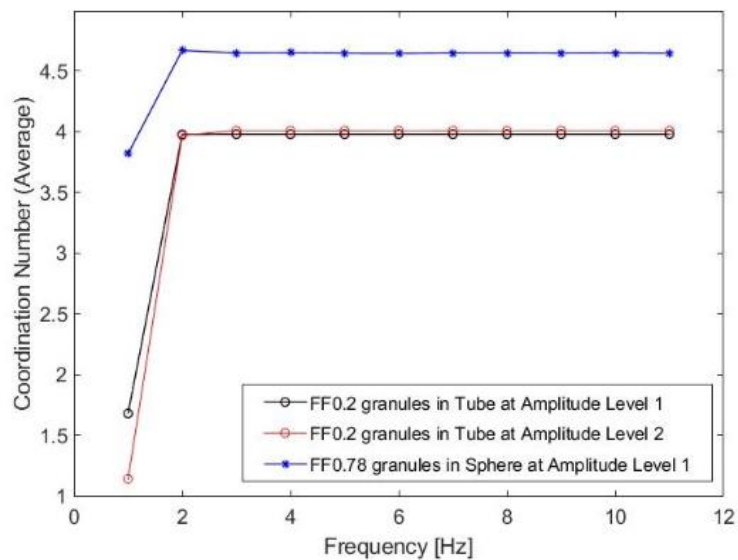


Figure 3. 34: Coordination number change trend for all cases

3.11- Conclusion of the Chapter

In this chapter, the physical and dynamic nature of granular structures, their contact interactions and various phenomenal information regarding the collisional processes have been introduced. Also, some of the specific terms have been studied accordingly using the DEM-based numerical studying software EDEM V2021.1. Discrete nature of granules and studying opportunity have been stated to be computationally expensive which directs the research community to work on various modelling strategies. DEM-FEM couples analysis opportunities have been one of them. The equivalent isotropic solid structure modelling methodology, therefore, have been introduced in this chapter. Metallic and viscoelastic materials have been studied in EDEM and the data obtained from the numerical analysis have been used in the equivalent material calculation procedure. The change of the equivalent material properties over various frequency levels have been stated towards the end of the chapter. At the end, two different cavities have been researched in terms of the

equivalent solid structure material modelling convergence. The last study has been thought to be a kind of validation opportunity of the equivalent isotropic solid medium characterisation given in this chapter.

Chapter 4: Specification of the Resonator

Natural frequency is a property of all structures caused by external vibration at the same or close frequency levels. The structure, under oscillating force at the natural frequency, experiences higher amplitude than other frequency levels at the same amount of oscillating force. Natural frequency or resonance phenomena depend on the structural geometry and the structure's material properties. As a result, the reason structures resonate is the relationship between inertia properties and the structures' elasticity.

Structural dynamic properties are defined by the natural frequency, the mode shapes at that natural frequency, and damping as energy dissipative assets [154]. Resonance significantly impacts the structural behaviour; for instance, a structure is oscillated by an external force at a level close to the structure's natural frequency. Under these conditions, resonance tends to manipulate the structural behaviour and develops mode shape at the resonant frequency. On the other hand, when the oscillating force is applied to the same structure at the frequency away from the resonance, the structure tends to be disturbed with a lower displacement amplitude.

Mainly, structures are aimed to be controlled to avoid experiencing high amplitudes. As a result of the knowledge of resonance, understanding the properties of the structures through various approaches has been a crucial step. Once the structural properties have been analysed, vibration treatment can be developed accordingly. In addition, the resonating structures can be used to control the structural vibration impacts on the main structure. Since it has been aimed to control structural vibration using resonator in this research, a design of a single resonator is proposed in this chapter. Intended geometry of the resonator is introduced, and the production methodology is studied appropriately. Design steps of the resonating structure and parameter-based numerical study based on these steps are introduced in this chapter with specific resonator selection and its eigenfrequency solutions.

4.1- Broadband Absorption Using Resonators

Vibration absorption is an achievable property in mechanical systems using various techniques. In several applications like electromagnetism, where the wavelength is relatively

small, absorption is available through periodic arrangements and Bragg scattering mechanism resulting in the so-called band gap phenomenon(see Chapter 2). For the longer wavelength, the Bragg scattering is not beneficial. On the other hand, controlling or manipulating the mechanical energy in the form of vibration is achievable with the arrangement of so called local resonators leading to sub-band gap phenomenon [82].

Attaching another resonator to the system maintains a resonance frequency alteration and controls the behaviour of the primary structure [97]. Local resonator application on the primary resonating system shifts the eigenfrequency of the primary structure to another level, mostly close to the eigenfrequency of the locally resonating structure. As a result, mechanical energy is dissipated from the primary structure by the attachment. Unlike the Bragg Scattering case, locally resonating structure applications do not require a specific number of resonators or arrangements on the primary structure. An additional resonating structure might divide the frequency response or add another frequency peak which is the eigenfrequency of the attachment to the system response. This frequency response is observed in the undamped dynamic vibration absorber [155].

In the damped vibration absorber case, the amplitudes received from the system are reduced because of the damping induction. The damping might impact the primary structure response while having effect on the coupled response between the primary structure and the local resonator attached to the system in this example. According to the knowledge of the vibration absorbers, using a vibration absorber might be a reason for a zero amplitude at the primary structure's resonant frequency [156].

Considering a system with a primary structure with a considerable mass and attached locally resonant structures on that primary structure; the mass impact on the primary structure because of the resonators would be expected to be low. When the locally resonant structures have equal or close eigenfrequency properties, the frequency response would be similar to the single absorber case since the attachments behave like a single structure. When the eigenfrequency of the absorbers is at various levels, the frequency response of the primary mass is expected to vary, and a typical damping application is called *broadband vibration damping*. For instance, mechanical properties in [4] have been tuned to be homogenised

within the individual absorbers level. Pai, P.F. [4] studied the beam as a primary mass and distributed small spring-mass systems longitudinally (see Figure 4.1).

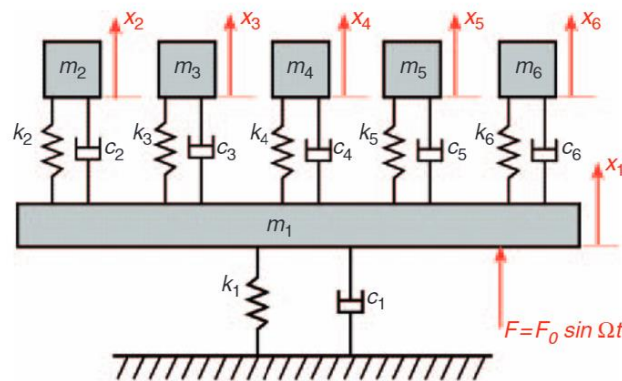


Figure 4. 1: Metamaterial formation using a mass-spring attachment on a beam [4]

The study [4] has been an example of elastic wave absorbers where the inertia forces of the resonators work contrary to the external amplification. This interaction changes the wave speed and avoids wave propagation through the structure. They showed the vibration absorption over a broad range of frequencies using resonators. They also showed the additional damping element on these locally resonant structures. In the first example, the spring-mass system shifted the resonating properties without much reduction in the amplitude levels (Figure 4.2-a). A damping property on each resonator resulted in reduced frequency response amplitude while showing a similar shift in the frequency levels (Figure 4.2-b). In addition, varying the eigenfrequencies of the resonators opened up broadband frequency absorbing opportunities (Figure 4.2-c) [157].

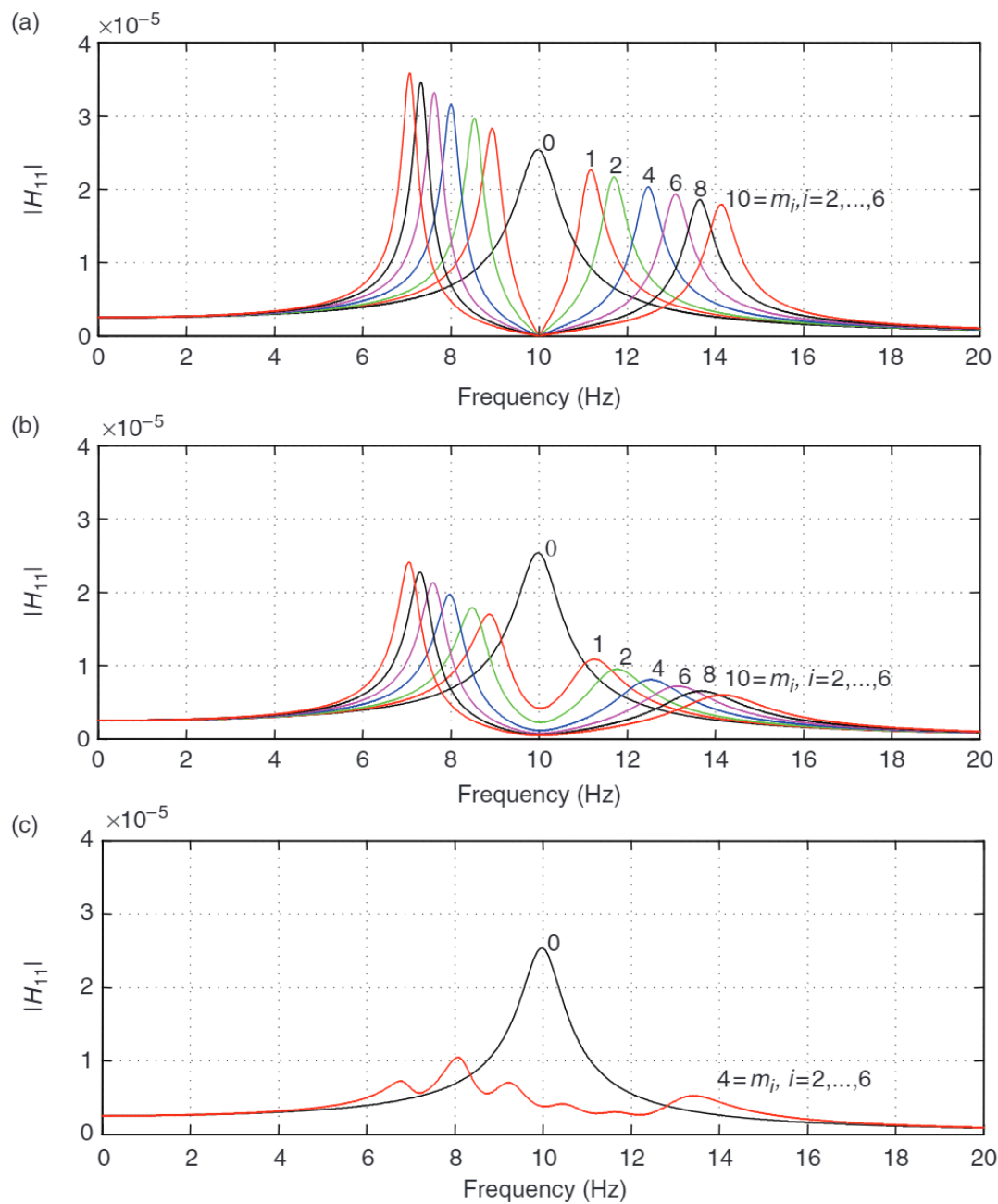


Figure 4. 2: FRF of various situations: (a) increased DOF using equal absorbers, (b) additional damping on resonators, (c) varied eigenfrequency impact on FRF [157]

Locally resonant structures in a periodic arrangement have shown increased the number of freedoms of the whole system [158]. This assumption has been made by Nouh et. al. by assuming multiple secondary systems are attached to the SDOF system, which is an augmented SDOF system. This application promotes the reduction of the high amplitude vibration impacts where the eigenfrequency is lower or at the same level as the vibration-

induced system. Therefore, the periodically arranged locally resonant structures behave like multiple dynamic absorbers [158].

Like the elastic structure and wave modulation examples, periodically arranged sonic crystals have been used for sound scattering. Sound scatterers have been modelled as acoustic metamaterials and worked in the low-frequency area with long wavelengths. Therefore, similar to the previously explained working principle, these structures worked as locally resonant structures which showed effective material properties [159].

Additionally, coupling between the Bragg Scattering and the local resonance has widened the sub-band gap properties [85]. This application has been called the *resonant Bragg* [85]. It has been noted that this application would be a novel noise reduction and vibration suppression option [85].

According to the information given in this part of the chapter, vibration absorption and modifying the main structure dynamic properties are possible using locally resonant structure attachments. Therefore, in this study, the aim is to control the main structure response, a beam, in this case, using a locally resonating structure. The designing methodology of the resonators is given in the following subchapters.

4.2- Numerical Simulation with COMSOL Multiphysics

COMSOL is a commercially developed Finite Element Method (FEM)-based studying interface to scientifically model, analyse, develop, and optimise multi-physics problems. There are add-on modules for users to produce modelling depending on the physical properties of the structures and their environments. These modules in COMSOL Multiphysics provide geometry, material selections, coupled physics applications and various post-processing options. The modules and their processes can be applied to wide range of engineering fields and physical phenomena.

Structural Mechanics in COMSOL Multiphysics (V5.0) has been used for all analysis in this study, providing eigenfrequency, time-dependent, and frequency-dependent analysis. Specifically, an analysis is prepared using either an Eigenfrequency or a Frequency-dependent solution. Frequency-dependent analysis has been prepared using the parametric

sweep of the frequency from 50 Hz to 1200 Hz with 5 Hz steps. The meshing of the structures has been prepared using dimensions of the smallest parts of the solid structure in the modelling since the solid structures used in this research have relatively small inclusions. A coarse meshing and too fine meshing would not give an approachable result; therefore, the mesh of the whole structure has been designed around the smallest details. The main structure with the resonator attachment is given in Appendix 4.1 with meshing and material properties details using Figure A4.1 and Tables A4.1 and A4.2. In this study, five elements per wavelength have been used to mesh the geometry and at the boundaries and the areas where force has been applied the finer mesh has been used. In order to apply the load, the centre of the main structure has been selected as the point of excitation which has sinusoidal impact. The ends of the main structure (beam) has been clamped to restrict movements in direction of the z-axis.

4.3- Numerical Model of the Host Structure

Modelling a locally resonant structure to treat the vibration impact requires primary structure modelling. A clamped-end conditioned beam is used as the main structure with the given geometry in Figure 4.3. The holes arranged in line on both sides of the beam through the length are prepared to attach the resonators to examine their coupling and damping properties. In order to fasten the structure on the test rig, there are 12 mm-sized circular holes through the beam. The total length is 475 mm, the width is 75 mm, and the thickness of the beam is 5 mm which made of using structural steel. This geometry is modelled in COMSOL and produced using machining tools for the experimental studies (see Chapter 6).

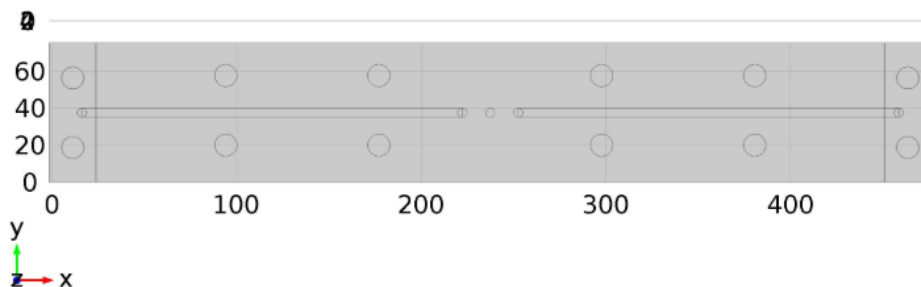


Figure 4. 3: Beam model in [mm] dimensions using COMSOL Multiphysics

Structural loss factor, a type of damping property provided with the material itself, is not considered in the numerical analysis since it is relatively small for the structural steel. The beam's mode shapes are studied using an eigenfrequency solver in COMSOL Multiphysics, while the frequency response analysis is studied through a frequency-dependent solver. The modes of the beam in an order are at 141.27 Hz, 388.39 Hz, 423.19 Hz, 524.85 Hz, 763.11 Hz, 820.69 Hz and 1154.8 Hz. In comparison between the mode shapes, the fourth and the sixth modes are the mixed modes (bending and torsion); whereas the first, the third and the fifth modes are the pure bending modes (Figure 4.4). The bending modes are the specific interest of this research since the resonators are modelled to be displaced in the z-direction. Figure 4.4 shows the mode shapes at these eigenfrequencies specifically demonstrating the presence of nodes and antinodes.

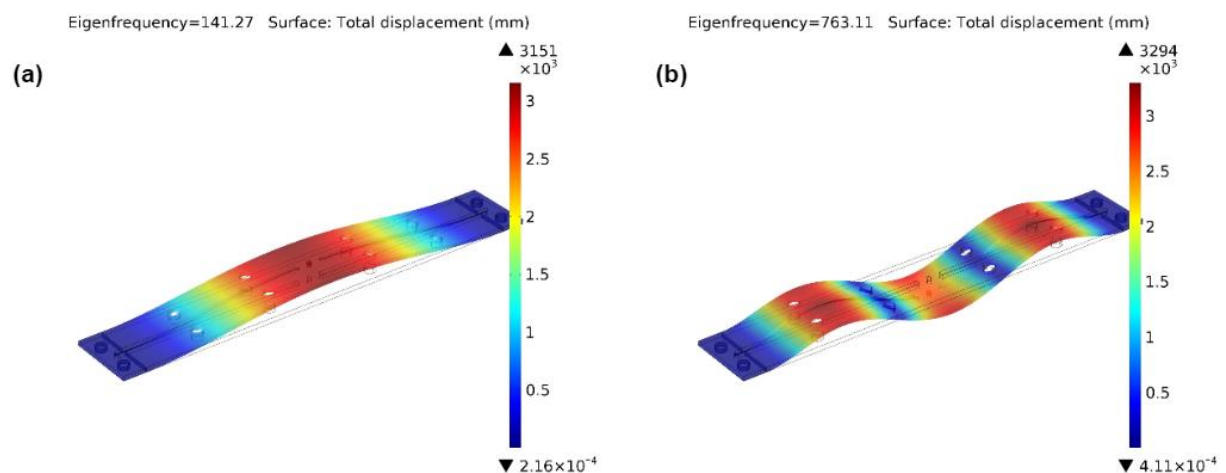


Figure 4. 4: Bending modes of the beam; (a) the first mode, (b) the fifth mode

On the other hand, using the material properties of the beam, which is structural steel, the eigenfrequencies of the bare beam can be calculated with Equation (4.1) [160]. This equation includes coefficient β , which is defined with the boundary conditions of the beam. The series of coefficients for each mode are set to $\beta_1L=4.73$, $\beta_2L=7.85$ and $\beta_3L=10.99$ [160]. I in the equation is the second moment of area of the rectangular structure; in this case, the beam is considered a rectangular structure. According to the equation, the first mode is at 146.8 Hz; the second mode is at 404.24 Hz; the third mode is at 792.317 Hz.

$$\omega = (\beta L)^2 \sqrt{EI/\rho AL^4} \quad (\text{Eq. 4.1})$$

Comparing the lower eigenfrequency levels and corresponding mode shapes with higher order eigenfrequencies and their corresponding mode shapes, the beam has shown complex behaviour in higher orders since the geometry of the beam has complex details. In order to avoid the complex behaviour of the beam, it has been decided to work through the lower orders of eigenfrequencies. Therefore, it has been aimed to control the beam through its first three bending modes.

4.4- DMTA Testing of 3D-Printed Samples of the Resonator Material

Dynamic Mechanical Thermal Analysis (DMTA) is used to assess the mechanical properties of polymeric materials. 3D printing requires layer by layer material printing to comprise a structure that creates porosity in the printed structure. As a result of porosity in the structure, less material is composed in the equal volume for the same solid structure made of the same material. In order to gain the valuable data to characterise the properties of polymer-based structures, DMTA testing has been processed using Metravib viscoanalyser (Metravib Xpander VA 2000) at various frequency and displacement levels. DMTA testing machine provides reliable and reproduceable information from the specimen by cost effective and less footprint properties.

During the DMTA test, the material is subjected to a sinusoidal strain or stress. The test machine records the response to changing temperature and frequency [161]. The data is evaluated to acquire the material properties obtained with the 3D printing, which helps to predict the structure performance.

In this research, 3D-printed structures are planned to produce resonating dampers. DMTA analysis is required for the 3D-printed polymeric structures to assess the material properties. PLA (Polylactic Acid) and ABS (Acrylonitrile Butadiene Styrene) are planned to prepare samples in order to evaluate their mechanical properties in the DMTA test procedure. 20 mm x 10 mm x 10 mm sized rectangular solids are printed out from Ultimate Cura (3D-printing application-based machine) [162] with a 65% infill level with the material. The printed sample is shown in Figure 4.5. When printing is finished, mass is measured, and the density of each sample is calculated through a simple mass-density-volume evaluation. The total mass of the PLA sample is 1.8 g, and the calculated density from the volume of the structure is 900 kg/m³.

On the other hand, the ABS sample mass is 1.9 gr, and the calculated density from the volume of the structure is 950 kg/m³.

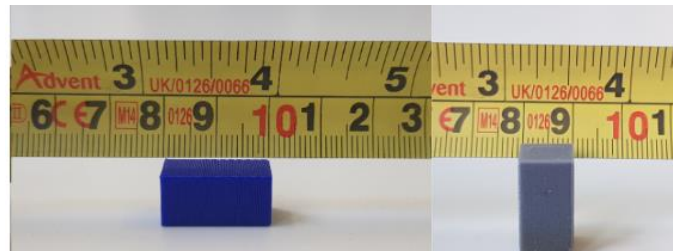


Figure 4. 5: 3D-printed test sample

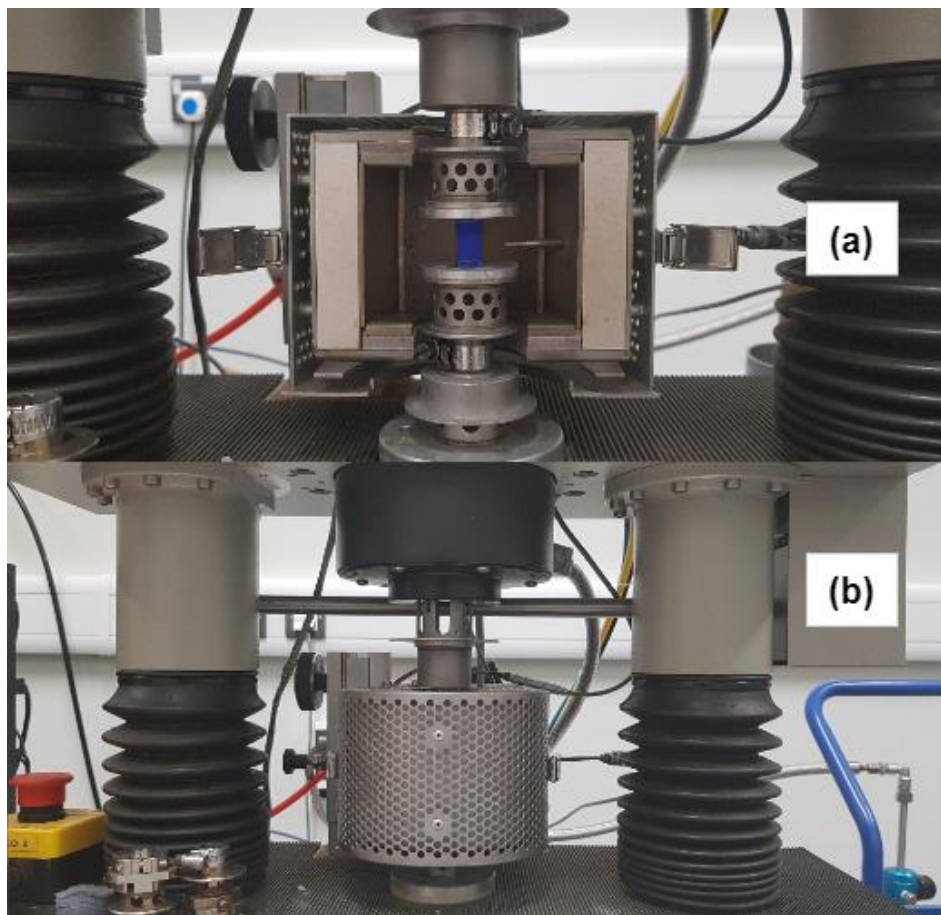


Figure 4. 6: DMTA test machine (a and b) and 3D test sample mounted to the machine (a)

Figure 4.6 is a taken photo from the DMTA machine. Figure (4.6-a) has the sample mounted on the machine plate, and (4.6-b) is the test machine's 'closed and ready to analyse' setup. Frequency sweep analysis is set from 10 Hz to 100 Hz by 5 Hz steps, while the temperature changes are set between 25°C and 40°C by 5°C increments. When the DMTA test machine proceeded with a complete step of frequency calculation on the sample at the same

temperature level, the procedure raised to another temperature level within the same frequency ranges. Once one temperature step has been completed through all frequency levels, the other temperature analysis is started to analyse automatically. Thus, a tension-compression test assesses the sample at various temperatures and frequency excitations. The applied dynamic stress is 0.001 Pa, and the strain value is fixed to 0.0001. The data for these samples provide information on the Young's Modulus, storage modulus and stiffness properties. The loss factor of the material is calculated using the storage and loss modulus ratio. Stress ratio (R) of each sample has been calculated for all temperature and frequency combinations using the maximum and minimum dynamic stress levels. The stress ratio for ABS sample is -5.9 while it is 0.42 for the sample made of PLA, which are in the expected ranges ($-\infty, +1$) for the stress ratio gained from DMTA testing [163].

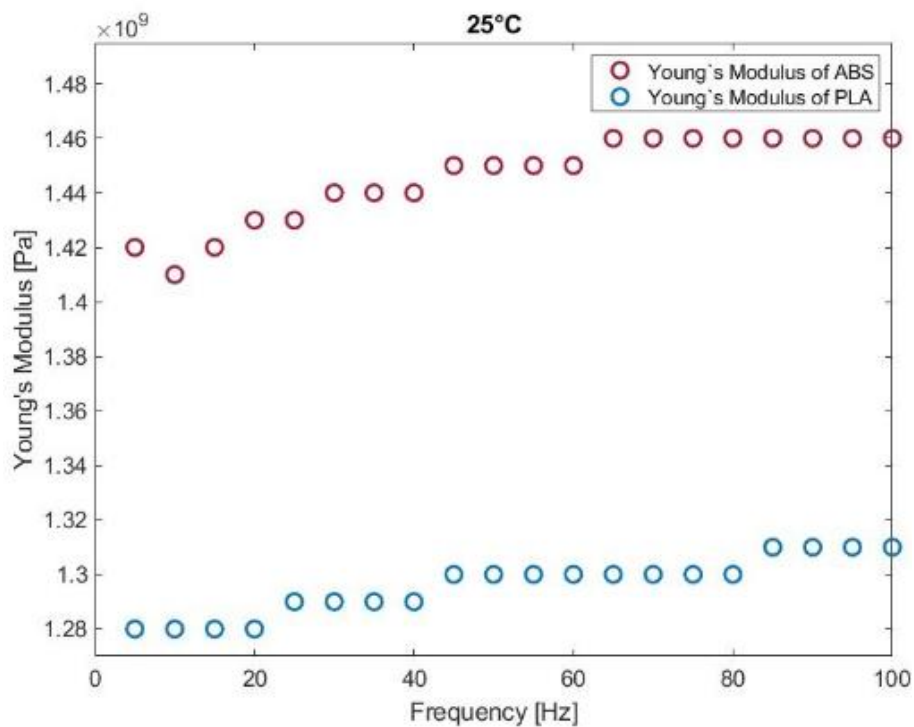


Figure 4. 7: Young's Modulus range of ABS and PLA from DMTA test at 25°C

Since all the research analyses are planned at room temperature, 25°C results are considered after a general evaluation of all temperature levels. Figure 4.7 shows the Young's Modulus captured at 25°C measured over the range of frequency levels. Storage Modulus (E') which is a measure of required energy to distort the sample and Loss Modulus (E'') which is lost energy during one cycle of testing can be found using DMTA test of selected materials of the

samples [164], [165]. Data of these properties have been shared in Appendix 4.2 (Table A4.3 and Table A4.4). The data show that the Storage Modulus values are larger than the Loss Modulus values which makes the tested sample's material can be considered as an elastic material [161]. Relationship between these properties as given in Equation (4.2), indicates damping or energy dissipation in the material.

$$\tan\delta = E''/E' \quad (\text{Eq. 4.2})$$

Comparing two thermoplastic filling materials informs that PLA has stronger and stiffer nature while ABS has lower rigidity but makes lighter structures. In addition to ability to make light structures using ABS, this material provides opportunity in 3D-printed prototyping and low-stress on the printed structures [166]. As a result of this simplified comparison, ABS has been decided to use as 3D printing filament.

Table 4. 1: DMTA resulted ABS material properties

Young's Modulus [Pa]	1.45E+09
Poisson's Ratio [-]	0.35
Density [kg/m ³]	950

DMTA test has been prepared for the 65% infill rate of the 3D-printed sample, which means the data in the table is available for the same printing properties and setup details for the same sample materials. Otherwise, performing a new mechanical-thermal structural property test (DMTA) is recommended. The data given in Table 4.1 is used to model the resonator in COMSOL Multiphysics.

4.5- Geometry of the Resonator. Particle Damper

The resonator's geometrical shape should be considered first to analyse the resonator geometry. In this research, granular structures have been aimed to take place in the resonator for investigating their damping abilities (Chapter 7). Therefore, damper geometry and its impact on structural interactions have been informed by particle damping-related literature.

In the earlier studies, soft to hard materials were studied regarding the geometry of the granules and the damper's geometry affects the energy dissipation caused by the granules [15]. According to this study, empty volume in the granular packing, which is defined as the clearance ratio, significantly impacted particle interactions under the excitation which is given in Chapter 7.

This study includes large and small granules with equal mass amounts (see Chapter 7). According to the analysis, smaller granules require less volume than large ones because the smaller sizes of the granules can be placed into the cavity with a more regular arrangement. In addition, replacing the single particle with the same mass amount of multiple particles provided improved energy dissipation with less sensitivity to the damper geometry [20].

Several examples of literature presented that the particle damper geometry is not the only parameter controlling particle damping efficiency [20], [147] and [167]. It is noted that regardless of the geometry of the damper, placing them on the highest amplitude area of the exciting structure, for example, the antinode points of the resonating structure, provides more energy dissipation [19].

The geometry of the resonator used to place granular structures is modelled as a spherical cavity in this research. This decision is made because the spherical particles will be placed into the cavity. The damping efficiency has been noted in many sources due to the interactions between the geometries (granules and the cavity walls). To increase the contact area of the particle-particle interactions and the particle-wall interactions, sharp edges of damper geometry have been avoided by selecting a spherical cavity geometry. As a result, the damper cavity has been selected as a spherical structure, and resonating properties have been studied for this geometry, as given in the other sections of this chapter.

4.6- Numerical Model of the Resonator

Spherical geometry eigenfrequency analysis is prepared using the ABS material properties from the DMTA test analysis as introduced in the previous section. The eigenfrequencies have been evaluated through various spherical geometries. Figure 4.8 illustrates the interested mode shape of the geometry for the selected spherical structure. According to

this, the spherical geometry illustrates the eigenfrequency at 1071.5 Hz when the geometry has a single fixed-point attachment. It is assumed that the fixed surface attachment (base) to the spherical geometry would reduce the eigenfrequency of the interested mode shape.

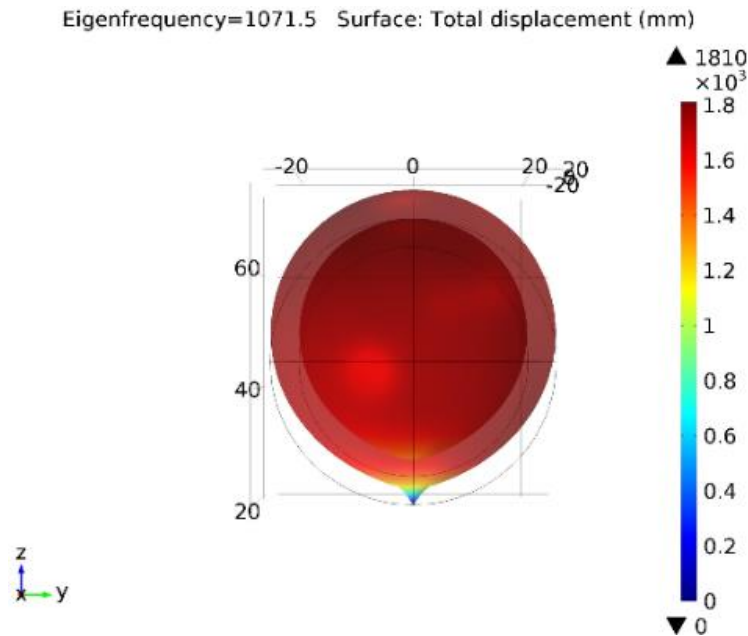


Figure 4. 8: Spherical cavity eigenfrequency at interested mode shape, sizes in mm

The idea of the base structure to connect to the spherical cavity is to place the whole structure (cavity and supportive base) on the beam to treat the excitation impact. This, also, aims to protect the form of the enclosing cavity geometry. Therefore, a structure should have a supportive base attachment underneath the spherical cavity. A cylindrical geometry has been modelled for being the supportive base to the spherical cavity. The meshed structures consisting of the spherical cavity and the cylindrical support base are given in Appendix 4.3 using Figure A4.2 and the mesh details are given in Appendix 4.3 (Table A4.5). The material properties of the resonator is listed in Table A4.6. These two parts have a contact area after they are attached, and this contact part would control the eigenfrequency of the whole resonator. Therefore, several diameter sizes and heights for the supportive base have been parametrised for different analysis details. The analysis boundary condition has been decided according to the attachment relations on the beam; therefore, the structure has been fixed constrained from the bolt hole.

The main parameter has been selected as the diameter of the supportive base, which is 11 mm, 22 mm, 50 mm, and 66 mm. These numbers for the diameter of the supportive base have been selected according to the diameter of the spherical cavity. The diameter of 50 mm for the supportive base equals to the diameter of spherical cavity. The others have been selected as either smaller than the cavity diameter or larger than the cavity diameter. Contact area height is limited to the radius of the supportive base (R_{sb}). Starting from such a small height to maintain contact and increasing the contact height to the radius of the supportive base (h_{sb}) develops a series of contact height options. Evaluating the Equation (4.3) provides several height options for the supportive base $h_{contact(1,2)}$ according to the introduced height idea for the contact area between the cylindrical support and the spherical cavity.

$$h_{contact(1,2)} = (2R_{sb} \mp \sqrt{(2R_{sb})^2 - (2h_{sb})^2})/2 \quad (\text{Eq. 4.3})$$

According to this equation, the contact area's height receives a series of numbers used to find the eigenfrequency of each geometry. The details of the calculations for each diameter size of the supportive base can be found in Appendix 4.4.

Equation (4.4) is created to calculate similar geometrical shape and their corresponding eigenfrequency details. The contact area calculation MATLAB code can be found in Appendix 4.5; however, this equation can be used to calculate any eigenfrequency of cylindrical base-spherical structure inclusion by feeding the equation with the radius of the geometries.

$$f(x) = f(x_{max}) \sum_{n=1}^N p_n \left(\frac{x}{R}\right)^{N-n} \quad (\text{Eq. 4.4})$$

In this equation, the polynomial function recovers the polynomial coefficients, p_n , where n takes values from 1 to N , which is the maximum size of the polynomial fit (which is given in Appendix for each cylindrical base dimensions, Appendix 4.6 (Table A4.7)). So, in MATLAB, the order of polyfit is $(N-1)$; therefore, the polyfit $(x, R, (N-1))$ is calculated using the equation. The half-length of the spherical cap in contact with the cylindrical base is x , and R is the radius

of the spherical cap (Figure 4.9). The maximum size of x is limited to the radius of the cylindrical base (R_{sb}). Calculating this equation provides a series of natural frequencies.

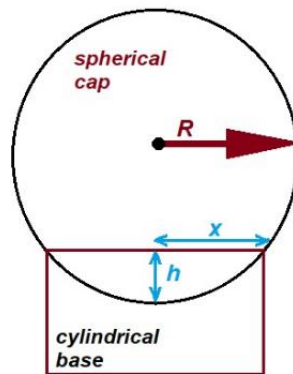


Figure 4. 9: Geometry used for the analysis of quantifying the contact area

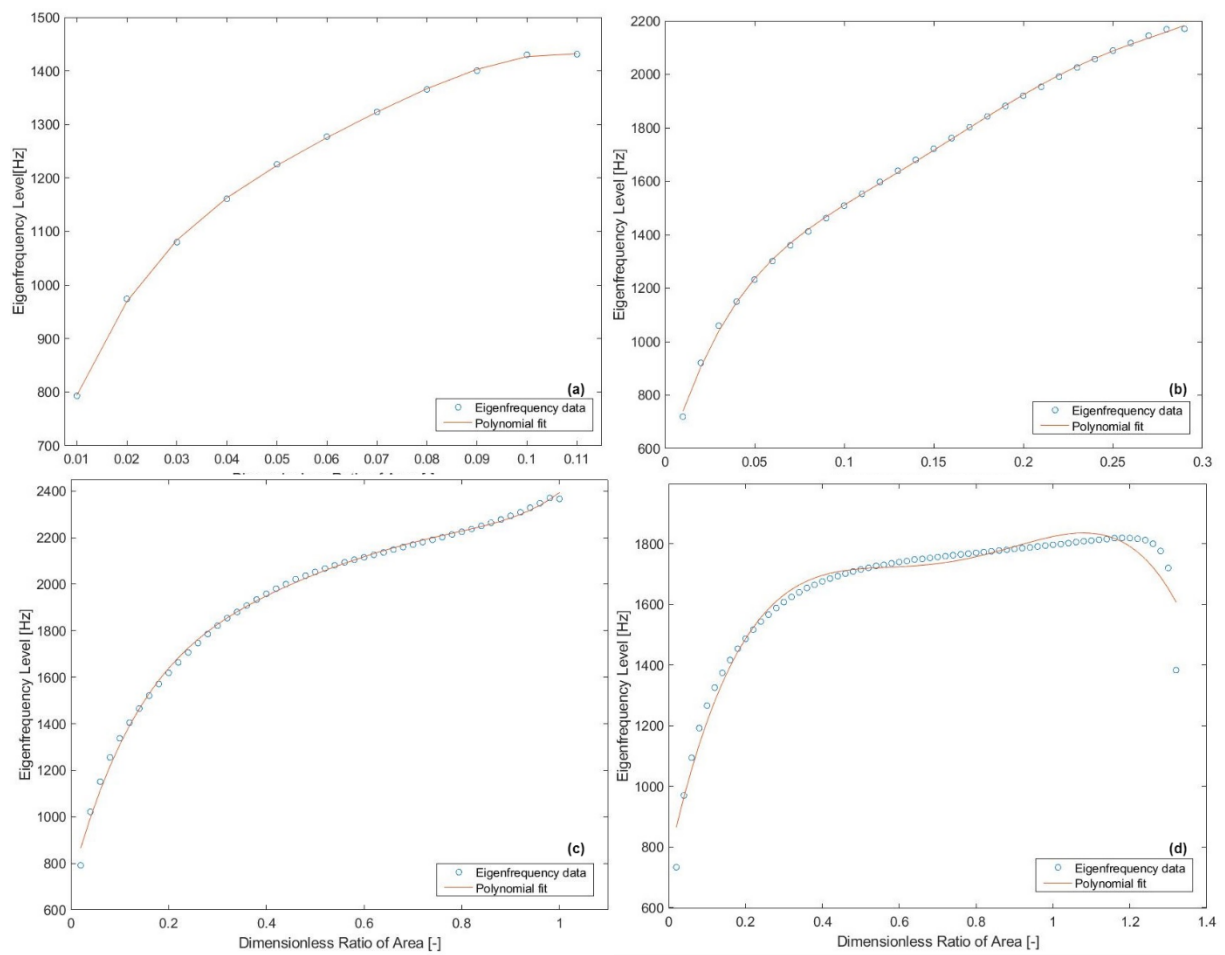
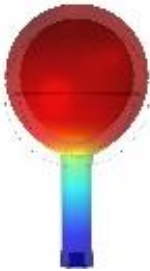
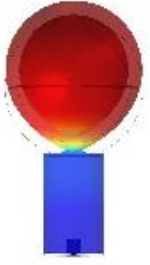
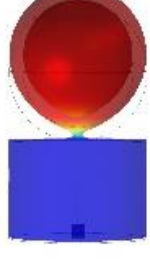
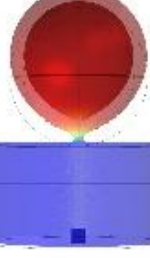


Figure 4. 10: Contact area and corresponding eigenfrequency for the geometries: (a) supportive base diameter 1 (11 mm), (b) supportive base diameter 1 (22 mm), (c) supportive base diameter 1 (25 mm), (d) supportive base diameter 1 (66 mm)

Figure 4.10 shows the details of each contact area calculation as dimensionless area and corresponding eigenfrequency of the interested mode shape for the given supportive base diameters. The figures (Figure 4.10-a, b, c, and d) have been prepared using *the polynomial fit* in MATLAB [168].

Table 4. 2: Corresponding eigenfrequency and mode shape details for the area ratio of 0.1

Outer Diameter [mm]	Eigenfrequency [Hz]	Mode Shape
11	1430	
22	1412	
50	1151	
66	1094	

According to the results obtained from cylindrical supportive base-spherical cavity analysis, the contact area between the cylindrical support and the spherical cavity controls the structure's stiffness as a resonator. As a result, the SDOF properties of the structure are

controlled, and the eigenfrequency of the structure is changed through different contact lengths (Table 4.2). An approach to creating a response of the resonating structure through the stiffness change has been accomplished by modelling the contact between the parts of the resonator with this method.

As a result of this study, resonating structure geometry design methodology has been created, and the results are provided in this subchapter. The resonating structure spherical part to place the granular structures have been introduced in the previous subchapter. A 22 mm cylindrical base diameter has been selected to model the resonating damper. Even though the eigenfrequencies of the interested mode shape are similar, especially for the first two parameters, the resonator's design is selected using the second parameter.

4.7- Investigation of Resonator Properties

According to the bare beam eigenfrequency result evaluated from numerical analysis, a locally resonating damper with a spherical-shaped volume is required. As explained in the previous subchapter, the volume is decided to be used for placing the granular structures. The spherical volume must be maintained with a cylindrical base since the damper is attached to the beam at several locations. The spherical-shaped section of the geometry should illustrate the mode shape as in Figure 4.8 to alter from the response of the main structure to which the damper will be attached.

As a result of the analysis of the resonator geometry, the diameter of the cylindrical base should be strong enough to manage the granular placement and the excitation conditions. Eigenfrequency analysis of the decided geometry from 'the polyfit analysis' (Figure 4.10-b) requires minimal contact between the spherical and cylindrical parts. The results show contact height of the maintained parts should be between the first and the second parameters since the eigenfrequency of these levels are either higher or lower than the eigenfrequency of the beam. Individual modelling and eigenfrequency analysis have been performed to evaluate the resonating damper geometry (Figure 4.11) critically.

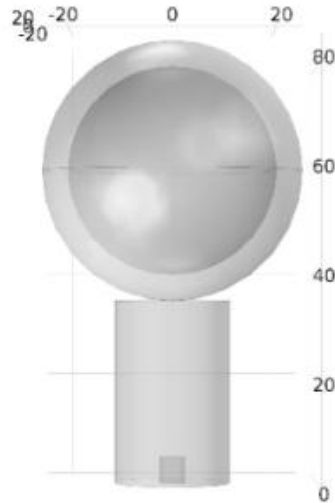


Figure 4. 11: The resonating damper geometry modelled in COMSOL Multiphysics

Appendix 4.3 is designed to show the meshed geometry and material properties of the resonator. Also, the boundary conditions for the structure have been explained in this subchapter. Eigenfrequency analysis of this geometry has multiple mode shapes; however, the spherical part should be the only part to experience the deformation in the structure, which has to be similar to Figure 4.8. Figure 4.12 shows the first six mode shapes of the whole structure, including the mode shapes of different parts. Figures 4.12 a-e include the mode shapes of the whole structure (spherical and cylindrical sections) from 17.307 Hz to 603.11 Hz. These mode shapes are not considered in this study since they are assumed to be weak. This results in the interested mode shape at 860.63 Hz, as shown in Figure 4.12-f. The spherical section has a deformed mode shape similar to the previously observed mode shape for a single fixed point on the spherical shell (see Figure 4.8). In this mode shape, the spherical part resonates, and the cylindrical part is stable as it experienced low deformation.

The resonator modelling for all numerical and experimental studies is decided according to this study's outcomes. Production of the resonator is accomplished through the 3D-printing options using ABS material with 65% infill rate. After the 3D-printing process has been accomplished, the spherical cavity and the cylindrical support have been glued to each other from at the contact area of 0.08 mm.

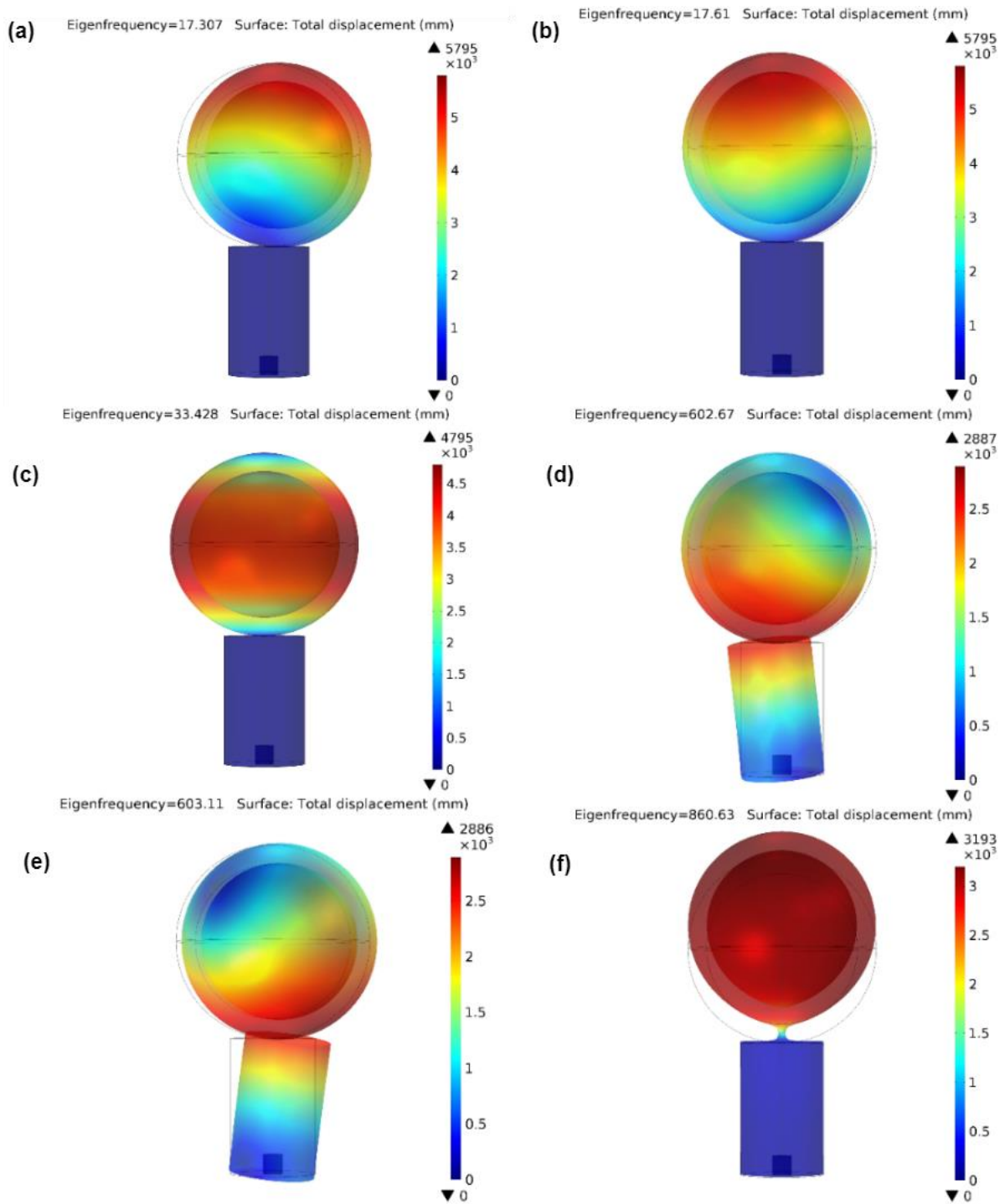


Figure 4. 12: Resonator mode shapes at various eigenfrequency levels (a-f)

4.8- Conclusion of the Chapter

This chapter has been prepared with the idea of producing a resonating damper planned to use for granular structure attachment to dissipate the vibration energy from the main structure. According to the research on locally resonant structures, placing resonator on the

antinode point or close to the antinode point helps treat the undesired energy from the main structure. Since the antinodes corresponds to the maximum deformation of the solid structures, using the resonators in these places would help them to treat the excess energy. Therefore, a resonant structure design has been studied in this chapter.

The resonating structure is produced using the Ultimate Cure 3D printing opportunity. In order to decide on the filling material for the 3D printing, two different filling materials have been used to print out samples. These samples have been processed in DMTA testing to evaluate the printed structure material properties. As a result of this process, the filling materials' properties, loss properties and storage properties have been found. Resonating structure production material has been decided to be ABS according to the findings of the DMTA testing. These material properties have been used in all numerical studies for the resonating structure.

Since the resonating structure is planned to be filled with granular structures, additional literature research has been conducted through particle damper geometry. As a result of this research, it has been found that the decision on the geometry of granular packing cavity requires more analysis. However, modelling a spherical cavity for granular packing has been decided to increase the contact between granules and the cavity walls.

An eigenfrequency analysis procedure has been followed in order to find a beneficial cavity geometry. The cylindrical support and the spherical cavity contact area have been studied within a parameter-based progressed theoretical analysis. A generalised polynomial equation has been developed for sphere-cylinder inclusion geometry studies. The findings from the equation have been studied in the eigenfrequency solver of COMSOL Multiphysics. The cylindrical support has been decided to have 22 mm in the diameter.

As a result of material testing, geometry design research (based on parameters of the dimensionless area between the contacting structures) and eigenfrequency analysis on decided resonating structures have been processed. Then, the mode shape of the structure was evaluated.

Chapter 5: Periodically Arranged Locally Resonating Structures

Vibration and related issues have been visited in this thesis several times with its properties and disturbing impacts on engineering applications. Expressly, it has been noted that the vibration significantly impacts damaging structures when they resonate. Absorption of the vibration energy from the systems is one of the aims of damping applications promoted by engineers and researchers in this field. Damping applications reduce the impact amplitude or the structure's disruption energy.

Even though resonance is not a desired situation in structures, it has been thought that the resonating properties and its dynamic processes would be beneficial to reducing the excessive energy from the other systems. There are several examples of resonator usage on a base structure to mitigate its undesired dynamic properties by keeping the resonance frequency of the attachment structure close to the natural frequency of the base structure [169]. In these application examples, once the vibration impact hits the base structure at its natural frequency, undesired energy is “absorbed” by the resonator or converted into other forms of energies [170]. Attached resonating structure shifts the resonance of the base structure and prevents excessive or undesired vibration. Using multiple resonators in specific arrangements known as the periodic arrangement has provided excellent dynamic properties [100]. This application requires relatively large structure to place many numbers of resonators where the performance of the arrangement is defined by the unit cell.

This chapter introduces structural interactions with periodically placed resonators on the main body (the beam introduced in the previous chapter). These locally resonating structures are referred as metamaterials and are studied to explain the coupling phenomena between the resonators and their tunability with the beam to reduce the structural vibration impacts. A particular interest present the performance of metamaterial over the broadband frequency interval.

Metamaterials and Subunits

Metamaterials are artificial structures developed in applications of electromagnetic and optics at first [171]. Later, the metamaterials found their application in acoustics to

treat/control vibration in the air [172]. In solid mechanics, mass-spring-damper systems with resonating properties provide mechanical damping opportunities in general application and, in metamaterial applications, these structures have shown interesting mechanical properties such as negative material properties (i.e. density and stiffness) under certain conditions. Negative material properties prevent frequency response or wave propagation, resulting in cloaking application. According to the metamaterial knowledge, prevented or cancelled frequency ranges are known as the stopband of the structure.

Bragg scattering and the local resonance have been explained in the chapter of Literature Review. These two options are the main reasons for the stopband formation within a material. As a result of the Bragg scattering application, destructive/constructive interferences are formed in the acoustic wave field. However, Bragg scattering requires the unit cell size comparable with the acoustic wavelength. This size requirement for a unit cell limits the application of Bragg scattering at low-frequency levels [173].

On the other hand, locally resonating structures, as explained in the previous parts, dissipate the energy in shear, torsion or bending moments using the inertia forces of the structure. Compared to the Bragg scattering size limitation, locally resonance structures do not require a specific size limit for the unit cell. Also, they provide low-frequency stopbands in specific applications [157], [82] and [159].

Periodically arranged structures manipulate or modify the wave propagation within a structure [80], [81]. Studying the periodic structures in a long arrangement in real applications might be applicable when many unit cells are used in periodic array. However, it is not viable to model numerically an infinitely long finite structure using many unit cells in periodic arrangement. This would increase the computational cost. On the other hand, the periodic conditions provide modelling opportunity to reduce the computational cost, by imposing the periodicity conditions [169]. The distance between the two identical parts of the structure is called the lattice constant (L), which equals the unit cell size.

Bloch-Floquet Method is one of the options to express an infinitely long structure as the single unit cell. Bloch-Floquet conditions defines quasi periodic solution of the wave propagation problem where solution in any unit cell is the solution in the primary cell with

the phase shifted in accordance with the given geometry of the periodic arrangement [169]. Therefore, the unit cell approach reduces the computational expenses since the periodic boundaries behave like a finite size model.

The problem becomes an eigenvalue problem where the band structure analysis is performed with a parameter sweep study over the Bloch wavenumber (k) and frequency. The recovered numerical dispersion relationship is evaluated in terms of the wave modes acting in the field.

Dispersion curves provide information on the frequency ranges where wave propagation is forbidden. These frequency intervals are known as 'stopband' or band gaps. At the same time, the frequency range where waves are allowed to propagate are known as 'passband'. Tracing the frequencies and k-space (wave number) scanning are options to observe the persisting modes as they deliver the band structure via FFT applied spectra ($\omega a / 2\pi c$ vs FFT) or band structure computation ($\Gamma X M \Gamma$ vs $\omega a / 2\pi c$) using the reciprocal vector representation [174].

In some cases, analysing a part of Brillouin zone would be helpful in order to save computational effort. Irreducible Brillouin Zone (IBZ) is used when the reciprocal lattice has more than one representative unit cell dimension. The primitive unit cell defines the first IBZ. The Bloch-Floquet conditions and unit cell modelling using the IBZ representation are used in this chapter to model the coupling between the local resonators and local resonators and the supporting beam.

Dynamic Vibration Absorption and Periodically Arranged Resonators

According to the literature examples, the metamaterial formation can be defined with the negative material properties [175]. Therefore, what makes a structural arrangement or the structure itself metamaterial is not clearly distinguished. The separation between structures, which might be because of Bragg scattering or local resonance, is another difference in the definition of the metamaterial. Additionally, as the application field changes, the metamaterial properties also change. For instance, electromagnetic, acoustic, or mechanical metamaterials require various properties, which is not necessarily be the same.

In this research, the metamaterial is defined by its locally resonating properties. The resonance is adapted to the base structure eigenfrequency, which is assumed to have the same mode shape. Also, since the interested frequency range is at lower bands, the base (main) structure modes and standing waves on the structure are studied. Therefore, the size of the base structure is assumed to be smaller than expected in large arrangements. These details are shown in numerical analysis with relevant results.

5.1- 1D Periodic Array of Resonators

This subchapter discusses and evaluates specific unit cell sizes to analyse the dispersion relations of unit cell and any attachment resonators when the unit cell experiences resonance at relatively high frequencies. The unit cell size has been modelled in smaller sizes than the bare beam modelled in the previous subchapter. The unit cell is constrained not to be displaced on the x-axis, and periodic conditions are applied through the y-axis to implement periodic conditions to both ends. This exemplary analysis has been thought to show the resonator inclusion impact on a solid structure. In this study the unit cell is set at various dimensions in accordance with the separation between resonators attached to the periodic cells, which makes the smallest unit cell size 60 mm, then, in the next case 70 mm unit cell size is studied. The maximum unit cell size studied is 170 mm, and increment starting from the unit cell size 70 mm is 20 mm. In both cases, the bare beam has been modelled in the first IBZ by applying the k-value from zero to 1 by 0.025 increments, and this step is thought to be fine enough for capturing each Bloch wave number result.

1D Periodic Array of Unit Cells

The corresponding eigenfrequencies of the unit cell under the given boundary conditions have been analysed in the dispersion relation. First of all, the boundary conditions have been specified in Figure 5.1 below. Figure 5.1(a) shows the layers where the periodic boundary conditions have been applied. Also, Figure 5.1(b) illustrates the displacement constraints which has been prescribed for x-axis of the unit cell. These boundary conditions have been applied to all of the various sized beam and unit cell modellings. The meshed unit cell geometry and material properties are given in Chapter 5-Appedix (Mesh Properties of the Unit Cell (L=170 mm) and Material Properties of the Unit Cell (L=170 mm)).

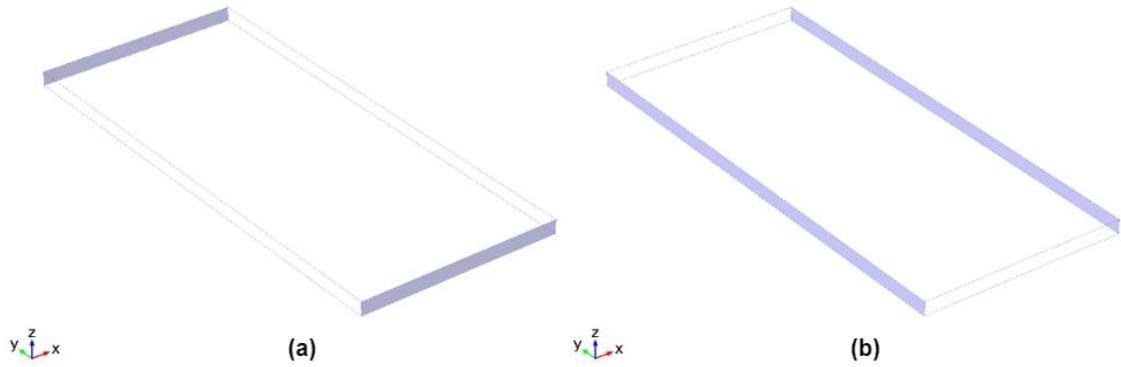


Figure 5. 1: Boundary conditions of the unit cell: (a) periodic boundaries applied layers, (b) prescribed displacement applied layers

The first eigenfrequencies illustrated in Table 5.1 belong to different size of the unit cell. Corresponding mode shapes are also given next to the eigenfrequency levels. According to the table, all the unit cells experience bending type mode shape at specific frequency levels. It has been noted that increasing the unit cell size has resulted in lower eigenfrequency levels for a given Bloch wavenumber.

Table 5. 1: Unit cell eigenfrequency data at the first mode shape for $k=0.975$

Unit Cell Size	$\omega(1)$	Mode Shape-1	Unit Cell Size	$\omega(1)$	Mode Shape-1
60 mm	3174.5		70 mm	2337.2	
90 mm	1417.9		110 mm	950.48	

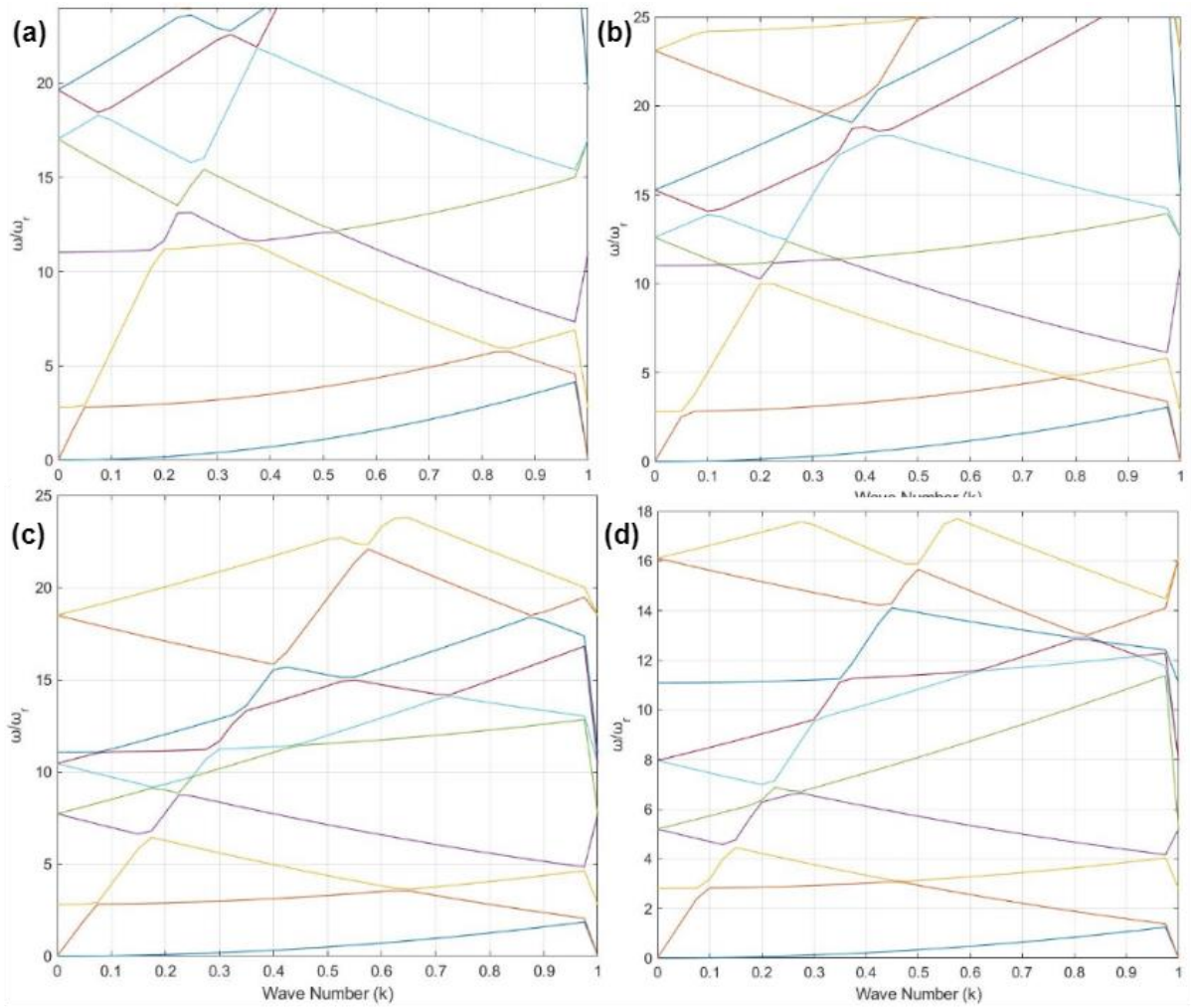
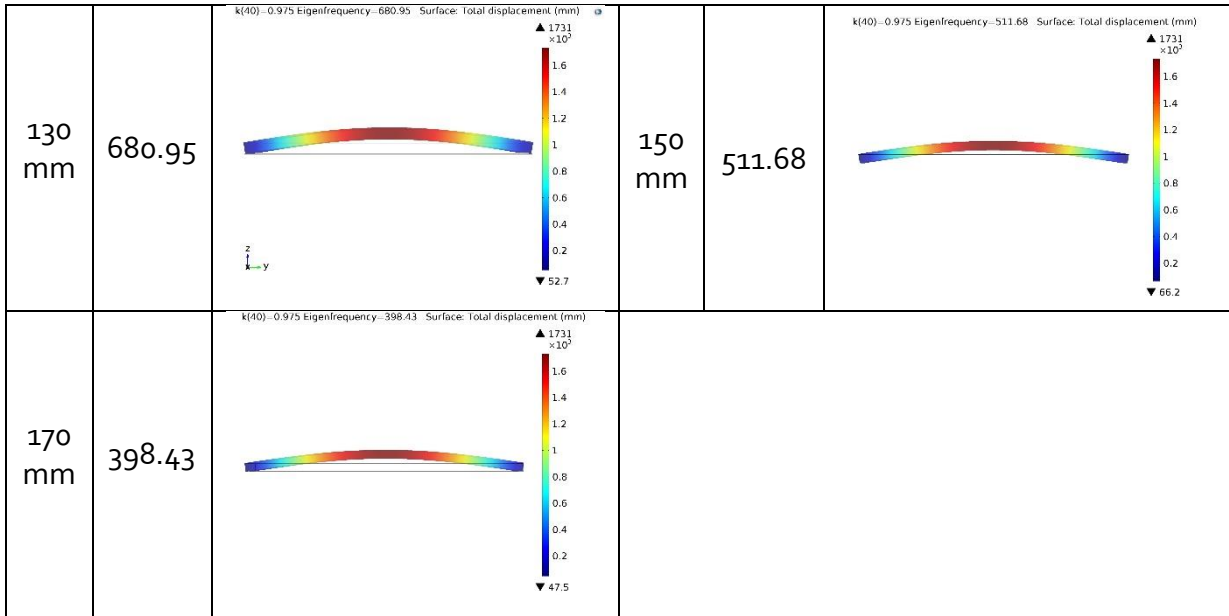


Figure 5. 2: Dispersion relations of unit cell sizes (a) 60 mm, (b) 70 mm, (c) 90 mm and (d) 110 mm

Figure 5.2 and Figure 5.3 are prepared using the data obtained from dispersion analysis of various unit cell sizes. Each subfigure illustrates the relationship between the Bloch wave number and corresponding eigenfrequencies. Each analysis result has shown two modes starting from zero frequency ratio when $k=0$. These figures demonstrate the observation made in Table 5.1, where frequency solution corresponding to a given wavenumber (k) has lower values as the unit cell size is getting larger. The eigenfrequency of the individual unit cells at each mode (ω) has been divided by the natural frequency in question ω_r , which was defined in Chapter 4.

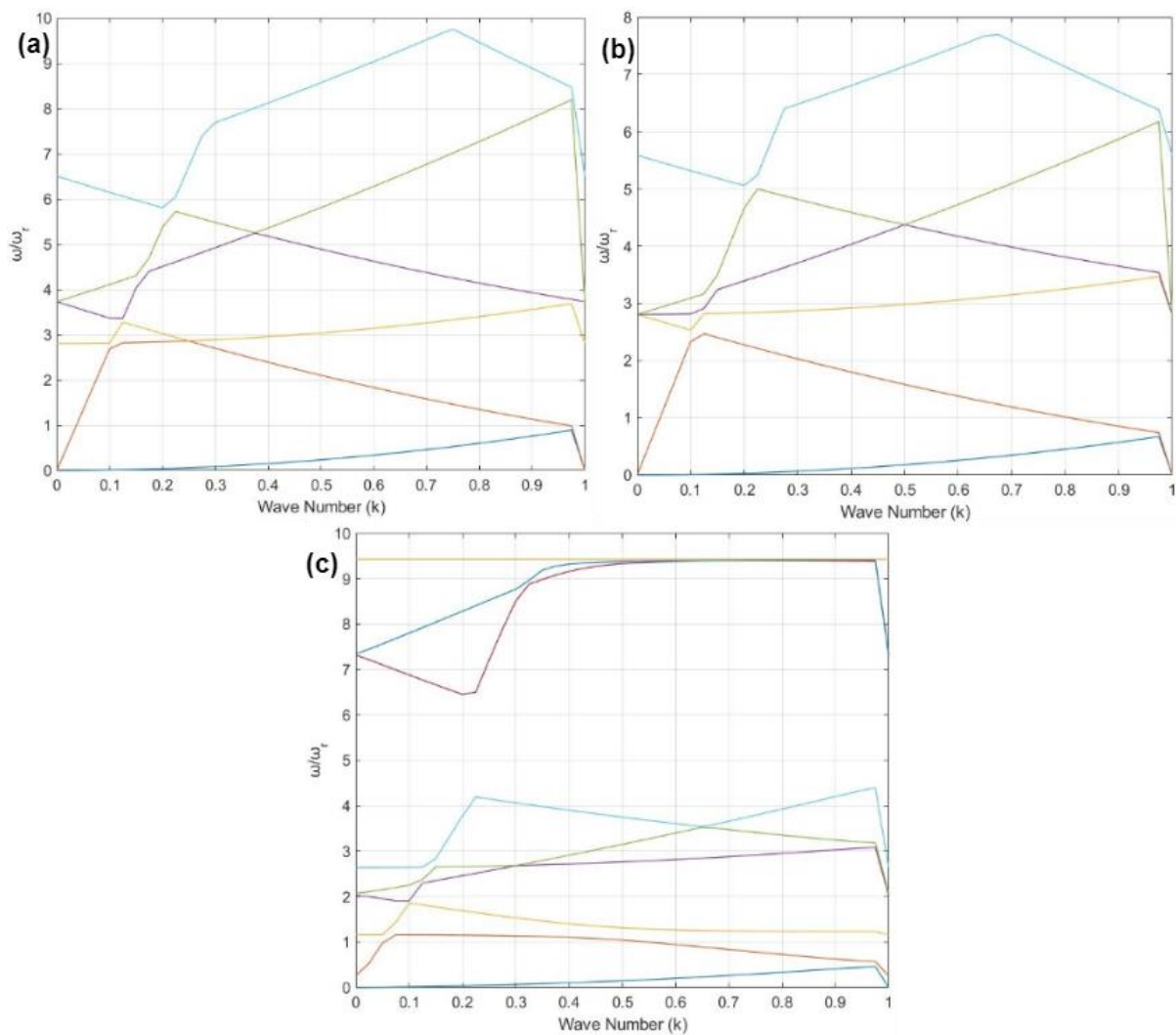


Figure 5. 3: Dispersion relations of unit cell sizes (a) 130 mm, (b) 150 mm and (c) 170 mm

Conversion of the modes through the unit cell is experienced for all the unit cell sizes which can be traced over the mode shapes and dispersion lines in Figure 5.2 and Figure 5.3 details. The mode conversion which changes through the Bloch wavenumber (k) is shown in the example of the unit cell size of 130 mm, as shown in Figure 5.4.

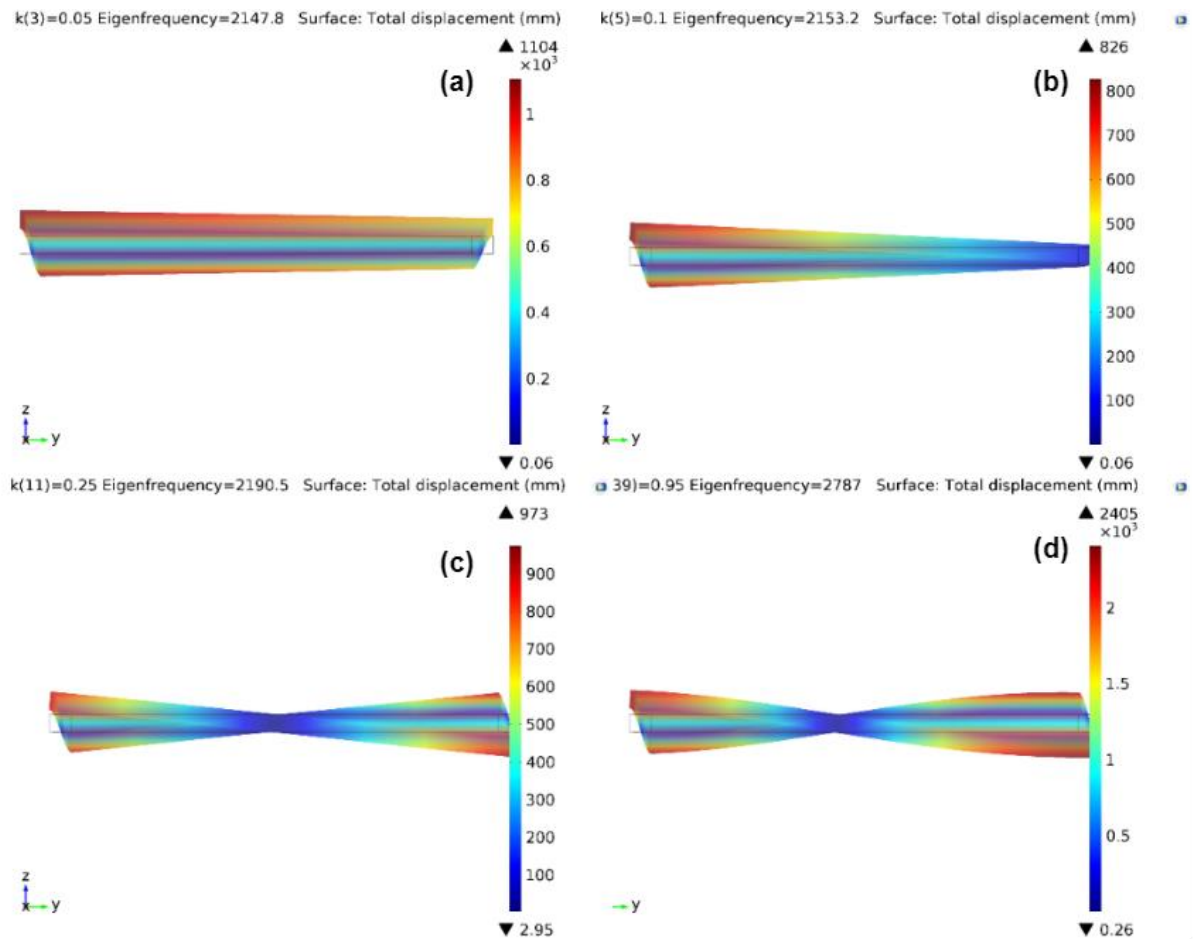


Figure 5. 4: Conversion points through the first dispersion line for $L=130$ mm

Searching the mode shapes in detail would provide more information regarding the unit cell behaviours at various dispersion lines. Therefore, the mode shapes at the Bloch wave number of $k=0.05$ is evaluated through a few dispersion lines. They are given in Figure 5.5. The first mode (Figure 5.5-a) is a whole unit cell motion through the z -axis, while the second mode (Figure 5.5-b) is another whole unit cell motion through the y -axis. Similar to Figure 5.4 a and b, the third mode shape has the conversion for this Bloch wave number ($k=0.05$) as shown in Figure 5.5-c. Figure 5.5-d contains the first bending mode of this unit cell size ($L=130$

mm). These mode shapes can be traced from the dispersion lines through the points of mode intersections as expressed in terms of the wavenumber and frequency.

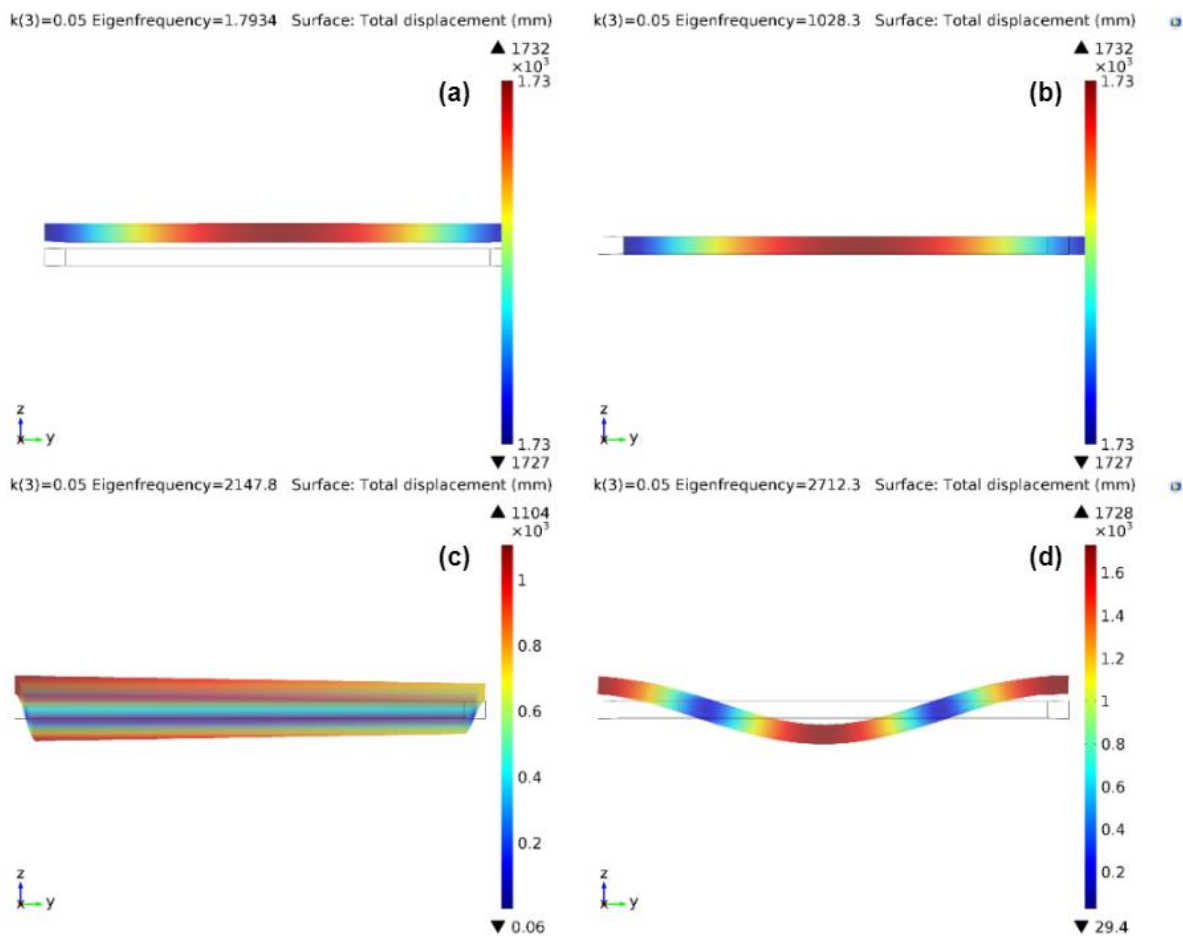


Figure 5. 5: Evaluation of wave number (k) 0.05 on the dispersion relations with the mode shapes

According to Figure 5.5, the first three modes are either a motion of the unit cell or the conversion mode; the first bending mode is observed in the fourth mode. Figure 5.6 evaluates the first bending mode through various Bloch wavenumbers. It can be seen from the figure that the corresponding eigenfrequency of the mode decreases as the Bloch wavenumber reaches the edge of the first IBZ.

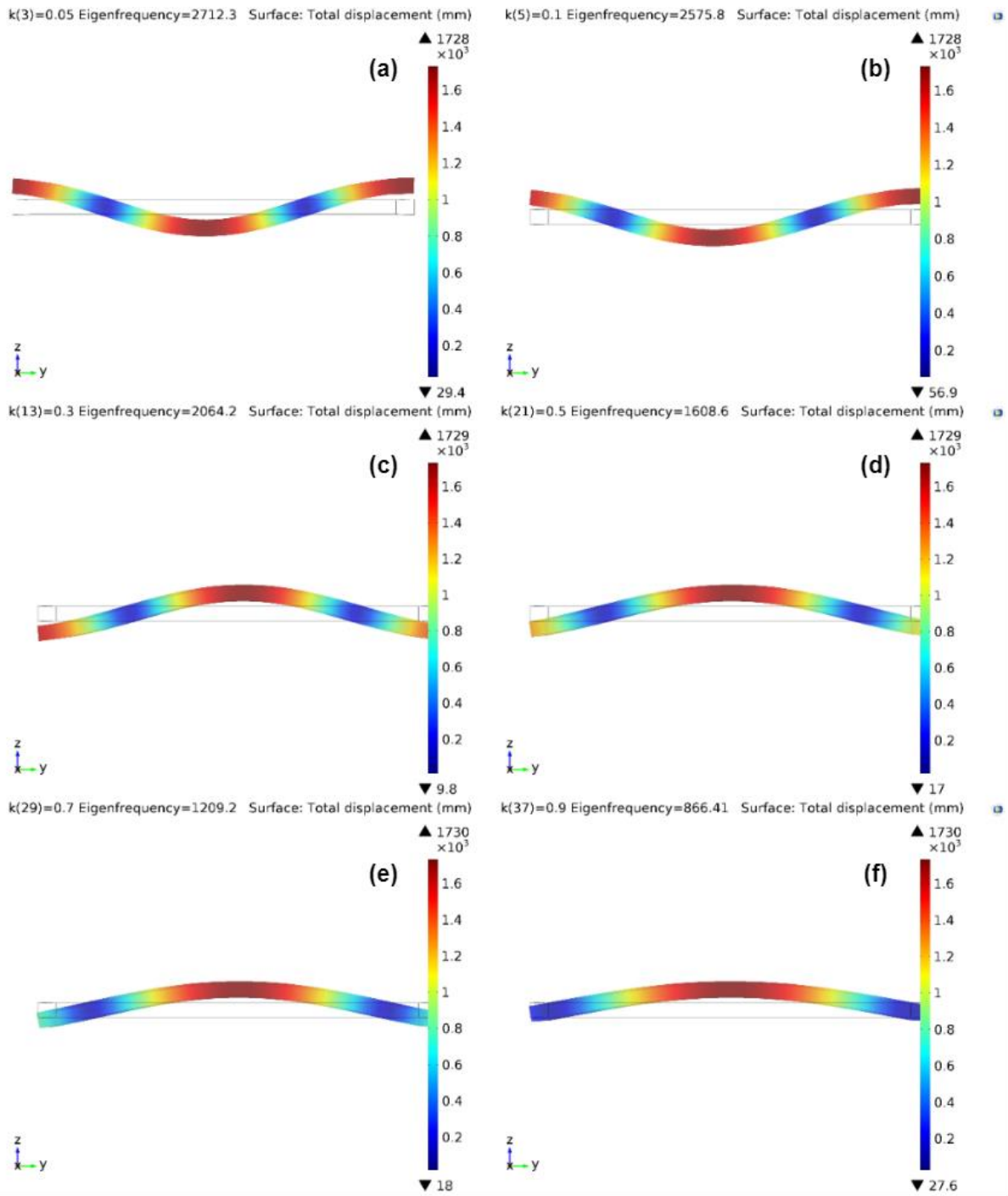


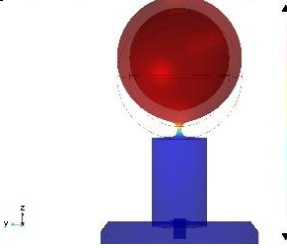
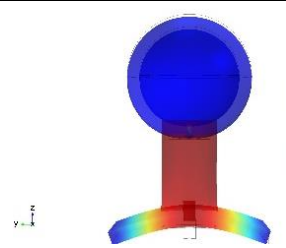
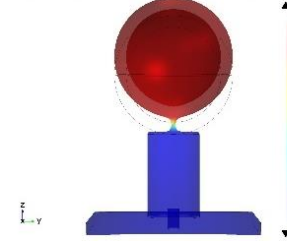
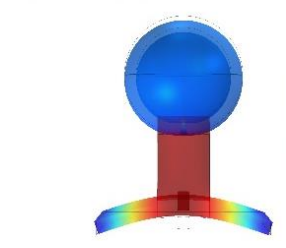
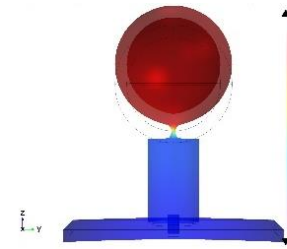
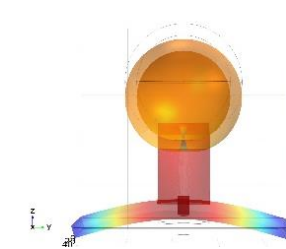
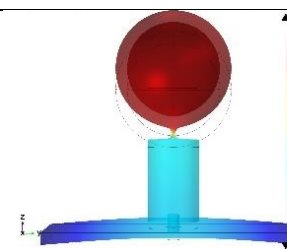
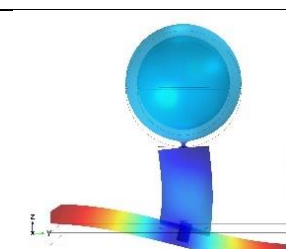
Figure 5. 6: Bending mode transition through the Bloch wave numbers for $L=130$ mm

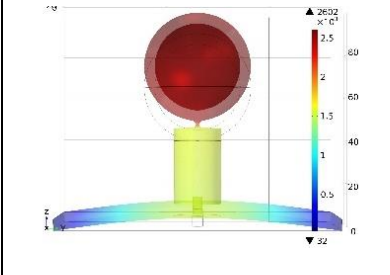
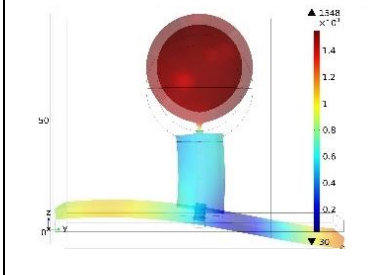
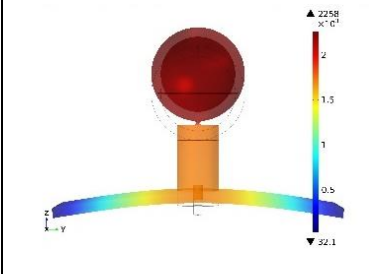
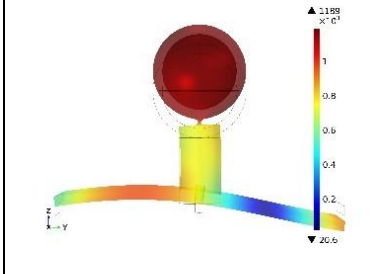
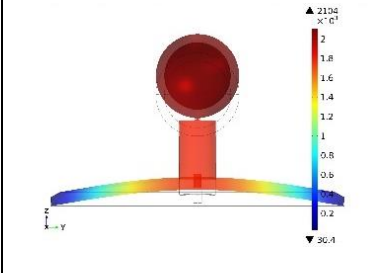
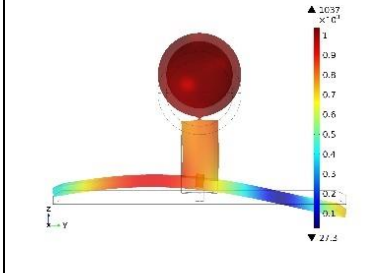
As a result of this analysis, the case of controlling the bending mode on the unit cell would be possible by tracking this mode on the dispersion relations figure.

Periodically Arranged Resonators

According to evaluated mode shapes and eigenfrequencies in the previous subchapter, the smaller the unit cell size, the higher the corresponding eigenfrequency. Eigenfrequency levels have been higher than the resonating inclusion eigenfrequency until the unit cell size of 130 mm. This subchapter part is prepared by attaching the resonating structure to the unit cell, and dispersion relations are evaluated for various Bloch wave numbers. Table 5.2 is prepared using the results of eigenfrequencies and mode shapes for the first two modes.

Table 5. 2: Resonator attached unit cell eigenfrequency data at the first two mode shapes for $k=0.975$

Unit Cell Size	ω (1)	Mode Shape-1	ω (2)	Mode Shape-2
60 mm	963.31		3124.5	
70 mm	951.69		2343.8	
90 mm	905.53		1496.4	
110 mm	779.71		1072.9	

130 mm	615.59		789.07	
150 mm	479.5		601.88	
170 mm	380.17		474.48	

As a result of given eigenfrequency and corresponding mode shapes, resonating inclusion has impacted the mode shape and resonance frequency of the first mode of the unit cell. Eigenfrequency and mode shape relations in the table confirmed expectation; when the eigenfrequency of the unit cell is close to the resonating structure eigenfrequency, the unit cell and resonator become coupled system. According to this, the unit cell size of 110 mm and larger sizes have resulted in similar eigenfrequency with the resonator. The reason behind this behaviour is that the resonator impacted the behaviour and illustrated resonating properties as seen in the mode shapes in the table.

Smaller-size unit cells have resulted in higher eigenfrequency levels than the resonating inclusion resonance frequency. On the other hand, all the unit cell dispersion analysis results at the first eigenfrequency and corresponding mode shape have been because of the resonating inclusion when the inclusion has been attached to the unit cell. This can be seen in the Figure 5.7 demonstrating with mode shapes around the resonant frequency of the attachment.

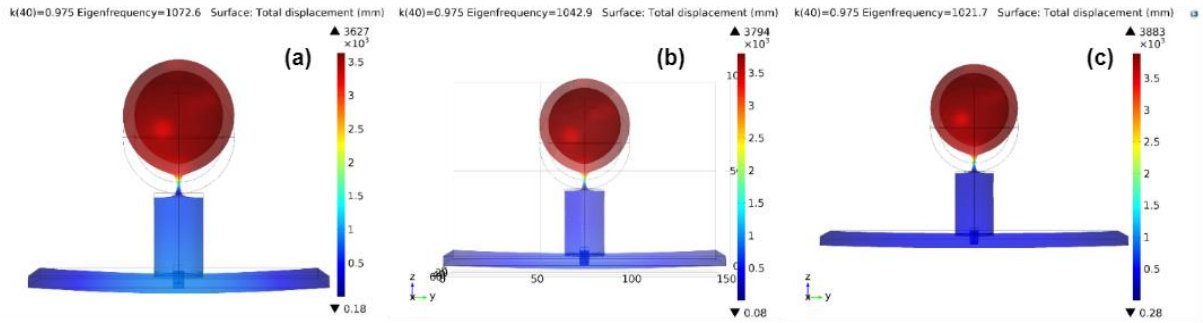


Figure 5. 7: Resonance of the inclusion on the unit cell size (L) (a) 130 mm, (b) 150 mm, and (c) 170 mm

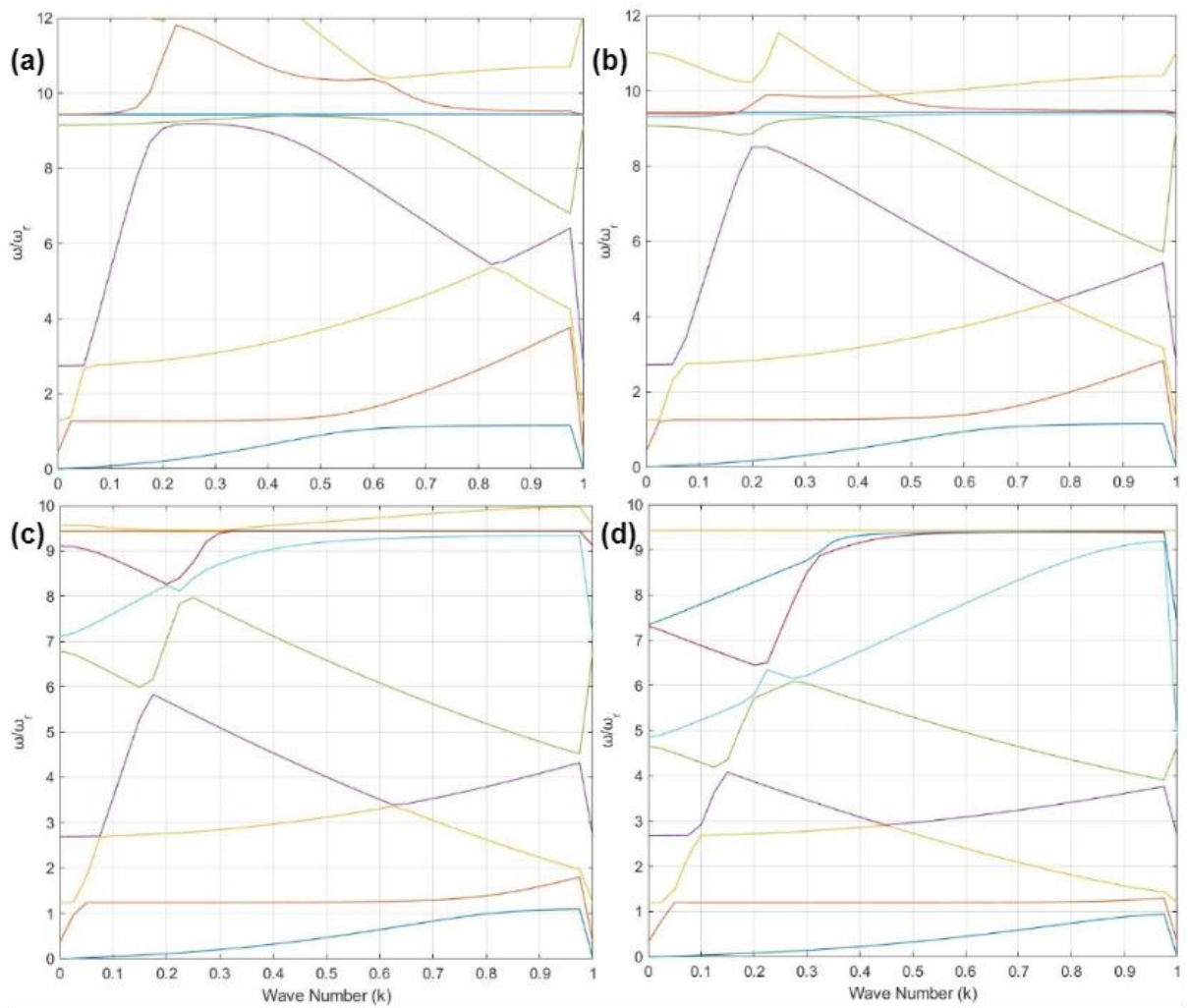


Figure 5. 8: Dispersion relations of resonator attached unit cell (a) 60 mm, (b) 70 mm, (c) 90 mm and (d) 110 mm

Resonating inclusion attached results shows that using a smaller-size unit cell demonstrates a full bandgap at higher eigenfrequency solution . This can be tracked over the dispersion

curves given in Figure 5.8 and Figure 5.9. According to the figures, controlling the second line (and in some cases, the third mode) would give the system's desired modes, as noted in the previous subchapter. In addition, controlling these modes would provide a band gap where no propagation is allowed.

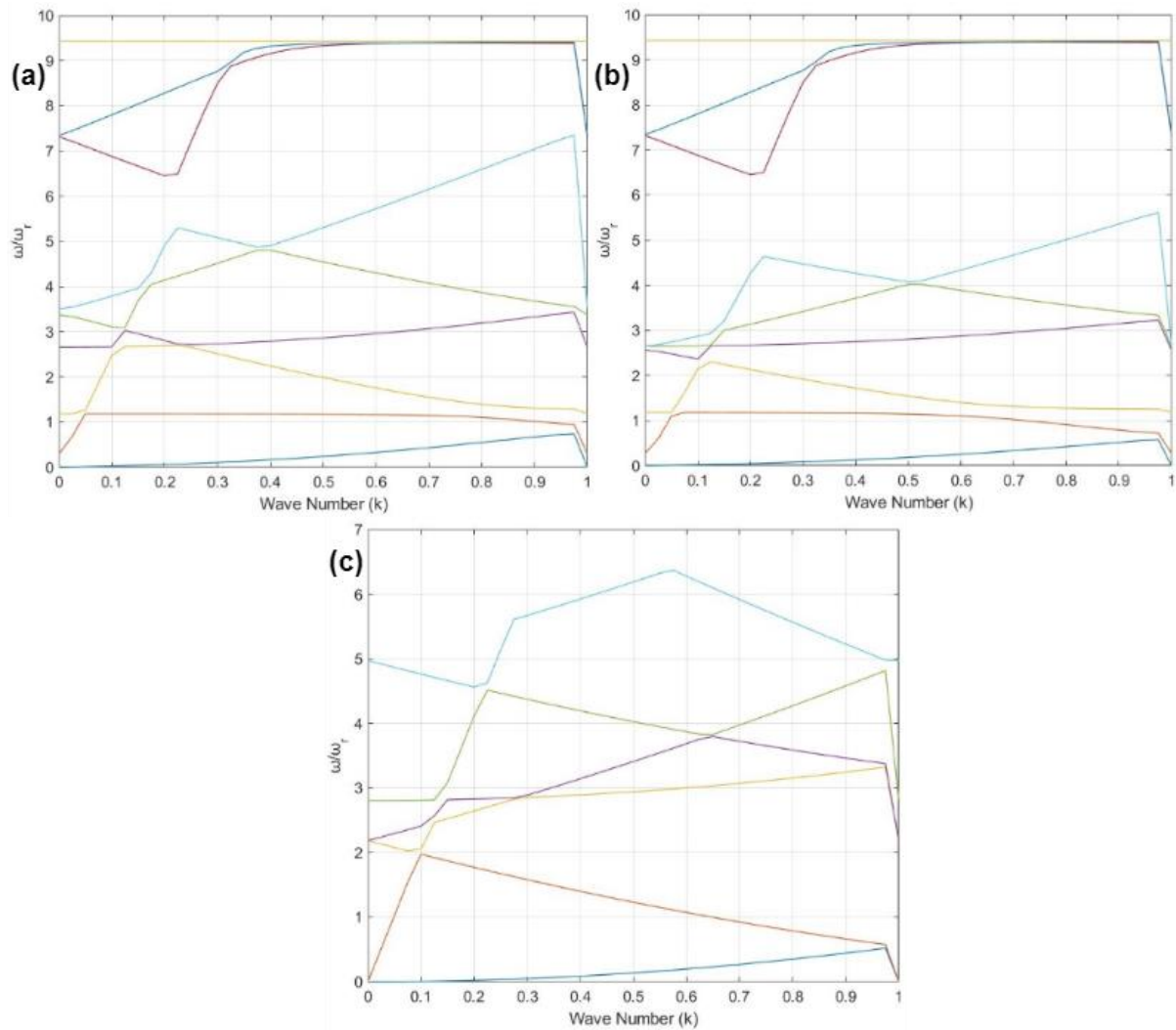


Figure 5. 9: Dispersion relations of resonator attached unit cell (a) 130 mm, (b) 150 mm, (c) 170 mm

Comparing the mode shapes at low Bloch wave numbers ($k=0.05$) provides information on the behaviour and inclusion impact on the unit cell. A unit cell without an inclusion has experienced one longitudinal and one transversal motions in order of modes (Figure 5.10). On the other hand, adding an inclusion to the unit cell has provided one longitudinal motion, one resonating structure effect, one transversal motion and one conversion in the same order of the modes (shown in Figure 5.10 from a to d). Also, all results have conversion modes

because of the lack of conditioning on the axes to model unit cell, similar to the earlier beam modellings.

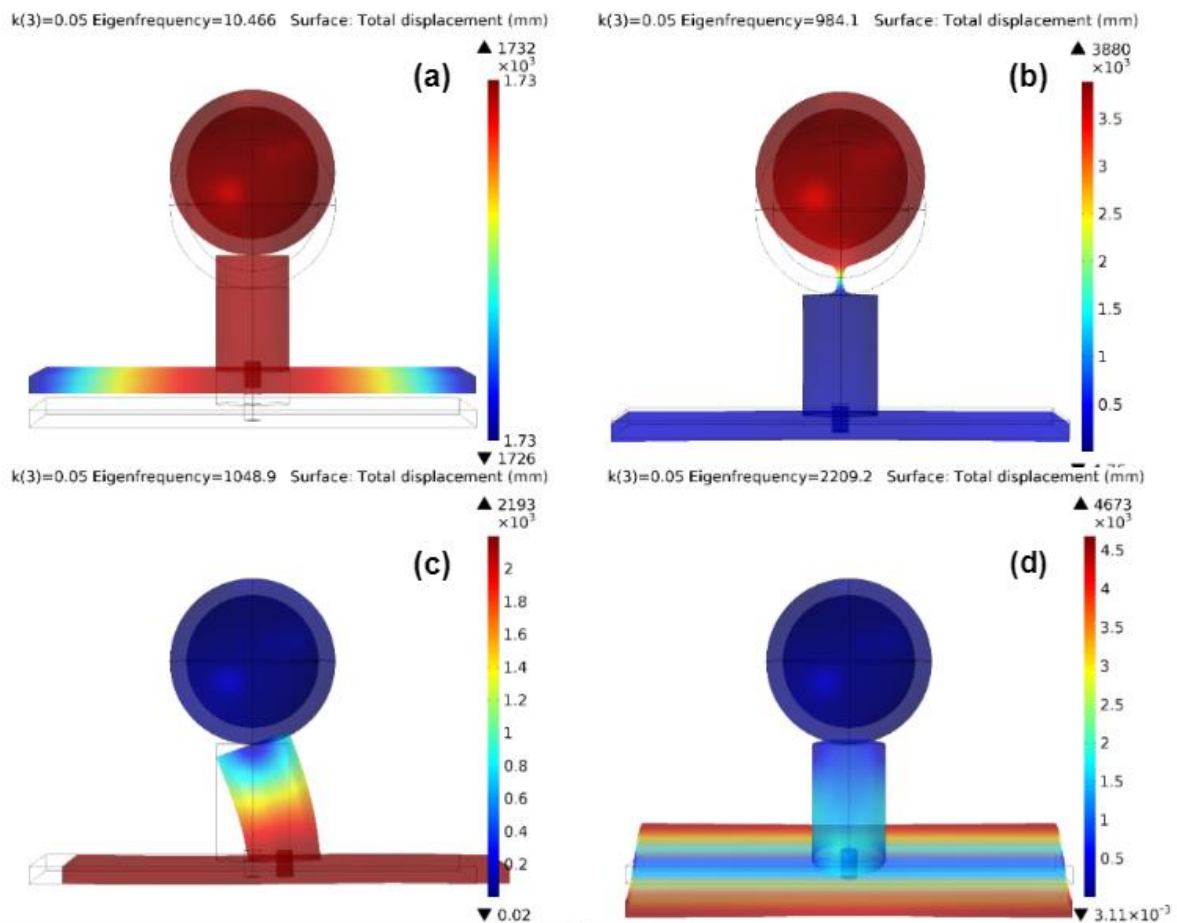


Figure 5. 10: Resonating inclusion impact on the unit cell (L=130 mm) at k=0.05

The unit cell analysis results show that the structures resonate at the eigenfrequency levels, which are relatively high. However, attaching resonating structures has changed the unit cells' dynamic behaviour. As one can see from this evaluation, resonating inclusion impacted the unit cell by including standing wave formation in the periodic arrangement. This additional impact breaks the modes of the unit cell and provides a band gap. Furthermore, since the motions are given in Figure 5.10 (a and c) are not interested modes of the unit cell, since these modes are the thickness modes controlling them would provide much beneficial formation of band gap.

Overall, the resonating inclusion used in analyses has proved that in the case of high eigenfrequency properties of the base structure have been modified by the resonating

inclusion. This has been succeeded by adding standing waves. As a result, this has provided a gap where no propagation is allowed. In addition, in the case of closer eigenfrequency relations between the base structure and the resonating inclusion, the resonator inclusion and the unit cell have an additional resonance which is the coupled resonance.

This research provided in this subchapter has shown that the resonating structure attachment on the unit cell modifies the dispersion relations and Bloch wave number solutions, resulting in band gap formation. Resonator placement has been found beneficial in modifying the dispersion of waves in the periodic structures, especially when the structure experiences high eigenfrequency modes.

5.2- 1D Periodic Arrangement of Beam with Resonators

Periodic arrangement in the finite structure in this research would not be enough to evaluate a response of a periodic structure. The total size of the beam and the number of resonators used in the experiment (Chapter 6) would not be enough to consider an infinite structure example when they are in periodic arrangement. In this subchapter, the beam (exact model given in the previous chapter) has been used to study the dispersion relations of both when the beam has no inclusion and resonator inclusion attached to it.

Considering the bare beam as a unit cell and resonators attached to the unit cell are the cases in this subchapter. As a result of the research on the infinitely long structures using the unit cell modelling, assumptions and evaluations can be made through the travelling wave dispersion relations by checking the mode shapes of the unit cell and the Bloch wavenumber solution properties. Each structure is expected to show its resonating properties in its modelling options.

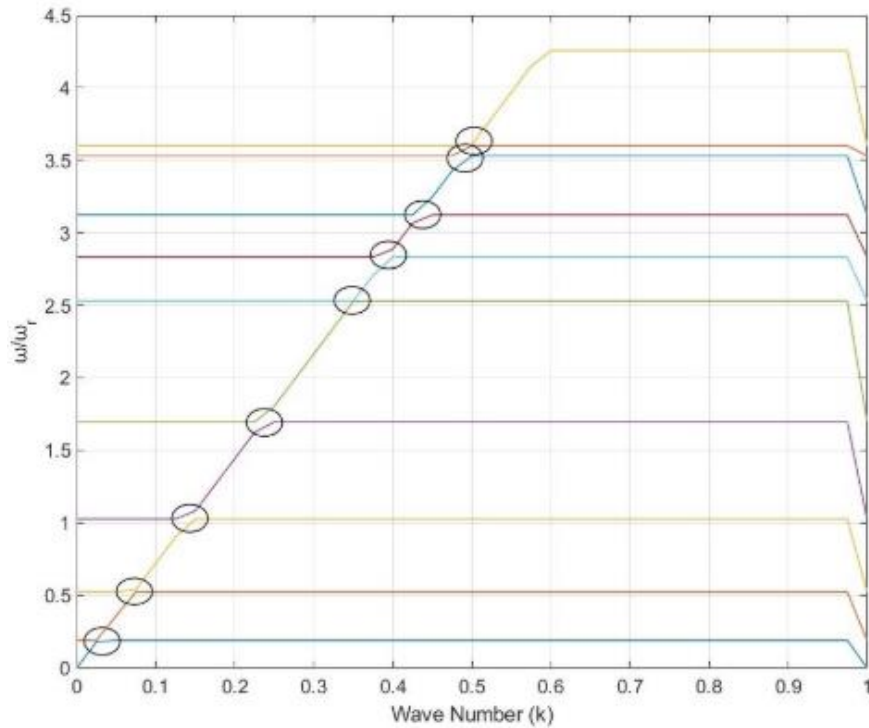


Figure 5. 11: Dispersion relations of bare beam unit cell modelling

Similar to the previous subchapter, the bare beam is modelled in the first IBZ by applying the k -value (Bloch wavenumber) from zero to 1 by 0.025 increments, and this step is thought to be fine enough for capturing each Bloch wave number result. Each horizontal line in Figure 5.11 represents a solution for the Bloch wavenumber. This means there is a specific eigenfrequency solution for each wave number (k), and different mode shapes can be observed in the given unit cell. The representation of the eigenfrequency solutions are the same as in the previous subchapter. Bending modes are the interested mode shapes in this analysis, as well as in all of the dispersion relation analysis. This is accomplished by applying the fixed conditions to both ends of the beam-sized unit cell, as in the finite structure modelling, in addition to the periodic conditions. In order to reduce the complexity expected from modelling of the bare beam, holes, and empty areas through the length of the beam are not included in the periodic structure modelling.

There are solutions for the bare beam, and they only show the bending modes as seen in the figure through the horizontal lines of the dispersion relations. Additionally, the diagonal lines of the dispersion relations represent only displacement through the thickness, which are considered as the mode conversion areas and specific band gap areas. Controlling the beam

modes and excluding the effect of the thickness from the beam would result in proper full band gaps emerging in the dispersion figure. Also, as seen in the eigenfrequency solutions of the beam (given in Chapter 4), the bare beam unit cell performs like a resonator. Each dispersion line represents the eigenfrequency solution at specific Bloch wavenumber for the unit cell, and their contact points represent the conversion points. Therefore, these diagonal line areas are assumed to be the discrete stop bands (Figure 5.11), and the contacting points of two dispersion lines are the conversion points between two modes. According to the figure, a travelling wave takes place in the structure since it is an infinite structure representation. As a result of the travelling wave solution, the structure and any attachments on the unit cell are expected to show resonating properties in the dispersion relations.

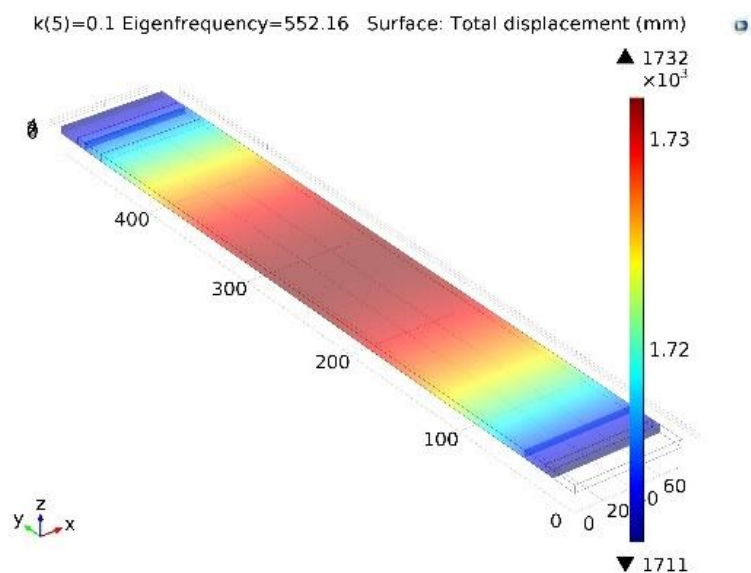


Figure 5. 12: Representation of mode shape corresponding to the diagonal line on dispersion relations

Figure 5.12 represents the mode shape of one of the diagonal lines on the dispersion relations of the bare beam unit cell analysis. As seen in the figure, the beam does not illustrate any mode shapes through the length of the beam but shows the mode shape through the thickness, which is not the interested mode shape in this research.

Periodically Arranged Single Resonator on Beam

A single resonator is attached to the unit cell (as cluster of resonators) of the bare beam at the central position in order to study impact of these resonators on the dispersion relations of the beam. Since the beam acts like a resonator, the impact of the attached resonator has

shown coupled resonator properties; this, also, will be investigated in Chapters 6 and 7. The solutions for the Bloch wavenumber (k) are reduced to smaller resonance frequencies in the case of resonator attachment(s). Although the eigenfrequency of the resonator is a little higher than the beam eigenfrequency, specifically at the third mode of the unit cell, the coupling between the resonator(s) and the beam is in good agreement in terms of the mode shape and the eigenfrequency level, which results in a reduction in the eigenfrequency ratio.

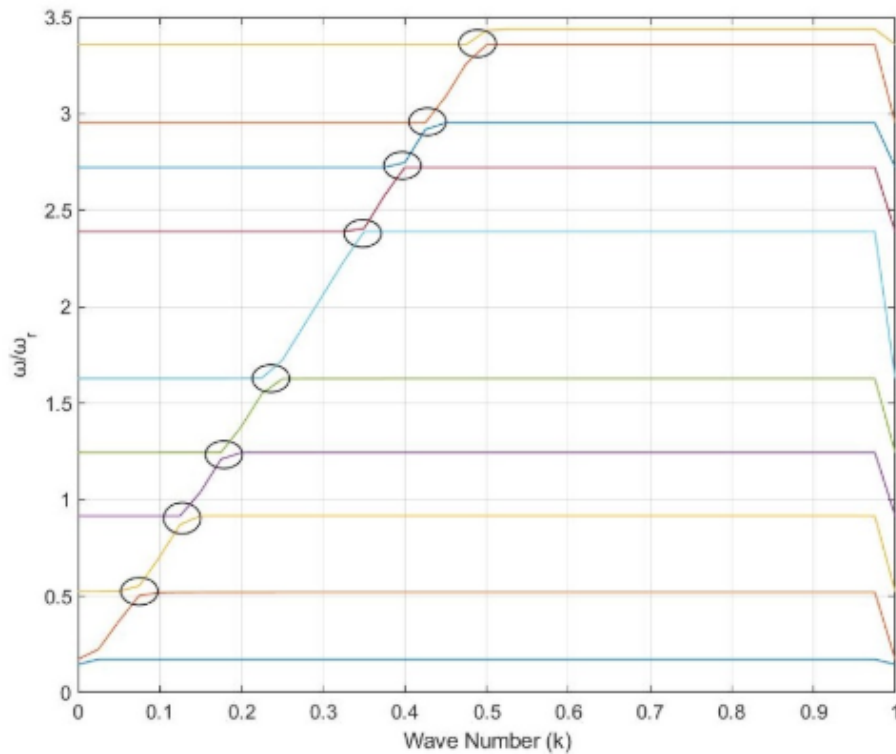


Figure 5. 13: Dispersion relations of single resonator attachment on bare beam unit cell modelling

In addition to the coupling between the resonators (the beam and the attached resonator), there are noticeable gaps in the dispersion relation Figure 5.13 which can be observed through tracing the diagonal lines as noted earlier. In fact, these lead to the conversion points which would provide proper bandgaps in case of removal. Even though there are discrete gaps, they represent the stopband properties of the total system where there is no wave propagation or interested frequency response from the structures. Similar to the bare beam unit cell analysis, the discrete stopband areas in the dispersion relations have a unique behaviour with a complicated (undesired) mode shape and their dynamic relations, as shown in Figure 5.14 below.

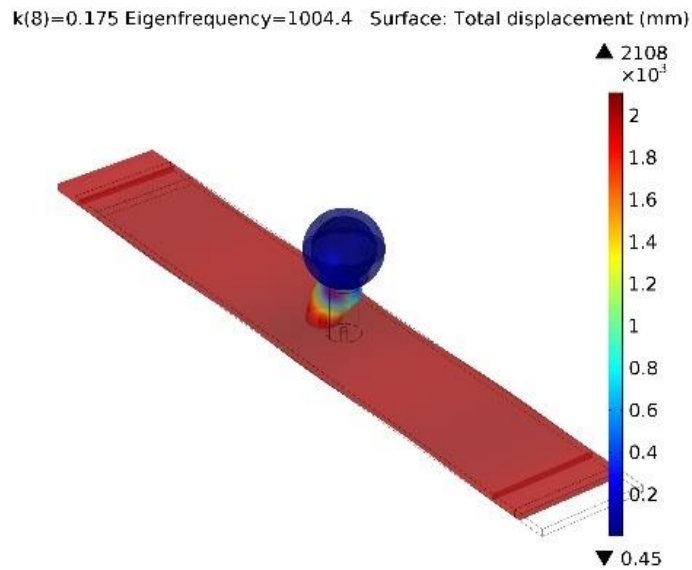


Figure 5. 14: Corresponding mode shape in the diagonal line on the dispersion relation

The elliptical shapes in Figure 5.13 (and more in the future figures) are used to define the conversion points in the dispersion relations. The conversion means that there is mode-changing behaviour at these points. Thus, the modes on the dispersion relation start from the bending mode, continue with the gap area which includes the whole unit cell mode through the thickness (thickness mode), make contact for a mode conversion point, and follow with another bending mode.

Periodically Arranged Multiple Resonator on Beam

Multiple-resonator placement on the bare beam unit cell is another research idea to investigate the coupling phenomena between resonators in the unit cell. Since the bare beam as a unit cell shows resonating properties and provides a discrete number of stopbands in addition to the proved relation with the resonator attachment, multiple resonators placed on the beam unit cell are expected to provide additional stopbands. Therefore, two, three, four, and five resonators have been placed on the beam unit cell as shown in Appendix 5.3 (in Figure A5.2). Figure A5.2 illustrates the thickness mode of each resonator arrangement on the 1D-periodic arrangement while showing 90 mm arrangements of the resonators as given in the upcoming examples. The dispersion analysis has been analysed through the same numerical analysis strategy explained in the previous infinite structure modelling.

Conversion of modes through the dispersion lines is expected since the beam is not conditioned to be deformed as in these conversion areas.

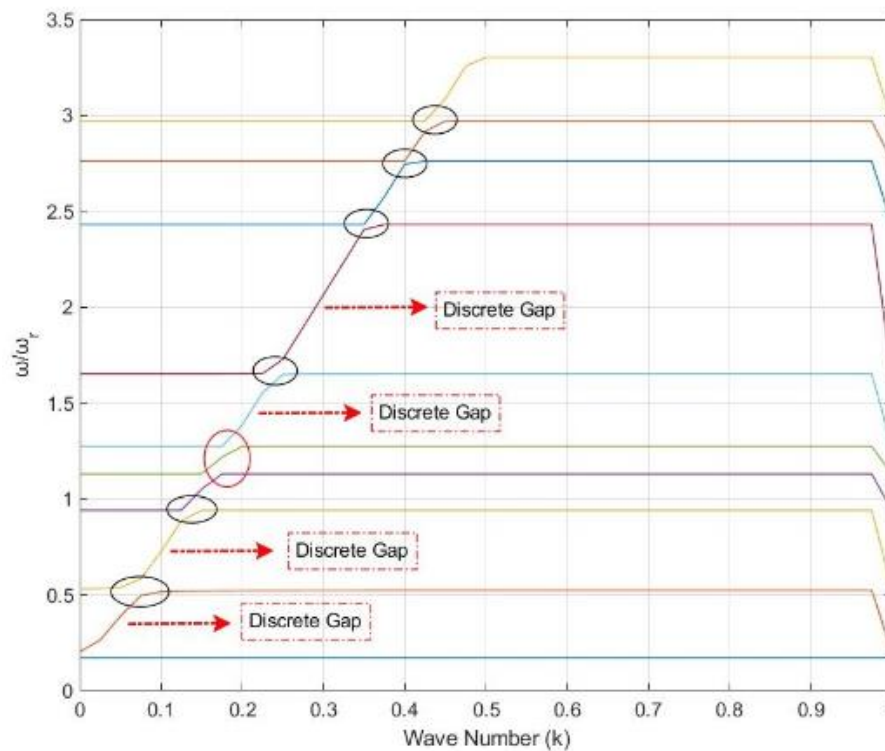


Figure 5. 15: Dispersion relations of double-resonator attachment on bare beam unit cell modelling (d=30 mm)

In the first example, a two-resonator has been attached at a 30 mm distance from the centre of the unit cell. Figure 5.15 represents the dispersion relations for the two-resonator attached unit cell. Several dispersion lines show the bending mode of the resonator attached system. A discrete number of gaps, which are the stopbands, are observed in two-resonator with this specific arrangement option. The beam and attached resonators do not allow frequency sweep or wave propagation at these discrete positions. The second mode frequency ratio has been increased, as seen from the dispersion relation at $k=0$ and $\omega/\omega_r=0.5$. Even though the frequency ratio at the third mode is not changed, the number of dispersion curves increased in the frequency ratio interval between 0.5 and 1.5 which means there are more tuned resonators attached to the beam.

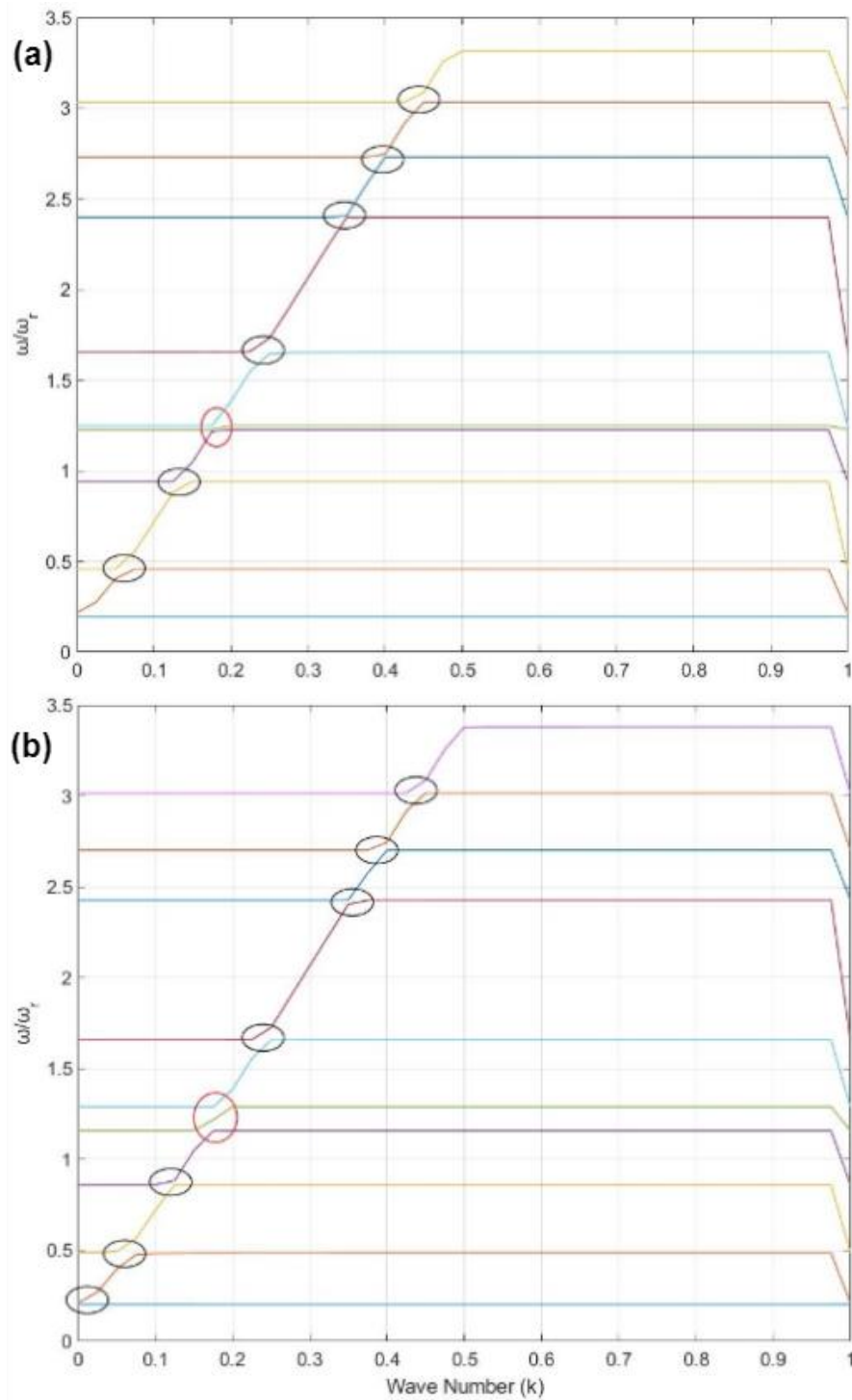


Figure 5.16: Dispersion relations of double-resonator attachment on bare beam unit cell modelling: (a) $d=90$ mm and (b) 130 mm

The second example of the two-resonator attached symmetrically around the centre of the unit cell (Figure A5.2) has been analysed using 90 mm between the resonating structures. Figure 5.16-a provides information of the dispersion relations of the two-resonator

attachment. Compared to the previous example, this arrangement has closer dispersion lines and smaller frequency ratios between $\omega/\omega_r=[1-1.5]$, influenced by coupled resonators. In addition, strongly coupled resonators' behaviour appears between $\omega/\omega_r=1$ and $\omega/\omega_r=1.5$ given in the red-elliptic area. Conversion between the mode shapes is highlighted using the black ellipses on the dispersion figure. Comparing the red ellipse with the black ones, the resonators show tuning through all lines. However, strong coupling is only observed within this frequency band which results in closer dispersion lines. The discrete gaps are observed in this figure with changes at the level of discrete stop band sizes. As discussed in Figure 5.10 in the case when thickness modes are not excited the dispersion diagram will demonstrate fully formed stopbands.

When two resonators are attached at 130 mm distances from the centre of the beam (Figure A5.2-a), the dispersion relations are similar to the case when the resonators are 30 mm apart (Figure 5.16-b). This is because the resonators are close to each other in the first case, where they behave like one resonator at the centre where the antinode of the beam is placed. Similarly in a 130 mm distance case, the resonators are placed close to another antinode point. Also, the dispersion figures demonstrate the presence of the conversion points between two following dispersion lines which are in some cases separated by a gap. The gap around the conversion points, which has already been noted in the previous results, would be eliminated using finer increments in the Bloch wavenumber (k) steps while setting the analysis.

In a general evaluation for two-resonator attachment on the beam-sized unit cell, a symmetrical arrangement increases the opportunity of modifying the stopband area to lower frequency ratios.

Figure 5.17-a contains the dispersion lines acquired from the three-resonator attachment at a 90 mm distance from the centre of the unit cell. There are three resonators in this example (Figure A5.2-b), and one of the resonators is placed at the centre of the unit cell. Increased number of resonators impacted the second mode shape with an increased frequency ratio, which might be related to the centrally positioned resonator. There is a widened stopband area on the fourth dispersion line. Basically, only the red-elliptical-shaped area has shown a strong coupling between the resonators; thus, they showed closer dispersion lines.

Conversion of the modes between $\omega/\omega_r=1$ and $\omega/\omega_r=1.5$ demonstrates excellent close relations. This might result from the coupled resonator in the system (the unit cell itself and the attached resonators).

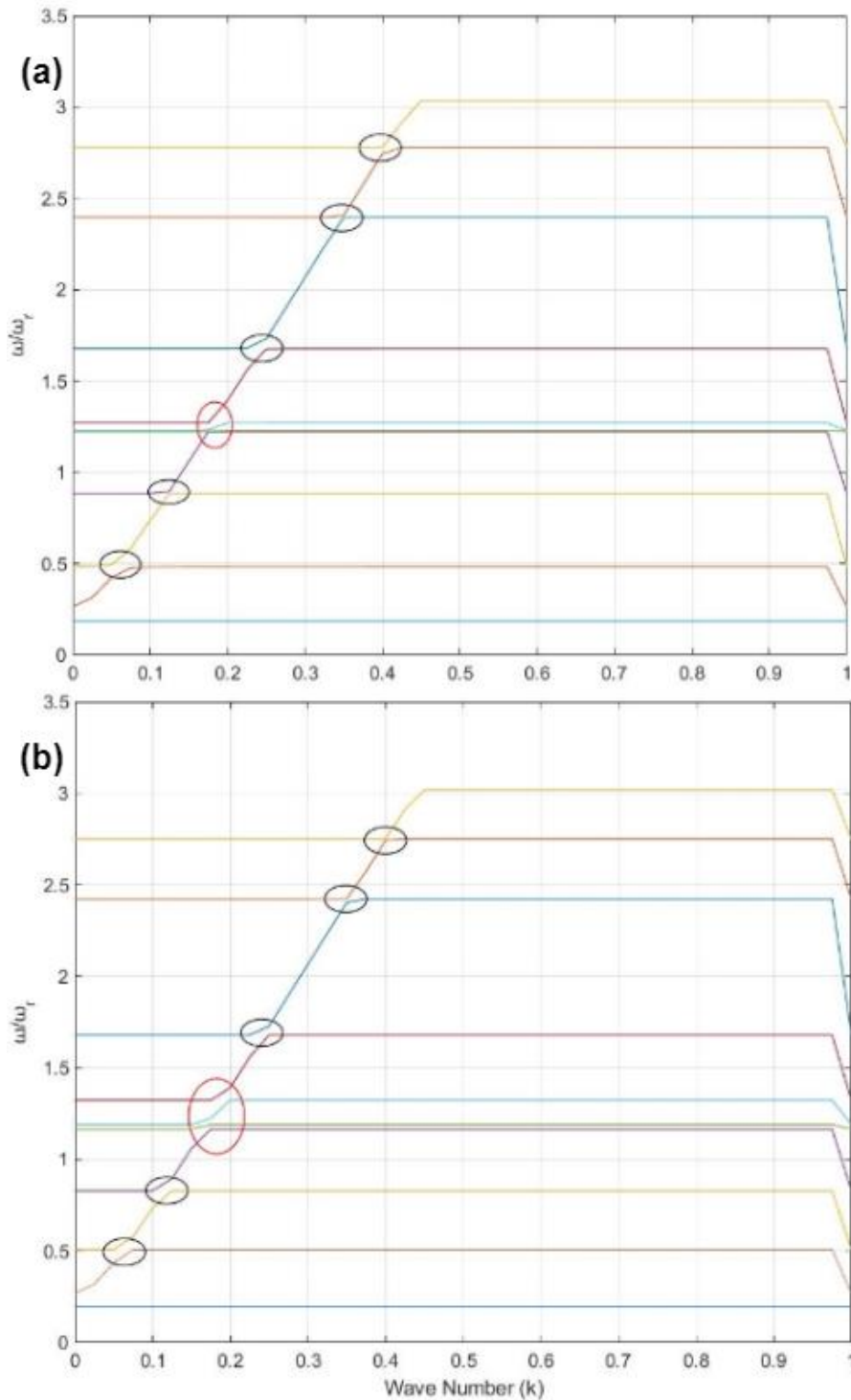


Figure 5. 17: Dispersion relations of three-resonator attachment on bare beam unit cell modelling: (a) $d=90$ mm and (b) 130 mm

Three-resonator attachment with 130 mm distances on the beam-sized unit cell is increased the frequency ratio (ω/ω_r) of the second and the third mode shape solutions (Figure 5.17-b). Although the number of solutions in $\omega/\omega_r=[0.5,1.5]$ is equal to the previous case (Figure 5.17-b), there are gaps between the dispersion lines; it appears to be the coupling is weakened in this arrangement. This additional solution in that range results from the unit cell's resonating properties which shows similar eigenvalues to the tuned resonators on the unit cell. Accordingly, the resonators (the beam and the resonators) demonstrate excellent coupling.

In general, even though there is no symmetrical arrangement as an infinite structure, the periodic arrangement of resonators and their symmetrical arrangement on one unit cell shows tuned resonator's behaviour. Therefore, the number of resonators on the unit cell significantly impacts the dispersion relations.

The beam-sized unit cell with four resonators have been analysed for the dispersion relations (Figure A5.2-c). In this case, there is 70 mm distance for the resonator arrangement which is from each other and the centre of the unit cell. Figure 5.18-a has interestingly reduced frequency ratio on the third dispersion line. From the third dispersion line, there are tuned resonator solutions through $\omega/\omega_r=1.5$. This improves the discrete stopband opportunity while increasing the number of solutions because of the elevated number of resonators on the unit cell and their coupled dynamic properties. Also, these eigenfrequency solutions on the dispersion figure corresponds to reduced Bloch wavenumbers (k) than a smaller number of resonators attached cases. This is an observation related to the whole structure dynamic behaviour, which means that almost all wavenumbers have a representative eigenfrequency solution, specifically at the lower frequency ratios. In addition to this information, conversion points do not show empty areas which indicates the resonators and the unit cell demonstrate great coupling which resulted in immediate mode changes.

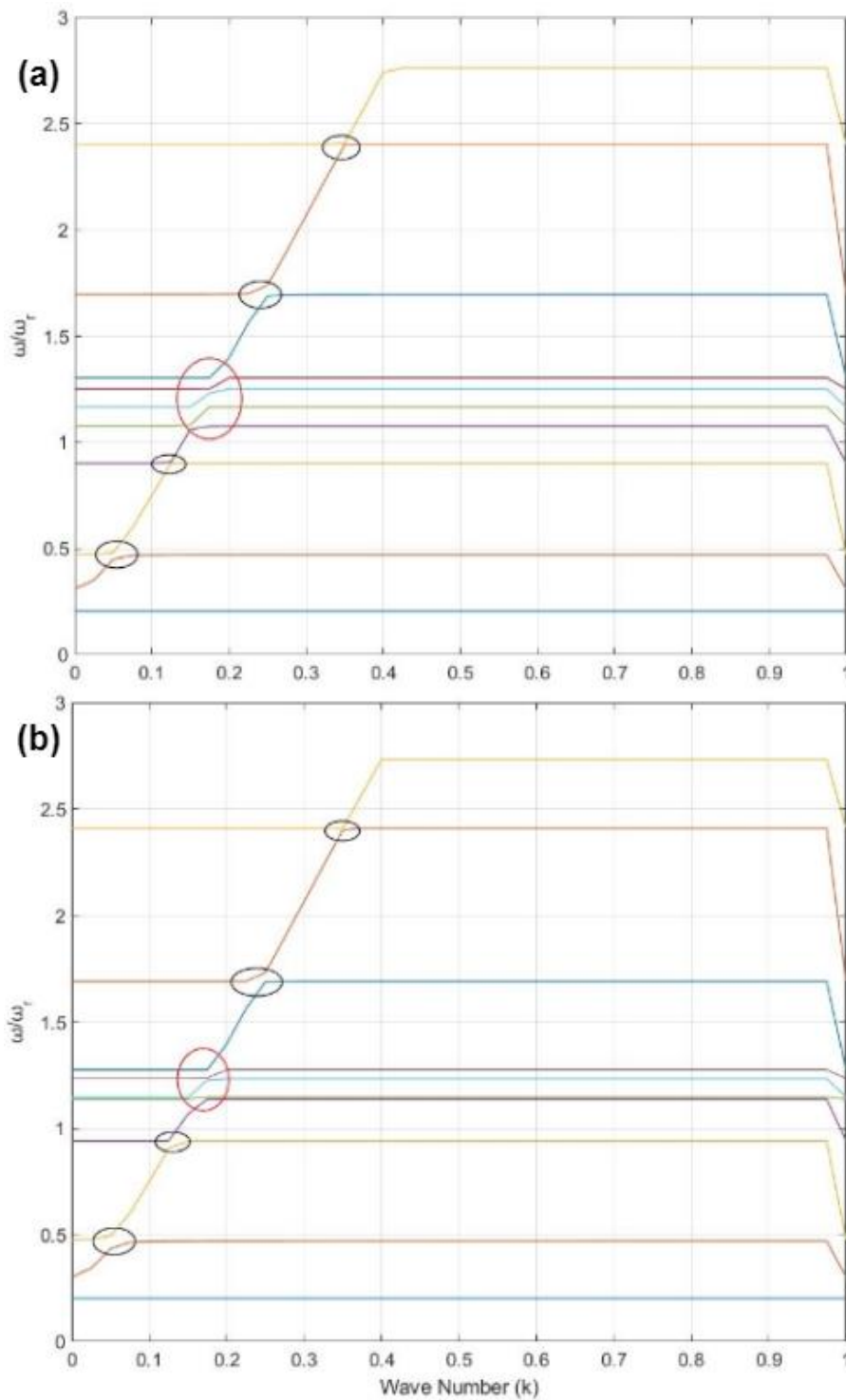


Figure 5. 18: Dispersion relations of four-resonator attachment on bare beam unit cell modelling: (a) $d=70$ mm and (b) 90 mm

Four-resonator with 90 mm distance on the beam-sized unit cell as shown in Figure 5.18-b has shown similar dispersion properties as in the previous case because of the coupled resonators on the unit cell (Figure 5.17-b). In fact, a specific area in the red ellipse shows

strongly coupled resonators and there are increased discrete frequency stopband properties starting around $\omega/\omega_r=0.5$.

In the case of five-resonator attachment on the beam unit cell with a distance of 70 mm from the centre of the unit cell by adding one resonator at the central position (Figure 5.19-a), the first three mode shapes have been in a similar trend in the dispersion relation analysis as in the previous case (four resonator attachment, Figure 5.18-a). As mentioned before, the diagonal lines through the dispersion relations illustrate the discrete stop band positions. These are widened by reducing the lower bound frequency ratio in this case. Therefore, it can be assumed that there is an improved stopband opportunity where the waves do not propagate.

Figure 5.19-b illustrates the dispersion relations of the five-resonator with a 90 mm distance on the beam-sized unit cell (Figure A5.2-d). This is a complete case where the resonators are periodically placed on the unit cell. In this case, one is placed in the central position, and the other four are placed at 90 mm and 180 mm of the beam on both sides with no extra area left at the end of the beam. According to the case, the small frequency ratios (ω/ω_r) and related mode shapes have shown similar behaviour as shown in Figure 5.18-b. However, there is an area which includes six dispersion lines with a strong coupling because of the resonators on the unit cell (given in the red elliptical area). This means there is an enhanced conversions provided by the resonators in the system (beam and resonators). Compared to the previous case, the lower bound of this area is taken to a higher frequency ratio, which might be because of the placement of five resonators including the centrally positioned one.

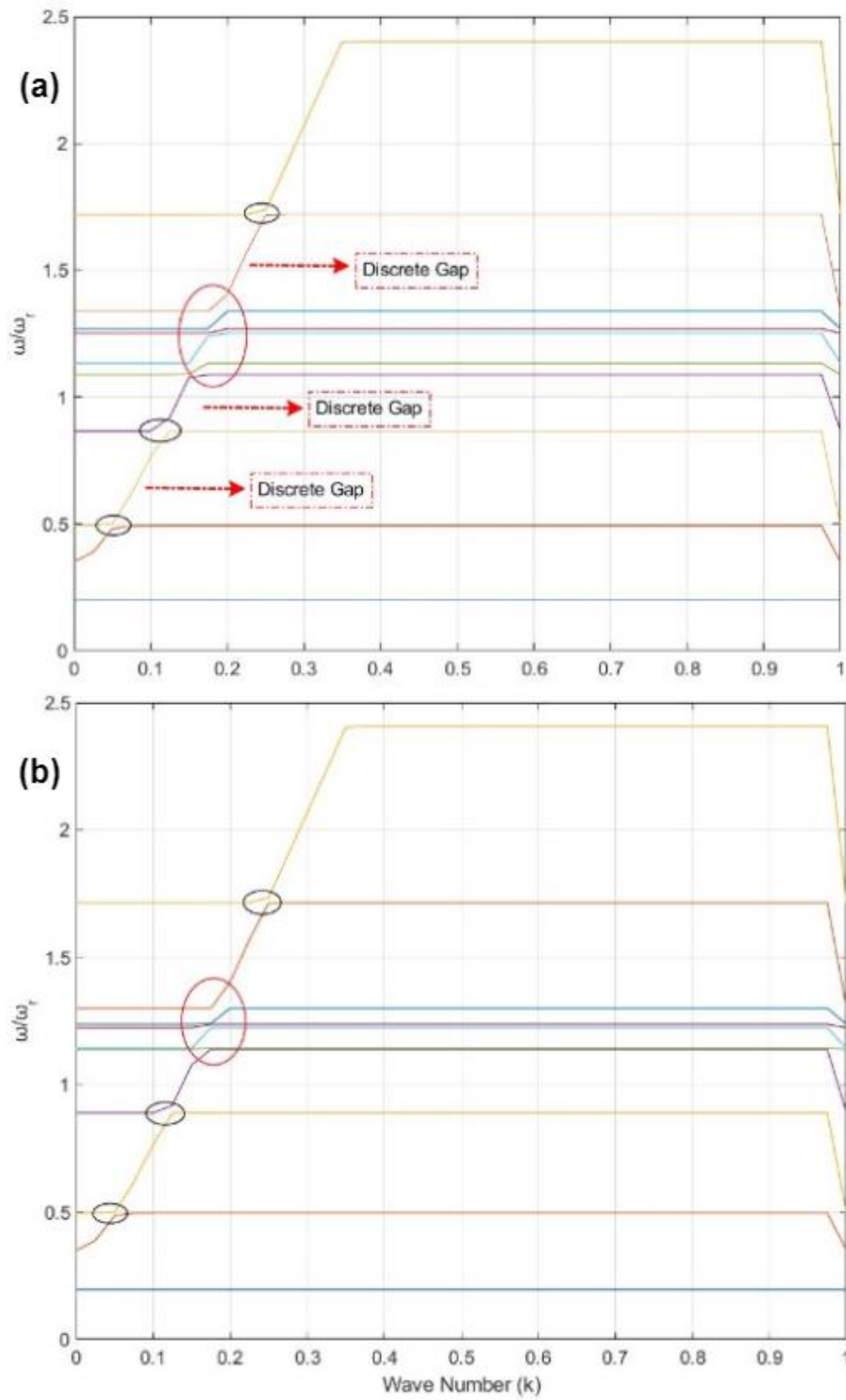


Figure 5. 19: Dispersion relations of five-resonator attachment on bare beam unit cell modelling: (a) $d=70$ mm and (b) 90 mm

In this part of the chapter, original size of the beam has been used as a unit cell to analyse the dispersion relations caused by the cluster of resonators. The beam is modelled as in a periodically arranged structure, and resonators are attached to the beam in various placements. The outcome of this study is that an increased number of resonators on the unit cell controls the low-frequency ratio dispersion lines. These low-frequency ratio dispersion lines have shown similar behaviour in the variety of four-resonator attachment cases, which has not been changed in the other cases. However, depending on their attachment distances, an increased number of resonators have illustrated wider discrete stop band properties and more coupled resonances.

5.3- Conclusion of the Chapter

The unit cell modelling have shown that there are longitudinal and transversal modes dependent on the size of the unit cell. Resonator attachment has modified the dispersion relations of the unit cell. For instance, the dispersion curves and associated stopbands have been taken to low-eigenfrequency levels because of the resonator impact. In addition, there has been coupling between the system elements and shifted eigenfrequencies.

The beam modelled in the previous chapter has been studied as a unit cell to evaluate the dispersion relations and impact of resonator multiple arrangement. It was expected to see the individual resonance properties of each resonator and the beam unit cell itself. However, these results have shown conversion impacts in addition to the expected results. Weak and strong coupling areas have been observed in the beam unit cell analyses. According to the dispersion figures, diagonal lines are closer when the number or resonator is increased on the beam. This explains the resonators impact on formation of the dispersion lines and modified gaps.

Overall, using a resonator on a host structure either results in resonance around the resonator eigenfrequency or lead to a higher eigenfrequency than the original resonator natural frequency provided coupling phenomena on the dynamic properties. In addition, the resonator established eigenfrequency shifting behaviour while illustrating bandgap opportunities. Here, in this chapter, in addition to these options, it has been shown that there

is conversion between structure modes. The assumption has been made that if some modes are not excited in the structure the whole structure would provide a complete bandgap.

To conclude, this study is an example of the evaluation of coupling between the structures and controlling the modes of the host structure by using a specific arrangement of resonators which have natural frequency similar to the host structure.

Chapter 6: Dynamic Absorption Using Locally Resonating Structures

This chapter is prepared to introduce structural vibration and resonance relationships. Locally resonating structures are introduced to explain the coupling between the resonators and their tunability to reduce the structural vibration impacts. Through the end of the chapter, primarily introduced resonator geometry is used for the numerical and experimental analysis for a specific frequency range and individual eigenfrequency analysis.

6.1- Vibration Absorption Using Locally Resonating Structures

Damping applications using resonating structures might be similar to the traditional absorption techniques [176],[177]. Metamaterials have been specified in periodically arranged structures to treat the solid structure in larger arrangements. Therefore, stating the differences between the vibration absorption techniques and metamaterial application might be hard because of the small-sized periodic arrangement on the beam used in this research. However, if the focussed frequencies are limited to the standing waves, then using a single subunit to define the metamaterial would be enough since this arrangement would illustrate the band properties [178]. Otherwise, travelling waves would require a larger structure and more subunits to dissipate the energy and observe the band properties. These situations have been detailed in the previous chapter.

According to the given explanations about the metamaterial applications using finite structure modelling, a pretty long structure and many absorber arrangements are required. However, in the case of a relatively small-sized structure and a smaller number of absorber arrangements, the main structure's standing waves and mode shapes would be beneficial in comparing absorbers' impact. In general, placing the resonator at the point where the acceleration and displacement are the highest in certain mode shapes would help reduce the frequency response at those frequency levels. Therefore, placing the resonator at the antinode points will be beneficial. On the other hand, placing the resonator where the amplification and displacement are the lowest, which is zero, would not be useful for energy distribution. Thus, the resonator placed on the node points and closer to the nodal points will

not be helpful in terms of absorbing the excess energy from the main structure. The chapter results have been analysed and evaluated according to the information.

In this research, the interested frequency range is at the lower bands of the main structure, and the base (main) structure modes and standing waves on the structure are studied with and without resonator attachments. The base structure has been introduced in Chapter 4 and used in this chapter in numerical and experimental studies. The resonator properties are evaluated experimentally to define individual eigenfrequency properties. However, there might be differences between the resonators after the production. The numerical and experimental analysis options study single and multiple resonator attachments with various placing options. The result prepared according to this research plan are introduced in this chapter.

6.2- Numerical Analysis of Finite Structure Modelling

Single Resonator Impact on the Base Structure

Resonator material properties have been searched using a rectangular sample through the DMTA test, detailed in Chapter 4. Material properties have been evaluated and decided for the 3D-printed resonator in order to feed the numerical studies. A locally resonating structure is thought to be placed on the bare beam to analyse the energy dissipation. Bare beam numerical analysis details and results have been given in Chapter 4. Analyses using resonator attachment are prepared by placing the single resonator at the centre of the beam, and its place is changed through the length of the beam by 10 mm distances.

Figure 6.1 contains single resonator attached beam trends for three different resonator placement cases in order to evaluate their energy dissipation properties. The cases in the figure have been selected according to their benefits when placed on the bare beam. The resonator placements, $d=0$ mm, $d=70$ mm and $d=130$ mm, are the cases in which the beam has experienced the highest displacement values for specific mode shapes. Therefore, resonator attachment on or near these points is expected to benefit energy absorption and frequency response. FRF amplitude calculations in the frequency sweep analysis have been the same throughout this thesis. Inertance has been calculated for FRF representation using

the accelerometer and the force transducer data. As seen in the figure through the y-axis (FRF amplitude representation), these single resonator placements have impacted the amplitude of the beam in the first mode. Also, the resonator attachment reduced the response of the beam on the third mode and the shifted eigenfrequency levels.

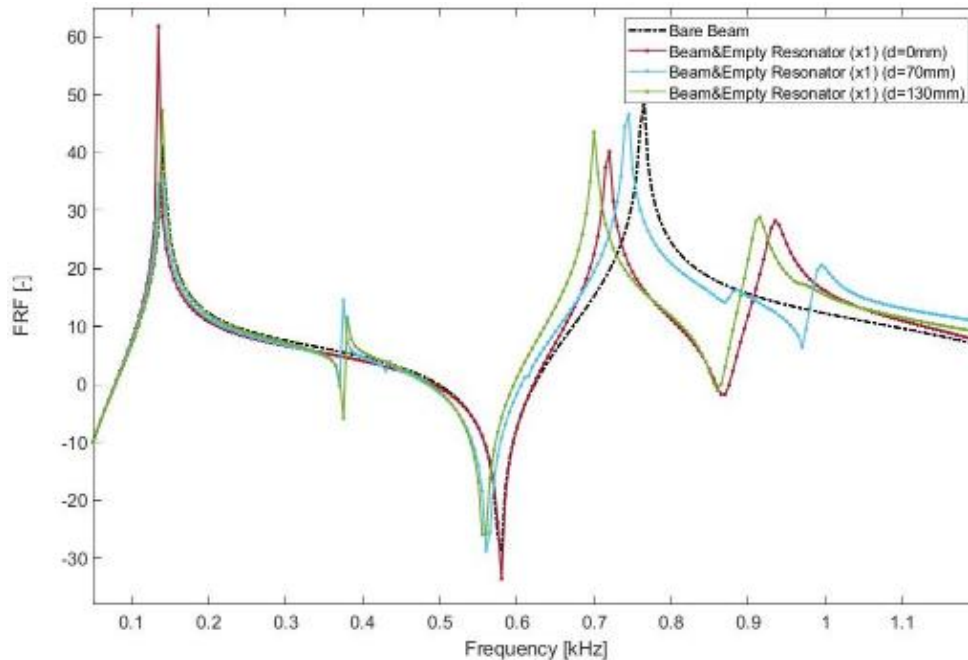


Figure 6. 1: Frequency response of empty single resonator attachment on the beam

Resonator attachment has provided an additional mode around 0.9 kHz. Since the resonator impacted the beam by taking the beam mode to a lower frequency level, there is a gap opportunity on the third mode of the bare beam. This result has shown the impact of the resonator on the beam as reduced eigenfrequency and observed gap even in the single resonator case.

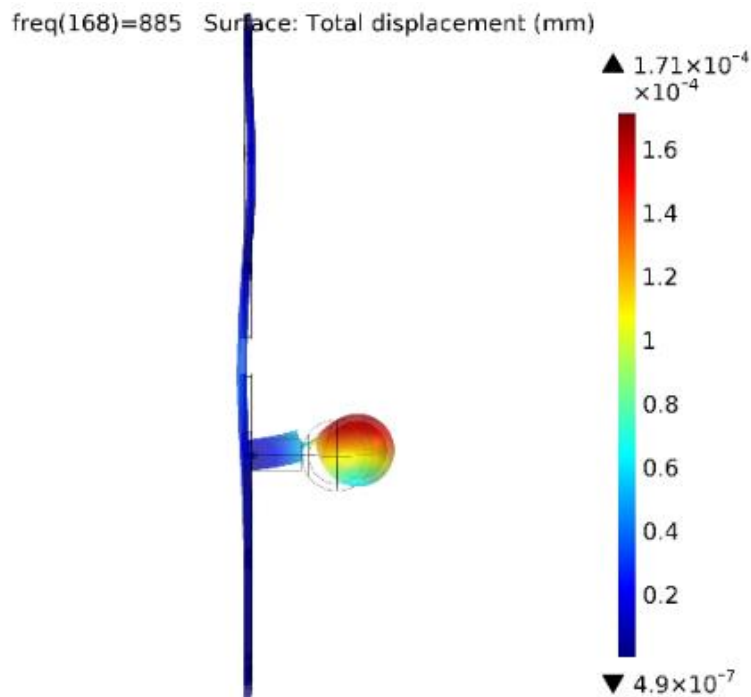


Figure 6. 2: 70 mm attachment resonator impact on the beam

Specifically, the resonator placement at 70 mm has an additional peak in the frequency response. Evaluation has been made at this frequency where this additional peak appears. According to this, there is one resonator mode at 885 Hz (Figure 6.2). Following mode shape at 995 Hz includes the mixed mode shape of the beam and the resonator.

Multiple Resonators Impact on the Base Structure

In order to search resonating structure relations with each other and the bare beam, multiple resonator attachments through the beam are studied numerically. The resonators are placed through the length of the beam over both sides at 10 mm distances. The figures given in this part have been prepared by selecting the most beneficial or the least beneficial attachment options. Tunability of the resonators and energy absorption are evaluated in the figures given in this part of the chapter.

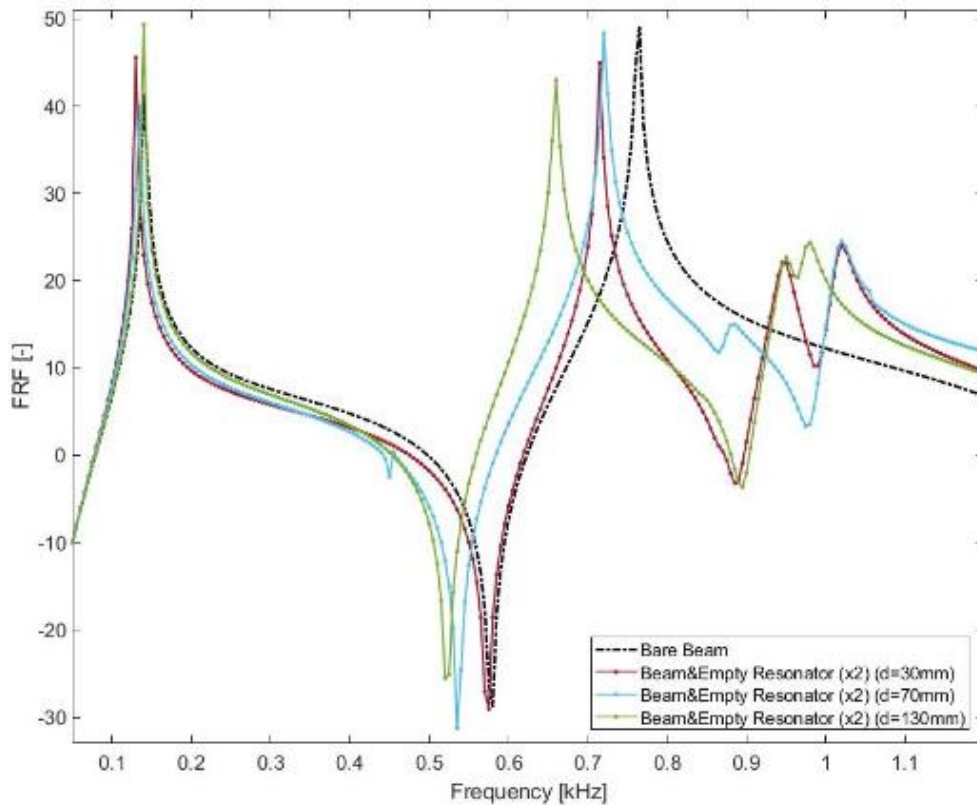


Figure 6. 3: Frequency response of two empty resonators attachment on the beam

Figure 6.3 has been prepared using the two-resonator attachment cases on the bare beam. Since the geometry of the resonators, the centre of the beam must be empty; however, the closest placement for the resonators is 30 mm off from the centre. The first peak is almost the same for all arrangements since the mass of resonators is lighter than the beam's mass, so there is almost no mass effect on the FRF. Also, the second mode that appeared in the previous case, around 0.4 kHz, disappeared because of the resonator arrangement on both sides of the beam. The third mode shape of the beam has been reduced to a lower frequency level for each arrangement; in fact, the least eigenfrequency has been recorded from 130 mm distance for the resonators. The frequency response of the beam is at high levels, which is the beam mode shape in general, and the resonators have shown tuned resonators behaviour in higher frequencies. In addition, the trend for each arrangement includes three peaks for the interested frequency range, which is assumed to be the individual resonator's impact, as well; each mass-spring system must have an eigenfrequency as a dynamic property.

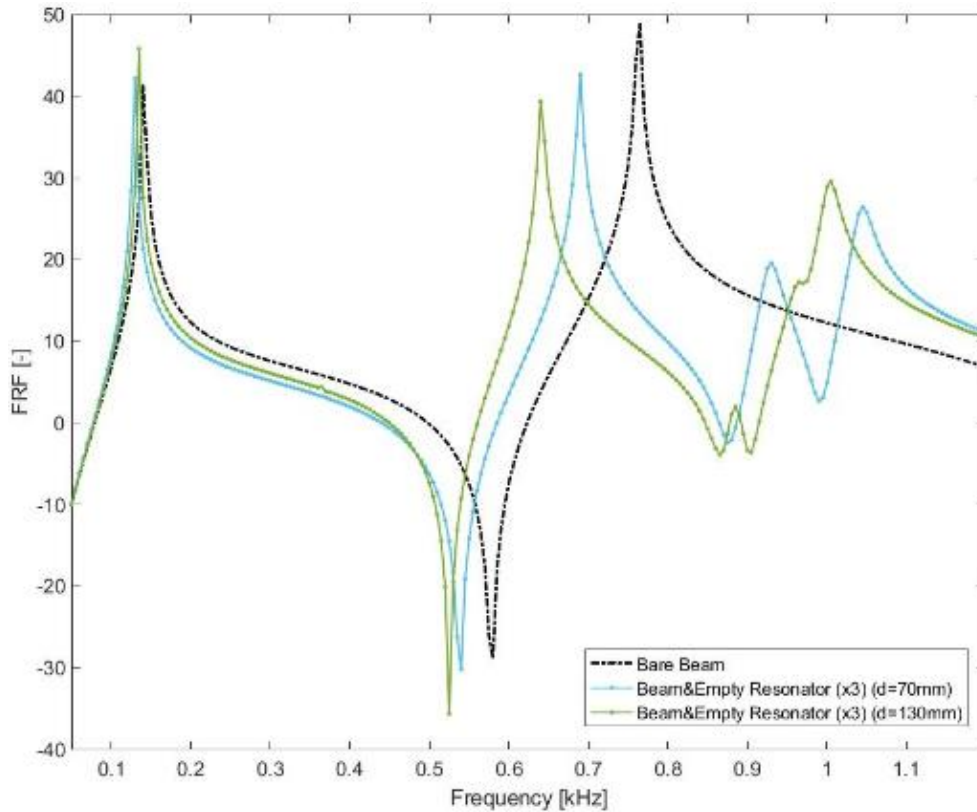


Figure 6. 4: Frequency response of three empty resonators attachment on the beam

Figure 6.4 is prepared using three-resonator attachments on the beam, and a comparison has been made with the bare beam properties. Because of the resonator geometry, a 30 mm distance between the resonators placement has not been an option in this case. There is a centrally positioned resonator in the three-resonator arrangement. According to the 70 mm arrangement, resonators have impacted the system by reducing the eigenfrequency level of the bare beam, which corresponds to the coupling between the beam and the resonators. Compared to the previous case, the centre's resonator has resonance properties at 930 Hz and 1045 Hz, where all resonators have been coupled at these frequencies. The results in this figure resemble the add-up formation of the single resonator and two-resonator attachment in Figures 6.1 and 6.2.

The antinode point attachment (130 mm) has been the most beneficial arrangement regarding resonator coupling and eigenfrequency reduction (Figure 6.4). The frequency level of 640 Hz is where the central resonator and the beam experience coupled resonance. It has been expected that coupling between all structures through the frequency ranges. On the other hand, this arrangement includes antiresonance in the frequency response, which

means the strong amplification on the beam has had a controversial impact on the frequency response of two of the resonators, which is observable at around 900 Hz. This arrangement has shown more coupled resonator properties in addition to the experienced antiresonance.

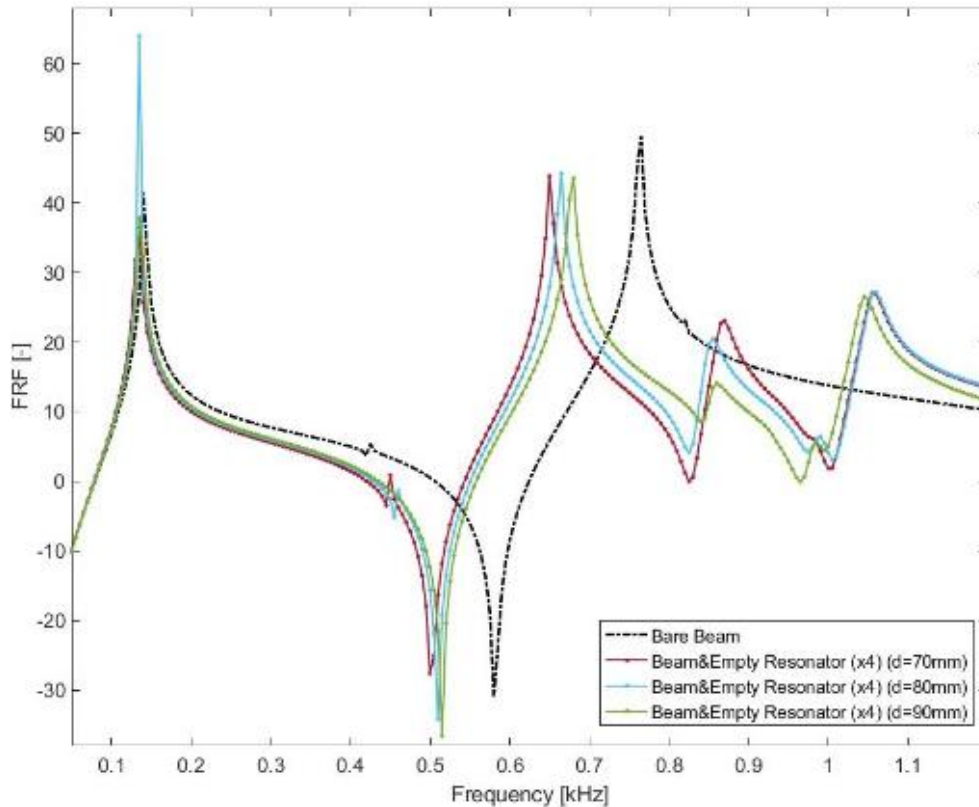


Figure 6. 5: Frequency response of four empty resonators attachment on the beam

Four-resonator attachment has been exemplified in Figure 6.5 by using 70 mm, 80 mm and 90 mm distances applied between the resonators. Since the number of resonators attached to the beam is an even number, the centre of the beam is left empty in all four-resonator arrangement cases. The arrangements of the resonators are similar in these comparative cases; however, the number of peaks for the 5-DOF system is a maximum of four after 500 Hz. It might be related to the antiresonance since there are examples of antiresonance in the figure. This also might be related to the tuned resonators, which shaped four peaks for the eigenfrequencies. The first peak after 500 Hz is the coupled beam-resonator mode, assuming the resonators couple with each other.

In fact, checking the mode shapes of these arrangements has shown that there were always either two resonators coupled with each other or the beam. Also, the number of peaks might

be related to the resonator's behaviour as coupled masses. In addition, using multiple resonators at a specific distance provides a gap where the bare beam third mode shape appears. Also, 70 mm in the previous cases is not as beneficial as in this arrangement. The reason behind this is to have two resonators placed at 70 mm, like the previous analysis, and there are two other resonators placed at 140 mm, which is close to the antinode point of the beam. This arrangement controls the beam, reduces the amplitude of the frequency response, and reduces the eigenfrequency of interest for a whole structure.

Five-resonator attachment on the beam has been studied in an arrangement similar to the previous one (the four-resonator case, Figure 6.5), and frequency sweep trends are shown in Figure 6.6. However, in this case, a resonator is placed at the centre of the beam. When the resonators settle in a close position, there is a mass and resonance impact on the first mode shape. The beam resonance properties have been reduced to the lower eigenfrequencies, while the presence of the resonators has slightly impacted the FRF amplitude. There is a wider stopband with no high amplitude properties in the frequency response using this five-resonator arrangement. The behaviour has been about the coupling between resonators and the beam when mode shapes are checked over resonance frequencies.

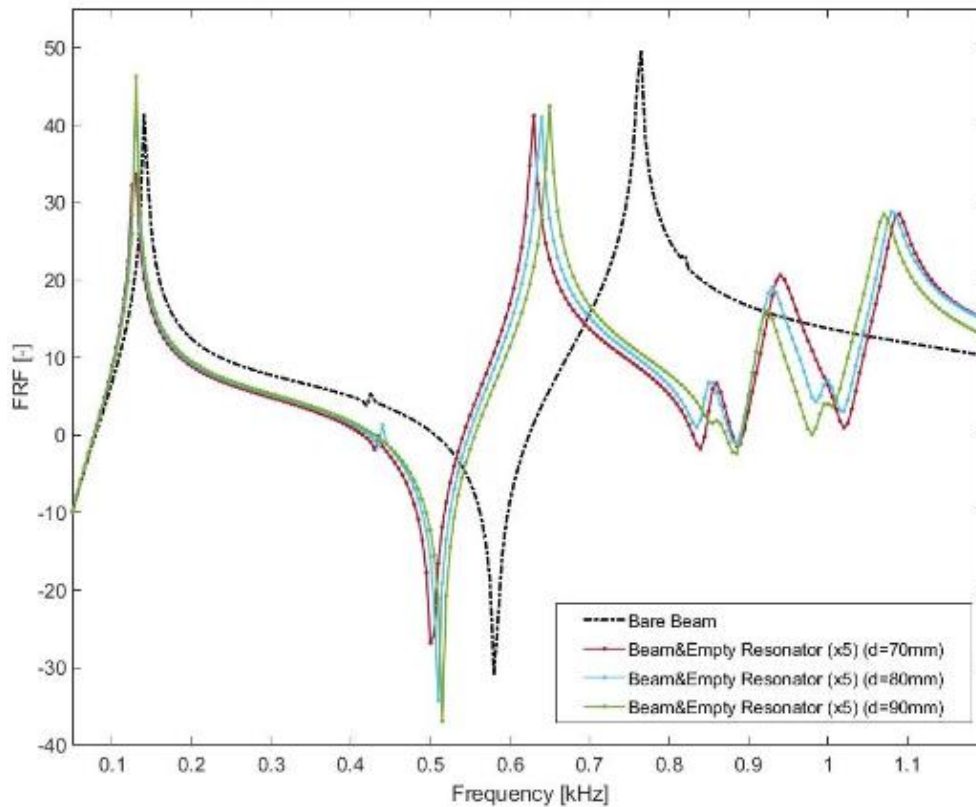


Figure 6. 6: Frequency response of five empty resonators attachment on the beam

Compared to all other resonator arrangements, an increased number of resonators reduced the resonance frequency, and coupled resonators showed up at slightly higher frequencies, providing a gap between 0.6-0.95 kHz. Only the three-resonator arrangement with 130 mm distance resulted in a wider stopband property. On the other hand, this arrangement includes antiresonance in the frequency response, which means the strong amplification on the beam has had a controversial impact on the frequency response of one of the resonators, which is observable around 0.85 kHz and 1 kHz. As a result of this subchapter, resonator impact on the beam has been evaluated and proved that the resonator in the multiple arrangements would provide a frequency gap at the third bending mode of the beam since their periodic arrangement. Even though this arrangement has unique periodic properties, the resonators have tuned behaviour and impact the way of the frequency responds.

6.3- Generating a Frequency Gap Using Resonators

In the previous subchapter numerically analysed finite beam with single and multiple resonator arrangements have been analysed close to the centre of the beam where the

excitation hits the beam. In this subchapter, the same analysis configurations are evaluated at another point readings away from the beam's centre.

The idea behind comparing the readings from two different positions is to evaluate since the excitation might impact the reading from the accelerometer in the first case (close to the centre). However, since the bare beam has split toward the length of the beam, the new reading point is not in the middle of the beam. Therefore, it is off centre by 5mm near the beam's end. Figure 6.7 is prepared using different resonator composition results of readings from the point away from the centre of the beam.

Single resonator attached beam results, centrally positioned resonator and the resonator at 70 mm cases, have shown similar frequency response properties compared to Figure 6.1. The second bending mode, around 0.4 kHz, is not much visible as in Figure 6.1. The reason behind this might be the position of the reading point. However, empty resonator 70 mm placement has experienced resonance at around 375 Hz, similar to the other resonator placement cases. The reading point for this case is at the antinode of the 375 Hz frequency ; therefore, the frequency response has been at high values for this specific case.

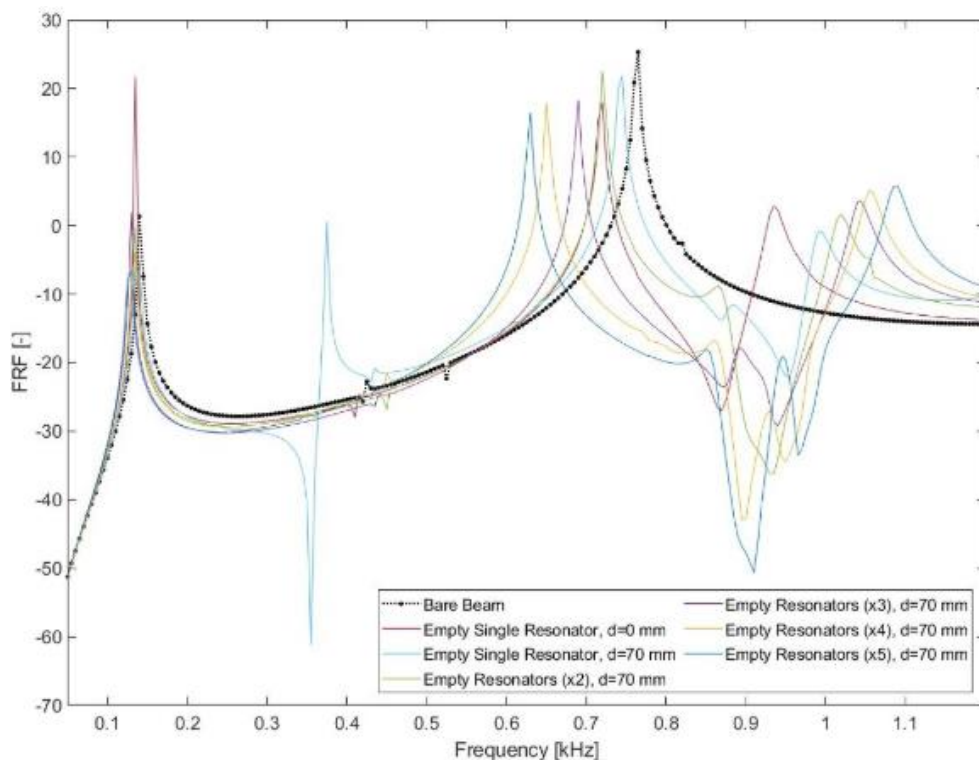


Figure 6. 7: Comparison of various cases by reading the acceleration away from the centre of the beam

Two-resonator with a 70 mm distance from the centre of the beam resulted in lower frequency response through the frequency sweep and similar peak frequencies according to the resonances performed on the beam. Compared to the reading around the centre of the beam (Figure 6.3), the response read between 0.85 kHz and 1.1 kHz has resulted in almost zero frequency responses. This means the beam experienced almost zero acceleration through the ends of the structure by the resonator attachments.

The result of the three-resonator with 70 mm distance placement showed that the frequency response through the end of the beam had been reduced compared to the central beam reading (Figure 6.4). Specifically, the reduction in the frequency response has been observed at the coupled resonator's impact area, around 0.9 kHz. According to this result, the resonator impact on the beam composed a kind of frequency gap around this frequency level. On the other hand, peak formations according to the resonances have shown similarities with Figure 6.4.

Four-resonator with a 70 mm distance composition has shown a frequency gap starting from the beam resonance frequency (0.65 kHz) to the coupled mode resonance frequency (1.1 kHz). In Figure 6.5, frequency response has shown great reduction within this frequency band, which shows the beam did not experience the forced vibration resulting in a bandgap.

A five-resonator with a 70 mm distance between the structures case has shown the beam has a great frequency gap, including the resonator's resonance. The bandgap formation starts from 0.6 kHz until 1.1 kHz. Compared to Figure 6.6, the frequency response of the beam has been reduced through the end when the reading is close to the end. Also, Figure 6.6 shows the coupled resonance around 1 kHz, which has not been read in Figure 6.7. However, the second bending mode frequency amplification has been recorded in this case, around 0.4 kHz. This is possibly about the reading point position, as detailed earlier.

The results in this section of the subchapter contain the comparisons of accelerometer readings from two different points on the beam. The mentioned figures for various cases have the frequency response trends of the accelerometer reading from around the centre of the beam. Since the excitation impact is at the centre of the beam and the excitation point corresponds to one of the antinodes of the beam, naturally, the structure experiences the

highest acceleration at this point. However, the idea was to receive reduced acceleration impact and it was decided to take the reading from another point on the beam. Therefore, the accelerometer reading point has been selected close to the end of the beam.

As a result of this evaluation, resonator placement on the beam has modified the frequency response as once more provided results support the findings and assumptions. Especially multiple resonators on the beam, which might be considered uniquely periodically arranged resonators, have shown a reduction in the frequency response. Another explanation for this phenomenon is frequency bandgap due to the array of resonators on the beam. Considering any larger beam and periodically arranging multiple resonators on that large structure would result in a bandgap. Similar analysis implications were studied in [179], [75] and [90]. In these studies, the mass ratio of the attached structures and the exciting structure has been studied at various levels and compared with each other's frequency response and the main structure's frequency response. In addition, these studies have been included with the various damping ratios, which will be explained in Chapter 7.

6.4- Validation of Base Structure Analysis

The bare beam, resonator, and attached beam properties have been simulated numerically, and results have been evaluated in Chapters 4, 5 and 6. These chapters include eigenfrequency responses, frequency responses and dispersion relations of these structures. Since the structural issue has been evaluated in many ways numerically, it requires an additional option to verify and validate the findings. Therefore, beam and resonators have been manufactured using structural steel (for the beam) and 3D printing of ABS (for the resonators).

Once the manufacturing process has been completed, the experimental testing rig has been prepared. The testing is planned to be used for the bare beam at first. Then the resonator placements in order to define their individual properties are planned. When these identifications are completed, the beam is planned to be used to evaluate the resonators and their tunability properties. The beam and empty resonators have been used in this chapter. Chapter 7 is dedicated to the granular structure attached resonator(s) in the experimental studies.

Numerical studies have included the eigenfrequency analysis in order to define the dynamic properties of the bare beam. In addition to the eigenfrequency solution of the bare beam, Frequency Response Function (FRF) is used to illustrate the system's response to the frequency sweep analysis. Excitation is applied at a minimal force from the centre of the beam, and response is recorded from another point close to the centre. FRF is calculated through the ratio of the response to the applied force on the beam. The force is applied to the beam at the central point (237.5 mm, 37.5 mm, 0 mm). The minimal force is decided to be such a small value to keep the particle damping application in the solid-like phase in the excitation procedure. This is experimentally validated by taking the force transducer and accelerometer data.

The force is applied through z-direction to the beam, and the acceleration data is captured from the point 5 mm away from the excitation point (237.5 mm, 42.5 mm, 0 mm). Applied frequency sweep is from 50 Hz to 1200 Hz with 5 Hz sweeping step. Figure 6.8 illustrates the experimental study scheme, which includes LDS V406 (by Brüel & Kjær) shaker, PA 100EC (by Data Physics) amplifier, Dytran 1053VX Force transducer, Dytran 3225F1 Accelerometer, PicoScope 2000 Oscilloscope, and a laptop to set up the software for the data analysis. The signal produced by the amplifier is processed through a Dytran 4102C power source unit which has connection with the PicoScope. PicoScope is connected to the laptop which has been designed to produce the frequency sweep analysis steps at a specific amplitude and with 100 kS/s sampling rate. The shaker produces the amplified force impact on the structure while the force transducer is measuring the applied force. The accelerometer takes the reading from the structure and the data from each reading component have been transferred to the laptop. No estimators were used when setting PicoScope for the experimental analysis. The accelerometer and the force transducer sensitivity information were set to increase the input quality from the data readings. Also, Hamming window was applied to prepare the raw readings for the spectrum analysis.

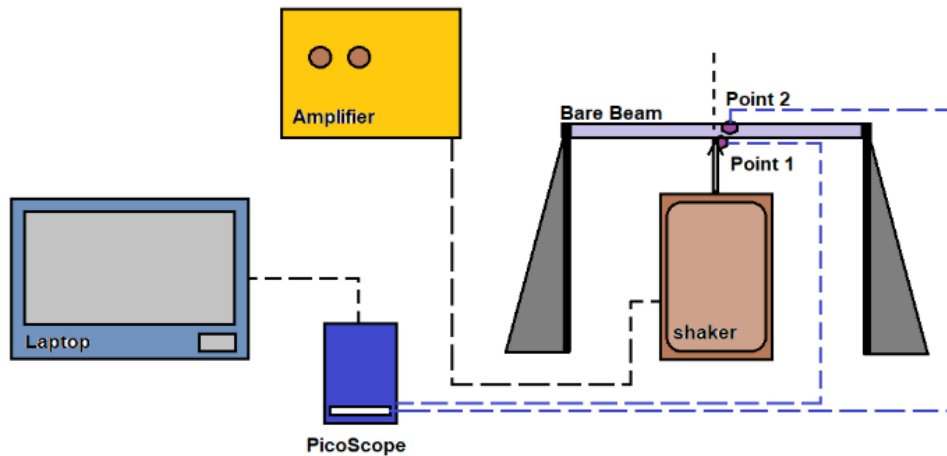


Figure 6. 8: Experimental rig diagram

The beam is produced using structural steel material after modelling it in SolidWorks 3D drawing software (Figure 6.9). Force transducer and accelerometer are attached to the test rig on Point 1 and Point 2 respectively as shown in Figure 6.8. There are four 10 mm holes at each corner of the beam in order to mount the beam on the experimental rig. Through the length of the beam, there are eight additional holes to fix the beam in smaller sizes for the sake of analysis aims (given in Chapter 4). For instance, the smallest size of the beam has been used in the experimental analysis of the resonators. By changing the setup, the beam would get opportunity to capture the resonators' eigenfrequency.

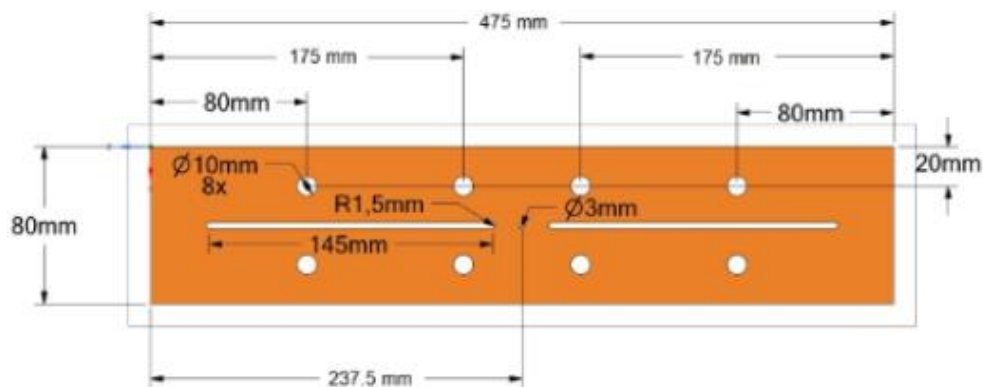


Figure 6. 9: Beam model for production

The beam has been mounted on the experimental rig using 10 mm nuts (x4), and the shaker is connected to a stinger to transfer the excitation energy to the beam. The shaker position in the research is through its vertical and lateral positions. The accelerometer is studied in two different beam points for each study option. This has been a required step in the

experimental analysis since the beam has multiple physical inclusions in the frequency response. Therefore, the FRF might include additional beam modes depending on the data recording point.

The accelerometer sensitivity is 10mV/g, while this sensitivity might change $\pm 10\%$. The healthy reading range is 1.6-10000 Hz for this accelerometer. The sensitivity of the force transducer is 2.2 mV/N, while the sensitivity might change $\pm 10\%$. Its compression range is 2.22 kN, and its maximum compression is 44.5 kN. In addition, according to the data sheets of the accelerometer and the force transducer, their resonant frequencies are at much higher levels than the interested frequency range of the research. So, the experimental reading would not be impacted by the dynamic properties of the system elements.

PicoScope is a Pico Technology-developed oscilloscope and software to read analysis details. According to the data sheet and user manual, the full-scale measurement range is ± 20 V, and the input channels measurement range is ± 100 V. Also, the operating temperature is between 0 °C and 50 °C. It is based on a box which acquires the data from the experimental system to the computer using USB 2.0 or 3.0 via electrical cables. In the experiments, the frequency sweep started from 10 Hz and stopped at 4 kHz with 2 Hz increment; however, we are looking for the frequency range until 1.2 kHz (1200 Hz). The data has been sampled every 10 μ s, and the sample rate on PicoScope has been implemented as 100 kS/s, making 2097148 samples for each frequency sweep analysis.

Force transducers and accelerometers have been defined with their sensitivity levels according to the user manual of each system element. To prepare raw data for the spectrum analysis the Hamming Window was applied to time series through the PicoScope software settings. Hamming Window provides improved quality of the signal processing from the data obtained in the experiments and removes spurious harmonics caused by PicoScope spectrum analyser. Each test has been reanalysed six times without stopping the signal interaction, and PicoScope can capture 30 tests at once without stopping the signal generation.

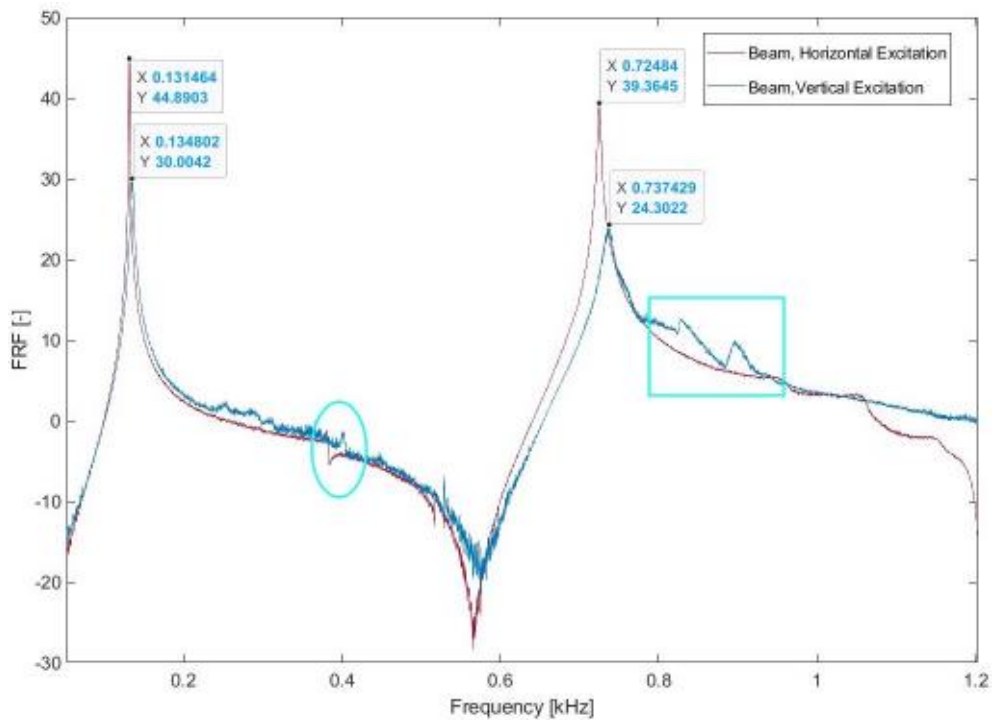


Figure 6. 10: Bare beam horizontal and vertical test results

The bare beam has many inclusions in the dynamic properties because of the structure's geometry, for instance, the slits through the length and the holes to mount the beam in various positions. Both vertically and horizontally placed beam on the test rig has been experimentally studied by reading the acceleration from the same points. According to the vertical and horizontal positioned beam-shaker analysis, there are similarities and differences. Figure 6.10 shows the experimental analysis results for both excitation conditions. The similarity is that they showed the same eigenfrequency FRF peaks. However, their amplitude resulted in different levels. This might be about the mounting on the experimental rig or related to the complexity of the geometry including the attachment of the beam to the test rig. The peaks around the 400 Hz, which is taken into an oval shape, are about the second bending mode shape of the bare beam. This can be validated from the numerical simulation analysis by taking the acceleration data from another point on the beam or simply checking the eigenfrequency mode shapes. The rectangular-shaped area included differences between the two experimental analyses. This is about the mounting properties of the beam to the experimental rig; however, the beam has many other inclusions which might be seen in the experimental analysis only. These inclusions show that

the complex geometry of the beam allows additional mode shapes, even the mixed modes, especially because of the slit through the length of the beam [180], [181].

6.5- Experimental Analysis of Resonating Structures

Individual Resonator Testing and Variation of Resonance Properties

The eigenfrequency analysis in numerical options and followed design methodology on the resonating structure has helped to decide the resonating damper geometry. The details can be found in Chapter 4. The production has been processed through the 3D printing options using ABS filling material (in the standards of ASTM D3039, density of 1.04 g/cc, 2.25-2.28 GPa of Flexural Modulus) in Ultimate Cura [162]. Spherical and cylindrical parts have been printed out as separate sections, and they have been glued as shown in Figure 6.11.



Figure 6. 11:3D-printed and maintained resonators

There are six resonators, each of which has 30 gr of mass. These resonators are analysed through the frequency sweep on the bare beam to find each eigenfrequency individually. However, the test setup has the opportunity to attach only a specific resonator at the centre. Therefore, each resonator has been attached to the bare beam close to the centre, which is 30 mm off. Figure 6.12 illustrates the centrally positioned resonator, and that resonator is the specified resonator for the central position.



Figure 6. 12: Shaker-Beam-Individual resonator setup

As a result of the frequency analysis for these resonators, each resonator has close but different eigenfrequencies. This might be a result of various contact relations of each resonator. Since these printed structures are glued to each other, there might be various additional properties.

Figure 6.13 (a and b) illustrates the shaker-beam dynamic test analysis results for each resonator attachment from the full frequency range (0.05-1.2 kHz) and the area of the eigenfrequency peaks. Each eigenfrequency has been highlighted in rectangular boxes. Even though they have been picked through the shaker-beam dynamic tests, it is proper to specify these eigenfrequency points by evaluating and comparing the bare beam test results. Therefore, the bare beam test results have been compared with the individual resonator attached test results. In addition to these outcomes, some resonator properties have been found close to the bare beam properties. Therefore, there are coupled behaviour in Figure 6.14, especially the frequency range between 0.8 kHz and 0.85 kHz. The eigenfrequency levels for each resonator have been specified after a wise evaluation of the dynamic properties obtained in the figures.

According to the full-scale beam size dynamic test results, there might be a mixture of modes or coupled behaviour of the resonator and the beam. Therefore, aiming to specify the

resonator's eigenfrequency and ensure the resonator mode's presence between the 0.8-0.85 kHz frequency range, the bare beam size has been scaled to the smallest level using the test setup options. There are nut holes through the beam, as specified in the previous subchapter, used to scale the length of the beam when mounting on the test rig. The dynamic test has been run several times using various options such as the bare beam, an empty resonator attached beam, and steel particle-filled single resonator attached to the beam (explained in Chapter 7).

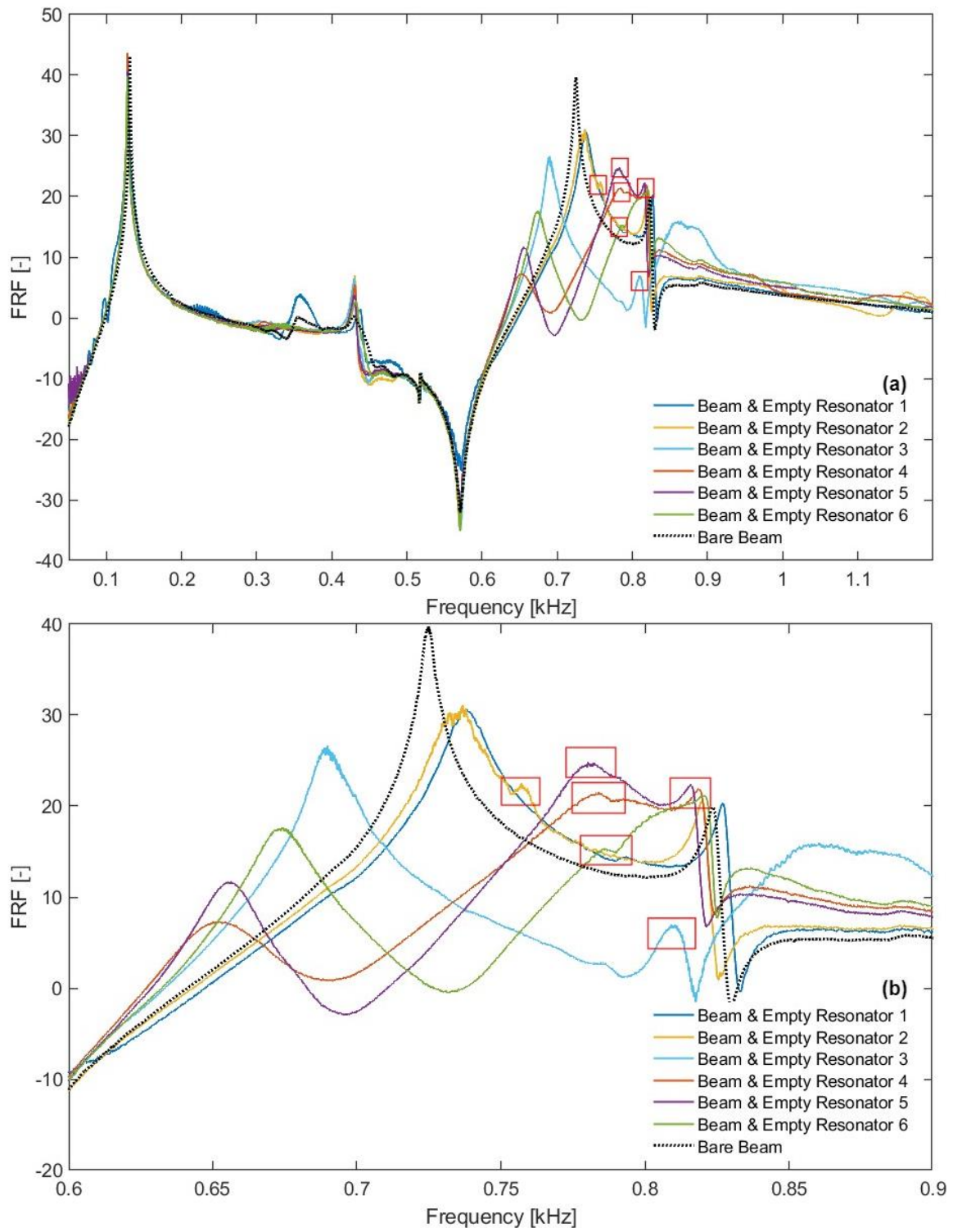


Figure 6.13: Frequency response of each resonator (a) 0.05-1.2 kHz, (b) close-up looking

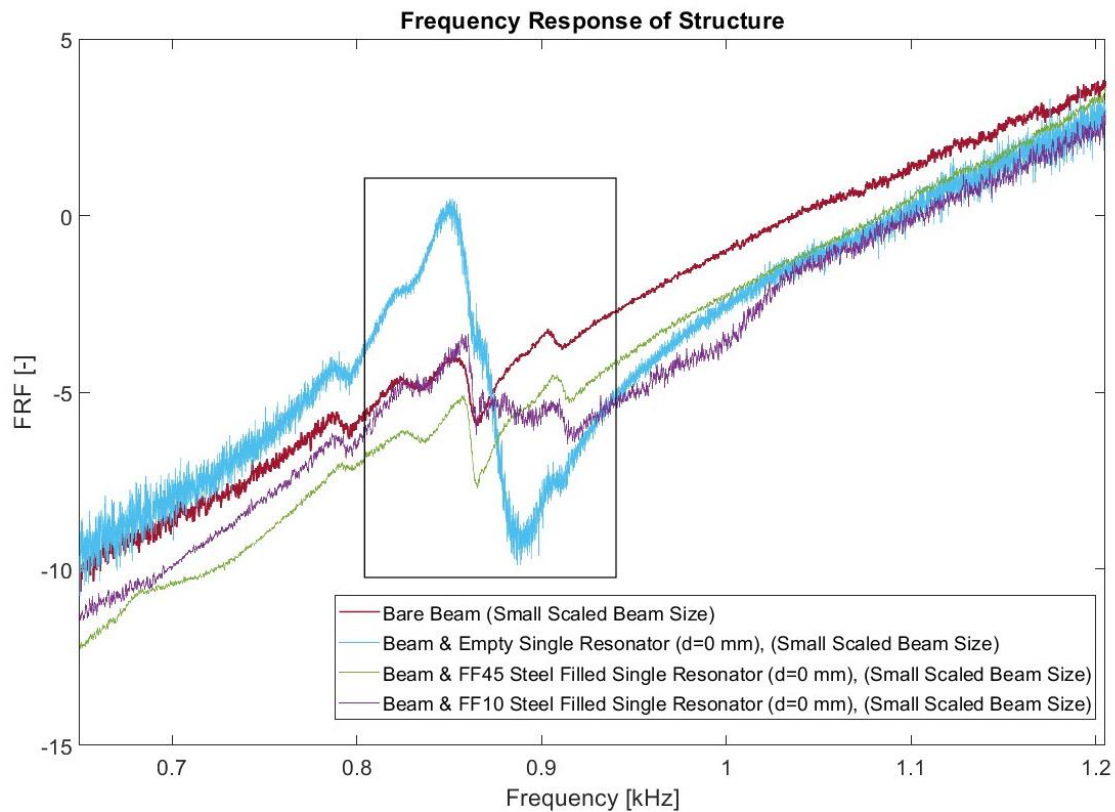


Figure 6. 14: Small-scaled beam dynamic test results

Figure 6.14 shows the small-scaled beam dynamic test results from the bare beam, the empty resonator attached to the beam. The solid blue line shows the empty resonator attachment on the beam, indicating a resonance related to the attached structure. Solid green and solid purple lines, particle placed resonator cases at various amounts for the granules, also support the empty resonator attached case result. Even though the particle placement in the resonator cavity controlled the frequency response amplitude because of the absorption controlled by the granules (this impact is explained in Chapter 7), there is an obvious peak at similar frequency levels.

The numerical studies in this research are based on identical properties for all resonator attachment, while in the experimental results it is expected that all vibration absorbers are unique. Since the experimental eigenfrequencies differ from the numerical results, the studies in this chapter are evaluated separately from the numerical results. On the other hand, since the eigenfrequencies are close to each other, the experimental results are also compared to the numerical results.

Response of Single Resonator Attachment on the Beam

The bare beam and resonating structure attachments have been studied using a variety of positions in order to analyse their frequency response and dynamic properties in modification of the bare beam dynamic properties in the numerical options as shown in the previous subchapter. In addition, dispersion relations of the resonators have been analysed by modelling the bare beam as a unit cell, as given in Chapter 5. Aiming to validate these studies and evaluate the produced structures in the dynamic event, which is previously explained in frequency analysis, experimental studies using the resonators and the bare beam are prepared on a shaker-beam dynamic test scheme.

Experimental analysis using resonators attached to the beam is similar to the finite structural analysis in numerical studies. The resonators are placed on the beam as single or multiple arrangements using a 10 mm distance from the centre or between them; there are 10 mm steps in each case. Frequency response is calculated using the data captured from the shaker's force transducer and the beam's accelerometer readings. The acceleration data is captured from the position through the length of the beam, which is assumed to be the less noisy point to have a healthy reading. Because of the complex geometry, this is considered where the nonlinear inclusion of the beam is avoided.

The first example of the experimental analysis is the single resonator attachment on the beam placed at the centre, 70 mm, and 130 mm from the centre of the beam. Figure 6.15 includes the bare beam frequency response to evaluate the resonator impact on the beam. According to these analysis results, the resonator placed on the beam has impacted the frequency response. The first peak at around the third mode shape of the bare beam is the coupled beam mode in the case of resonator attachment, and the closest relatively smaller-sized peak is the resonator mode. In addition to these, Figure 6.15 demonstrates noisy data trends mostly because of the way resonating structures are attached. Also, replacing the single resonator on the beam at various positions breaks the symmetry of the two sides of the beam. Therefore, the case of 130 mm attachment has noisier trend in this figure. In addition to these, it is worth mentioning the possibility of external and internal impacts on

the experimental rig caused by the environmental noise and technical attachments on the rig.

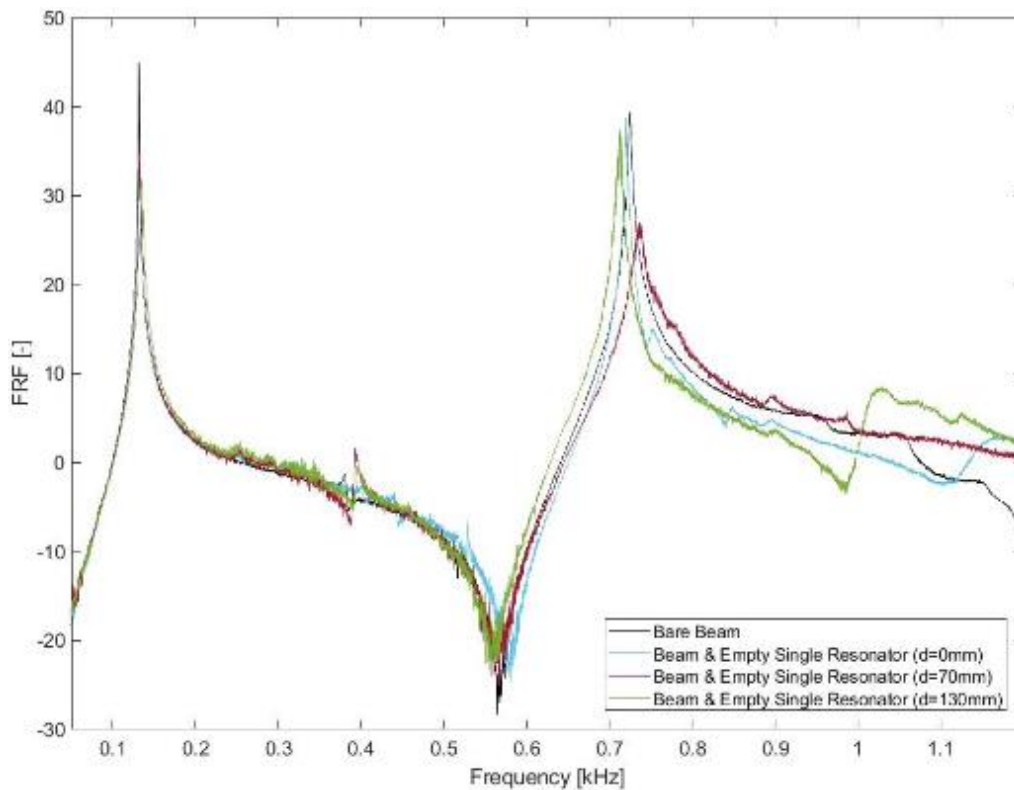


Figure 6. 15: Single resonator attachment on the beam frequency response analysis

Adding a tuning structure on the antinode point for the third bending mode of the beam controls the dynamic behaviour of the beam by changing the frequency level and the amplitude of the whole structure, as seen from the resonator attached case results. Depending on the resonator attachment distance from the centre of the beam, the beam mode, and the resonating frequency level differences, as mentioned about the frequency gap, the largest frequency gap area has been recorded in the 130 mm placement case. In this case, the frequency gap has been between $\omega_{beam}/\omega_{resonator} = [0.802, 1.017]$. Other examples for the placement of the resonator have illustrated a narrower gap.

The additional peak that appears at around 1 kHz for the case of 130 mm placement is thought to be an effect of constraining the beam at one side of the beam and ruining the symmetry properties of the beam. However, the 130 mm placement of the resonator beam arrangement has been similar to the numerical case by showing the best frequency response.

The second bending mode of the beam has been more observable for the case of 70 mm placement, similar to the result given in Figure 6.1. In general, single resonator placement on the beam has been proved to couple between the attached resonator and the beam.

Response of Multiple Resonators Arrangement on the Beam

Multiple attachments on the beam have been studied by adding up to five resonators on the beam at various positions using the same placement strategy as in the numerical analysis.

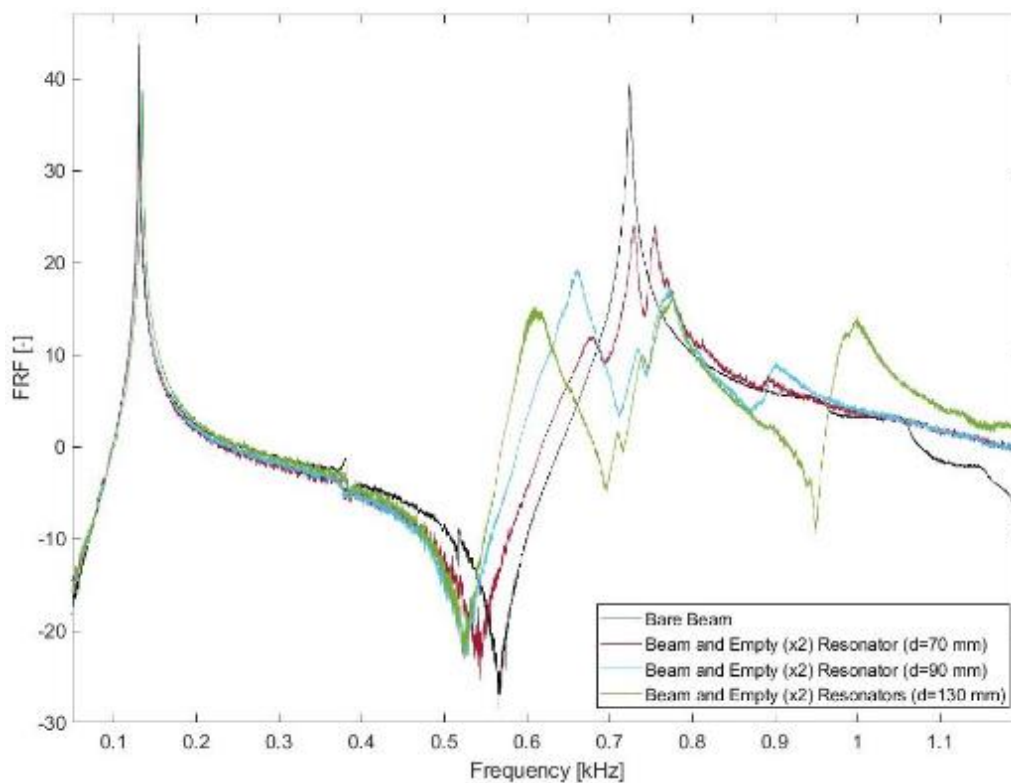


Figure 6. 16: Two-resonator attachment on the beam frequency response analysis

The two-resonator attachment on the beam is shown in Figure 6.16. Specific positions such as the antinode point of the beam, which is 70 mm off from the centre, have shown coupled resonators behaviour stronger than the other resonator arrangement cases. In this case, the coupled beam eigenfrequency has been reduced to around 670 Hz. Two other peaks at 730 Hz and 755 Hz are thought to be the resonance of the tuned structures. In the other placement options, it is obvious that the increased distance between the resonators has resulted in additional mode shapes, which might be an only disturbance or torsional modes at the beam. However, the resonators absorbed the excess energy from the beam since the

frequency response amplitude had been greatly reduced. The largest frequency gap has been recorded in the case of 130 mm placement of the resonators. In this case, the frequency gap has been between $\omega_{beam}/\omega_{resonator} = [0.933, 1.193]$. Other examples for the resonator placement have illustrated a narrower gap; for instance, the 70 mm placement has shown the narrowest gap in the frequency range.

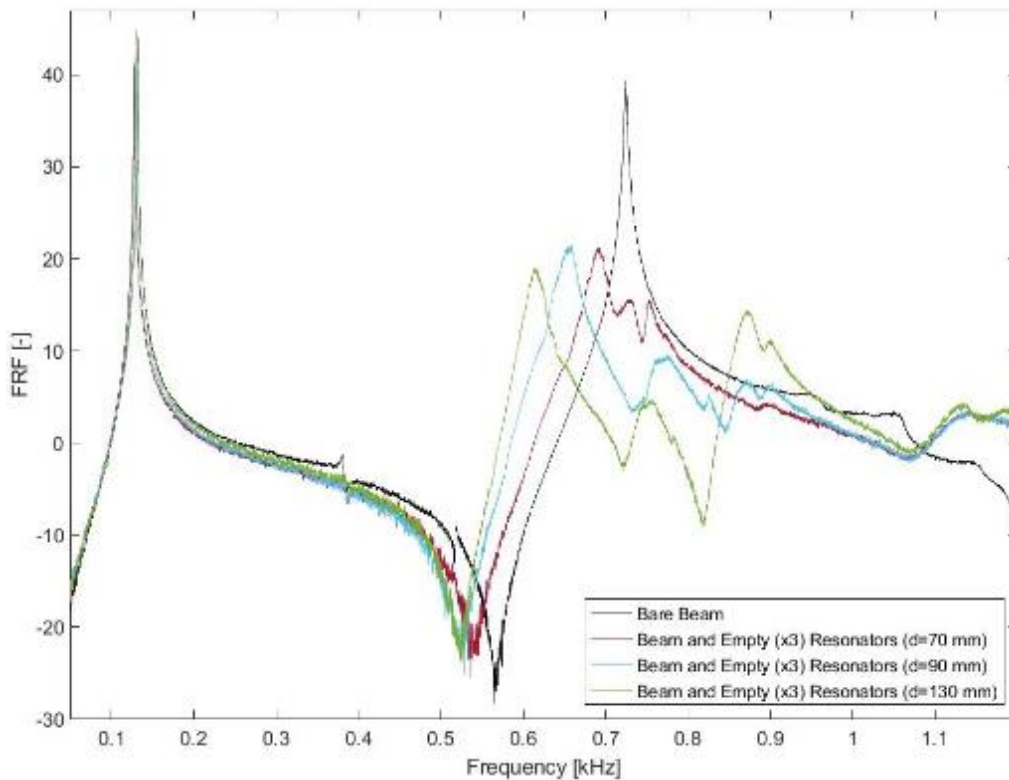


Figure 6. 17: Three-resonator attached beam frequency response analysis

Figure 6.17 shows the three-resonator attached beam's frequency response analysis results for various attachment options. According to the figure, the resonator attachment place has a great portion on changing the frequency response. This is because of the size of the beam; controlling the beam's dynamic properties is modifiable by placing the resonators at specific positions.

Coupling between the resonators and the beam is seen in the figure; the first peaks around the third mode shape of the bare beam are the coupled beam modes, following peaks are mainly about the resonator modes or their intercoupling on the beam. Placing the resonator at the centre of the beam has shown controlling behaviour on the frequency response of the beam; this is obvious when this case is compared to the two-resonator placement cases

(previous figure). Also, an array of resonator impacts can be observed in the figure. Placing the resonators in a wider arrangement better controls the beam's dynamics. The frequency response has been silenced between 0.6 and 0.9 kHz, which can be considered a stopped frequency response gap. The frequency gap has been between $\omega_{beam}/\omega_{resonator} = [0.831, 1.180]$ in the 130 mm distance case. Other examples for the placement of the resonator have illustrated a narrower gap.

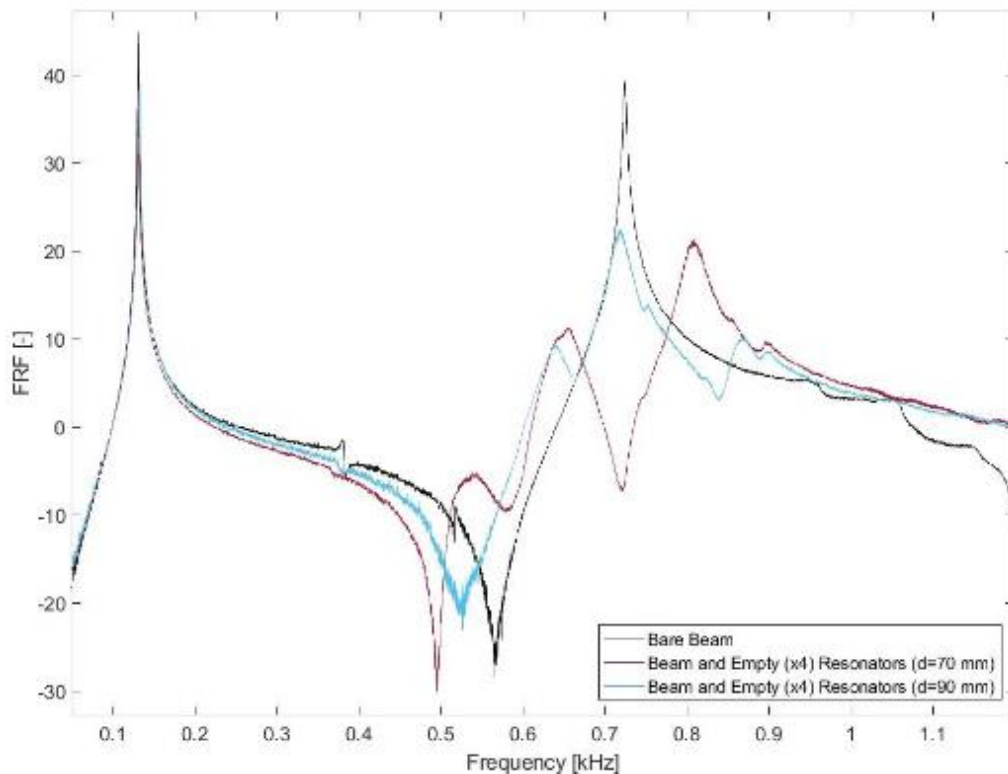


Figure 6. 18: Four-resonator attachment on the beam frequency response

Figure 6.18 shows the case of the four resonators attached to the beam at various places keeping the symmetrical arrangement from the centre of the beam. The arrangement of four resonators at the antinode points has reduced the frequency response of the beam itself greatly; this can be considered as the applicability of damping from the tuned resonators. The frequency gap has been between $\omega_{beam}/\omega_{resonator} = [0.895, 1.347]$ in the 70 mm distance case. Another example, the 90 mm distance case, for the placement of the resonator, illustrated a narrower gap. Also, the higher peaks around 800 Hz are related to the tuning between the resonators attached to the beam. Changing the distance between the resonators provides additional beam mode shapes like torsion or a mixed mode shape, including all structures on the system. As a result, the empty four-resonator arrangement on

the beam has provided an excellent reduction in the FRF amplitude. It opens the frequency gap, which might be a useful application opportunity.

In the case of five-resonator attachment on the beam at various positions, the resonators' beam response has been modified with a reduction or losing the beam mode shape. In Figure 6.19, the modification is seen as the damped behaviour of the beam, and a gap appears at the third mode shape of the bare beam area. Resonator mode shapes have been recorded as tuned resonators. Placing the resonators at the antinode position has provided a clearer vision of coupled resonators' behaviour. On the other hand, 90 mm placement of the resonators has been the most promising option for the frequency response control since the beam mode has been taken to a lower frequency while the rest of the frequency response has been at much lower levels. In addition to that option, the resonators in the array have used the whole beam available areas.

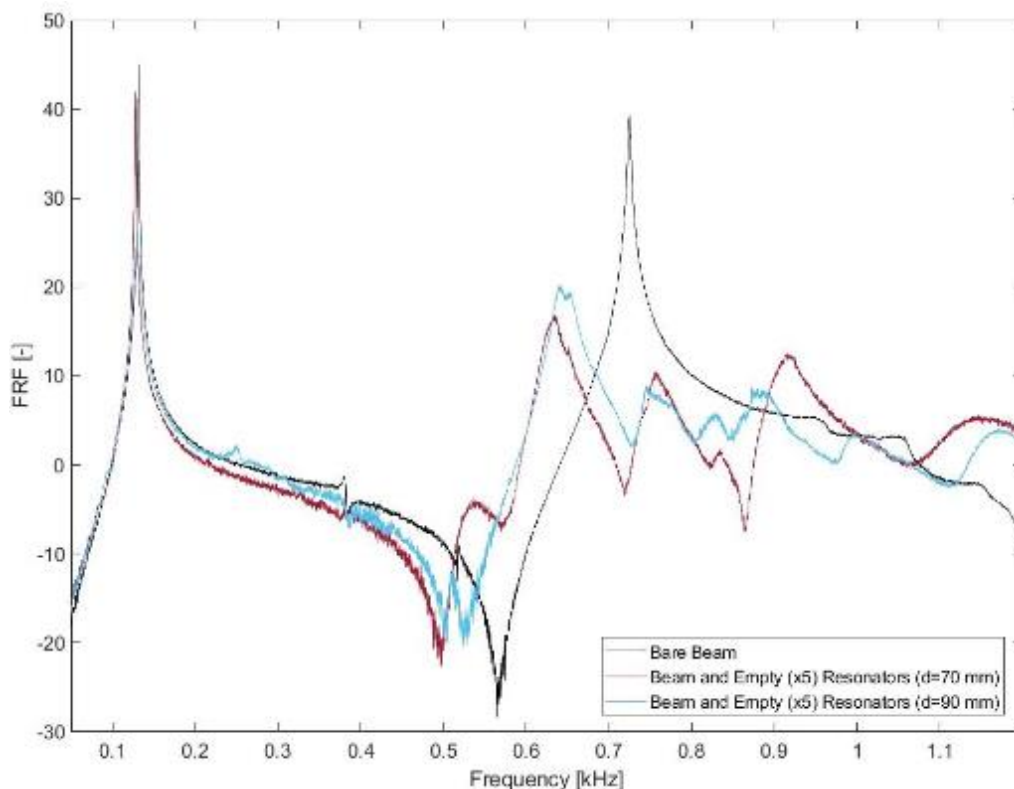


Figure 6. 19: Five-resonator attachment on the beam frequency response

Overall, using resonators on the beam has provided tuning behaviour. The coupling between the structures has resulted in damping and frequency level gap around the third mode shape of the bare beam. These resonators have controlled even the second mode shape of the

beam. Although there is a discrepancy between the resonating structure properties, they have shown the coupling and provided great damping properties.

Symmetrical arrangement and placement of the resonators at the antinode of the beam have provided additional quality of reduction in the frequency response. Comparing the multiple resonator arrangements with the single resonator attachment, the multiple resonator cases have added more mode shapes to the system, which can be tracked over the frequency response. These additional modes are related to the resonators' coupled behaviour, which can also be checked through the numerical analysis results.

Even though the beam size is limited to a maximum of five resonator attachments, it has been enough to prove the idea of resonating structures to modify the dynamic behaviour of the beam. The resonators have dominated the beam resonances used at various places on the beam, similar to the literature examples [157].

6.6- Numerical Investigation of Modified Resonators

A modelled resonator has been introduced in Chapter 4. This modelling has been studied numerically in the earlier subchapters of this part of the thesis. In addition to the modelling, the resonator has been produced using a 3D printing technique, as explained in Chapter 4.

Validation of the numerical studies has been conducted through experimental studies. Experiments of the research have been modelled using a structural steel beam fixed from both ends, as explained in the experimental study subchapter. Bare beam and resonator identification analysis have been studied in specific experimental conditions. Once the system dynamic properties have been defined, the resonator impact on the beam using both the single and the multiple resonator arrangement options have been experimentally studied. The numerical studies' resonators have the same design and dynamic properties. However, as explained in the previous paragraph, the production and manufacturing steps have impacted the properties of the resonators [165], [67]. The produced resonators have shown various eigenfrequency values. Since experimentally found eigenfrequency values for each resonator is more or less similar to each other, as given in comparison between the

small-scale beam and full-size beam results, they are not considered as barely different resonators.

Although the resonators are considered the same in numerical studies, evaluations have shown differences due to experimental studies. Therefore, to experience the difference in the resonating structures, they are modelled in COMSOL Multiphysics by changing the contact area of the cylindrical base and the spherical cavity. It has been mentioned that the contacting area of two resonator parts has stiffness controlling property by the design options given in Chapter 4. According to the experimental findings, the resonators are modelled here in numerical analysis to evaluate their performance. Because of the mentioned differences evaluated in experimental analysis, by making changes over the resonators in the numerical analysis setup, the resonating structures have had various eigenfrequencies: Resonator-1 (860.63 Hz), Resonator-2 (761.96 Hz), Resonator-3 (837.74 Hz), Resonator-4 (792.85 Hz) and Resonator-5 (857.88 Hz).

In the numerical study, two resonators have been used with various eigenfrequencies using Resonator-2 and Resonator-3 details (Figure 6.20). According to the frequency sweep analysis of these arrangements (70 mm and 150 mm). Node and antinode points for the bare beam are at around 70 mm and 140 mm in order. Resonator attachments at the 70 mm have resulted in similar frequency responses since the resonators have been placed at the node points. On the other hand, a 150 mm resonator arrangement has been placed at the antinode point of the third mode shape of the beam, which has modified the beam's response at high amplitudes. Also, two eigenfrequencies of the resonators can be observed from the FRF trend line in Figure 6.20.

The first peak in Figure 6.20, around 0.65 kHz, has been the beam mode, whereas the following two modes are expected to be the eigenfrequencies of Resonator-2 and Resonator-3. Two small peaks appear at higher frequencies which have been thought to be the coupled resonator modes.

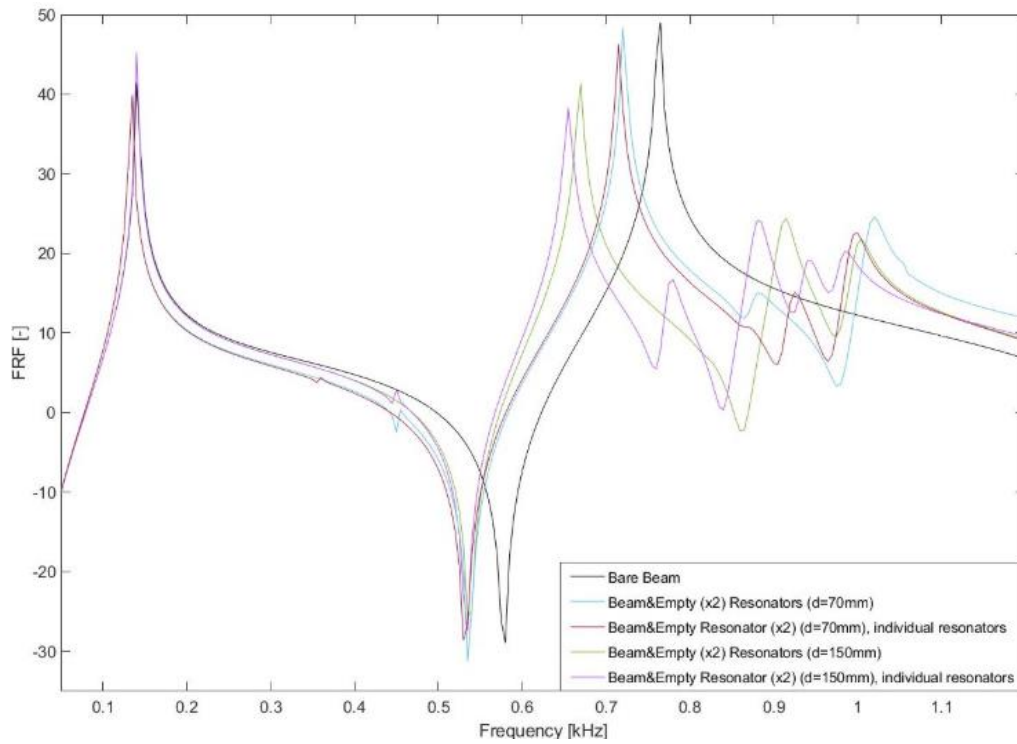


Figure 6. 20: Two-resonator placement on the beam with individual eigenfrequencies

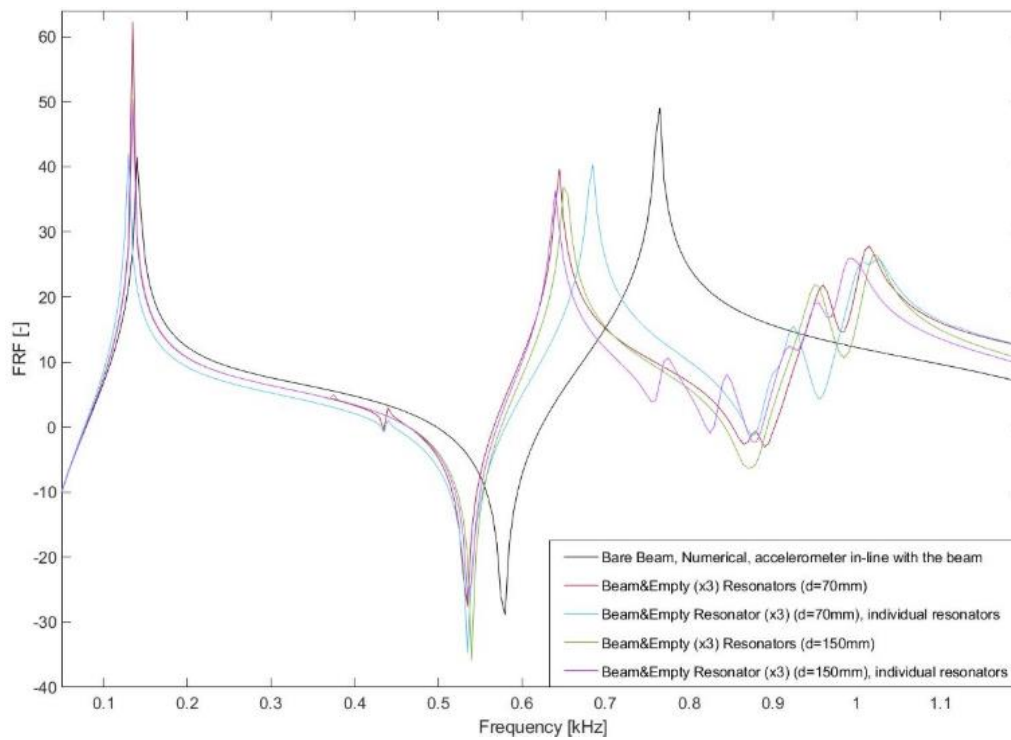


Figure 6. 21: Three-resonator placement on the beam with individual eigenfrequencies

Three-resonator arrangement (Figure 6.21) using Resonator-1 at the centre of the beam, which is the beam's point of excitation, has shown similar frequency response details for the 70 mm arrangement when compared to the same resonator usage case given in the same figure. Although using various resonators has shown similarities, especially in the case of the 70 mm arrangement, the beam resonance has been taken to the higher frequency level, which modified the frequency gap in a reverse way.

The resonator arrangement at 150 mm case shows differences from the original case in Figure 6.21. The coupled beam and resonator mode, the first peak around 0.65 kHz, has been similar to the same resonator used analysis result. Since the eigenfrequencies of Resonator-1 and Resonator-3 are close to each other, the frequency response has various coupled mode shapes after 0.65 kHz, and Resonator-2 has a smaller eigenfrequency in these resonators arrangement. Therefore, various coupled resonators' behaviour through frequency sweep analysis has been conducted.

In the case of a five-resonator arrangement (Figure 6.22), Resonator-1 has been placed at the centre of the beam. One side of the beam has been designed to have Resonator-2 and Resonator-4, while the other has Resonator-3 and Resonator-5. When various resonators have been analysed, the resonator placement of the 70 mm case has resulted in more complex mode shapes than the same resonator arrangement case. The reason behind this might be various resonator usage on the beam, and each resonator is coupled with the beam and neighbouring resonators. When this result is compared to the experimental result given in Figure 6.22, the 70 mm numerical arrangement result analysed using various resonator cases has many similarities regarding the eigenfrequency arrangement and mode shapes.

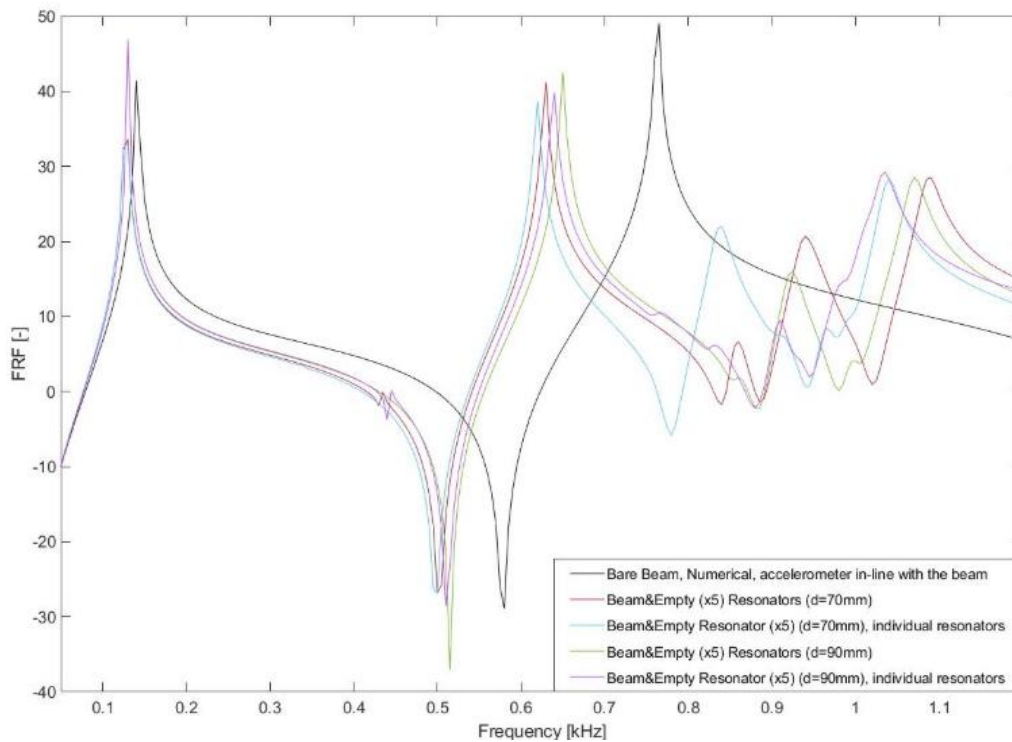


Figure 6. 22: Five-resonator placement on the beam with individual eigenfrequencies

Similar to the 70 mm arrangement case results using various resonators, their frequency response illustrated a complex behaviour when these resonators were placed at 90 mm apart from the centre. There have been many complex mode shapes and coupled resonators mode shapes through the frequency sweep analysis. However, the experimental analysis might have an evaluation and validation opportunity due to various absorbers analyses, providing more dependable results than the same resonator arrangement cases.

6.7- Conclusion of the Chapter

With frequency sweep analysis, numerical analyses have been made using the bare beam and various numbers/compositions of resonators attached to the beam under the sinusoidal excitation. Once these analyses have been finished and postprocessing accomplished, resonating structure attachment on the bare beam has been evaluated as the multiple arrangements on the beam produced a frequency gap [75], [182]. This has been evaluated in another way by taking another acceleration reading point (see Figure 6.7). In addition to that, experimental and numerical analyses have been evaluated together. In order to reduce the differences between these analysis results, the stiffness properties of the resonators have

been changed. The stiffness changes have obtained various eigenfrequencies; then, various resonator properties have been used in the numerical analysis.

Resonators in the unique periodic arrangement have resulted in a frequency window where the structure could not experience high amplitude or structural vibration impact. Therefore, as given in Chapter 5, the resonators have the property of controlling the frequency response of the main structure (the beam). As an overall evaluation of this chapter, the resonators in longer periodic arrangements in both the numerical and the experimental studies might be more beneficial for frequency response controlling and frequency gap opportunities. Completing this Chapter, the damping properties at broadband vibration frequencies have been successfully achieved by incorporating locally resonant structures with their tuneable dynamic properties like inertia in the dynamic structural systems.

Chapter 7: Dynamic Absorption Using Particle Filled Resonators

Vibration has been studied with its reasons and damping options throughout the thesis within the research question and aims limits. Granular structures are one of the options to improve the structural vibration absorption properties. Particle damping applications, which are the granular structure, have been introduced with interesting examples in Chapter 2 (Literature Review). In addition, granular structures have been studied in Chapter 3 with mechanical properties and dynamic interactions with their environmental elements like the enclosing cavity and the neighbouring granules in a packing. Therefore, theoretical information about the granular structures, granular packing and dynamic properties of the granules can be found in these chapters.

The resonating damper, which is given in Chapter 4, has been designed in a specific geometry. As explained in Chapter 4, the damper geometry is aimed at placing the granular structures in the cavity. This chapter uses various sized metallic and polymeric granular structures to fill the resonating damper cavity at various filling fractions. The particles aim to control the structural vibration and reduce the beam's frequency response amplitude when placed in a resonator. Since the damper geometry used in the research is a resonator, this chapter questions the resonance and benefits of granules. Equivalent material properties have been calculated over the range of material-filling fraction variations according to the data obtained from EDEM analysis.

Numerically modelled filled resonating damper geometry is studied in COMSOL Multiphysics as a finite structure under the forced vibration over a frequency range. Additionally, periodically arranged filled resonators are studied on the finite beam. Lastly, the granules are physically placed in the resonators to validate their excitation controlling behaviours and attached to the beam to run various experiments. The results obtained from these various analysis options have been evaluated and discussed through the end of the chapter. Studying the granular structures in the resonating dampers numerically and experimentally fulfils the main research aims stated in Chapter 1 .

7.1- Equivalent Material Properties

Granular structures and their relationships with the enclosing cavity and the relationship of granules in the void have been explained in Chapter 3. It was mentioned there that the granular packing and its dynamic properties must be studied more efficiently than the Discrete Element Modelling (DEM) option. This is due to reducing the computational cost and required analysis time. Therefore, a solid structure equivalent to the whole granules in the packing must be modelled.

The methodology developed in Chapter 3 has the steps to model an equivalent solid structure for representing the granular packing in the Finite Element Modelling (FEM) studying option. As a summary of the previously introduced method, a pack of granules has been studied at a certain frequency and amplitude conditions for a specific time duration in EDEM. The average coordination number between the granules under the excitation conditions and the hydrostatic pressure of the enclosing cavity before the excitation hits are used in the calculation procedure. Original Young's Modulus and Poisson's Ratio of the granules are also required. Equation 3.23 has been used to calculate the representative material Young's Modulus. This process has been renewed for each frequency increment as a representative step of frequency levels. For instance, in this research, the frequency ranges are between 50 and 1050 Hz with 100 Hz increments to calculate EDEM analysis. A series of equivalent Young's Modulus have been collected as a table to feed the FEM study for defining the Young's Modulus of the representative equivalent granular packing; in this case, it is a solid structure.

The volumetric geometry of solid structure to represent the granular packing has been calculated using Equation 3.16, and the shape, since the granules sit on the spherical geometry, has been modelled as a part of the cavity. For instance, if the filling fraction of the granules in the cavity was 45%, the solid representative structure fills 45% of the spherical structure as a portion of the sphere in the FEM study.

Poisson's ratio of the equivalent solid structure has been calculated using the original material property of the granules. Equation 3.21 is the analytical calculation for the equivalent Poisson's Ratio.

The equivalent material properties have been analysed in a convergence study, which is given in Chapter 3, to evaluate the stability of these newly adapted material properties [37]. According to the study, the equivalent material properties and the eigenfrequency of the solid representative structure have converged in several steps. Thus, this methodology has been considered beneficial in analysing the granular packing as a solid structure in FEM research steps.

Lastly, the density of the isotropic equivalent medium is required since it represents a solid structure. Equation 3.17 is used for the packing fraction calculation. Then, the density of the isotropic equivalent medium was calculated using the packing fraction and the original density of the granules in Equation 3.18.

This subchapter presents the options for various material families of the granules and their individual equivalent material properties for various filling fractions. The idea behind selecting various filling fractions is to evaluate the granular packing in terms of their dynamic behaviour and absorption levels.

Equivalent Material Properties for Metallic Granules

According to the explained methodology of the equivalent material properties corresponding to the granular filling as a solid structure, steel particles are used in this research. The metal granules of 1.59 mm in diameter sizes are used to fill the resonator geometry at various filling fractions. These filling fraction variations have been calculated through the previously explained methodology (Chapter 3.10). Therefore, steel particles fill the enclosing cavity at 10%, 25%, 35%, 45% and the most at 62% of the enclosing cavity volume.

Figure 7.1-a illustrates the cavity, which has been filled with 62% of its volume. This example is the highest filling fraction applied case of this specific size of granules. So, the cavity can be filled up to 62% of its void. In this case, the number of granules placed in the cavity is 9872, with 163 gr in total mass. Figure 7.1-b shows the equivalent structure modelled in the resonator. As it is obvious from the figure, granules have filled the cavity with some empty voids between the neighbouring granules. Therefore, the equivalent solid structure has been

at 62% of the total spherical volume, which equals the filling fraction. So, even though the cavity is filled with the particles, the filling fraction cannot be 100% since the granules would always have an empty volume with neighbouring particles. The only controlling property of the filling fraction is the size of the granules.

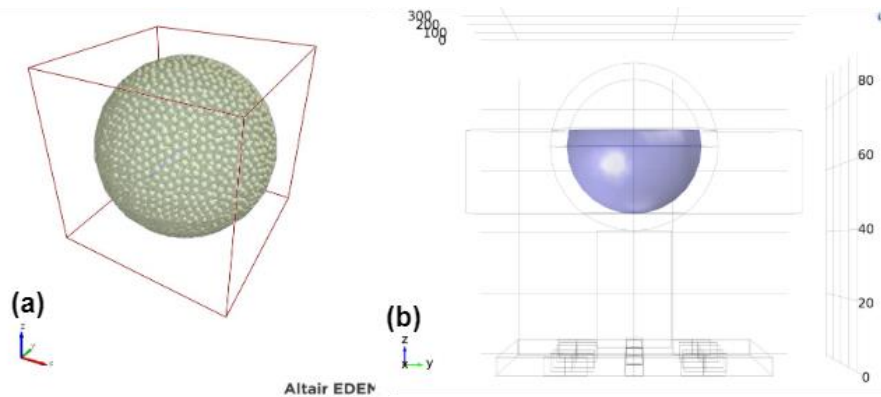


Figure 7. 1: Steel filled (62%) resonator in (a) EDEM, (b) COMSOL modellings

According to these illustrations, the representative (equivalent solid) structure material properties are given in Table 7.1 as the Equivalent Young's Modulus, Equivalent Poisson's Ratio, and density of the equivalent medium.

Table 7. 1: Isotropic solid structure material properties for 62% steel-filled granular packing

Frequency (f), [Hz]	Equivalent Young's Modulus (E^*), [Pa]	Equivalent Poisson's Ratio (ν^*)	Equivalent Density (ρ^*), [kg/m ³]
50	1.5840E+08	0.27	7771.5
150	1.5752E+08	0.27	7771.5
250	1.5700E+08	0.27	7771.5
350	1.5683E+08	0.27	7771.5
450	1.5660E+08	0.27	7771.5
550	1.5652E+08	0.27	7771.5
650	1.5643E+08	0.27	7771.5
750	1.5628E+08	0.27	7771.5
850	1.5622E+08	0.27	7771.5
950	1.5575E+08	0.27	7771.5
1050	1.5598E+08	0.27	7771.5

As seen in Table 7.1, the Equivalent Young's Modulus is changed over the frequency ranges while the Poisson's Ratio and the density for the isotropic medium have been the same for various frequency levels. There is a slight change in the equivalent Young's Modulus values between the frequency levels because granules in the cavity experiences different level of contact at each frequency impact and the coordination number controls the equivalent material properties. There might be various reasons behind this phenomenon discussed in (Section 3.10). A filled spherical cavity case for the steel particles has been used as an example for this subchapter. Material property tables for other filling fractions can be found in Appendix 7.1 (Table A7.1 to Table A7.4).

Equivalent Material Properties for Viscoelastic Granules

Materials used in this research have either metallic or plastic properties. Steel has been selected for metallic materials, and acrylic plastic and POM are the plastic materials to be evaluated.

Acrylic plastic granules of 3 mm in diameter sizes are used to fill the resonator geometry at various filling fractions. These filling fraction variations have been calculated through the previously explained methodology (Chapter 3.10). Therefore, acrylic plastic particles fill the enclosing cavity at 10%, 25%, 35%, 45% and the most at 47.5% levels of the enclosing cavity volume.

Figure 7.2-a shows the cavity filled with 47.5% of its volume, the highest filling fraction for three mm-sized granules. Figure 7.2-b shows the equivalent structure modelled in the resonator. As it is obvious from the figure, granules have filled the cavity with some empty voids between the neighbouring granules; therefore, the equivalent solid structure has been at 47.5%, which equals the filling fraction of the cavity volume of the sphere. In this case, the number of granules placed in the cavity is 1125, with 19 gr in total mass.

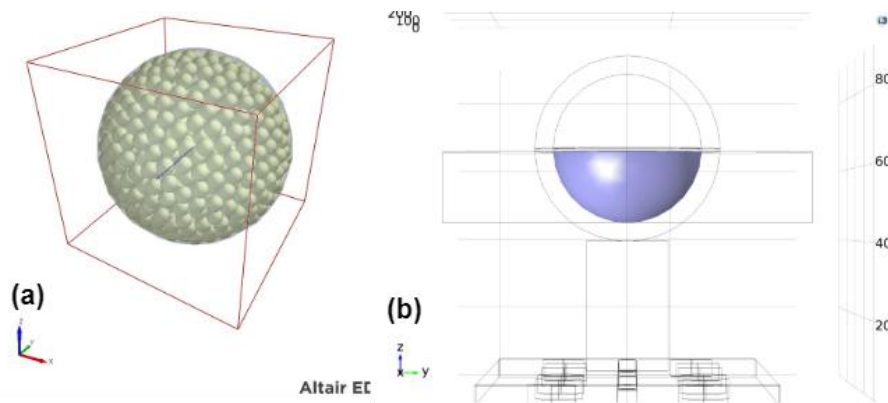


Figure 7. 2: Acrylic plastic filled (47.5%) resonator in (a) EDEM, (b) COMSOL modellings

Since acrylic plastic has a maximum of 47.5% of the total volume of the enclosing cavity, the equivalent material modelling is prepared according to this case's properties. Equivalent Young's Modulus, equivalent Poisson's Ratio, and material density have been calculated using the previously mentioned methodology. These material properties are given in Table 7.2 and are planned to be used in the solid structure modelling in COMSOL Multiphysics. Similar to the steel granular filling cases, there is a slight change in the equivalent Young's Modulus values between the frequency levels. The reason behind this change is the same as that discussed in (Section 3.10).

Table 7. 2: Isotropic solid structure material properties for 47.5% acrylic plastic filled granular packing

Frequency (f), [Hz]	Equivalent Young's Modulus (E^*), [Pa]	Equivalent Poisson's Ratio (ν^*)	Equivalent Density (ρ^*), [kg/m ³]
50	4.7191E+06	0.37	1178.1
150	4.7053E+06	0.37	1178.1
250	4.6796E+06	0.37	1178.1
350	4.6607E+06	0.37	1178.1
450	4.6449E+06	0.37	1178.1
550	4.6249E+06	0.37	1178.1
650	4.6039E+06	0.37	1178.1
750	4.5637E+06	0.37	1178.1
850	4.5754E+06	0.37	1178.1
950	4.5635E+06	0.37	1178.1
1050	4.5523E+06	0.37	1178.1

Since acrylic plastic has a larger size than steel particles, smaller-sized granules with plastic material properties are thought to be analysed to compare with the steel ones. Therefore, POM has been selected as plastic granules with a 1.59 mm diameter size. Because of the lack of material, the only filling fraction used with this material example is 7.5% of the enclosing cavity volume. Even though this filling fraction has not been corresponding filling fraction example in steel particles' case, it is planned to be analysed and compared with 10% of steel and 10% acrylic plastic particles, since these filling fractions are the lowest fillings for each granule types. It has been considered that the smaller-sized plastic particles would give a lower mass impact in the granular filling, and their dynamic properties would give ideas about their energy absorption. Figures 7.3-a show that 7.5% POM-filled spherical cavity from EDEM analysis and 7.3-b represent equivalent material added case from COMSOL Multiphysics. In this case, the number of granules placed in the cavity is 1194, with 3.6 gr in total mass.

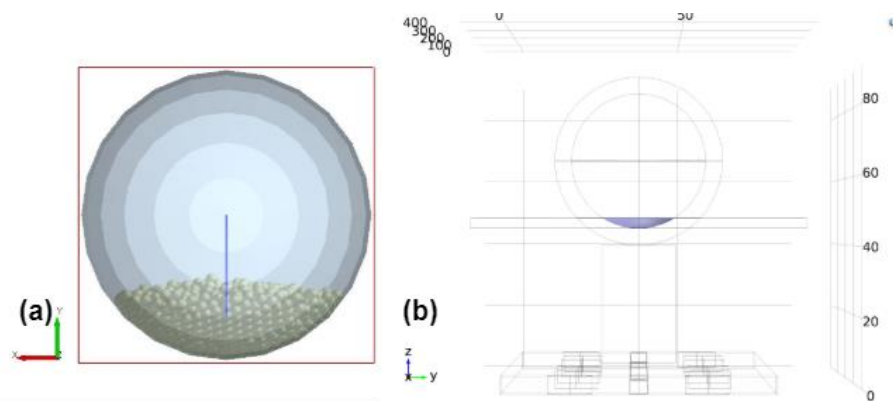


Figure 7. 3: POM filled (7.5%) resonator in (a) EDEM, (b) COMSOL modellings

According to the equivalent material modelling calculation given in Chapter 3.10, POM granules at a 7.5% filling fraction corresponding to equivalent material properties have been calculated. These material properties at various frequency levels are given in Table 7.3 below.

Table 7. 3: Isotropic solid structure material properties for 7.5% POM-filled granular packing

Frequency (f), [Hz]	Equivalent Young's Modulus (E^*), [Pa]	Equivalent Poisson's Ratio (ν^*)	Equivalent Density (ρ^*), [kg/m ³]
50	2.5598E+06	0.37	1410.75
150	2.5663E+06	0.37	1410.75

250	2.5645E+06	0.37	1410.75
350	2.5606E+06	0.37	1410.75
450	2.5576E+06	0.37	1410.75
550	2.5543E+06	0.37	1410.75
650	2.5490E+06	0.37	1410.75
750	2.5480E+06	0.37	1410.75
850	2.5456E+06	0.37	1410.75
950	2.5516E+06	0.37	1410.75
1050	2.5598E+06	0.37	1410.75

As seen in Table 7.2 and Table 7.3, the Equivalent Young's Modulus for acrylic plastic (3 mm) and POM (1.59 mm) granules are changed over the frequency ranges, while the Poisson's Ratio and the density for the isotropic medium have been the same for various frequency levels in individual cases. A filled spherical cavity case for the acrylic plastic particles and a 7.5% filled cavity for the PLA particles have been used as examples of plastic granules for this subchapter. The other filling fraction material properties for acrylic plastic granules are given as tables in Appendix 7.2 (Table A7.5 to Table A7.8).

Loss Properties of the Granules

The dynamic responses of the structures are characterised by the structural mass and stiffness properties, in general. In case of the dynamic absorption mechanism discussed in Chapters 4-6, these properties are the reasons for the "absorption" of the main system's energy by modifying the response of the system and shifting the eigenfrequency through the coupling between structures in that system. Damping the structure with dynamic absorbers and damping with a lossy material are two distinct mechanisms [183]. The damping of a structure is affected by resonance properties since the amplitude of the structure is reduced at resonance frequencies. In addition, as previously mentioned in Chapter 3, materials with low loss properties, such as steel, tend to interact more with the frictional losses. Otherwise, similar to the plastic materials, these structures tend to dissipate energy through viscous losses [39].

The loss factor is the intrinsic damping of plastic materials, which might be calculated through material characterisation techniques like DMTA testing or free oscillation techniques [165]. This property is the reason for the nonlinear behaviours of the structures [184]. Loss modulus and storage modulus are experimentally obtained data for the complex Young's modulus. The imaginary part of the complex Young's modulus is the loss modulus (E''), whereas the storage modulus (E') is the real part of the complex modulus. The ratio of the loss modulus to the storage modulus gives *the loss factor* of the material.

Alternatively, the loss factor of a structure would be available using the calculation method concerning the steady-state oscillation. Equation (7.1) stands for this calculation methodology [183].

$$\eta = D_w / 2\pi U \quad (\text{Eq. 7.1})$$

In this equation, D_w is the dissipated energy per cycle which is the energy required to maintain the steady-state situations of the structure while under applied force conditions. U is the stored energy in the structure; in other words, it is the structure's energy. The energy dissipated per cycle is calculated through the following equation (Equation (7.2)).

$$D_w = \pi c \omega X^2 \quad (\text{Eq. 7.2})$$

In this equation, c is the damping constant, and X is the highest displacement value obtained from the hysteresis loop; ω stands for the angular frequency of the excitation. The peak strain energy (U_{max}) is also available by calculating the slope of the hysteresis loop and the maximum displacement obtained from the hysteresis loop (Equation (7.3)).

$$U_{max} = 0.5kX^2 \quad (\text{Eq. 7.3})$$

Granular structures in a pack dissipate energy depending on the material properties of the granules. According to the given equations, analysis using various excitation amplitudes has been conducted to find the granular loss factor of the granular packing in the structure.

A cylindrical cavity with viscoelastic particle filling, which has been evaluated in Chapter 3, is evaluated in this case. EDEM analysis has been conducted at 655.89 Hz with 2e-5 m of

displacement amplitude. MATLAB calculation code, given in Appendix 7.3, calculates the loss factor properties through the energy dissipation and stiffness evaluations. For this reason, the displacement has been evaluated from the particle velocity information obtained from the EDEM analysis (from the excitation direction). Then, hysteresis loop shown in Figure 7.4 was prepared using the force-displacement information calculated for the five cycles performed by the particles.

The red circles in the figure show the maximum and minimum points obtained from the hysteresis cycle. Using these values, the stiffness of the granules and the peak strain energy have been calculated. Also, the damped energy has been calculated by subtracting the spring force that particles experienced from the total force of the particles. As a result, the loss factor of this amplitude level has been calculated as $1.57e-07$. The loss factor evaluated through this method is lower than the plastic materials, which are, in fact, the granules in the packing. Since the damping loss factor is proportional to the amplitude applied to the structure, different amplitudes have been studied using the same analysis methodology provided here. For instance, when the same analysis has been set for an amplitude of $5e-5$ m, the loss factor has been found as $7.57e-6$; and, for the amplitude level of $15e-5$ m, the loss factor was calculated at $4e-6$.

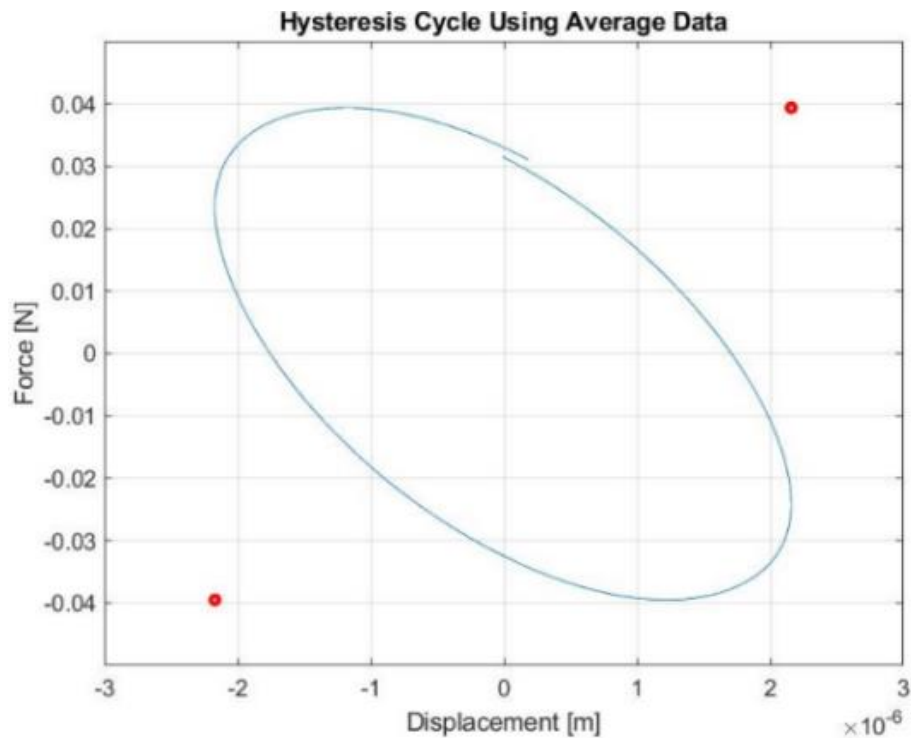


Figure 7. 4: Hysteresis loop for the granular packing

It can be seen that the recovered loss factors are relatively small and are expected to have little effect on the frequency response of the entire structure. Therefore, in this study the loss factor is omitted from the calculations and is not included in the material properties of the equivalent medium. It should be noted that this is only true for small amplitudes of excitation where the equivalent model is valid.

7.2- Periodically Arranged Nonlinear Dampers

In this subchapter, the stopband properties of the internal resonator with granular structure attachments are numerically studied using COMSOL Multiphysics. The analysis option has been previously studied in Chapter 4 for the locally resonant structures placed on the beam. The beam has been modelled as a unit cell, and the number resonator has been placed on the base structure. This subchapter has the same methodology of an added equivalent isotropic solid structure in the internal resonators. Since the base structure behaves like a resonator, the band properties of the whole system are expected to illustrate coupled resonances. Also, the granules illustrate nonlinear behaviour, as it was stated in Chapter 3, it has been generalised here as nonlinear dampers.

Single Resonator Impact on the Base Structure

A single resonator with various filling fractions on the unit cell has been studied in this part of the chapter. Examples of the analysis results are from the centrally positioned single resonator for both the metal particles and the plastic particles.

The metal particles, made of steel with 1.59 mm sizes, have been studied in the EDEM simulation technique at various filling fractions. The calculated equivalent isotropic solid structure material properties have been added to the analysis prepared in COMSOL Multiphysics. The steel filled resonator cases are at various filling fractions; 10%, 25%, 35%, 45%, and 62% (fully filled case). Similar to the other cases, the resonator has been replaced by 10 mm in each analysis. Figure 7.5 is prepared using the centrally positioned filled resonator's band property analysis results at the 10% filling (Figure 7.5-a), the 35% filling (Figure 7.5-b), and the filled resonator (Figure 7.5-c). Since the structures assessed at low frequencies would significantly show Bloch waves [185], the Bloch wave number has been evaluated in this example. According to the equivalent isotropic structure material modelling, the Young's Modulus for the filling is in the same order for the 35% filling and the 62% filling cases. On the other hand, the 10% filling case has a 10-time smaller equivalent of Young's Modulus for the corresponding material properties of the filling. Therefore, there would be a significant change in the dispersion relations compared to these three cases. In addition to these, as explained in the previous cases, applying smaller increments in the Bloch wave number in the wave solution would have resulted in less distorted dispersion lines.

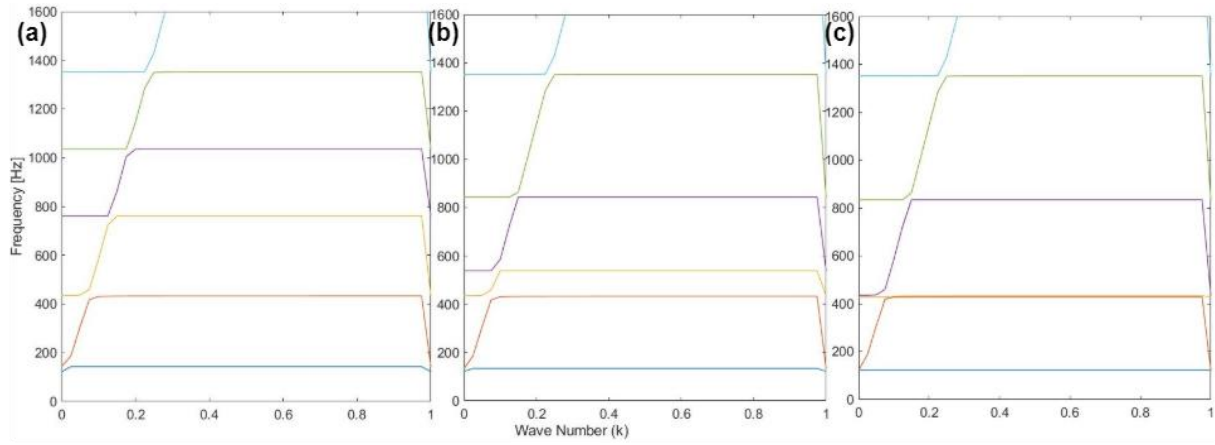


Figure 7. 5: Equivalent structure added single resonator placed unit cell analysis: (a) 10% steel filling, (b) 35% steel filling, (c) 62% steel filling

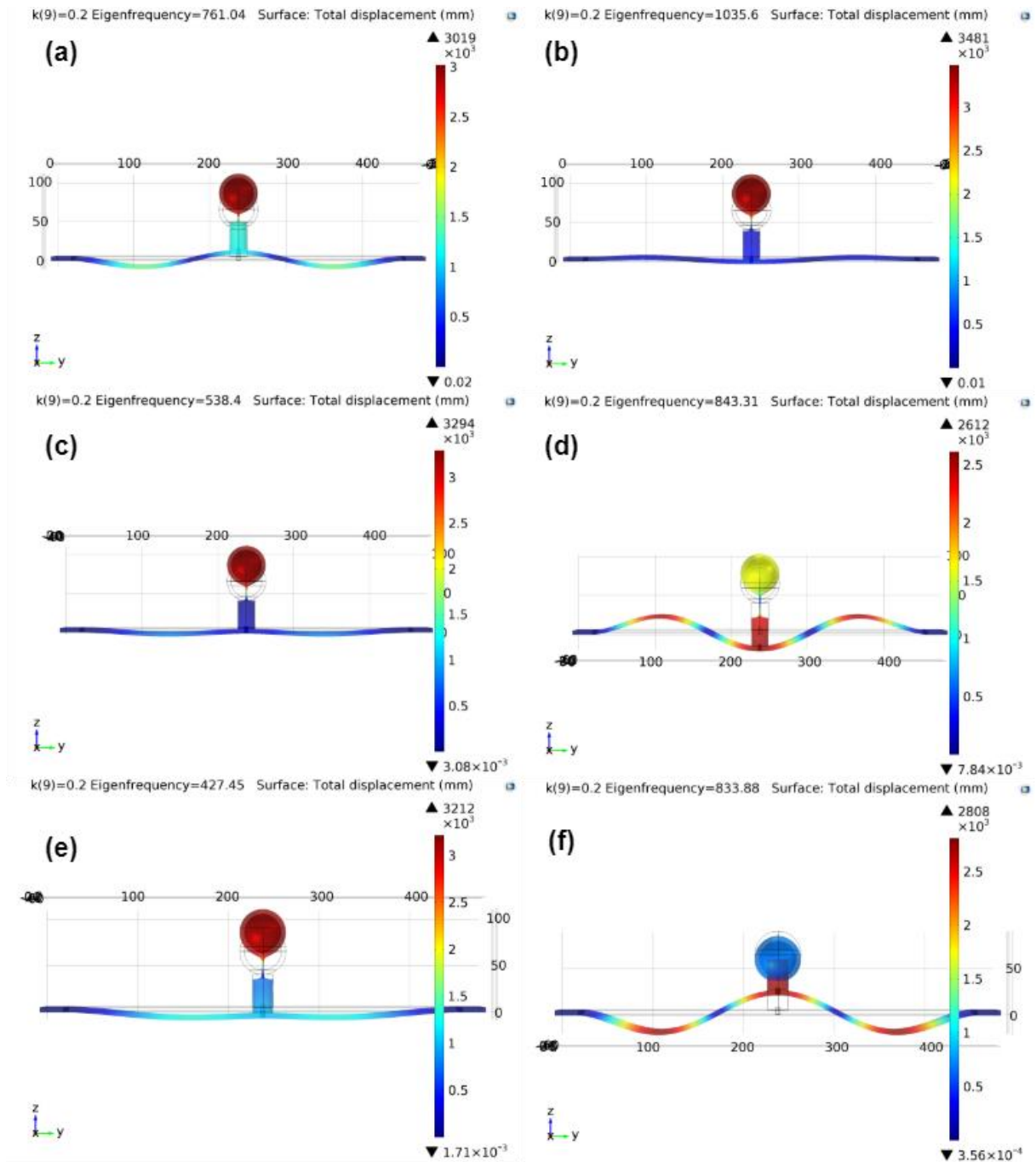


Figure 7. 6: Interested mode shapes of the unit cell with steel-filled single resonator: (a-b) 10%, (c-d) 35%, and (e-f) 62% filled cases

Lower bound modes have shown similar eigenfrequencies, essentially the unit cell's first bending mode. The beam modes have been shown in Chapter 5, and compared to the filled resonator cases, the modes have been taken to smaller frequency levels, which indicates the damping phenomena of the filled resonators. Increased filling fraction is equal to the

stiffened material usage in the resonator. Therefore, as shown in Figure 7.6, the interested mode shape has been taken to different frequency levels than the bare beam unit cell corresponding frequencies. The beam-resonator is coupled in two modes for Figure 7.6-a to d, which are the 10% and the 35% filled cases. However, the coupled mode for the 62% filled resonator case has seen in Figure 7.6-e only. This is related to the eigenfrequency change in the filled resonator case. As seen in Figure 7.6-e, the resonator and the filling inside the cavity corresponding to the beam mode. While corresponding to the unit cell, the resonators have also experienced mode conversion, specifically seen in Figures 7.6-a to d.

In the acrylic plastic-filled resonator placement cases at various filling fractions, the order of the equivalent isotropic structure Young's Modulus has seen the same orders (around $+e6$ orders). Therefore, the behaviours of the periodic array analysis of the various filling fractions would be similar in this case, as shown in Figure 7.7. In the figure given below, the lower frequency bounds have shown similar wave number propagations since these frequencies have been related to the modes of the beam (base of the unit cell). On the other hand, there are differences in the modes of the Bloch wave propagations after the first two dispersion lines. Even though the material properties have a similar order of magnitudes, increasing the filling fraction has been the reason for the dispersion lines taken to smaller frequency responses. This can be seen in Figure 7.7-c when the resonator has been fully filled with the acrylic plastic granules. This finding would be related to the change in the material impact on the resonator.

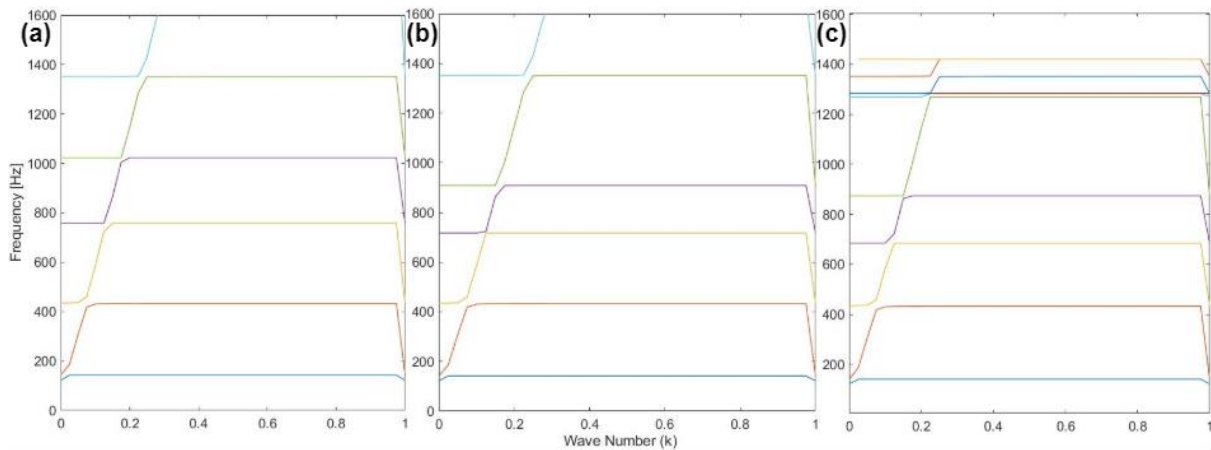


Figure 7. 7: Equivalent structure added single resonator placed unit cell analysis: (a) 10% acrylic plastic filling, (b) 35% acrylic plastic filling, (c) 47.5% acrylic plastic filling

In addition to the expected behaviours, starting from the fourth dispersion line, the corresponding frequencies have been taken to lower frequencies. Therefore, this should impact the interested mode shape of the unit cell. Figure 7.8 illustrates each unit cell property's interested mode shape, the bending-stretching mode. In addition to the similar behaviour in steel-filled resonator cases given in the previous case results, the fully filled single resonator has shown the coupled beam and resonator mode in Figures 7.8-e and f. This is related to the eigenfrequency of the filled resonator, which shows a close relation to the beam.

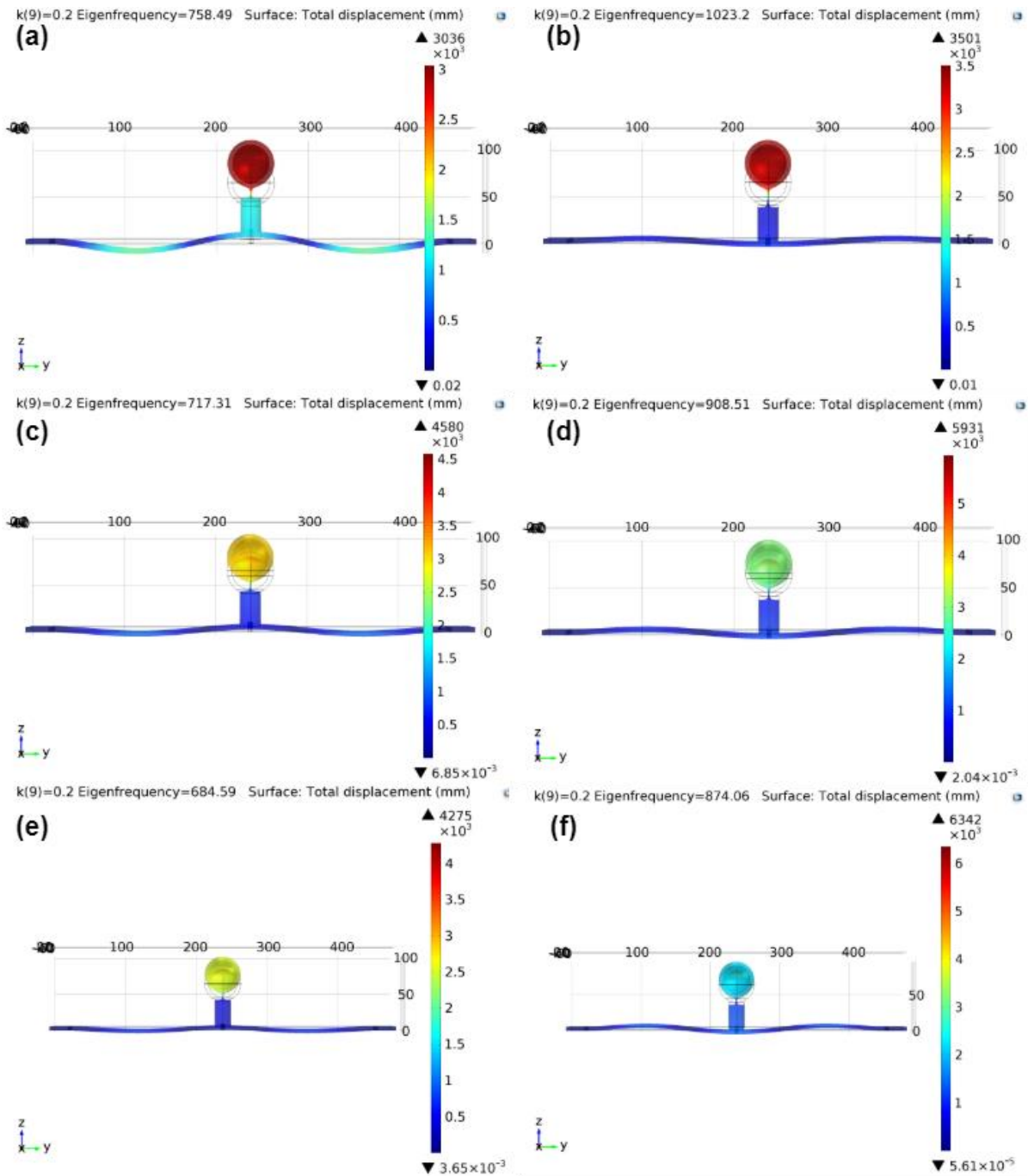


Figure 7. 8: Interested mode shapes of the unit cell with acrylic plastic filled single resonator: (a-b) 10%, (c-d) 35%, and (e-f) 62% filled cases

According to these given results, single resonator placement at the centre of the unit cell has provided symmetry in the unit cell. Because of this property, the unit cell modes show symmetrical deformation at both sides. Increased filling fractions have provided lower eigenfrequency levels to the unit cell. This is related to wave propagation speed change

because of the solid medium in the resonator, which is similar to the findings given in the source [186].

Multiple Resonators Impact on the Base Structure

This part of the subchapter is prepared with the impact of the multiple resonator idea. The empty resonators in the array have been studied in Chapter 5 and adding granular media inside the periodically arranged resonator is expected to show interesting phenomena. Therefore, various filling fractions and multiple resonator arrangements have been studied. This subchapter analyses the lowest and highest filling fraction levels for the metal and the plastic particles using the same setup in COMSOL Multiphysics.

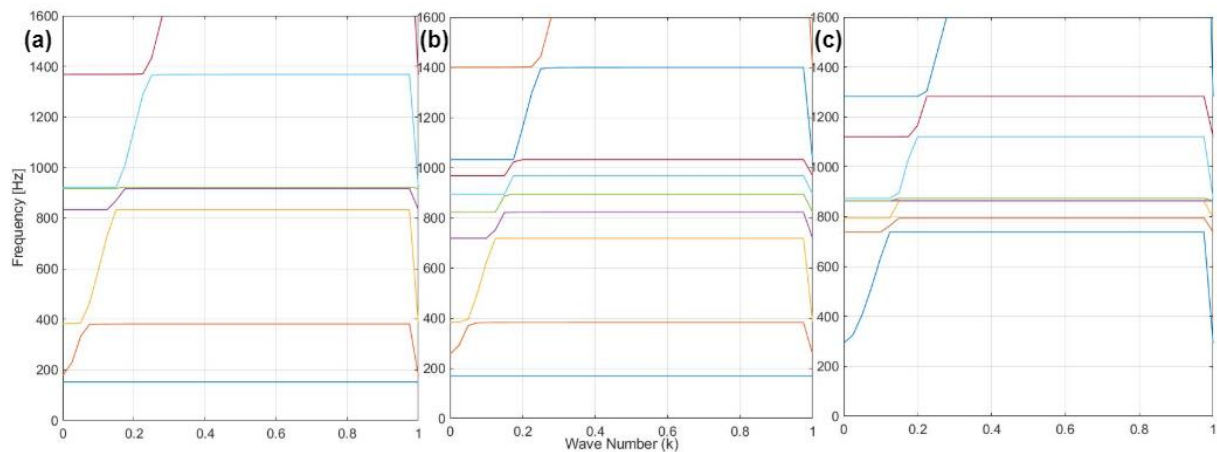


Figure 7. 9: The 10% steel-filled multiple resonators in array with 70 mm distance: (a) two resonators, (b) four resonators, (c) five resonators

Figure 7.9 illustrates the 10% steel-filled two (a), four (b) and five (c) resonators impact on the dispersion relations over the unit cell. The first two modes of the unit cell have shown similar dispersion relations. In addition, increased resonators on the unit cell have shown increased coupled properties between the resonators and the beam. This has shown in Figure 7.10 below. This figure has been prepared for a specific Bloch wave number to demonstrate the coupling phenomena between the resonators and the beam. At each mode of the beam through the same wave number, there are coupled structures which impact the deformation of the unit cell at various levels.

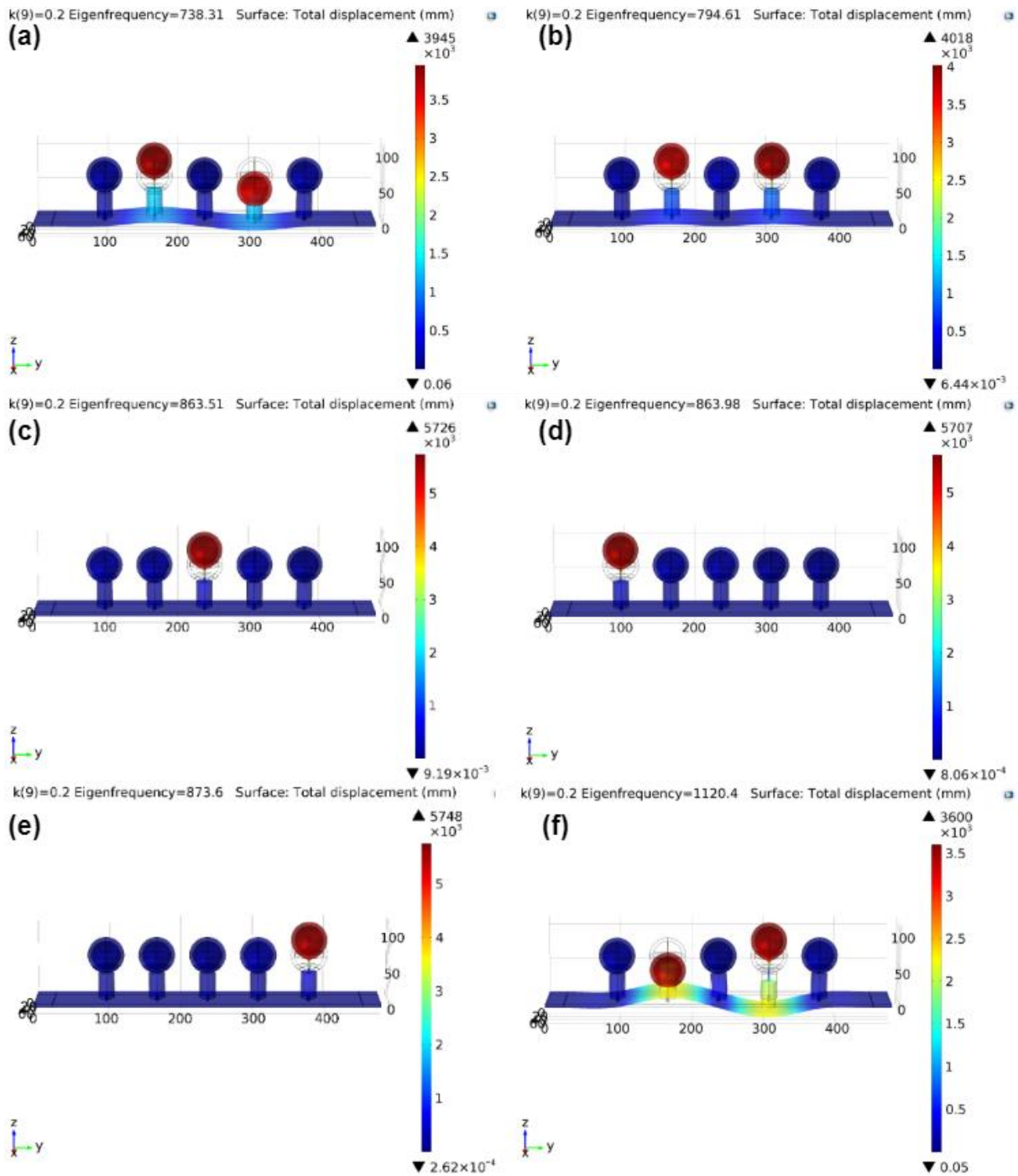


Figure 7. 10: Mode shapes of the unit cell with five resonators filled with 10% steel particles. Bloch wave number $k=0.2$

When multiple resonators in the array are filled at 62% of the cavity volume, the first two modes of unit cell have been impacted by filling. Increasing the number of resonators has resulted in a higher frequency of the first mode. The coupled resonator-beam modes are converging into one mode seen in Figure 7.11-c with the lower frequency mode starting at

around 375 Hz. In this case controlling the conversions between the modes (preventing the excitation of any other modes except bending) would lead to frequency band gap. This means a lower frequency gap would be possible by controlling the low order of modes of the unit cell by using the multiple resonators and filling inside the resonators.

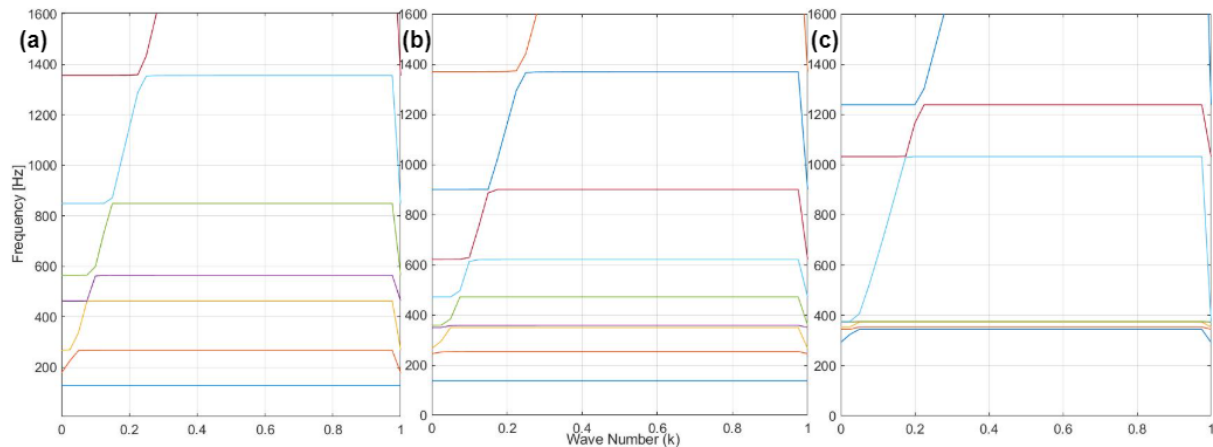


Figure 7. 11: The 62% steel-filled multiple resonators in array with 70 mm distance: (a) two resonators, (b) four resonators, (c) five resonators

Similar to the five resonators with the 10% steel filling, the fully filled five resonators have shown six coupled resonator-beam modes illustrated in Figure 7.12. When Figure 7.11-c and Figure 7.12 are related, the blue dispersion line in Figure 7.11-c, which has a frequency range between 380 Hz and 1050 Hz, includes the coupled modes of the structure in the unit cell. Since the unit cell has resonance properties, there are six various coupled structure modes. Also, compared to the single resonator with 62% filling fraction dispersion results, using a multiple resonator arrangement has increased the coupling between the structures and reduced the mode frequencies.

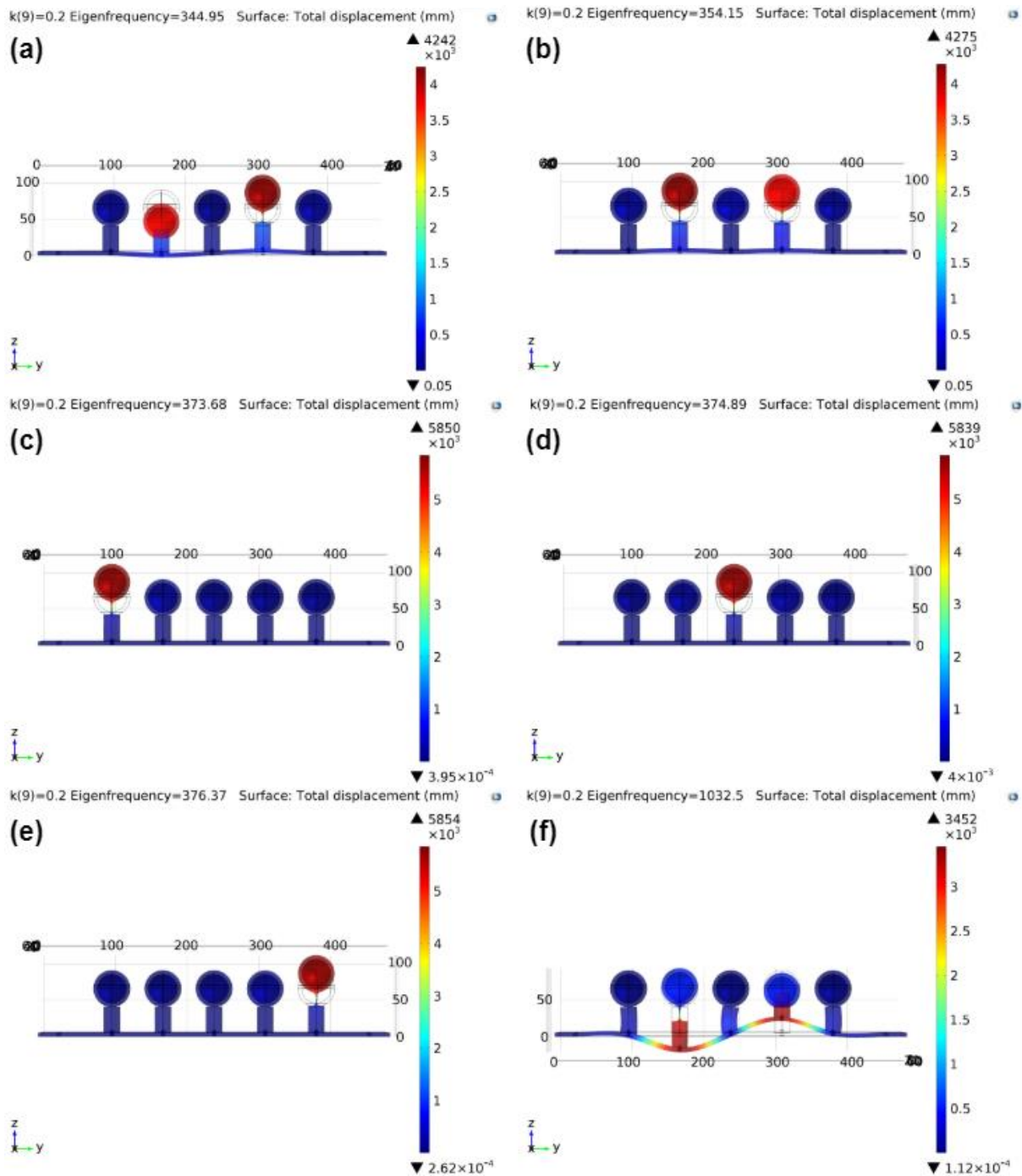


Figure 7. 12: Interested mode shapes of the unit cell with 62% steel-filled five-resonator modes

The next figure illustrates the acrylic plastic filled (10%) multiple resonator arrangement dispersion lines for two, four, and five resonators. Similar to the previous cases, the first two modes have been organised for the unit cell modes. The next dispersion lines include the coupled resonator-beam modes. Increased unit cell resonators have reduced

eigenfrequencies for the dispersion lines. Therefore, tuned structures in the unit cell have controlled the unit cell behaviour (Figure 7.13).

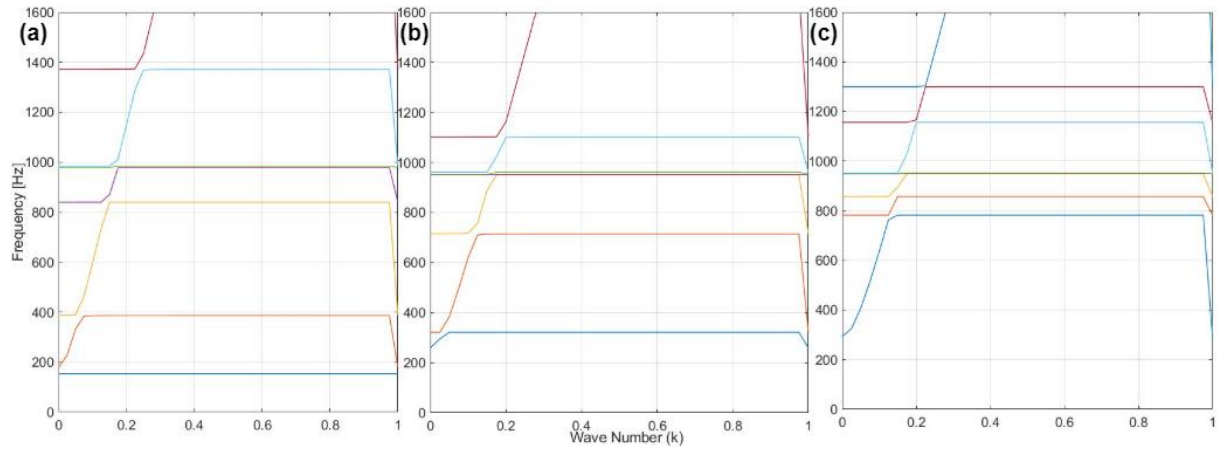


Figure 7. 13: The 10% acrylic plastic filled multiple resonators in an array with 70 mm distance: (a) two resonators, (b) 4 resonators, (c) five resonators

Dispersion relations for the five 10% acrylic plastic-filled resonators in unit cell have been analysed again through the mode shapes of the unit cell. Since the unit cell itself has shown resonance properties, there are six modes appear in Figure 7.14. Various structure-tuned resonances exist in each mode shape given in Figures 7.14-a to f. The last one, Figure 7.14-f, has shown the lowest displacement properties since the resonators have been placed close to the high amplitude experienced area.

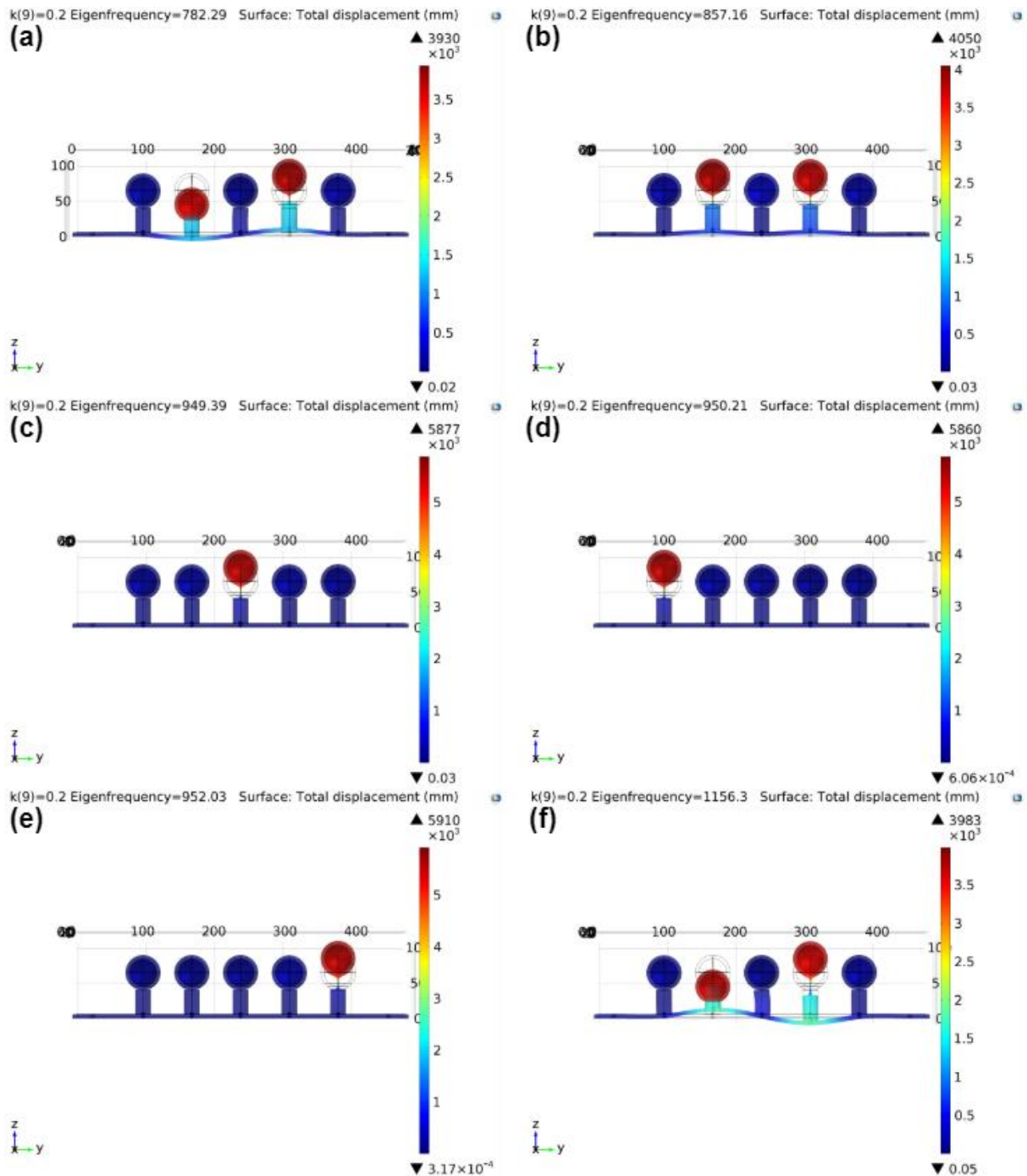


Figure 7. 14: Interested mode shapes of the unit cell with 10% acrylic plastic filled five-resonator modes

In the case of multiple resonators (fully filled) with the acrylic plastic particles, the unit cell's dispersion relations and frequency response are demonstrated in Figure 7.15. Interestingly, increased resonators on the unit cell have impacted the first mode of the unit cell and have taken the frequency level to higher values, as seen in the first dispersion line of Figure 7.15-c.

Filled resonators have controlled the lower modes of the unit cell and increased coupled structure phenomena.

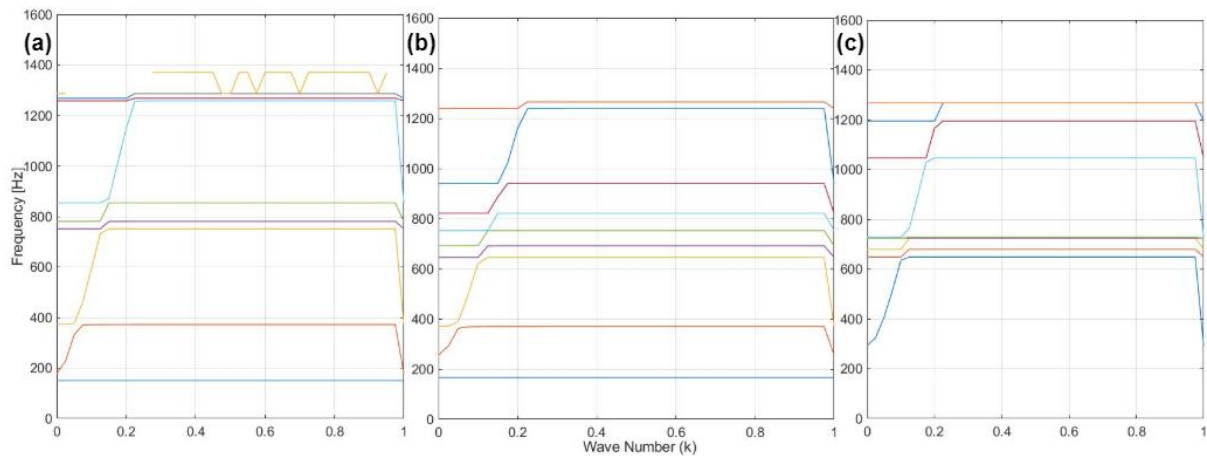


Figure 7. 15: The 47.5% acrylic plastic filled multiple resonators in an array with 70 mm distance: (a) two resonators, (b) 4 resonators, (c) five resonators

Even though the materials filled in the resonator have been the same, the number of resonators in the array has interesting properties. This is studied in the next figure. The fully filled five resonator arrangement has been analysed, and Figure 7.16 illustrates the coupled structure modes. Previously given dispersion lines in Figure 7.15-c has shown a compressed dispersion lines area between 600-800 Hz. Since these modes have been coupled, the eigenfrequencies at a specific wave number have been close. Using a resonating unit cell showed increased coupling within the structures used in the unit cell modelling.

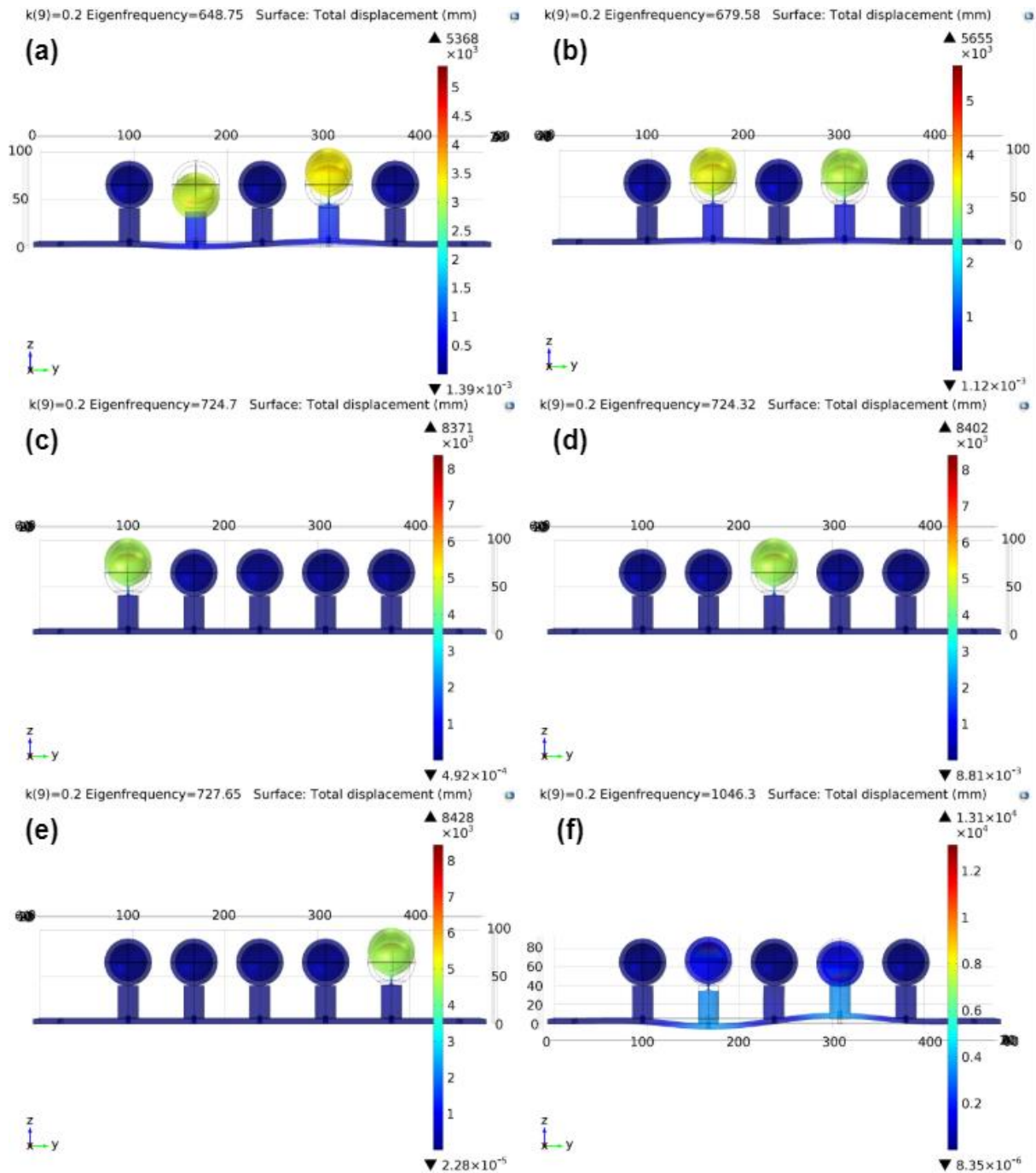


Figure 7. 16: Interested mode shapes of the unit cell with 47.5% acrylic plastic filled five-resonator modes

In general, the proposed unit cell has shown resonance properties which would increase the opportunity of the coupling behaviour within the placed resonators. Also, even though the filling materials have occupied the same volume, their equivalent material properties have been decisive in the mode shapes and the way the dispersion lines are organised. The filled equivalent isotropic materials have controlled the coupling between the structures in the unit

cell in the cavities. The eigenfrequencies (or, in general, the modes) can be effectively tuned, as seen in the given results, by changing the number of resonators on the unit cell and the filled material opportunity. Similarly, the geometry or the material properties of the proposed compositions have been studied in earlier research, which has resulted in tunability improvements [6].

No lossy material modelling has been studied in the unit cell analysis. Thus, the dispersion relation are plotted against purely real Bloch wave number indicating the location of the bandgaps.

In each case shown in Figure 7.12-f and Figure 7.16-f, the next eigenfrequency experienced section has been through the thickness of the unit cell, resulting in conversion points in the dispersion lines. The conversion points have been analysed and explained in Chapter 5 through the examples of the bare unit cell and the resonator attached unit cell dispersion relation analysis results.

According to the figures in this subchapter, coupled resonators can be used to control the conversion points within the modes and achieve effective bandgap.

7.3- Numerical Analysis of Finite Beam and Resonator Filled with Metal Particles

In this section, container filled with steel granular structure is analysed with discrete element method, and the corresponding equivalent isotropic solid structure modelling has been implemented through the explained methodology in Chapter 3. This subchapter aims to evaluate the frequency sweep analysis using COMSOL Multiphysics for equivalent isotropic structure placed into resonators attached to the finite beam. The equivalent medium is used here to replace steel particle using DEM-FEM hybrid approach.

Single Resonator Impact On the Base Structure

In this part of the thesis, various filling fractions of steel particles as equivalent isotropic solid structures are placed in the single resonator, and the stations of the resonator on the beam are changed by 10 mm to analyse the frequency response of the structures.

Figure 7.17 shows the equivalent structure numerical analysis results for the 10% steel particle attached single resonator case trends compared to the empty resonator attachment cases. In the empty resonator cases, the resonator and the beam have been coupled structures in most cases. The equivalent structure filling has shown another solid structure behaviour in the resonator and has added resonance peak to the third bending mode of the main structure (around 800 Hz) in the frequency sweep in all arrangements. The resonance frequency of the beam has been shifted to a lower frequency level (by around 10%) while the frequency response amplitude has also been reduced (by 1%). On the other hand, comparing the cases with/without particle filling in the resonator cavity at the first bending mode of the beam slight shift of the resonant frequency (by 1%) is observed. The mode has been impacted by the mass of the granules in the cavity and the smallness of the shift is expected due to the small added mass.

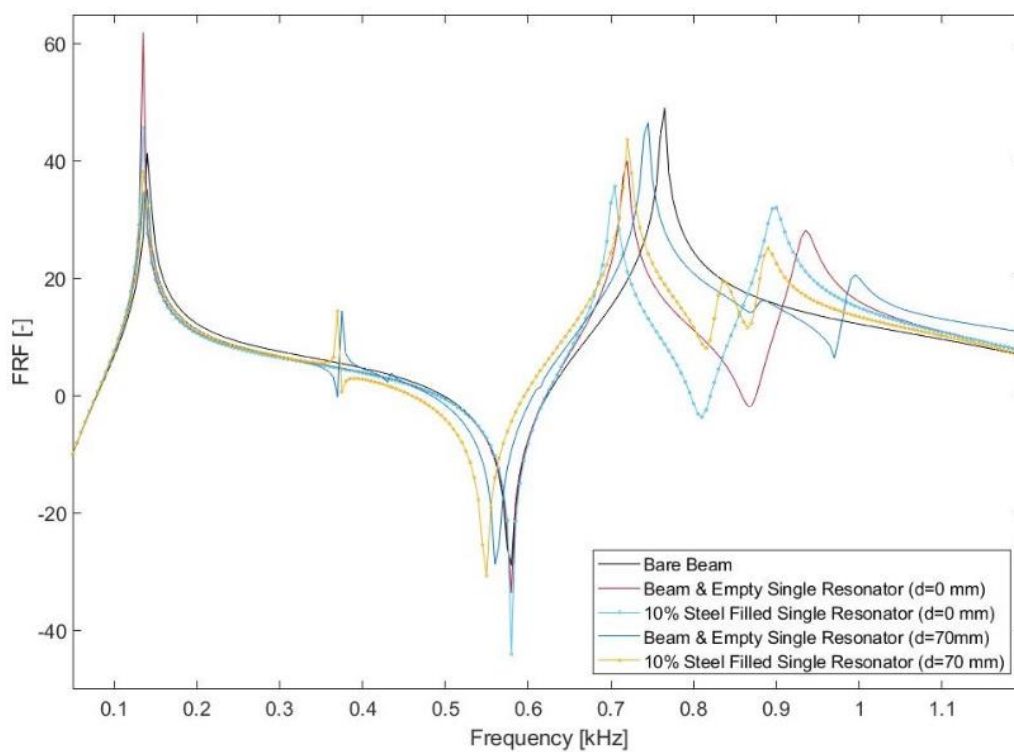


Figure 7. 17: 10% steel granule-filled single resonator placement cases

The numerical analysis results for the single resonator on the beam with 25% of steel particle filling replaced with an equivalent isotropic structure are shown in Figure 7.18. All filled resonator arrangement cases have preserved the coupling between the structures. However, mode shapes have seemed to be reversed. The main mode shape has been taken to a higher

frequency while the lower eigenfrequencies, for instance, at around 0.55-0.65 kHz, have been taken to a lower frequency. A mode conversion has been noted around the structure's natural frequency and dependant on the phase shift, which has been expressed in Chapter 2 [187]. In this case, oscillating structures in front of the destructive interference, the excitation amplitude, would help to convert one mode into different mode shapes [188]. Mode shape conversions have been demonstrated in Chapter 5 for the empty resonator cases.

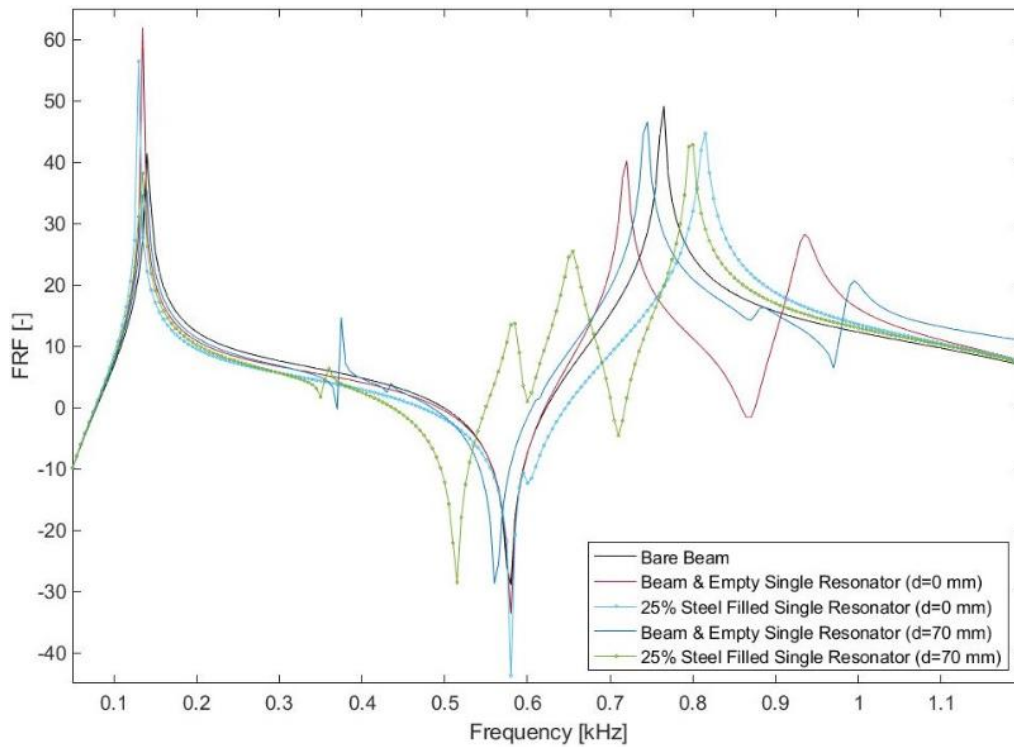


Figure 7. 18: 25% steel granule-filled single resonator placement cases

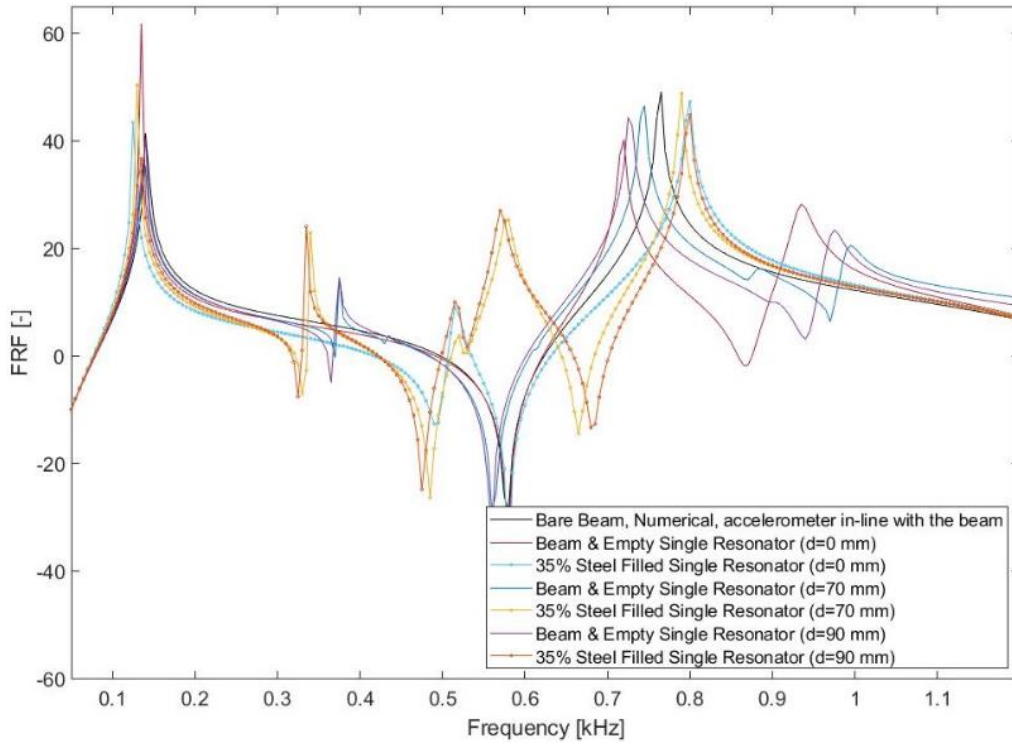


Figure 7. 19: 35% steel granule-filled single resonator placement cases

Figure 7.19 illustrates results for the 35% steel particle filled case. Placing this filling into the resonator has increased the eigenfrequency of the mode around the third bending mode of the beam. However, mode conversion has been observed in these results, similar to the previous case. Lastly, placing the filled resonator away from the centre of the beam increased the magnitude of the second bending mode of the beam. This would be related to the resonator’s presence near the nodal points.

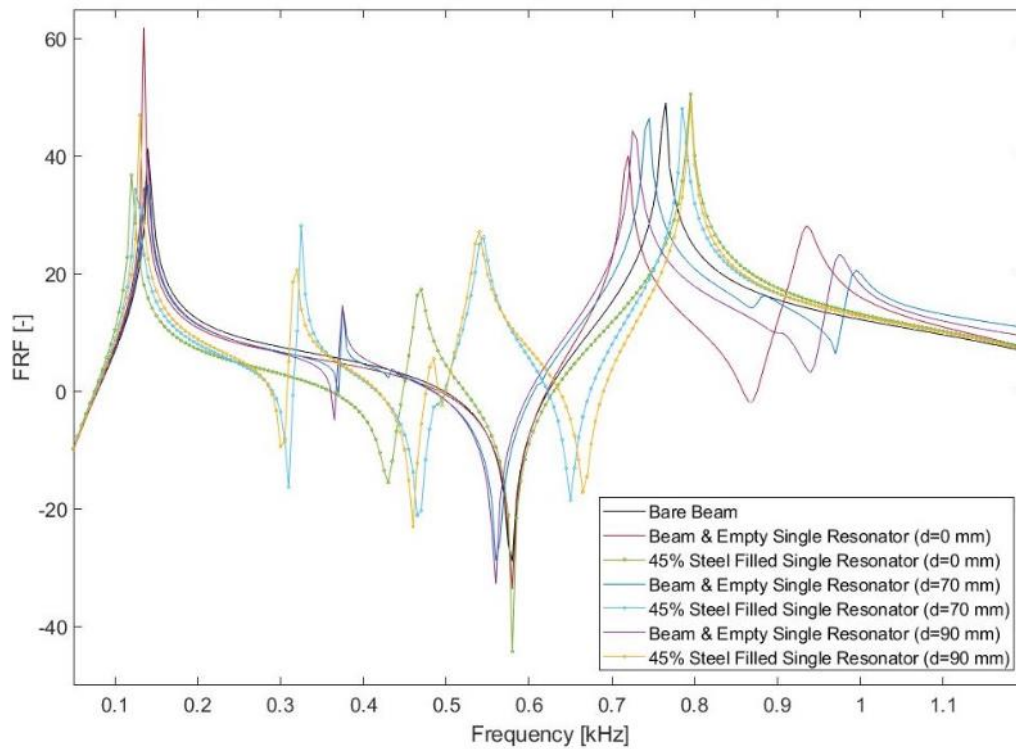


Figure 7. 20: 45% steel granule-filled single resonator placement cases

Figure 7.20 has the result of the equivalent isotropic structure for the 45% steel-filled single resonator. The main mode of the beam has been taken to a higher frequency level. Figure 7.21 illustrates a 62% filling fraction, the fully filled resonator case. The same analysis outcomes have been observed in this case, as well.

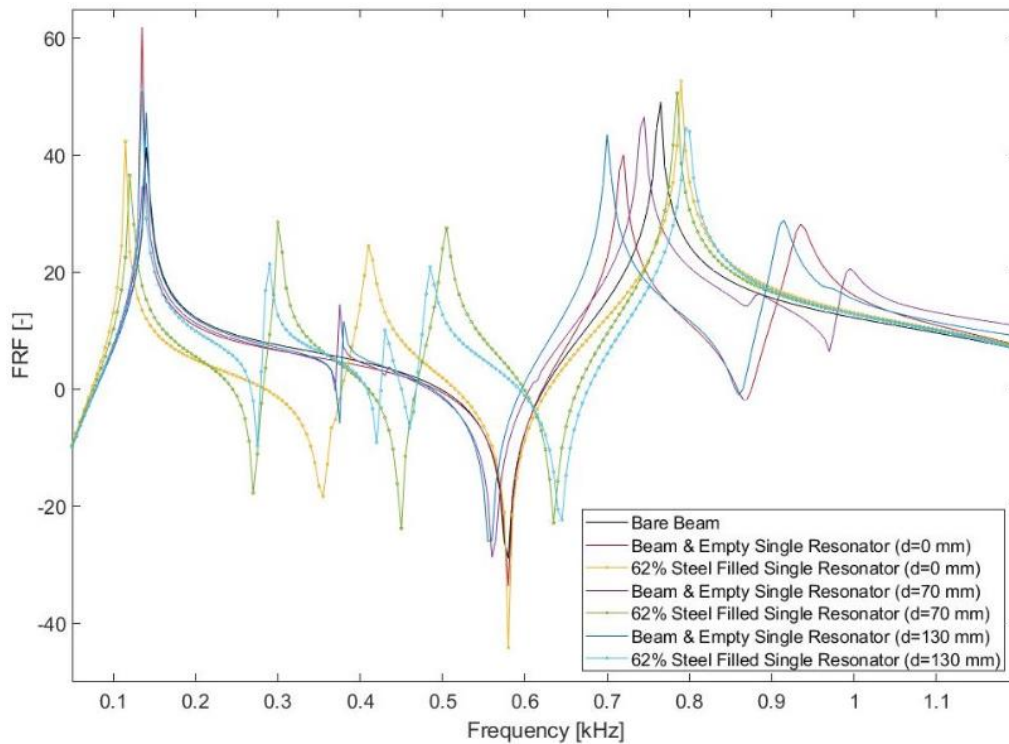


Figure 7. 21: 62% steel granule-filled single resonator placement cases

Overall, single resonator placement results have shown interesting behaviour; while the filling fraction in the resonator has been increasing, the frequency response analysis results have shown the mode conversion around the third bending mode of the beam. Also, the eigenfrequency level has been taken to higher frequencies which have built a small frequency gap around 0.8 kHz.

Multiple Resonators Impact on the Base Structure

This part of the subchapter is dedicated to evaluating the frequency response numerical analysis of the multiple resonator arrangement on the beam by adding the equivalent isotropic structure material properties.

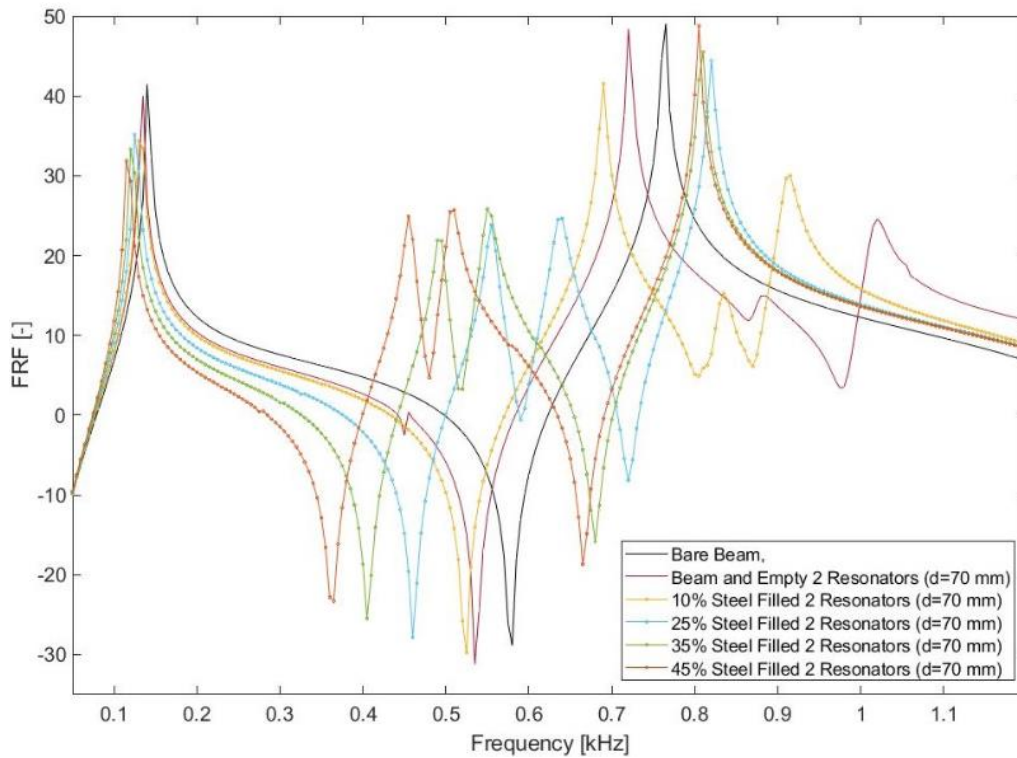


Figure 7. 22: Steel granule-filled two-resonator placement cases

Figure 7.22 demonstrates the two resonator arrangement results. Various filling fractions are included in this result. The beam resonance is observed at around 0.65-0.7 kHz levels at the empty and the 10% filled resonator cases. However, increased filling fraction results in the beam mode shifted to higher frequencies (around 0.80 kHz) and coupled structures behaviour has been seen at lower frequencies.

Figure 7.23 shows three resonators arrangement for various filling fraction numerical analyses. The filling fraction of the 10% analysis has shown similar properties to the case of the empty resonator; only the high-frequency mode has been taken to a lower frequency level. This result demonstrates that by increasing the filling fraction the frequency band showing coupling phenomena has been widened while the second bending mode of the beam is shifted to a lower frequency level.

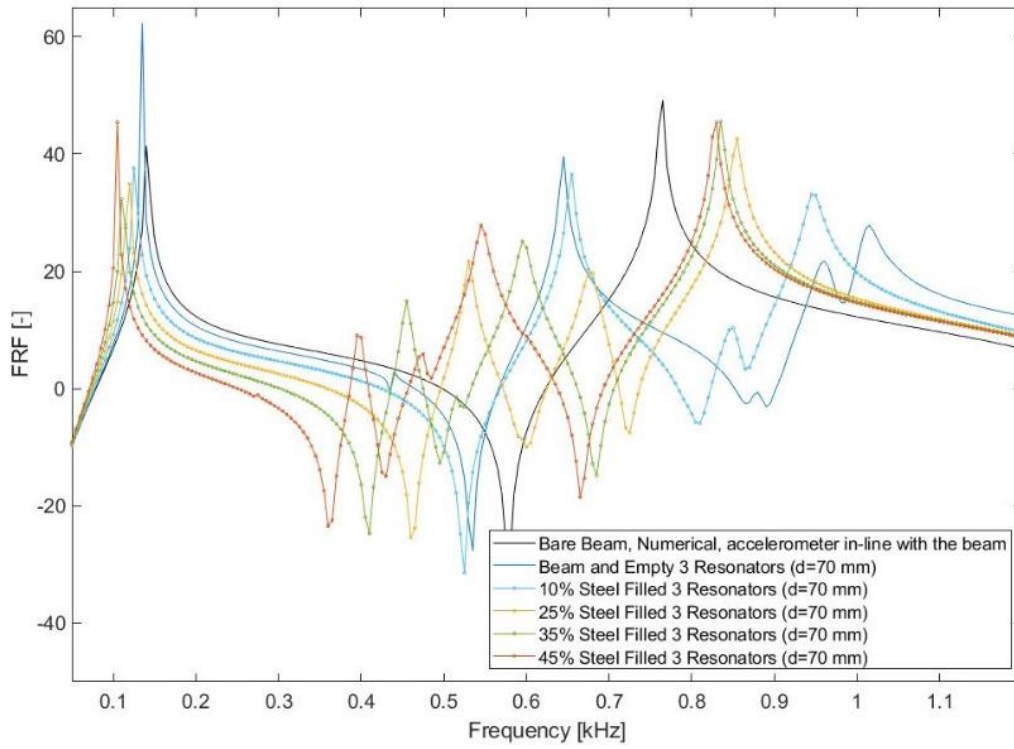


Figure 7. 23: Steel granule-filled three-resonator placement cases

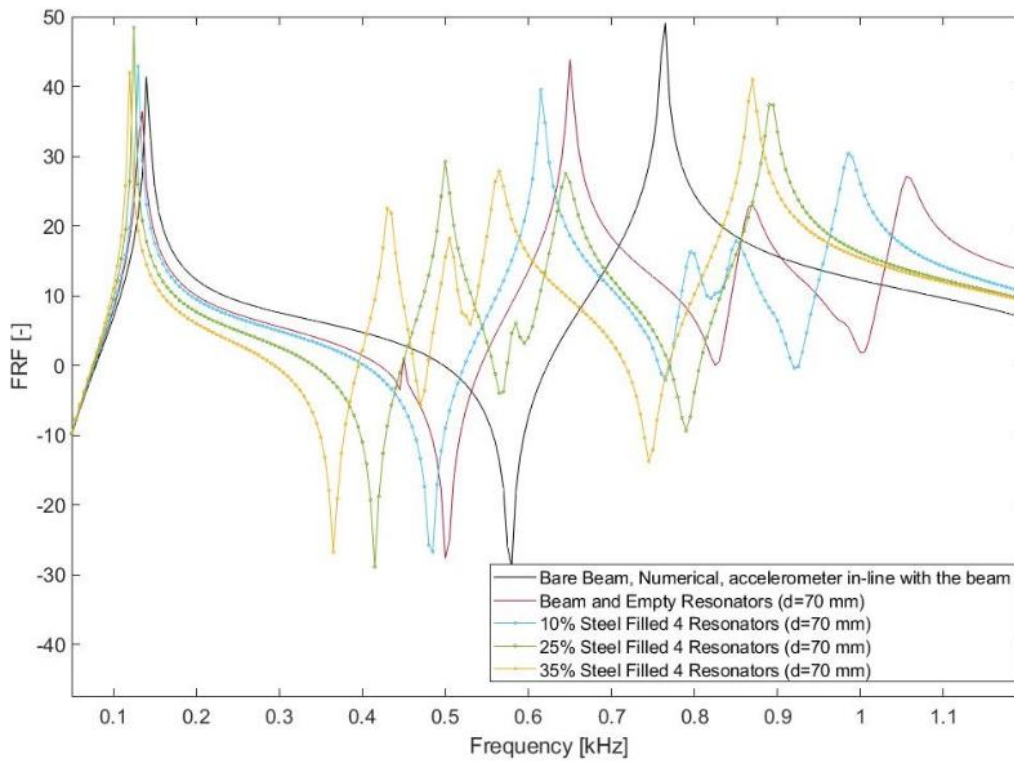


Figure 7. 24: Steel granule-filled four-resonator placement cases

Placing the four resonators with various filling fractions on the beam result is given in Figure 7.24. According to the results, the arrangement of four resonators opens a frequency gap at the third bending mode of the beam. In addition, the beam's second bending mode has disappeared in the filled resonators. Coupled resonators have been observed in these analyses, and mode conversion has also been observed.

Since the number of steel granules in the experiments is only enough to fill the 10% and the 25% filling fractions for the five-resonator arrangement, these two cases have been analysed in the numerical analysis (Figure 7.25). Similar to the previous case, multiple resonator arrangements with filling at both fraction levels have shown the frequency gap at the third bending mode of the beam. Also, the beam's second bending mode has disappeared in these cases, while the empty resonator case has shown this mode.

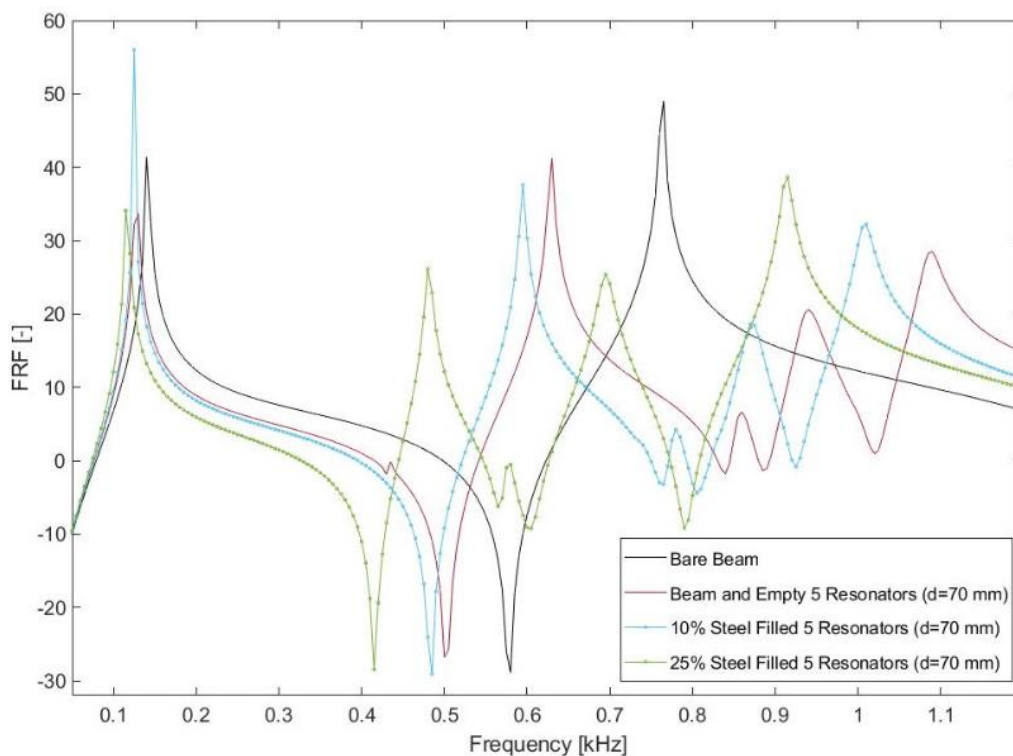


Figure 7. 25: Steel granule-filled five-resonator placement cases

Overall, multiple resonators filled with steel granules numerical analysis have shown the mode conversion and frequency gap while experiencing the coupling between them. However, the filled resonators have not greatly impacted the frequency response amplitude.

7.4- Numerically Analysed Plastic Granule Filling

Similar to the previous subchapter, acrylic plastic particles corresponding to equivalent isotropic solid structures is placed into single and multiple resonators that impact the frequency response of the beam and studied in this subchapter.

Single Resonator Impact on the Base Structure

Acrylic plastic and POM particles are placed in the single resonator, which is placed on the beam in order to analyse the frequency response of the whole structure.

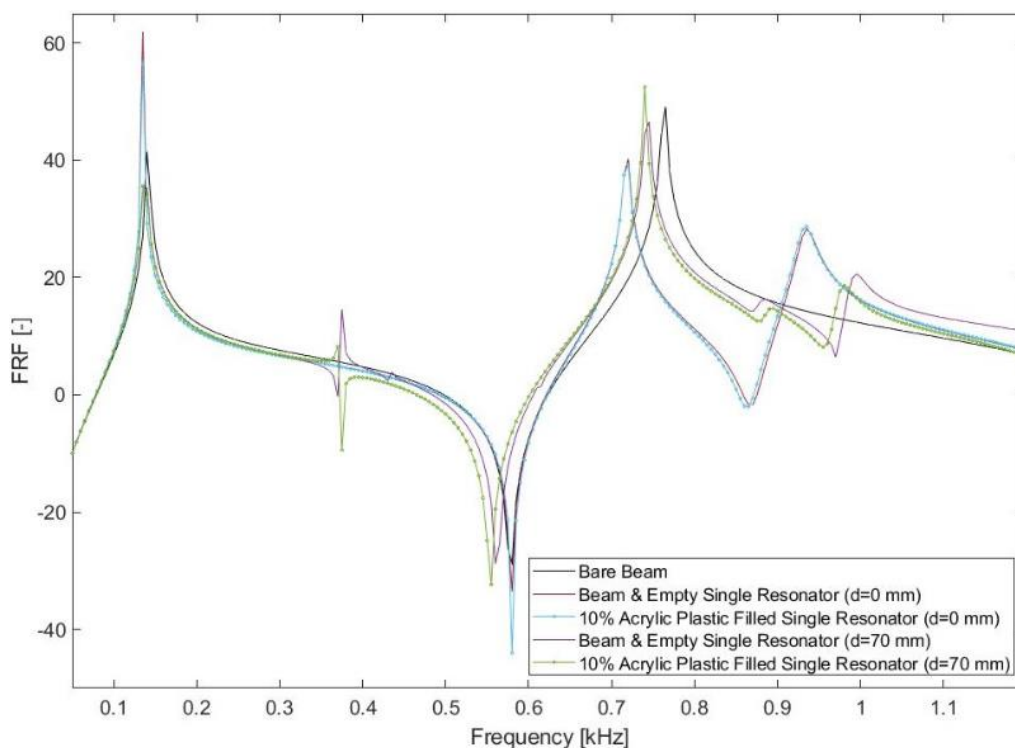


Figure 7. 26: 10% acrylic plastic granule filled single resonator placement cases

Figure 7.26 is prepared using the 10% acrylic plastic-filled resonator numerical analysis results in addition to the same arrangement of empty resonator case trends. In general, frequency sweep trends of the filled resonator have been similar to the empty resonator cases. However, 70 mm placement of filled resonator has shown higher frequency response which might be accelerating response of the granules at that excitation amplitude. Also, 70 mm is the antinode point of the second bending mode of the beam, which is the reason for the increased frequency response at around 0.375 kHz.

Figure 7.27 shows the 25% acrylic plastic filled single resonator numerical analysis results. According to the results, a centrally positioned filled resonator has shown an eigenfrequency reduction impact on the beam. At the same time, there is no observed additional peak in the frequency response regarding the filled structure in the resonators. However, the 70 mm resonator placement has shown that additional peak, the coupled structure mode. Also, this arrangement has illustrated narrowed frequency gap at the third bending mode of the beam.

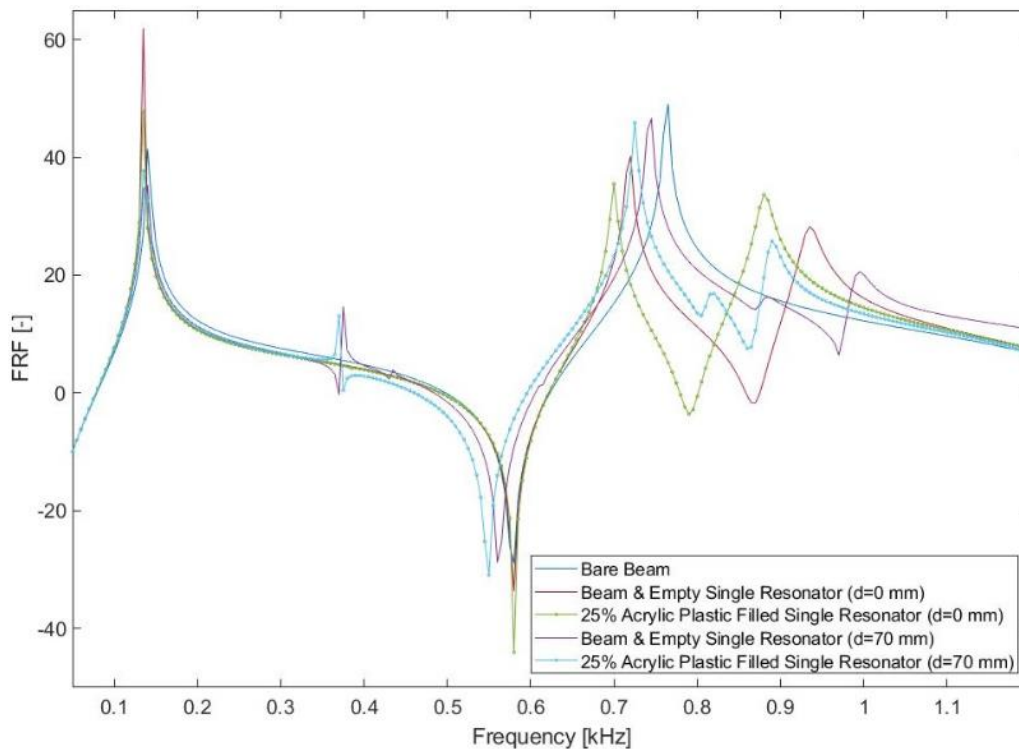


Figure 7. 27: 25% acrylic plastic granule filled single resonator placement cases

Figure 7.28 illustrates the 35% acrylic plastic-filled single resonator placement case frequency response trends. This figure has many similarities with the previous one. Therefore, the previous evaluation is acceptable for the 35% filled case results. The narrowed frequency gap area has been further narrowed in this case, which means the eigenfrequency peaks have been shifted towards each other. In addition, the magnitude of beam's second bending mode has increased in the 70 mm placement of the filled resonator.

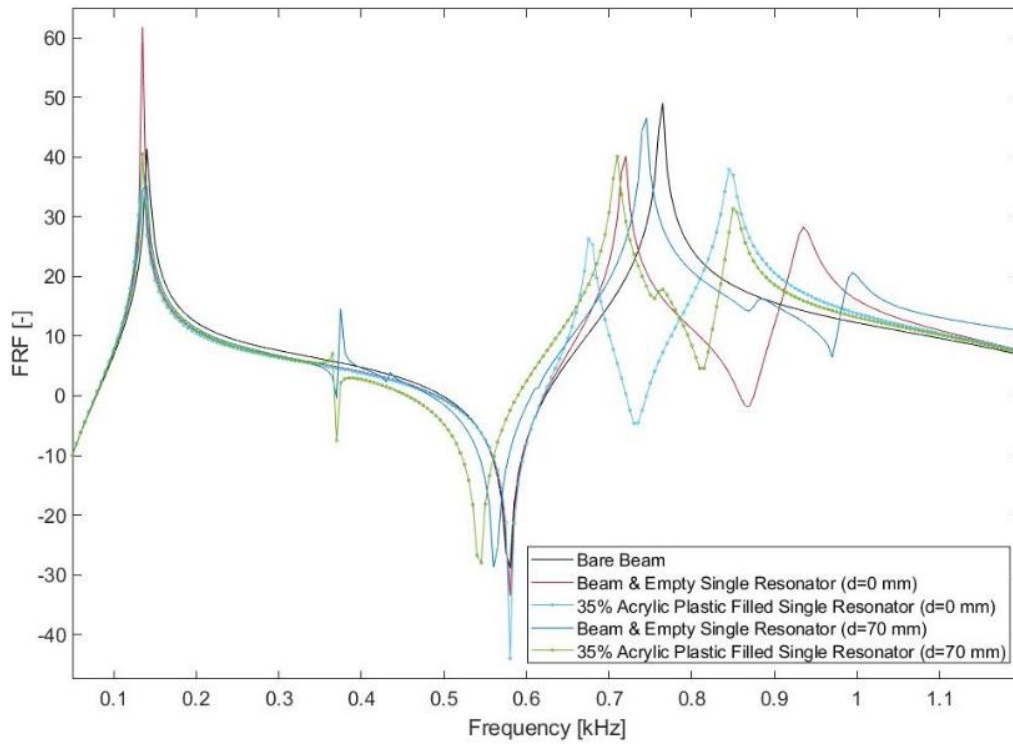


Figure 7. 28: 35% acrylic plastic granule-filled single resonator placement cases

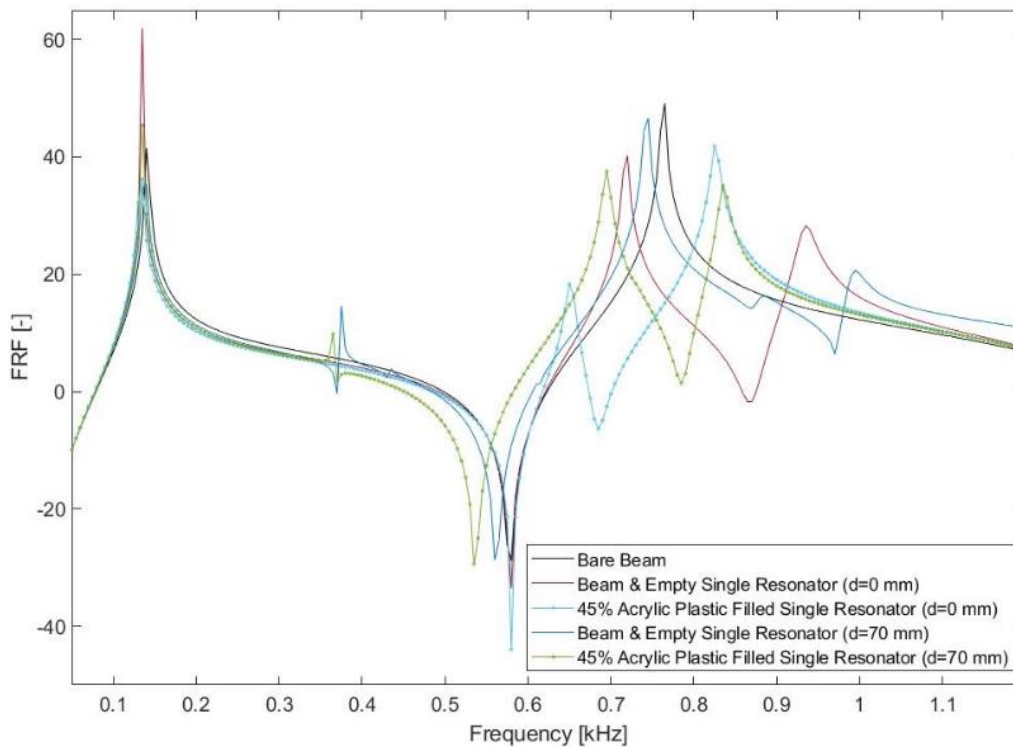


Figure 7. 29: 45% acrylic plastic granule-filled single resonator placement cases

The 45% acrylic plastic-filled single resonator placement on the beam frequency response analysis has been conducted numerically, and Figure 7.29 is given for the illustration of the frequency response. According to the results, a centrally positioned filled resonator has shown mode conversion compared to the same empty resonator case placement. In this case, the frequency response amplitude has been slightly impacted. Also, with particle (equivalent isotropic structure) attachment in the resonator, the frequency gap has been narrowed in the 70 mm placement case. The same explanations can be accepted as valid for the next figure (Figure 7.30) to evaluate the fully filled resonator placement frequency response analysis.

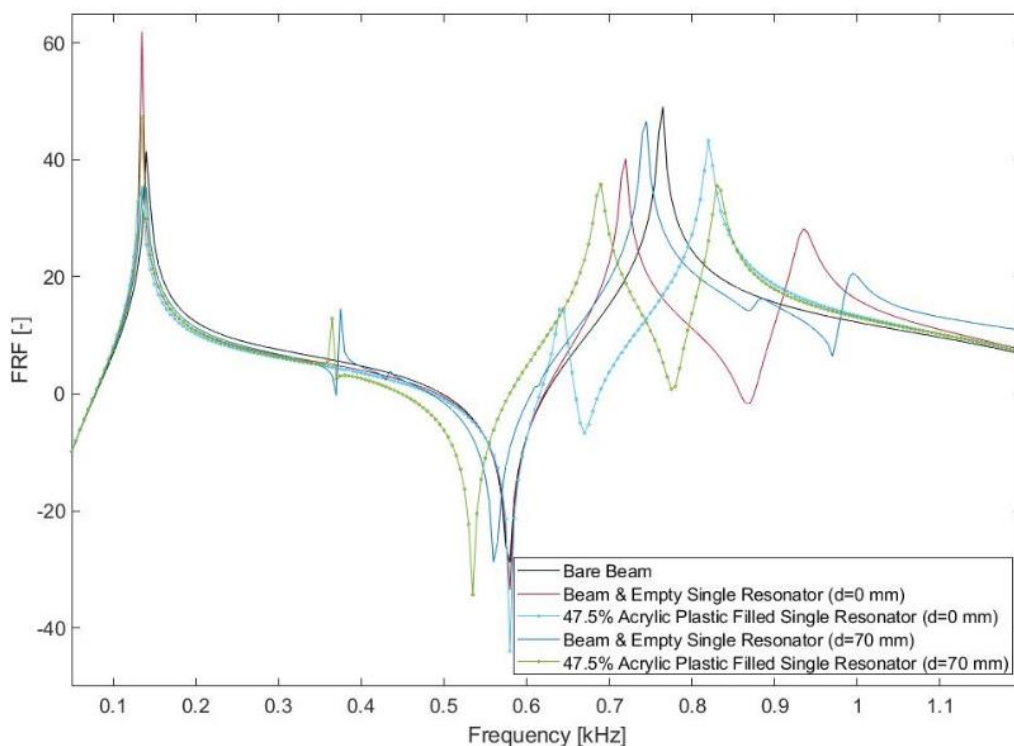


Figure 7. 30: 47.5% acrylic plastic granule filled single resonator placement cases

Figure 7.31 shows the frequency response analysis of the 7.5% POM-filled single resonator arrangement results. As seen from the figure, the trends for the filled resonator cases have been similar to the empty resonator cases. Amplitudes over the frequency levels have been changed by particles, in this case, the equivalent isotropic solid structures.

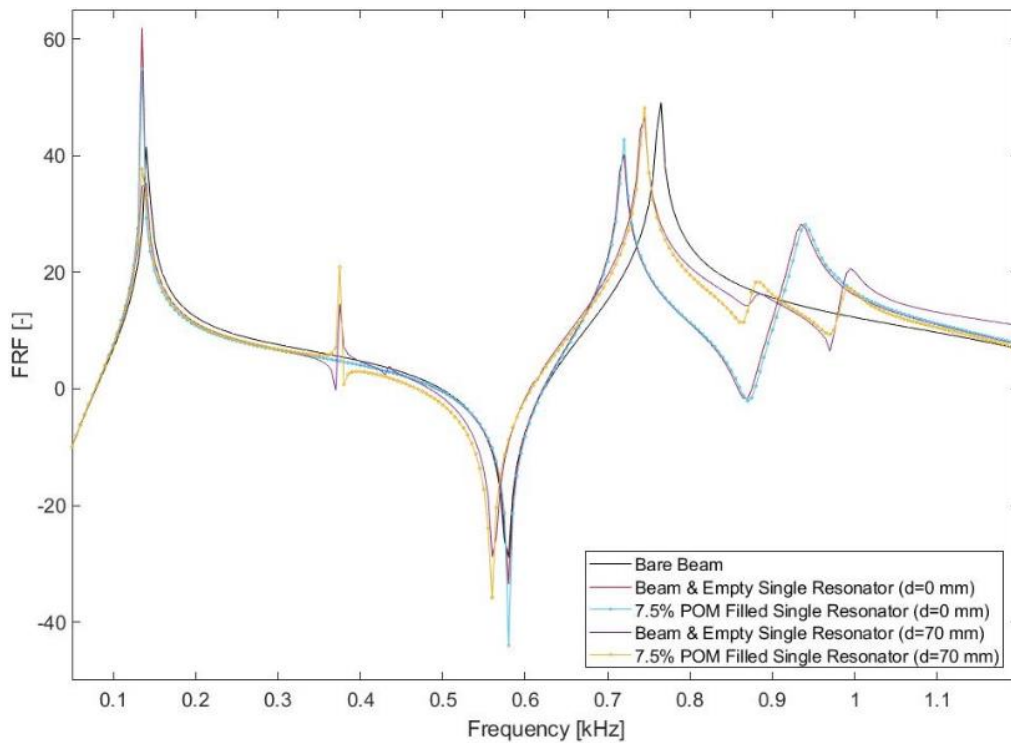


Figure 7. 31: 7.5% POM granule filled single resonator placement cases

In general, similar to the steel particle attached single resonator placement frequency response analysis of the beam, the mode conversion [187]–[189] has also been analysed in the plastic particle cases.

Multiple Resonators Impact on the Base Structure

Multiple resonators filled with plastic particles are aimed to analyse the beam numerically. Various filling fractions and a various number of resonators are planned in this part of the subchapter.

In the first example, Figure 7.32 is prepared the two resonator arrangement analysis results using both the empty resonator and the filled resonator cases. As seen from the figure, the frequency response amplitude has been reduced by increasing the resonator filling fraction, which stiffening the material corresponding to the granular structures in the filling. In addition, the increased filling fraction has narrowed the frequency gap around the third bending mode of the beam. Lastly, the response of the coupled structures has been accelerated.

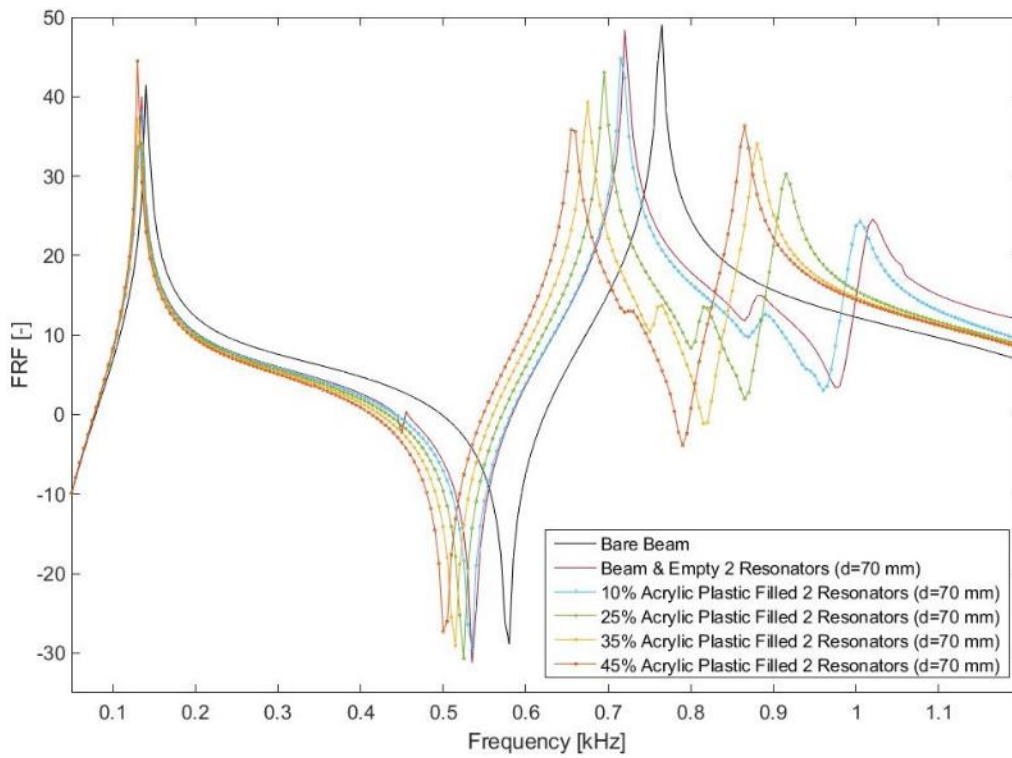


Figure 7. 32: Acrylic plastic granule-filled two-resonator placement cases

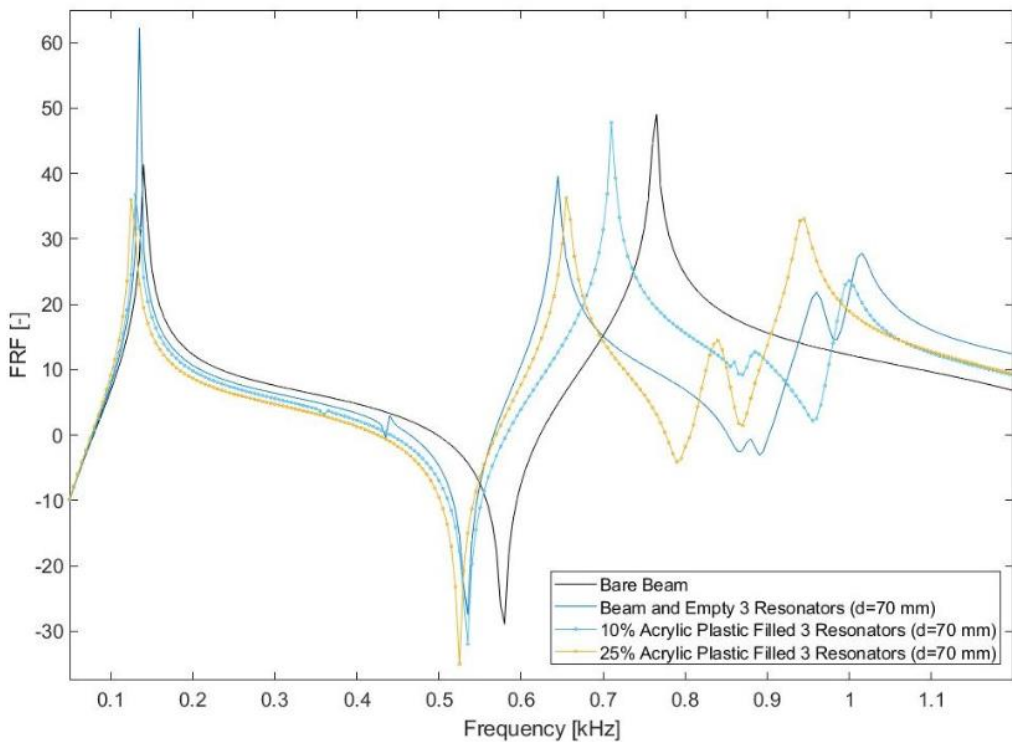


Figure 7. 33: Acrylic plastic granule-filled three-resonator placement cases

When the three resonators have been placed on the beam, either filled with the plastic particles or left empty, they have shown coupled resonators impact, as shown in Figure 7.33. However, the increased filling fraction has reduced the coupling properties in addition to the beam's frequency response amplitude. Unfortunately, the filling has not been beneficial in increasing the frequency gap at around 0.75 kHz frequency levels.

Since the amount of acrylic plastic granules is only enough to fill the 10% of the resonator cavity for the four and the five resonators, the next result shows one filling fraction trend in addition to the empty resonator arrangement trends.

Figure 7.34 is prepared using the frequency response analysis results of the 10% acrylic plastic filled and empty four and five resonator arrangements. The four-filled resonator arrangement has taken the system's eigenfrequency and coupled resonator properties to lower frequency levels compared to the empty four resonator case. Similarly, the frequency levels have been taken to lower frequencies in the five filled resonators case while changing the frequency response amplitude.

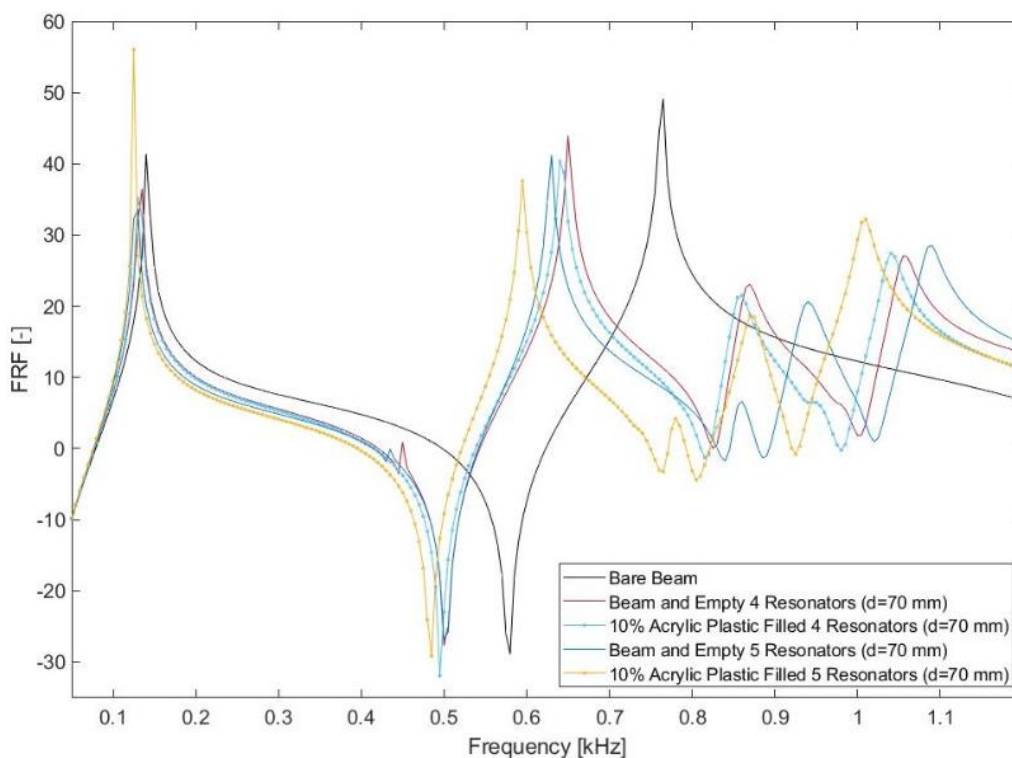


Figure 7. 34: Acrylic plastic granule filled four- and five-resonator placement cases

The mode conversion and the restricted coupling phenomena have been the generalised overall outcome from the multiple resonators with added acrylic plastic granules. Additionally, some cases have narrowed the frequency gap obtained in the empty resonator cases. Lastly, in the four and five resonator arrangements, the frequency response amplitudes have been slightly reduced by the granules in the resonator.

7.5- Experimental Results for the Resonators Filled with Steel Granules

In order to evaluate the effect of the steel granules at various filling fractions and the number of cavities placed on the beam, experimental analyses are planned at the shaker-damper test rig at similar conditions given in Chapter 6. The frequency sweep applied in these tests is between 50 Hz and 1200 Hz by increments of 2 Hz. According to the evaluations, the arrangements given in the figures below have been the most beneficial options. Therefore, this subchapter will evaluate steel particle attachments at various filling fractions while placing the filled resonator(s) on the beam at various stations. Evaluating the steel particle performance in the experimental studies allows one to compare them with numerical analysis of steel particle equivalent structure modelling analysis.

Single Resonator Impact on the Base Structure

Steel particle-attached resonators at different filling fractions are studied by changing the resonator place on the beam in this part of the subchapter. Resonator-1 is used for these studies.

Figure 7.35 represents 10% filled single resonator on the bare beam placement cases for two options: centre placement and 70 mm placement. According to the figure, a centrally positioned filled resonator has reduced FRF magnitude and shifted the frequency peak from around 800 Hz to a lower frequency which has been observed in numerical analysis, as well. The impact on the natural frequencies of the beam is noted to be small. 70 mm placement resonators have shown that the reduction in the frequency response amplitude with metal granules is similar to that with the empty resonator case. Also, granular structure effect at the third bending mode has provided smaller frequency peaks than the numerical analysis results. In this case, the experimental result and the numerical result do not match very well.

This might be related to the particle loss properties of the granules which have not been modelled accurately in the numerical analysis. In addition to this, the granules are discrete structures that might experience the nonlinear behaviour at various frequency levels. Also, the particle placement in the cavity changes the stiffness of the filled resonator which reduces the coupling between the dynamic properties of the resonator and the granular filling.

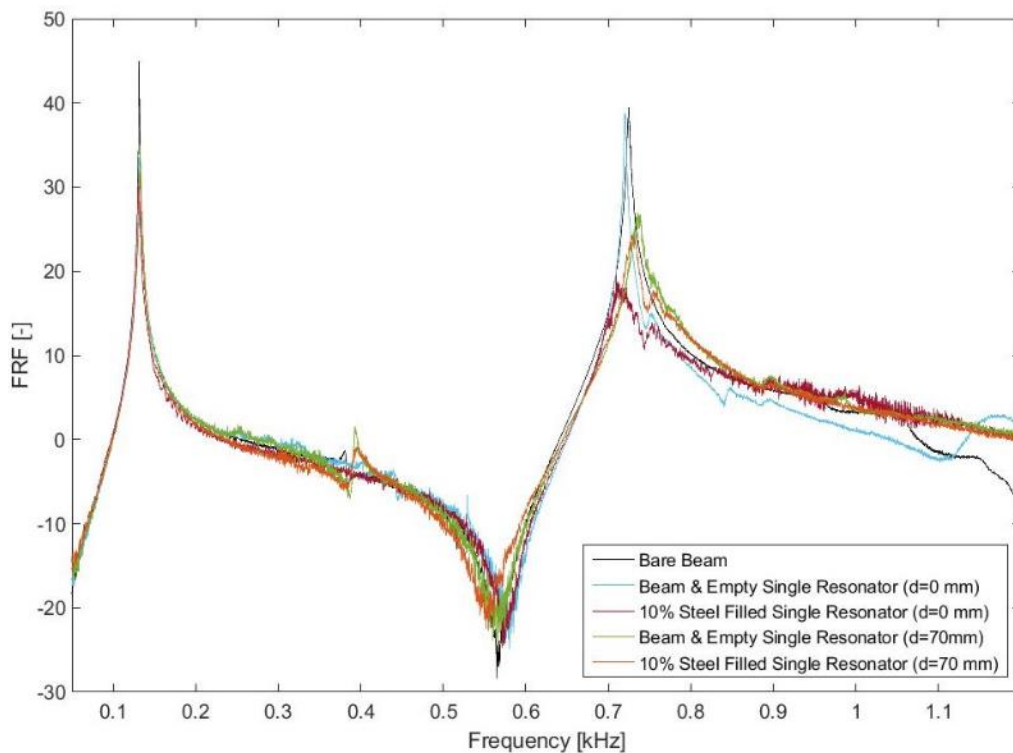


Figure 7. 35: 10% steel granule-filled single resonator placement cases

Figure 7.36 illustrates the filling fraction of 25 in the single resonator case. When a single resonator is filled with steel granules at 25%, the coupled beam-resonator mode takes place in the frequency response. This is observable from the divided frequency peaks between 0.7 and 0.85 kHz. In addition, granular structures attached to the resonator have greatly reduced the frequency response amplitude, and the amplitude reduction has been greater than in the previous case.

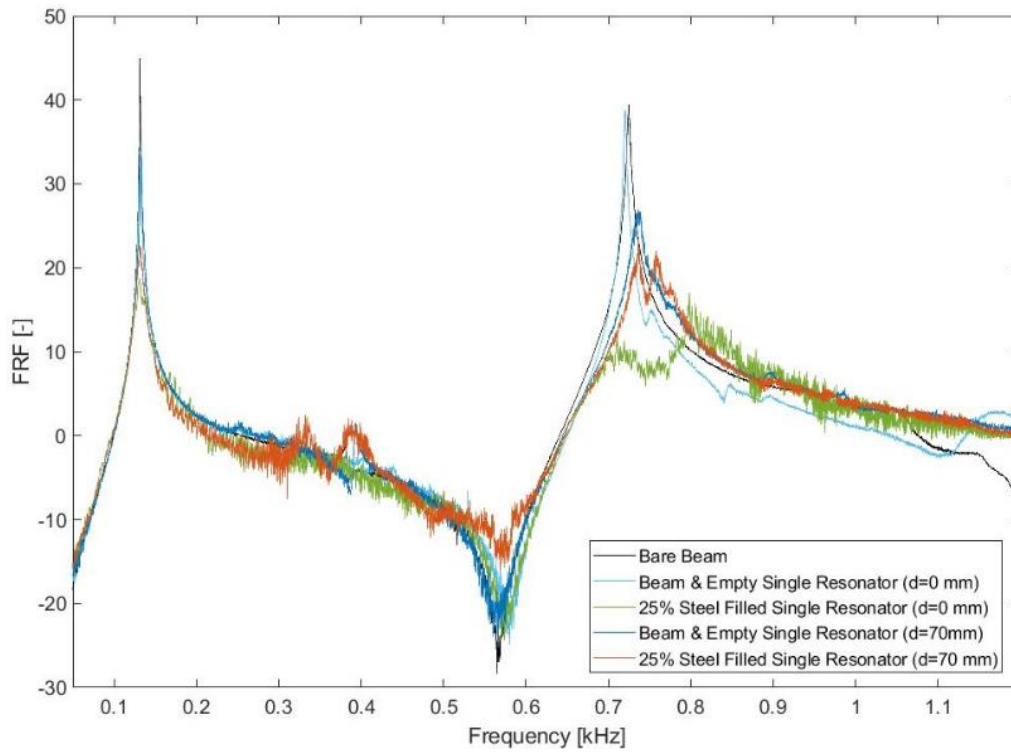


Figure 7. 36: 25% steel granule-filled single resonator placement cases

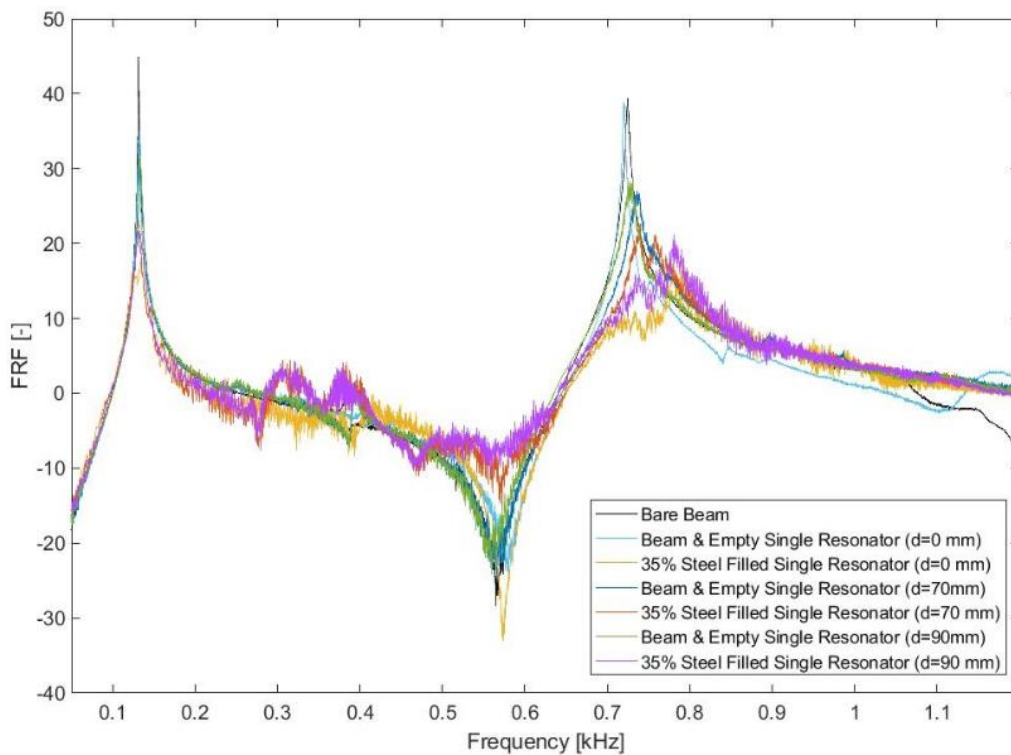


Figure 7. 37: 35% steel granule-filled single resonator placement cases

Figure 7.37 includes the 35% steel granules filled single resonator placement cases on the beam at the centre, 70 mm, and 90 mm stations. Similar to the previous cases, the granular filling has reduced the frequency response amplitude. This means the granular interaction has converted the excitation energy to kinetic energy between the granules. Also, because of the kinetic energy level changes, they change the momentum in general. Specifically, the second bending mode of the beam (around 0.4 kHz) has been affected by the presence of the granules. The magnitude of mode of the beam has been increased, which might indicate the nonlinear properties of the granular structures.

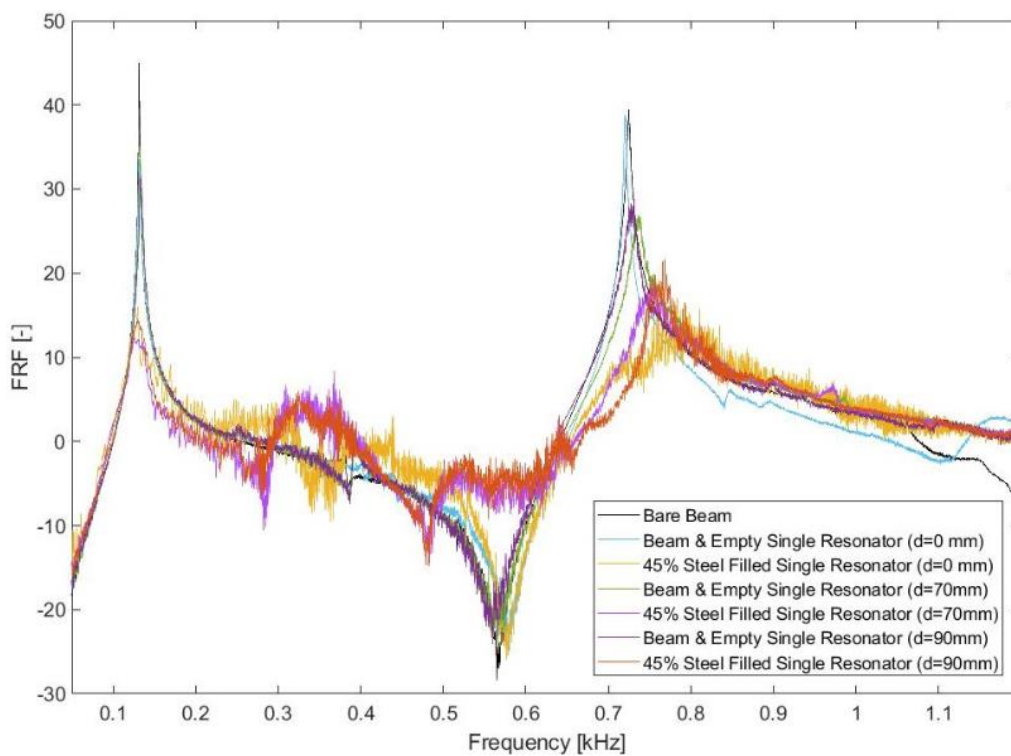


Figure 7.38: 45% steel granule-filled single resonator placement cases

Figure 7.38 illustrates the 45% filled resonator impact on the beam. In addition to the granular impact on the frequency response when the resonator has been filled at 45% of its volume, the beam's second bending mode has been affected. The coupled beam-resonator mode is observed at around 400 Hz. The granules experience high impact since the number of granules and the antinode placement of the resonator, and it increases the nonlinearity within the granules. Therefore, it is expected that the noise in the data will be high. This impact is similar to the previous case as shown in Figure 7.37.

A fully filled resonator case of 62% filled resonator has been available for only a single resonator case, and the frequency response analysis results are given in Figure 7.39. The resonator attachment stations have been at the beam's centre, 70 mm, and 130 mm. According to the figure, the fully filled resonator has less nonlinearity than in the previous cases. The granules stayed in contact and reduced the movability since the volume was filled with them. Therefore, the trends for the granular structure attached resonators have shown similar behaviour through the frequency sweep to the case empty resonator.

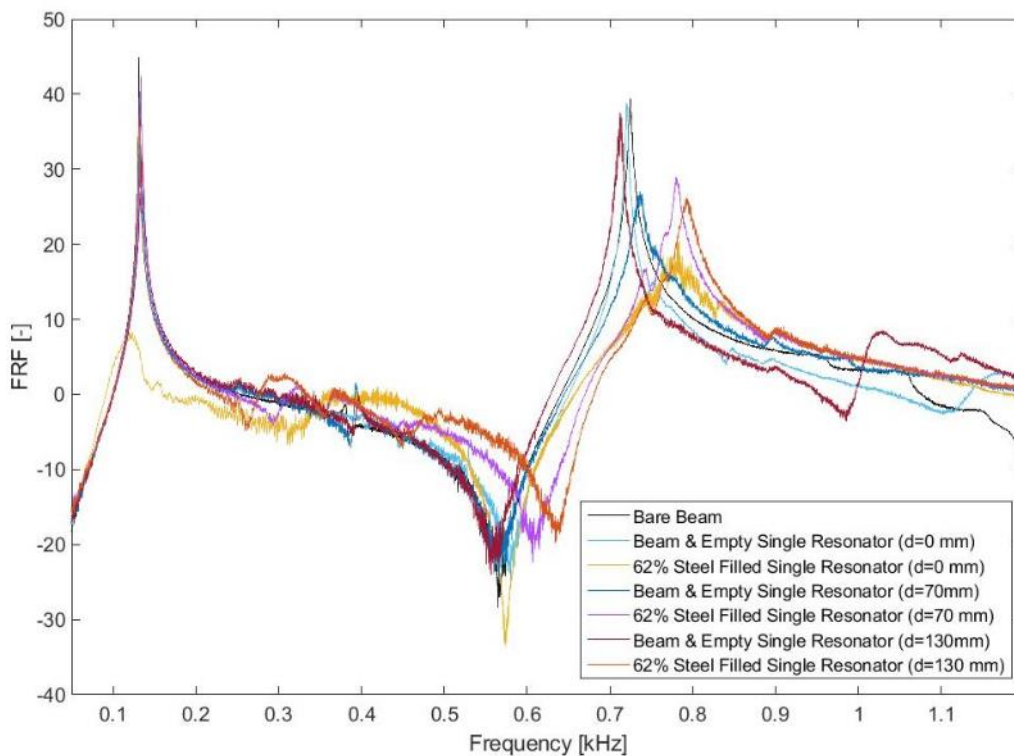


Figure 7. 39: 62% steel granule-filled single resonator placement cases

Overall, single resonator placement with various steel fillings inside the cavity has frequency response amplitude controlling properties. The kinetic energy conversion and momentum changes have mostly been experienced through the lower filling fraction cases. Also, specifically, the second bending mode of the beam has been more visible in the higher filling fractions cases. Lastly, the location of the resonator on the beam has impacted the dynamic properties of the overall system similar to the empty resonator cases.

Multiple Resonators Impact on the Base Structure

Multiple resonators (two, three, four and five) are placed on the beam to evaluate the number of resonators, their placements and various filling fractions for the steel particles in terms of their effectivity to control the dynamic properties of the beam. Also, in this part of the subchapter, coupled resonators are thought to be experienced since the filled resonators are placed in specific arrangements on the beam.

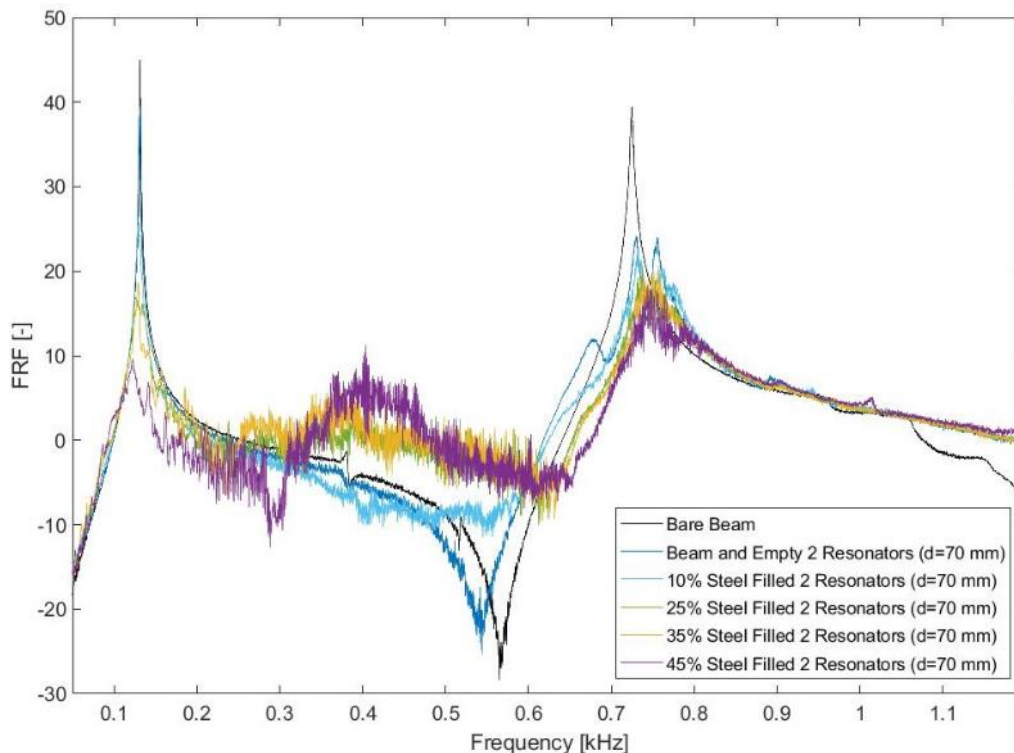


Figure 7.40: Steel granule-filled two-resonator placement cases

Figure 7.40 shows two steel-filled resonators placed with beam frequency response results. Empty resonators are coupled with each other and with the beam. As the particle filling increases, the coupling is controlled, and the frequency response amplitude is reduced. While the amplitude of the third mode is reduced, the magnitude of the second bending mode of the beam has been increased with the increasing number of particles in the cavity. In general, the beam has been stabilised with placed particle dampers.

Similar to the previous case, the beam response is controlled with the presence of particle dampers. However, in this case, one resonator is placed at the centre of the beam. Therefore, while the response of the beam is reduced, which is supported by [190], the frequency of the

third mode is also moved to a higher frequency level with increased particle amount in the cavity. Figure 7.41 shows that the peak frequency response of the beam is flattened. Coupled beam and particle damper modes have been taken to the lower frequencies. Similarly, to the previous cases, these results have noisy data trends since the particle amount, particle damper placement results in high impact.

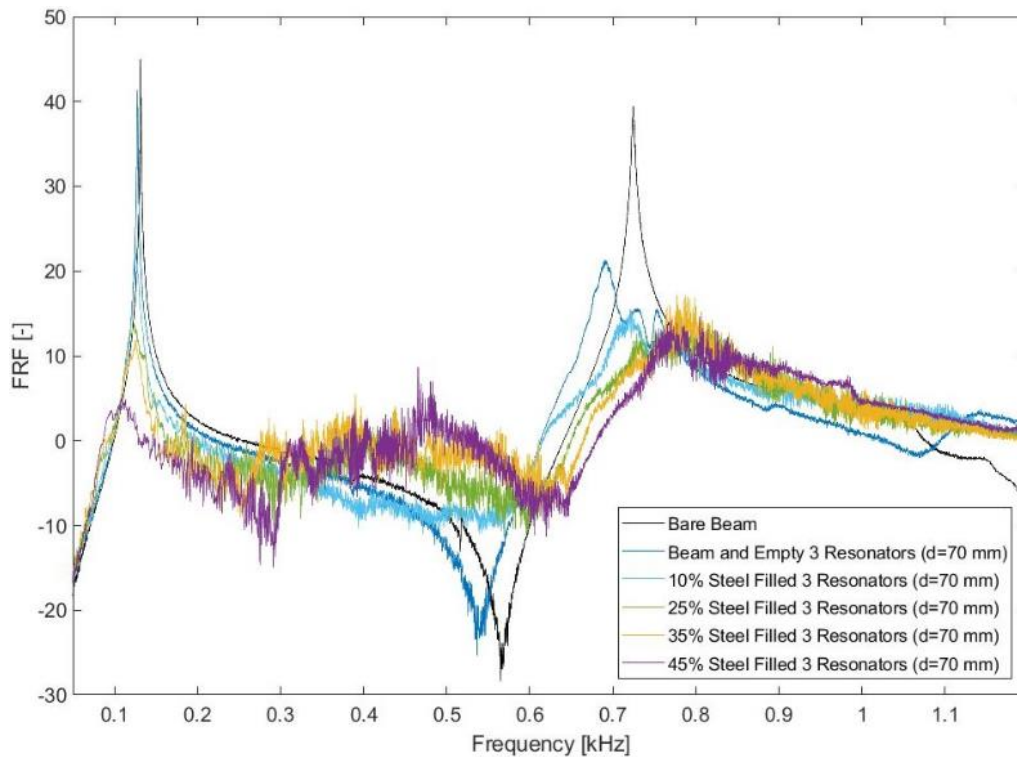


Figure 7. 41: Steel granule-filled three-resonator placement cases

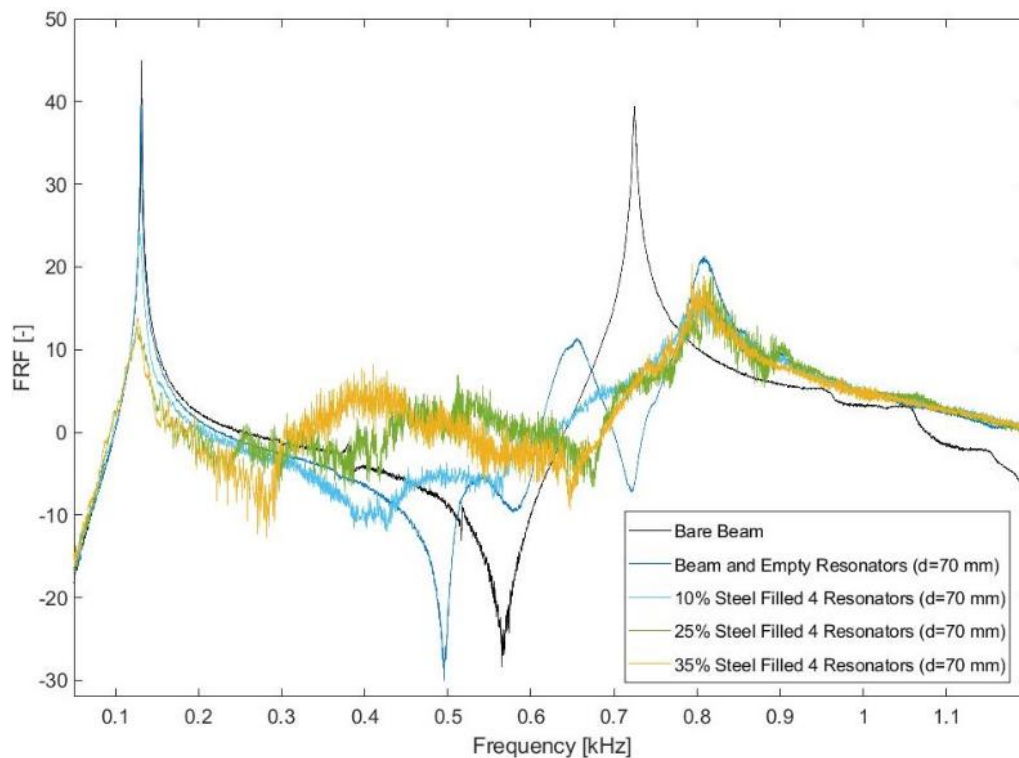


Figure 7.42: Steel granule-filled four-resonator placement cases

Figure 7.42 shows the four-resonator attachment cases at various filling fractions. The gap between the beam's second and third bending modes has been widened at the highest filling fraction given in the figure. The beam's response has generally been similar to the two-resonator case (Figure 7.40) since the centrally positioned beam is not in the case.

As the number of steel particles is only enough to fill five resonators up to 25% of the cavity volume, Figure 7.43 contains the results for a limited filling fraction case. Since there is a centrally positioned resonator on the beam, the response has been flattened in the particle-filled cases. Also, granular structure impact has been obvious in controlling the coupled structures. Even though the filled resonators are placed over the beam, there is no mass effect in the first bending mode of the beam. However, specifically 25% filled case result has shown the increase in the magnitude of the second bending mode. In general the FRF amplitude has been reduced by the increased particle amount, as shown in [191].

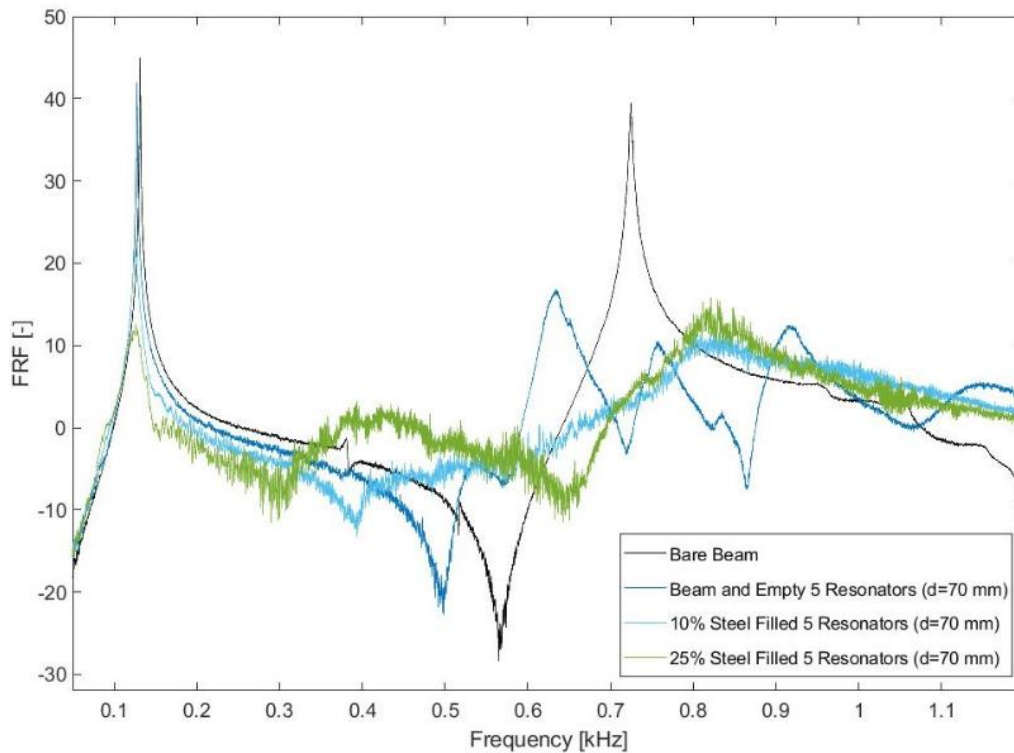


Figure 7. 43: Steel granule-filled five-resonator placement cases

In addition to these studies, particle attached single resonator is compared with the five empty-resonator cases (Figure 7.44). In this case, the particle-filled single resonator has equal mass to the five empty-resonator. This experiment aimed to evaluate the particle impact and compare the damping effectivity of the empty resonators with the particle-filled single resonator case. A fully filled single resonator with metal particles has been given in Chapter 3; the amount of particles, in that case, is recorded as 168 gr of particles. 130 gr of particles is an almost fully filled resonator case. Compared to Figure (62%), the first bending mode amplitude has been reduced similarly; however, the eigenfrequency around the third bending mode of the beam has increased to a higher frequency level. The nonlinear behaviour of particles has been observed through the frequency sweep. In general, using particle-attached single resonators would be more beneficial in controlling the beam performance (FRF amplitude) than the resonators placed in an array. However, periodically arranged resonators would provide coupled resonators behaviour with the shifted resonance.

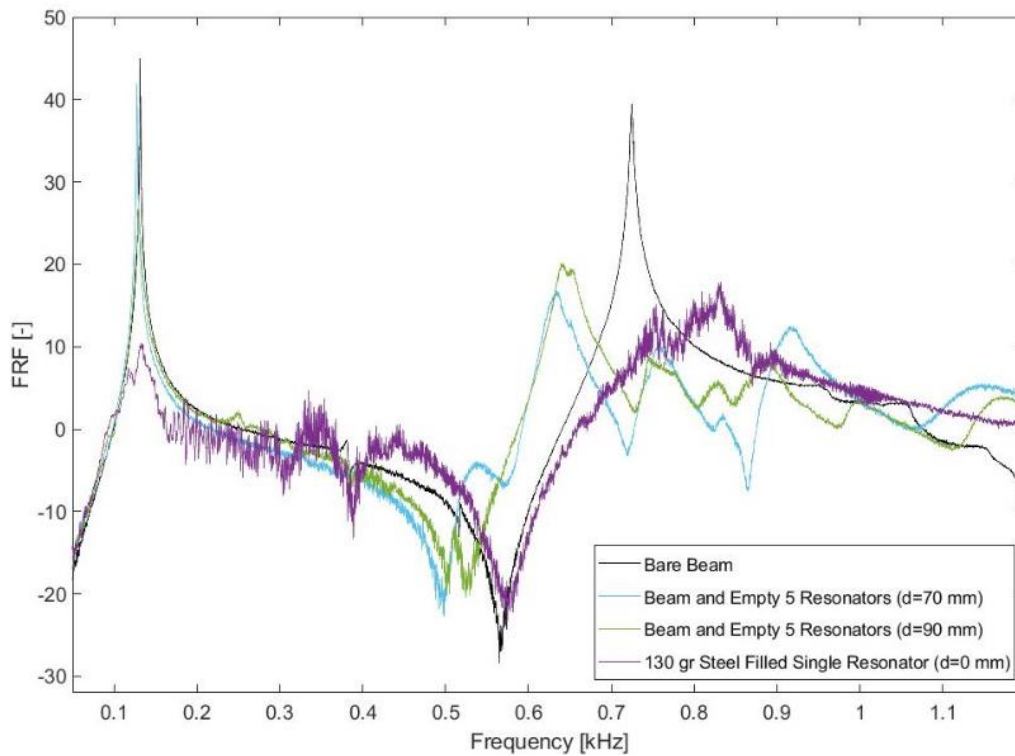


Figure 7. 44: Steel granule (130 gr) filled single resonator and five-empty-resonator placement cases

According to the results obtained using single and multiple resonators filled with various steel particles, even the number of resonators and the odd number of resonators showed an interesting difference. When a resonator is placed at the centre of the beam, the amplitude of the frequency response has been flattened. In addition, placing the resonators in the array has widened the frequency gap between the peaks of the frequency responses. Metal granules have been beneficial in controlling the beam's responses while controlling the coupled structural behaviour.

7.6- Experimental Results for the Resonators Filled with Plastic Granules

In order to evaluate the effect of the plastic granules at various filling fractions and the number of cavities placed on the beam, experimental analyses are planned at the shaker-damper test rig. The frequency sweep applied in these tests, and the resonator placements are the same as in the steel granular study cases. Acrylic plastic particle attachments will be evaluated at various filling fractions while placing the filled resonator(s) on the beam at various stations. Only POM particles have a single filling fraction; therefore, the evaluation for this particle is prepared for a single resonator case. Evaluating the plastic particle

performance in the experimental studies gives the opportunity to compare them with numerical analysis of steel particle equivalent structure modelling analysis.

Single Resonator Impact on the Base Structure

Acrylic plastic particles attached resonator at different filling fractions are studied by changing the resonator place on the beam in this part of the subchapter. Resonator-1 is used for these studies.

10% acrylic plastic granule-filled single resonator has been studied on the beam at various positions, and centrally positioned resonator and 70 mm placement frequency responses have been given in Figure 7.45. Compared to the steel granule 10% filling, acrylic plastic granules have shown higher frequency responses with less change in the eigenfrequency levels. Specifically, 70 mm placement of a 10% acrylic plastic-filled resonator has shown a much higher frequency response, which is probably about the particle's total mass. When the excitation hits the resonator, the particles experience interesting phenomena. This might be the changes through the phases of the granules in the packing, from the fluid-like phase to the gas-like phase; these transformations have impacted the beam with higher frequency response. In this case, particle nonlinearity [12] is hard to control since the volume and mass of the particles are very low [192].

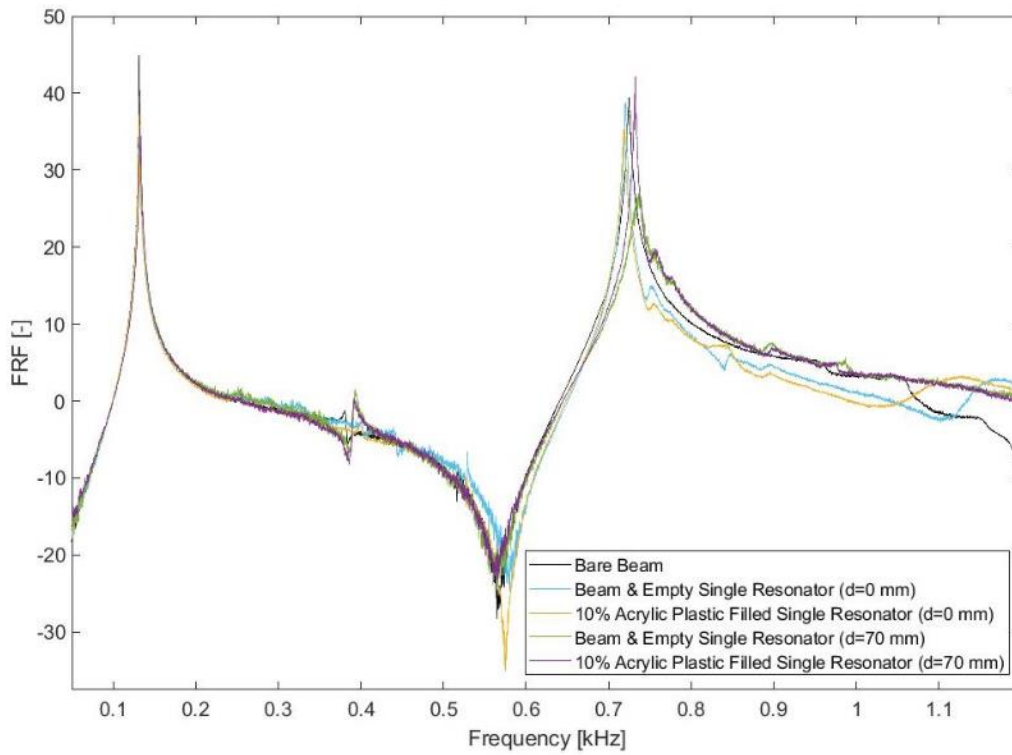


Figure 7. 45: 10% acrylic plastic granule filled single resonator placement cases

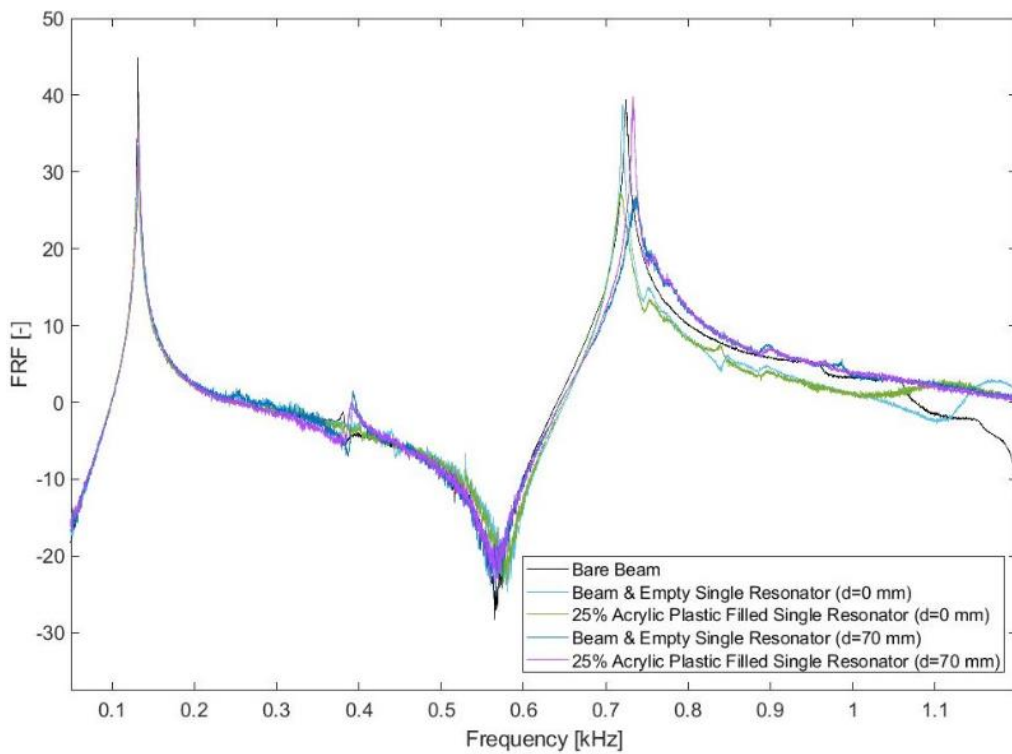


Figure 7. 46: 25% acrylic plastic granule filled single resonator placement cases

The same situations in Figure 7.45 have been observed in Figure 7.46 when the resonator is filled with acrylic plastic granules at the 25% of the volume. The only difference has been observed in the centrally positioned filled resonator case. The particles placed in the resonator helped to reduce the frequency response amplitude on the third mode of the beam.

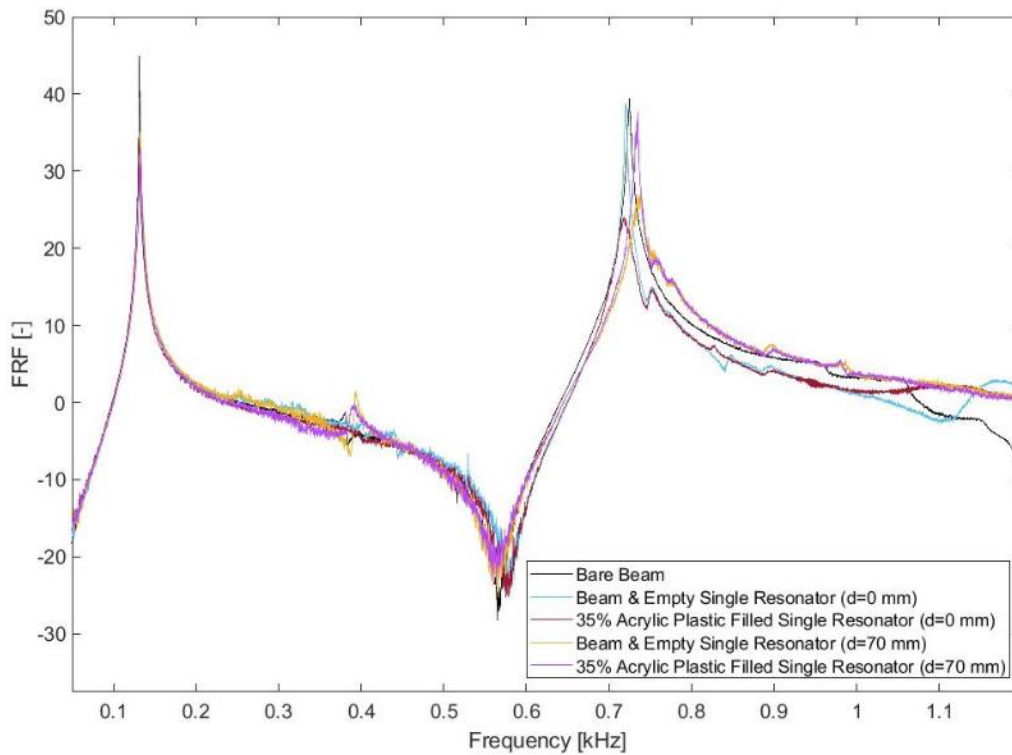


Figure 7. 47: 35% acrylic plastic granule-filled single resonator placement cases

Figure 7.47 illustrates the 35% acrylic plastic-filled single resonator placement impact on the beam results. Frequency response amplitude has been reduced by the aid of particles in the resonator cavity. Also, the coupling between the resonator and the beam has been preserved. The same situations have also been experienced in the 45% filled resonators case, except for one specific situation in Figure 7.48 below. 70 mm placement of the 45% filled resonator has lost the coupled resonator-beam trend, according to the result.

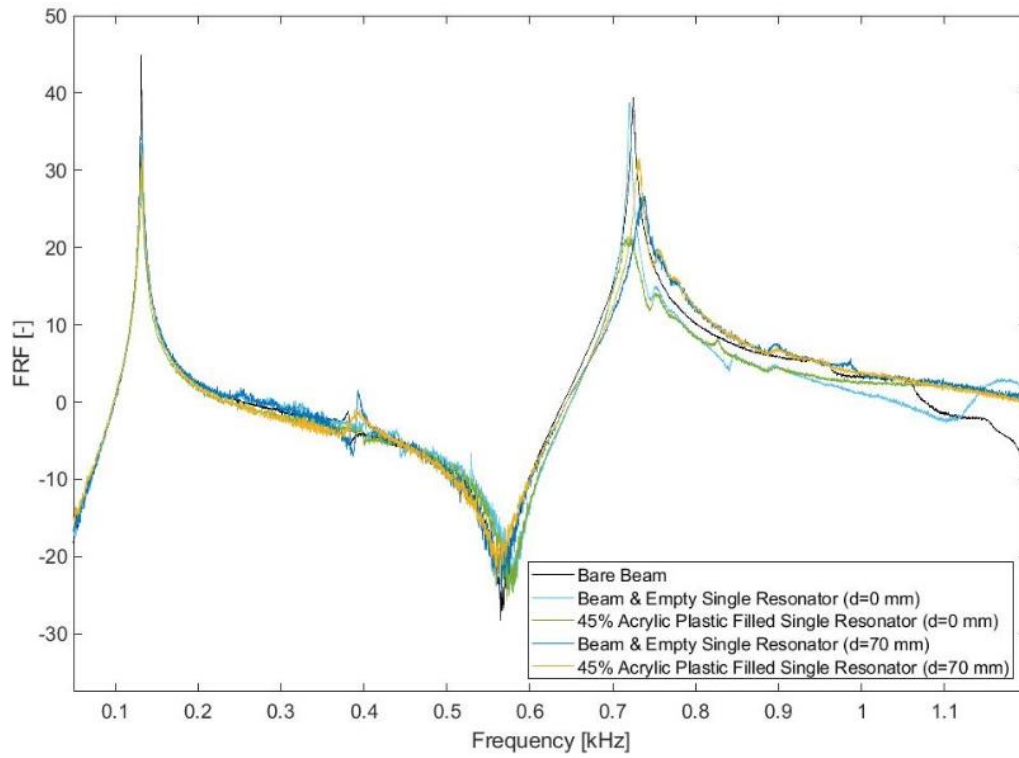


Figure 7. 48: 45% acrylic plastic granule-filled single resonator placement cases

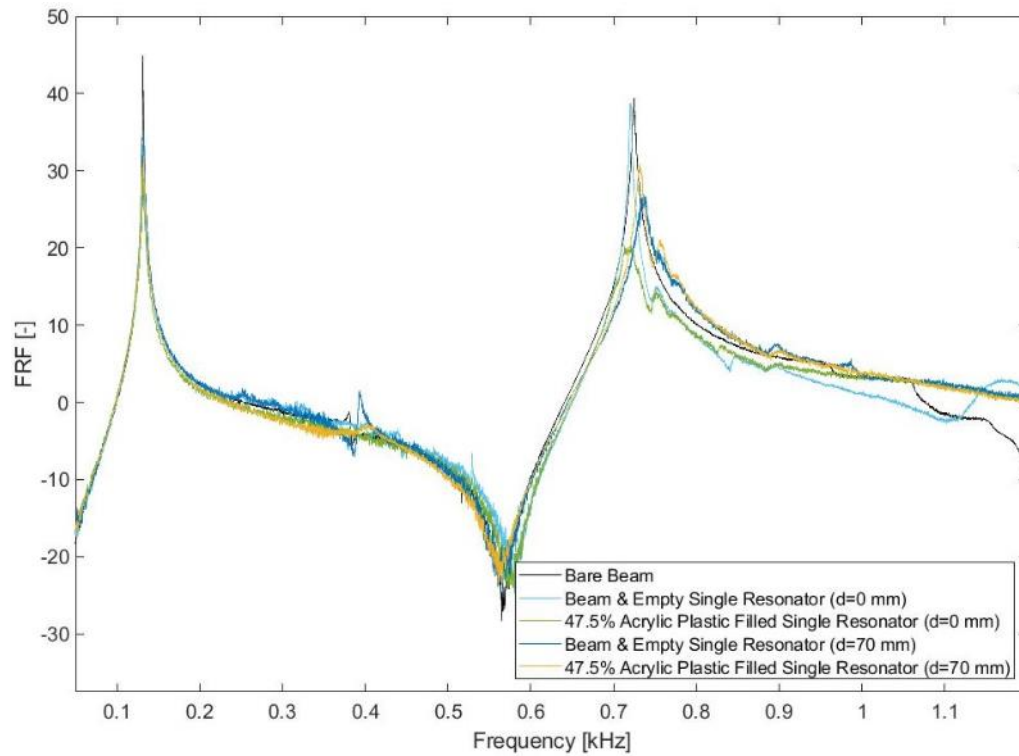


Figure 7. 49: 47.5% acrylic plastic granule-filled single resonator placement cases

According to Figure 7.49, the 47.5% acrylic plastic-filled single resonator, the filled resonator for this specific size of the granules, has shown similar amplitude reduction properties as seen in the previous result. The difference in the number of granules has been such a small level; therefore, the frequency responses for these two results have been at similar levels.

Figure 7.50 below contains the 7.5% POM-filled single resonator placement beam frequency response results. The 7.5% POM filling responses have been similar to the 35% acrylic plastic filling case results. This means that using different plastic granules in the resonator cavity would give more beneficial results in controlling the beam's frequency response even though the filling fractions are not the same. Also, the coupling between the structures has been preserved in the case of POM particle filling. Since the number of particles was only enough to fill the 7.5% of the resonator volume, the only exemplified result using POM particles is given in this figure.

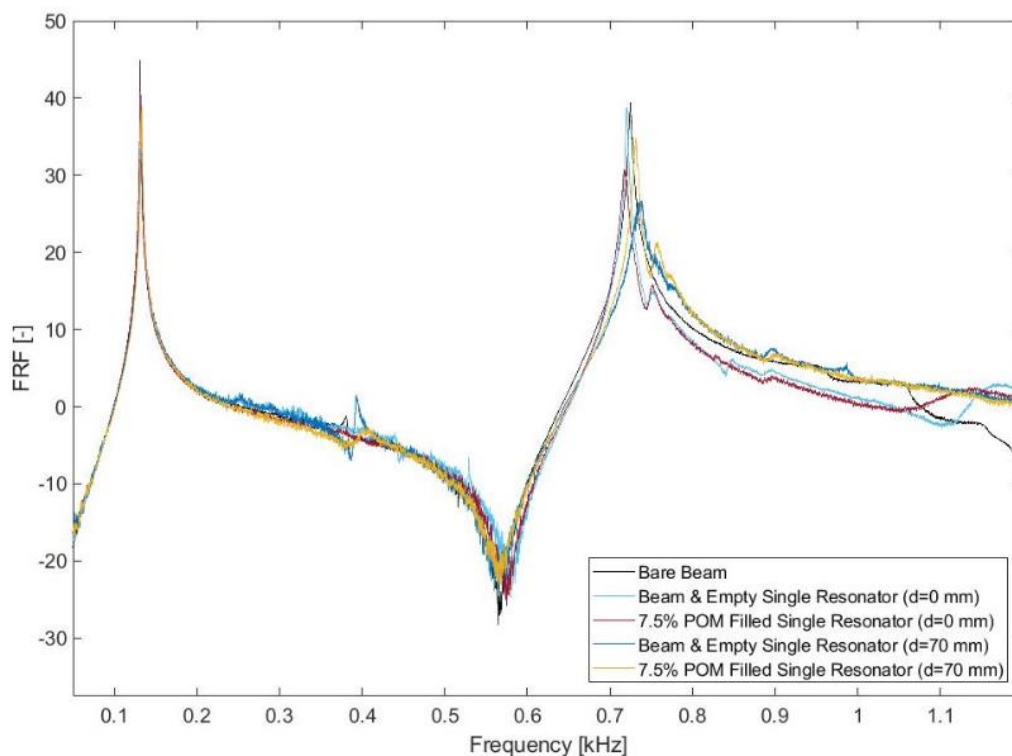


Figure 7. 50: 7.5% POM granule filled single resonator placement cases

Figures given in this chapter showed a single resonator with acrylic plastic and POM filling results. These results have shown frequency responses, in general, rather than frequency

level changes. Therefore, plastic granules might control the beam's frequency response at the same eigenfrequency level.

Multiple Resonators Impact on the Base Structure

In this chapter, multiple resonators with various acrylic plastic fillings are studied experimentally. Since the 47.5% filling of acrylic plastic and the 7.5% filling of POM particles have been available for only single resonator cases, their multiple resonator arrangement cases are not given here. The multiple resonator arrangement is evaluated over the frequency ranges, and their coupling properties are also questioned within the frequency response analysis.

Figure 7.51 illustrates the two-resonator placed on the beam with various filling fraction results. According to these filling fraction results, the resonator-beam coupling has been observed in each filling level of resonator analysis. Also, the increased filling fraction has slightly reduced the amplitude of the frequency response on the beam.

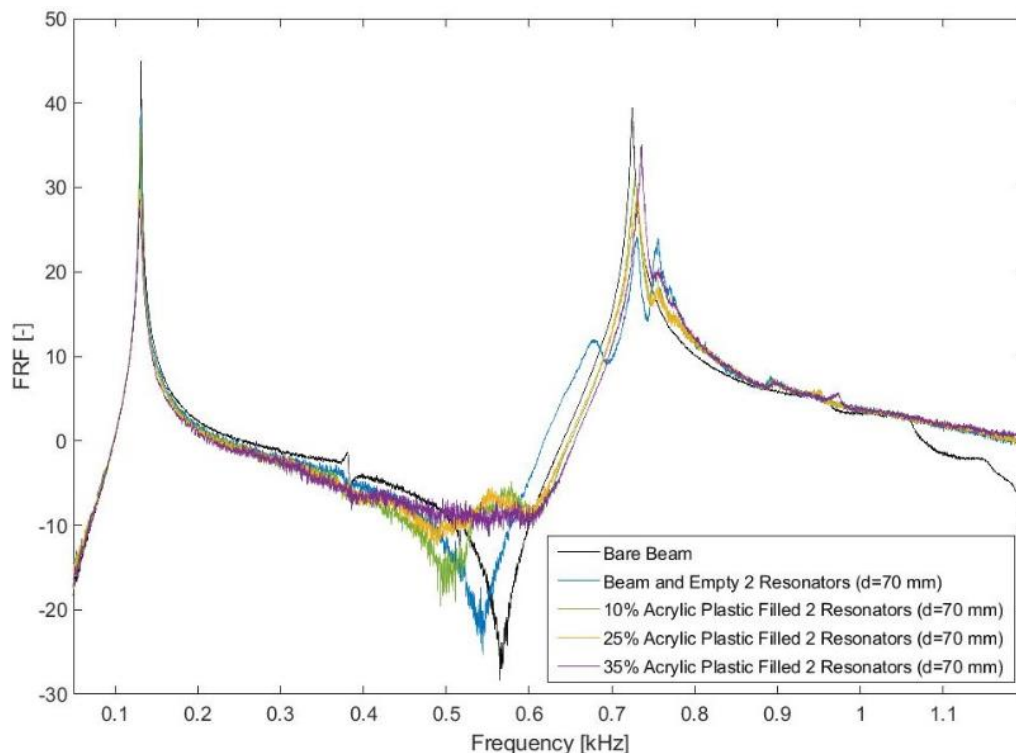


Figure 7. 51: Acrylic plastic granule-filled two-resonator placement cases

In the three-resonator arrangement using the 10% and 25% filling fractions given in Figure 7.52, the coupling has been controlled with particles in the cavities. In addition, the beam's frequency response has been recorded higher than the case of the empty resonator in the 10% filled resonator arrangement case. The second bending mode of the beam has been stabilised in both filling fraction cases. However, the third bending mode of the beam is taken to the lower frequencies at around 575 Hz levels.

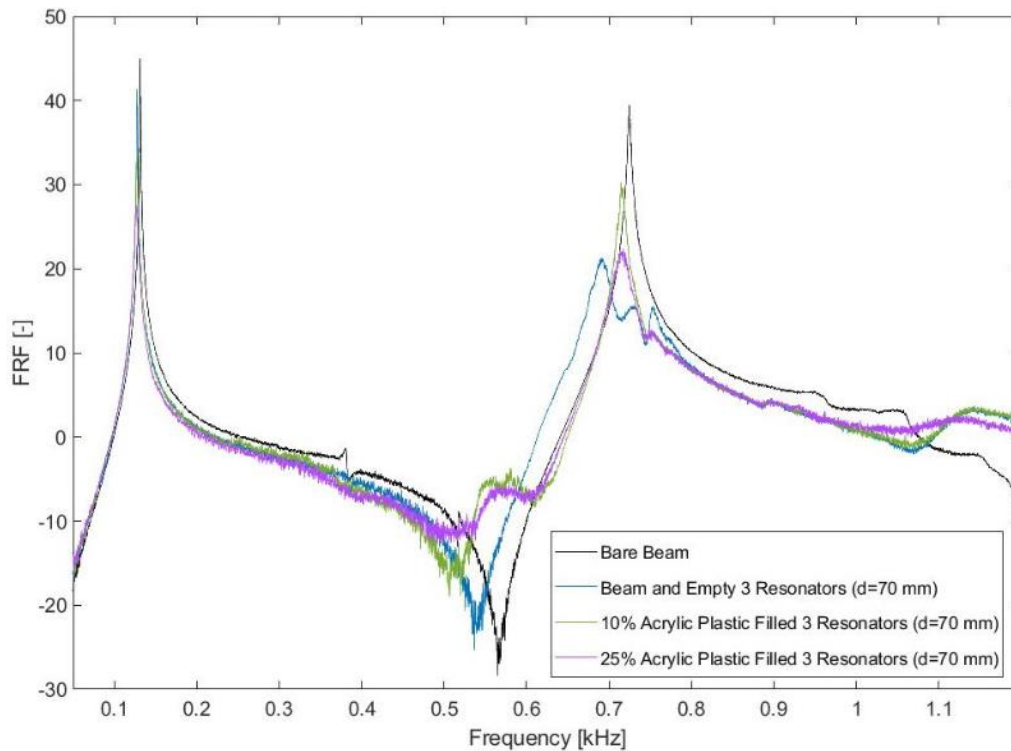


Figure 7. 52: Acrylic plastic granule-filled three-resonator placement cases

Figure 7.53 has only the 10% filling fraction case results with four and five resonator arrangements on the beam. In general, the frequency response amplitude has been reduced by the particles in the resonators. Also, the number of peaks for the beam's response is reduced when the resonators are filled with particles. Especially in the five resonators arrangement with the particles inside the cavities, the beam response is almost at zero levels at around the third bending mode of the beam. Compared to the small number of arrangements with the 10% acrylic plastic filled resonators, the five filled resonators result has shown much promising frequency response on the beam.

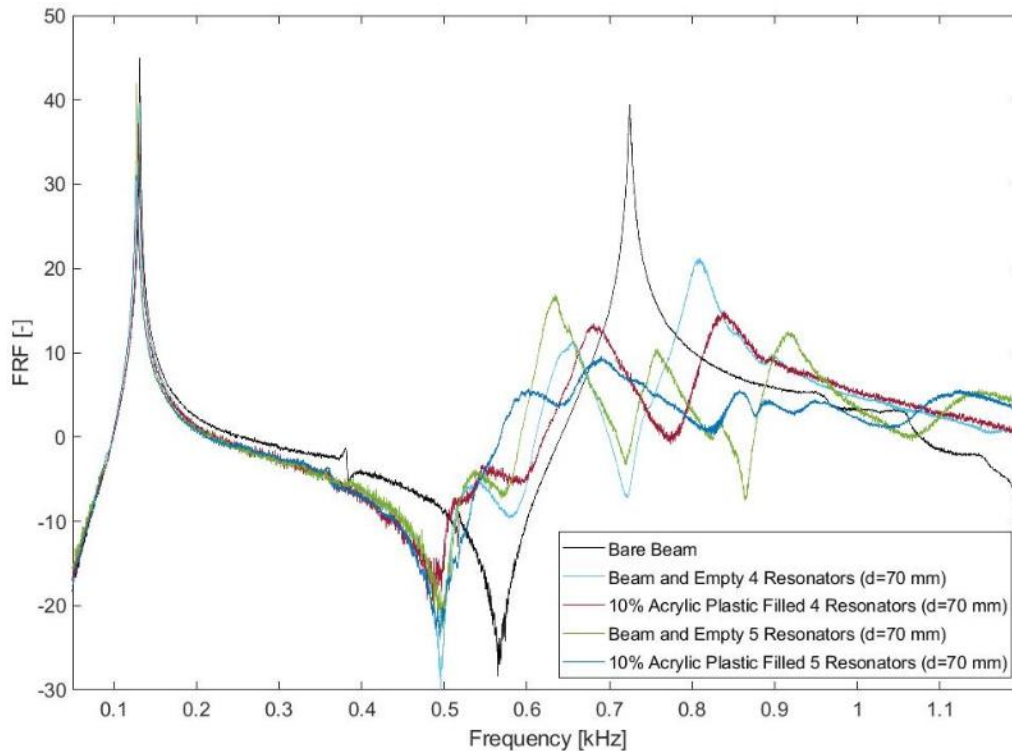


Figure 7. 53: Acrylic plastic granule filled four- and five-resonator placement cases

Overall, acrylic plastic particles with multiple resonator arrangements have similar properties to the empty resonators' cases. Although, four and five filled resonators at the 10% filling fraction have shown more effective frequency response analysis than all other plastic particle filled cases and the multiple empty resonators cases. The acrylic plastic-filled five-resonator arrangement has shown a less noisy trend when compared to the same arrangement with the steel particle replacement (Figure 7.43).

7.7- Frequency Response of Resonators with Mixed Granule Attached Beam

Metal particles and plastic particles have been studied previously to evaluate their impact on the resonators and the frequency response of the beam. This subchapter plans to mix and place these materials in the resonators at various filling fractions. Thus, the impact of the metal particles and the plastic particles would be available to evaluate together. The dominating particle would also be evaluated when these results are compared with individual particle cases as given in the previous subchapters. Also, this subchapter is an example of the segregation phenomena observed in the mixed granules, as explained in Chapter 3.

These filling mixtures are

- Mixture-1: 10% acrylic plastic and 25% steel particles mixture
- Mixture-2: 25% acrylic plastic and 10% steel particles mixture
- Mixture-3: 25% acrylic plastic and 25% steel particles mixture.

Single Resonator Impact on The Base Structure

This subchapter fills the single resonator with the previously mentioned mixture of filling fractions.

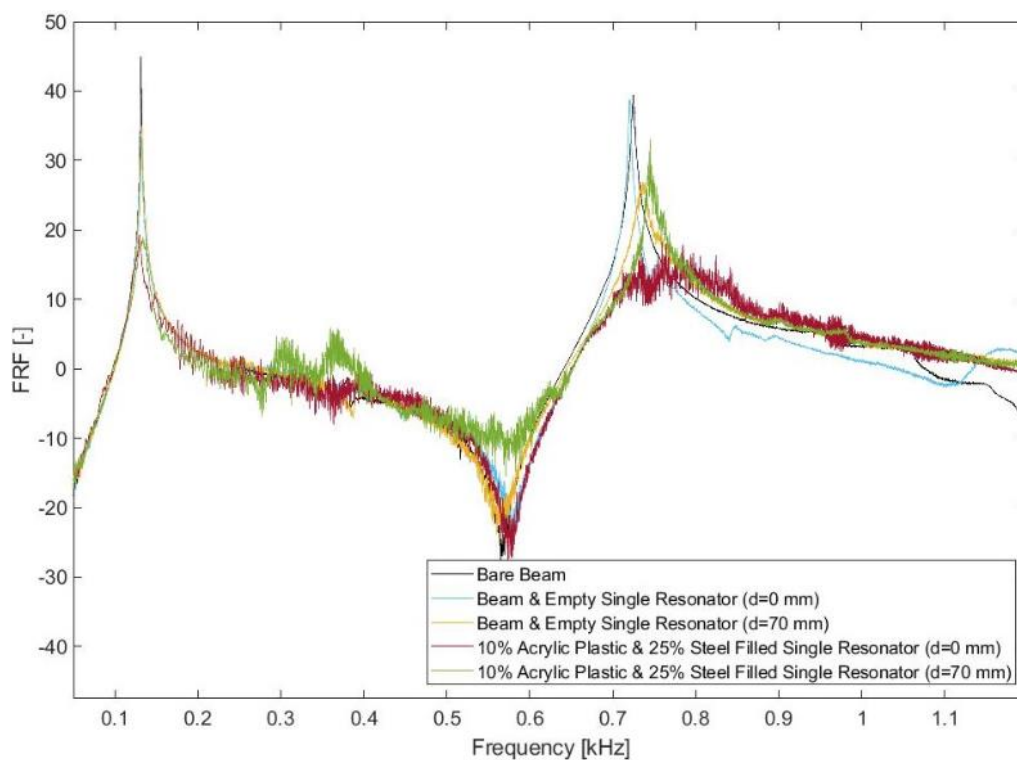


Figure 7. 54: Mixed granule-filled resonator placement cases

The first experimental analysis result, given in Figure 7.54, has a 10% acrylic plastic and 25% steel particles mixture. This means the amount of acrylic plastic is 4 gr in mass while the steel particles' mass is 65.8 gr in the cavity. The figure shows that a centrally placed resonator with a mixture of particles inside the cavity has flattened the response of the third bending mode of the beam. In contrast, 70 mm placement of the filled resonator has increased the amplitude at both the beam's second and third bending modes. This might be related to the

steel granules portion in the cavity since it is similar to what happened in the steel-filled cases.

The second example is given in Figure 7.55, using the 25% acrylic plastic and 10% steel particles filled resonator placement on the beam. Similar to the acrylic plastic-filled cases, the nonlinear phenomena of the particles have been controlled over the frequency levels. Even though the acrylic plastic mass is 10 gr, and the steel particles are 26.3 gr in the cavity, the volumetric portion of the acrylic plastic in the cavity is higher than the steel particles in this case. Therefore, the dominant particle, in general, is acrylic plastic in this case. However, in the centrally positioned resonator case, the steel particles have taken action and flattened the response of the beam. In contrast, the 70 mm resonator placement has increased the amplitude at the beam's second bending mode. In general, the nonlinearity has been controlled by the presence of acrylic plastic, but the frequency response is controlled mainly by the steel particles in this case.

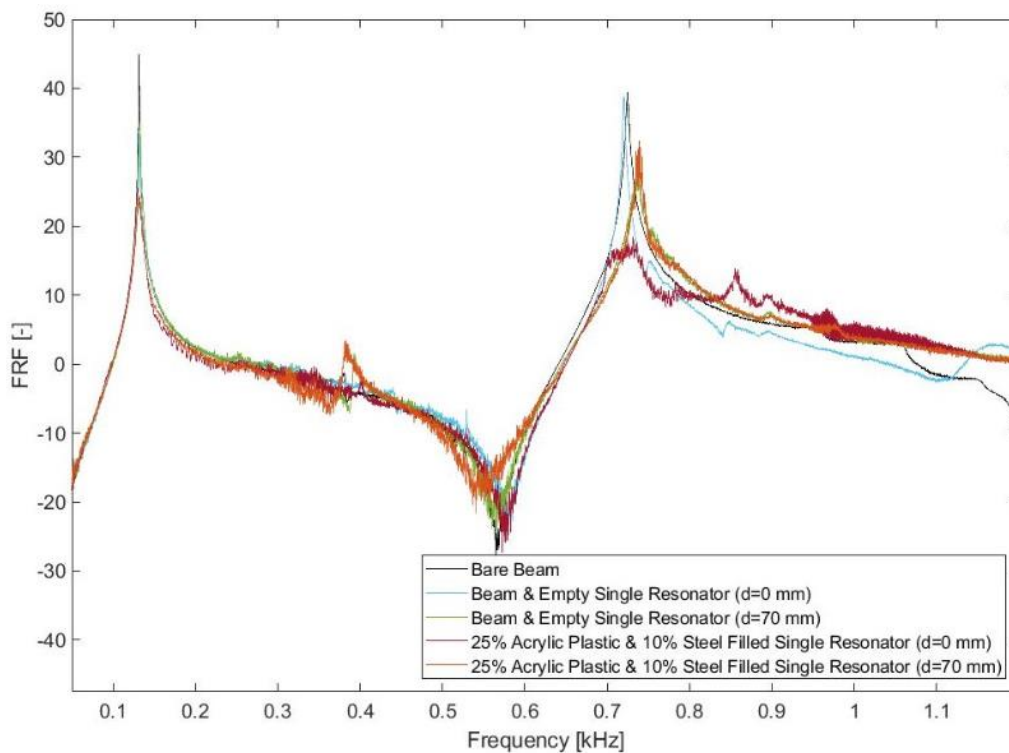


Figure 7. 55: Mixed granule-filled resonator placement cases

Figure 7.56 illustrates the 25% acrylic plastic and 25% steel particles placed resonator results. In this case, the volume of the particles is the same; however, the mass of the acrylic plastic

is 10 gr, and the steel particles' mass is 65.8 gr in the cavity. Similar to the previous case, the nonlinear behaviour of the particles has been controlled by the acrylic particles in the cavity. However, the steel particles have dominated the frequency response, in general. Additionally, on the third bending mode of the beam, the centrally positioned resonator has flattened the response, and the 70 mm placement resonator has slightly reduced the response amplitude.

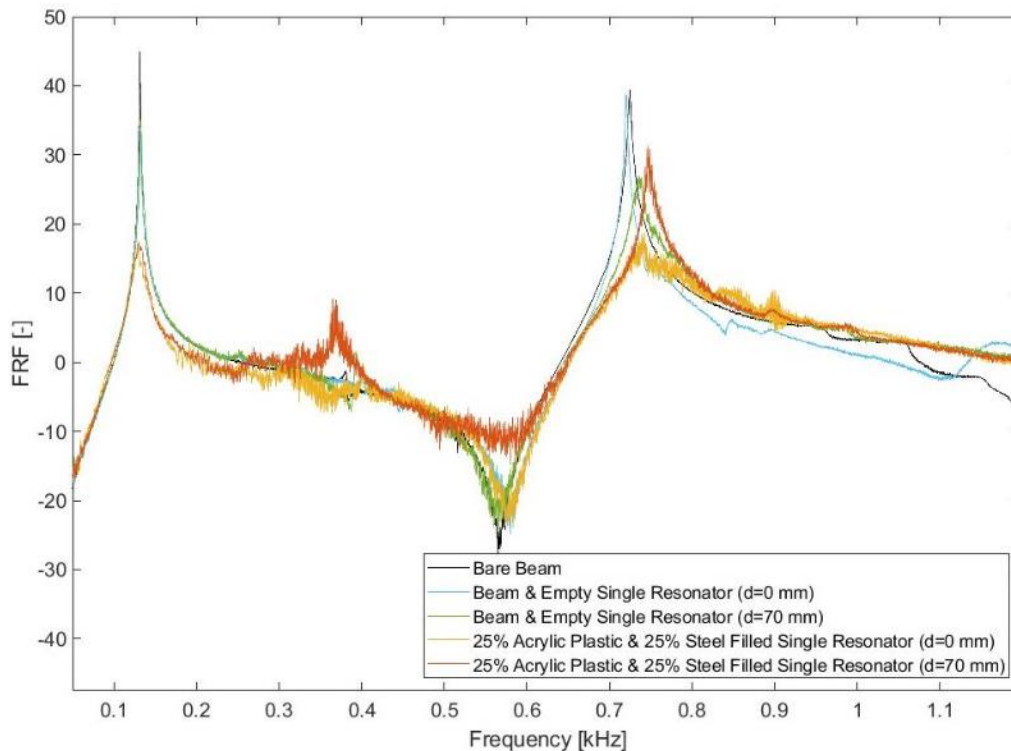


Figure 7. 56: Mixed granule-filled resonator placement cases

Overall, a single resonator with a mixture of particle placement on the beam frequency response analysis has shown that metal particles dominate the response even though the acrylic plastic particles control the nonlinear trend through the frequency sweep.

Multiple Resonators Impact on the Base Structure

Since single resonator attachment analysis has been accomplished using the mixture of granules in the cavity, it might be interesting to experiment with the multiple resonator arrangements using the same mixture of granules introduced previously in the resonators. Like all other numerical and experimental analyses, the resonator has been studied at various

stations on the beam with 10 mm distances from case to case. The beneficial ones are also given in this part.

In Figure 7.57, three various mixtures of granules have been analysed at 70 mm by placing two resonators. Mixture-1 and Mixture-2 responded similarly in the third bending mode of the beam and preserved the coupling between the resonators and the beam. On the other hand, Mixture-2 and Mixture-3 have responded in the same way overall until the third bending mode of the beam. These three mixture options have increased the amplitude of the second bending mode of the beam. Also, only Mixture-1 has reduced the frequency response amplitude.

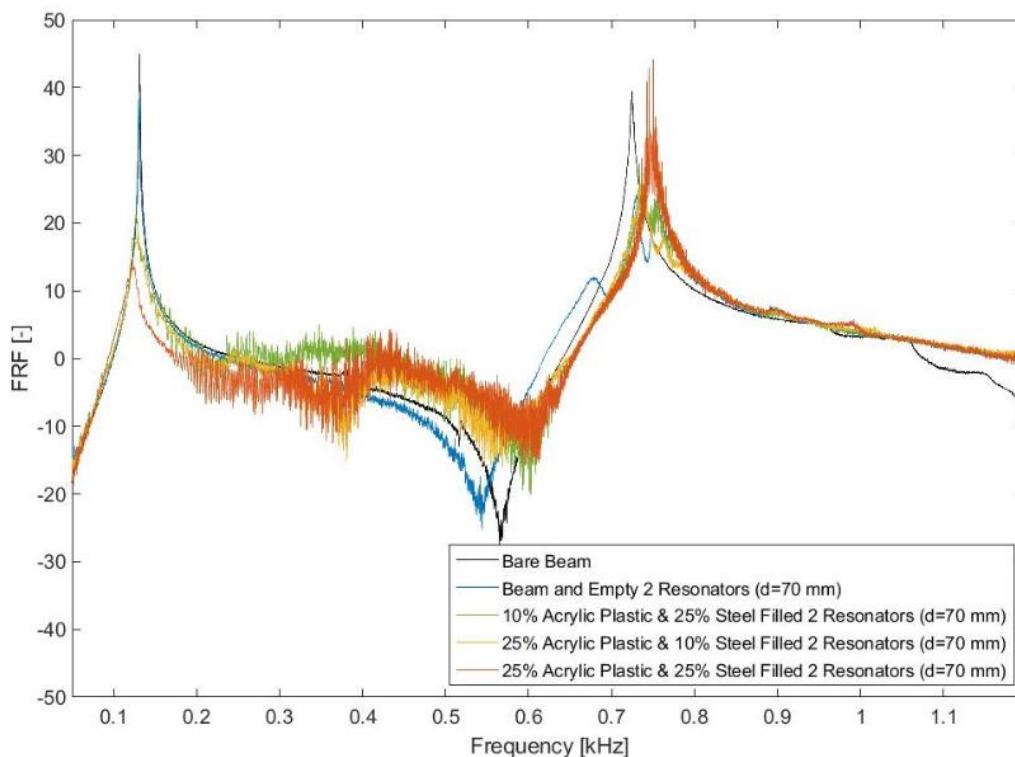


Figure 7. 57: Mixed granule-filled two-resonator placement cases

In the next example, Figure 7.58 shows three-resonator arrangements at 70 mm distances from each other by filling the resonators with the mixture's frequency response analysis results. According to the figure, all filled options have increased the eigenfrequency, which means the third bending mode of the beam has been controlled by postponing the resonance. Also, the third bending mode of the beam has been taken to a lower frequency

level. However, the least nonlinear case in these three filling options has been only the Mixture-2.

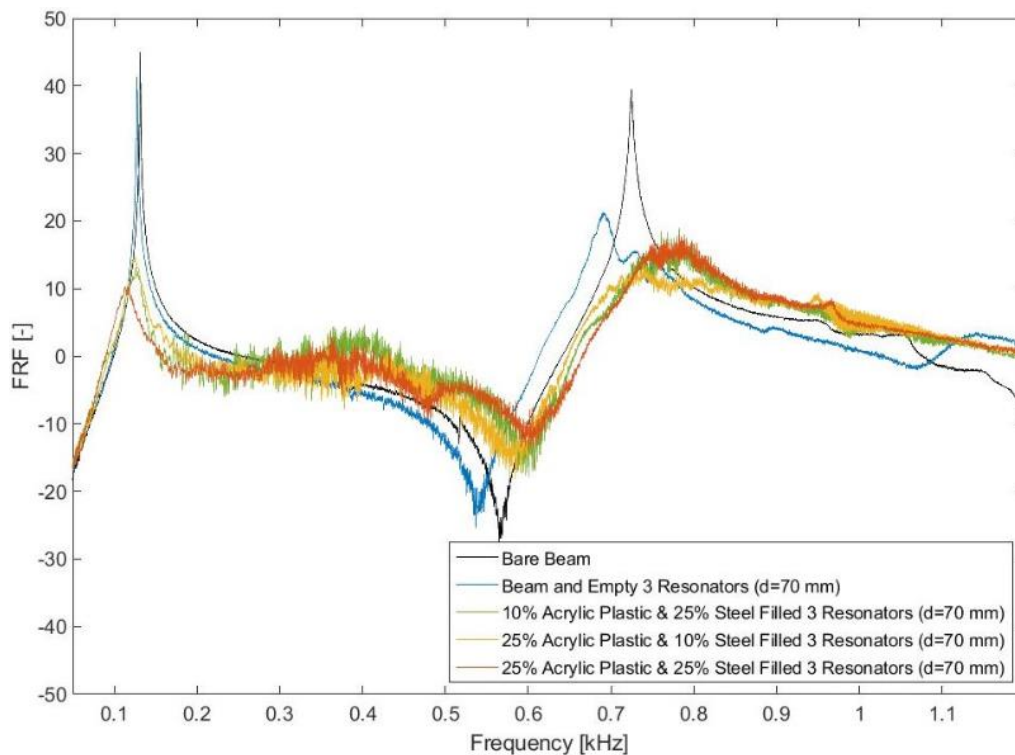


Figure 7. 58: Mixed granule-filled three-resonator placement cases

Figure 7.59 illustrates four and five Mixture-1 filled resonators in the arrangement of 70 mm distances on the beam frequency response analysis results in addition to the same arrangements of empty resonators. According to the empty resonator, as previously explained, the resonators and the beam have shown coupled behaviour. However, mixed particles have controlled the coupling between the structures. Four resonator arrangements of mixed particles filled resonators have shown this coupling to a lesser extent. Also, both arrangements have reduced the frequency response, similar to the only steel particle attached resonators case (Figure 7.43).

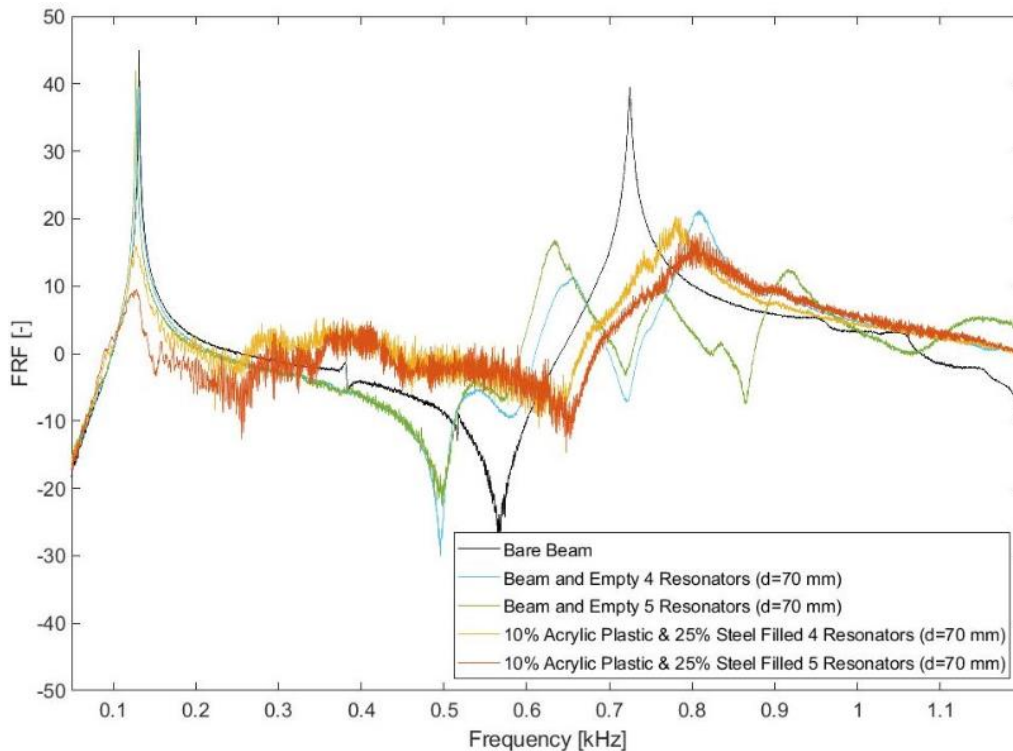


Figure 7. 59: Mixed granule-filled four- and five-resonator placement cases

To conclude, the mixed granules in the arranged multiple resonators have shown controlling behaviour of the frequency response. The system, in general, has behaved like one solid structure. Also, when the volume of acrylic plastic particles is higher than the steel particles, nonlinearity in the trend has been flattened. At the same time, the steel particles have increased the noisy behaviour (because of the nonlinear behaviour of the granules) through the frequency sweep. On the other hand, the reduction in the frequency response amplitude has not been changed more than the individual particle attachment in the resonator cases.

7.8- Conclusion of the Chapter

This chapter has been prepared to evaluate the impact of the granular filling in the resonators numerically and experimentally. The proposed equivalent solid structure material properties have been analysed in the numerical studies. As a result of the research on the equivalent material properties, it has been understood that the higher the filling fraction higher the equivalent Young's Modulus for the same filling material. The contact relations between the granules, as explained in Chapter 3, have been increased with the increasing filling fraction, resulting in higher corresponding equivalent material properties.

In addition, the loss factor analysis has been concluded with negligible impact for the granular attachments in the cavity according to the numerical analysis results. Therefore, the loss factor has not been applied to the numerical modellings in FEM. On the other hand, the loss factor calculation steps can be improved by analysing various conditions in DEM.

The dispersion relations of the single and multiple resonators with various filling fractions have been analysed numerically. As a result of the dispersion analysis, tuning between the structures used in the unit cell modelling has been noted as improvable property by controlling the number of resonators in the unit cell and the filling fractions, which is related to the material properties of the filling. The filling materials at the same volume would have different equivalent material properties, providing various interesting coupling behaviours. The unit cell modelling have shown that there are longitudinal and transversal modes. Resonator filled with the equivalent isotropic solid structure attachment has modified the dispersion relations of the unit cell. For instance, the dispersion curves and associated stopbands have been taken to low-eigenfrequency levels because of the filling impact. In addition, there has been coupling between the system elements and shifted eigenfrequencies.

In order to demonstrate the frequency response of the filled resonators, numerical and experimental analyses have been conducted. As known from [193], using high loss materials with low material properties, such as plastic materials, has been expected to improve the effectivity of the damping, specifically at low vibration amplitude levels. On the other hand, by increasing the vibration amplitude or lesser extent, the excitation frequency and granules in the structures would reduce the contact. As a result, the damping effectivity would be reduced [6]. This has been exemplified in the experimental studies. When the filled resonator is attached to/near to the antinode of the beam modes, the granules might experience nonlinear behaviour because of the amplification at the resonance frequency on the antinode. Therefore, the numerical results could not illustrate the increased amplitude levels of modes as seen in the experimental analysis. This states that the equivalent isotropic solid structure modelling might be invalid when the excitation amplitude is high. There might be nonlinearity inclusion for the equivalent material modelling. In addition, using stiff materials

such as steel granules, the interparticle frictional losses would be promoted at the high amplitude levels [62] and [38].

Interestingly, the experimental analysis using the resonator at the centre of the beam has shown particle damping behaviour on the force transducer impact. Compared cases have shown the particle damper placed at the central position would increase the energy absorption properties by the granules than the cases of resonators placement away from the centre. However, the working principle of the electrodynamic shaker and force level changeability at the resonance frequencies have been noted in the source prepared by Ewins [194]. This means that the changes in the force transducer readings would be expected.

Chapter 8: Conclusion

The research question of the thesis is given in the very first chapter as

"If particle dampers were evolved into the metamaterial, how this novel arrangement would affect the overall behaviour of the vibratory structure and how the nonlinear behaviour would contribute to the metamaterial performance?".

The thesis, therefore, considered the vibration-related situations by composing the various granular materials in a resonating damper and evaluated the impact of periodic arrangements and frequency response with/without granular structure in the resonators by attaching them to the main structure. The research included numerical and experimental analysis in addition to analytical calculations. A resonating damper is made of polymeric materials and built using the 3D printing opportunity. Therefore, DMTA analysis is required for the material and proceeded data provided the new material properties for the damper. A resonating damper is modelled, and eigenfrequency analysis of the damper is modelled in COMSOL Multiphysics (V5.0) using the obtained material properties. Three different particles have been used in this research: steel particles (1.59 mm), acrylic plastic particles (3 mm) and POM particles (1.59 mm). As noted in the thesis, the amount of particles to fill the resonating damper is at various filling fraction levels. A numerical model based on the Discrete Element Method (DEM) is studied in EDEM (V2021.1) to process the granular structures' behaviour. The data obtained from DEM analysis are used to calculate the equivalent isotropic solid structure materials. As mentioned earlier, each filling fraction of certain particle size and material is provided with individual equivalent isotropic solid structure properties. Since DEM analyses are performed at a series of frequency levels, the calculated equivalent isotropic solid structure properties have the corresponding series of material properties for each frequency level. The analysis amplitude is decided to be at low-vibration amplitude levels since the particles stay in contact as a solid medium and do not leave their original state easily.

The empty resonating damper is placed at various stations on the structural steel-made beam and performed a series of experimental and numerical analyses to evaluate the system's frequency response. Various filling fractions for individual granules are placed into

the resonating damper(s) and experimentally evaluated over the frequency analysis. Corresponding numerical analysis is performed using the equivalent isotropic solid structure material properties for introducing the filled granular portions. Thus, the resonator is studied in empty and filled options through numerical and experimental analysis opportunities.

The periodically arranged resonator is modelled in COMSOL Multiphysics using the unit cell modelling, and Bloch-Floquet Theory applied in the first Brillouin Zone. The resonator is studied using the same unit cell modelling methodology in empty and filling options. Since the isotropic loss factor for the filled materials is not available despite the research efforts, the dispersion relations are only meaningful and available for the empty resonator placed unit cell dispersion analysis. The filled resonator attached unit cell dispersion relations are given in the thesis, as well by aiming to put an effort and a step for the research community on the future studies. In addition to these efforts, [6], [37], [59], [60] have been published and presented using the research outcomes of the series of studies.

8.1- Main Conclusion of the Thesis

- Numerical modelling of the granular structure filled damper casing has been developed in EDEM based on the Discrete Element Method (DEM) for evaluating the behaviour and state of the granules. Equivalent isotropic medium has been characterised over various filling fractions of various particle sizes at different frequency ranges. The material properties obtained through this analysis have been given in Chapter 3.
- Amplitude-dependent behaviour of the resonating granular structure filled damper has been experimentally validated as given in Chapter 3.
- The 3D-printed sample's material properties have been processed from the DMTA testing. The resonating damper was modelled numerically and then built using 3D printing. The properties of the resonator and testing process have been given in Chapter 4. Eigenfrequency analysis in COMSOL Multiphysics has been studied with experimental validations for the newly built resonators.
- Empty resonators have been studied in numerical analysis options by placing the resonator on the beam as a unit cell. The dispersion relation studies provided that

even the empty resonator has controlling properties on the frequency response. In addition, adding more resonators on the beam to make a periodic arrangement has provided a frequency gap, which has been noted previously for the periodically arranged structures. The related analysis and findings are in Chapter 5.

- Empty resonators have been studied in numerical and experimental analysis options by placing the resonator on the beam at various locations as a finite structure analysis in Chapter 6. The studies provided that even the empty resonator has controlling properties on the frequency response. In addition, adding more resonators on the beam to make a periodic arrangement have provided frequency gap or even postponed eigenfrequencies.
- In addition to the frequency response analysis of the resonators, regardless of the filling material, it is advised that the accelerometer position should be away from the excitation impact area. The reason behind this thought is given in Chapter 6, the conclusion part.
- Granular structures tend to change their state under high amplitude levels; therefore, the analysis that has been processed in this thesis is at low-amplitude levels. Friction losses and viscous damping portions of the granules have been explained over the numerical and experimental analysis given in Chapter 7. Although both analyses have shown spectacular results, the experimental ones have more effective properties.
- The mixed granules have been studied experimentally, showing some interesting relations over viscoelastic and metallic particles. While the frequency response amplitude has been controlled, the nonlinear behaviour and noisy trends have been limited by the mixed granules in the resonator cavity. Additionally, the eigenfrequencies obtained from the individual granule cases have changed completely using the mixed granules in the cavity.
- Periodically arranged particle dampers on the unit cell modelling have shown the structures' coupled behaviour. However, the lossy part of the granules could not be added to the modelling as an isotropic structural loss factor. The analysis process for the loss factor was not enough to manage the processing of each analysis option. Therefore, it is advised to work on this property in detail to feed the material in

numerical modelling and find a beneficial frequency gap from the filled resonator cases.

- Even though the experimental analysis is processed in horizontal and vertical directions of the shaker test, vertical test findings have been more understandable since the particles dissipated more energy in this testing version.

As a result of these research steps and findings, granular structure placed damper has been a useful damping option, specifically at the low vibration amplitudes. Especially, using a locally resonating structure to control the main structure's behaviour has impacted greatly. Adding granules into the resonator has shown interesting frequency response changes while providing frequency gaps over the frequency range of interest. The findings of this thesis provide phenomenal understanding and impressive steps to build an effective and applicable damping opportunity at a broader range of frequencies for vibration damping technologies.

8.2- Future Research Ideas

The current research study has helped to understand the behaviour of the spherical granules at various material properties and filling fractions by adding them into the locally resonating damper. The equivalent isotropic solid medium characterisations have been introduced in the research for various frequency ranges, and frequency response and dispersion relation analysis have been studied for these structures. However, there are some slight limitations in this research that can be overcome in future research studies defined by the researcher.

- Since only spherical granules have been studied in this thesis, irregular-shaped granules might provide interesting findings. Therefore, various shapes of granules should be studied accordingly. EDEM has the opportunity to develop various granular shapes and import the outside modelled geometries opportunity; thus, EDEM can be used to model these various shapes of granules.
- The hydrostatic pressure of the granular structures in the resonating damper cavity has been recorded from EDEM analysis findings. In order to evaluate the hydrostatic pressure, an analytical methodology based on the cylindrical geometry calculations, which can be found in the literature studies, can be used to develop an analytical calculation methodology for a spherical cavity. Therefore, various filling fraction

impacts on the hydrostatic pressure, granular structure properties, and contact relations can be evaluated comprehensively.

- Each granular material and filling fraction have been modelled as an equivalent isotropic solid medium according to the EDEM analysis data in the COMSOL Multiphysics modelling. However, mixed granular structure cases do not have a representative material modelling that can be used in FEM analysis. Therefore, it is advised to work on the research on which DEM opportunities can be used to provide relative material properties for each mixing option. The percentages of the materials in the mixing can be used to relate to the new material properties calculation.
- Experimental studies in the thesis have shown noisy results from not only the granular matters. This can be seen from the empty resonator attached beam frequency response analysis and the bare beam results. Therefore, it is advised to prepare a certain, less flexible, and stiffer experimental rig which cannot be disturbed by outside sources. Therefore, the data obtained from this analysis would be more approachable.
- The equivalent isotropic solid structure material properties require more studying and addition of the nonlinear impact received at the higher amplitude experienced areas such as the antinode-placement on the beam. Thus, it is expected to demonstrate the real experience in the numerical studies, as well.
- Lastly, the structural loss factor of the granular fillings should be improved. This would provide an evaluation opportunity between the experimental and the numerical studies when granules are filled into the resonator cavities. Also, by applying a loss factor value in the unit cell modelling, the dispersion relations would offer lossy properties frequency gaps and stop band properties would be approachable easily.

References

- [1] Z. Lu, Z. Wang, S. F. Masri, and X. Lu, "Particle impact dampers: Past, present, and future," *Struct. Control Heal. Monit.*, vol. 25, no. 1, pp. 1–25, 2018.
- [2] M. Inoue, I. Yokomichi, and K. Hiraki, "Particle damping with granular materials for multi degree of freedom system," *Shock Vib.*, vol. 18, no. 1–2, pp. 245–256, 2011.
- [3] G. Arioli and F. Gazzola, "A new mathematical explanation of what triggered the catastrophic torsional mode of the Tacoma Narrows Bridge," *Appl. Math. Model.*, vol. 39, no. 2, pp. 901–912, 2015.
- [4] R. A. Ibrahim, *Vibro-Impact Dynamics Modelling, Mapping and Applications*, Volume 43. Springer Berlin Heidelberg, 2009.
- [5] F. Xie and A. M. Aly, "Structural control and vibration issues in wind turbines: A review," *Eng. Struct.*, vol. 210, no. December 2019, p. 110087, 2020.
- [6] S. G. Demiryurek, A. Krynkin, and J. Rongong, "Non-linear metamaterial structures: Array of particle dampers," *Proc. Int. Congr. Acoust.*, vol. 2019-Septe, no. September, pp. 4878–4884, 2019.
- [7] C. Wong and J. Rongong, "Control of particle damper nonlinearity," *AIAA J.*, vol. 47, no. 4, pp. 953–960, 2009.
- [8] A. Diatta, S. Guenneau, A. Nicolet, and F. Zolla, "Metamaterials and the Mathematical Science of Invisibility," Aix-Marseille Université 13397 Marseille cedex 20, France.
- [9] D. J. Colquitt, A. Colombi, R. V. Craster, P. Roux, and S. R. L. Guenneau, "Seismic metasurfaces: Sub-wavelength resonators and Rayleigh wave interaction," *J. Mech. Phys. Solids*, vol. 99, no. August 2016, pp. 379–393, 2017.
- [10] A. Colombi *et al.*, "Elastic Wave Control Beyond Band-Gaps: Shaping the Flow of Waves in Plates and Half-Spaces with Subwavelength Resonant Rods," *Front. Mech. Eng.*, vol. 3, 2017.
- [11] R.A. Ibrahim, *Vibro-Impact Dynamics: Model., Map. & Appl.* 2009.
- [12] I. Zaman *et al.*, "Study of passive vibration absorbers attached on beam structure," *Appl. Mech. Mater.*, vol. 660, no. November, pp. 511–515, 2014.
- [13] E. A. Areas, "EDEM Application Areas."
- [14] G. Takács and B. Rohal'-Ilkiv, *Model predictive vibration control: Efficient constrained MPC vibration control for lightly damped mechanical structures*. 2012.
- [15] C. Cempel and G. Lotz, "Efficiency of Vibrational Energy Dissipation by Moving Shot," *J. Struct. Eng.*, vol. 119, no. 9, pp. 2642–2652, Sep. 1993.

- [16] L. Tong and Y. H. Wang, "DEM simulations of shear modulus and damping ratio of sand with emphasis on the effects of particle number, particle shape, and aging," *Acta Geotech.*, vol. 10, no. 1, pp. 117–130, Feb. 2015.
- [17] R. D. Friend and V. K. Kinra, "Particle impact damping," *J. Sound Vib.*, vol. 233, no. 1, pp. 93–118, 2000.
- [18] J. A. Rongong and G. R. Tomlinson, "Amplitude Dependent Behaviour in the Application of Particle Dampers to Vibrating Structures," no. April, pp. 1–9, 2005.
- [19] L. Gagnon, M. Morandini, and G. L. Ghiringhelli, "A review of particle damping modeling and testing," *J. Sound Vib.*, vol. 459, p. 114865, 2019.
- [20] A. Papalou and S. F. Masri, "Performance of particle dampers under random excitation," *J. Vib. Acoust. Trans. ASME*, vol. 118, no. 4, pp. 614–621, 1996.
- [21] R. D. Nayeri, S. F. Masri, and J. P. Caffrey, "Studies of the performance of multi-unit impact dampers under stochastic excitation," *J. Vib. Acoust. Trans. ASME*, vol. 129, no. 2, pp. 239–251, 2007.
- [22] S. S. Simonian, "Particle Damping Applications," *Smart Struct. Mater. 1995 Passiv. Damping*, vol. 2445, no. July, pp. 149–160, 1995.
- [23] S. M. Zahrai and A. F. Rod, "Effect of impact damper on SDOF system vibrations under harmonic and impulsive excitations," *J. Phys. Conf. Ser.*, vol. 181, no. 1, 2009.
- [24] J. Park, S. Wang, and M. J. Crocker, "Mass loaded resonance of a single unit impact damper caused by impacts and the resulting kinetic energy influx," *J. Sound Vib.*, vol. 323, no. 3–5, pp. 877–895, 2009.
- [25] Y. Wang, B. Liu, A. Tian, D. Wei, and X. Jiang, "Prediction methods for the damping effect of multi-unit particle dampers based on the cyclic iterations of a single-unit particle damper," *J. Sound Vib.*, vol. 443, pp. 341–361, 2019.
- [26] S. F. Masri, "Effectiveness of Two-Particle Impact Dampers," *J. Acoust. Soc. Am.*, vol. 41, no. 6, pp. 1553–1554, 1967.
- [27] S. F. Masri, "Analytical and Experimental Studies of Multiple-Unit Impact Dampers," *J. Acoust. Soc. Am.*, vol. 45, no. 5, pp. 1111–1117, 1969.
- [28] S. E. Olson and M. L. Drake, "Development of Analytical Methods for Particle Damping," p. 10, 1999.
- [29] Q. Sun, F. Jin, G. Wang, S. Song, and G. Zhang, "On granular elasticity," *Sci. Rep.*, vol. 5, pp. 1–7, 2015.
- [30] W. Xiao, J. Li, S. Wang, and X. Fang, "Study on vibration suppression based on particle damping in centrifugal field of gear transmission," *J. Sound Vib.*, vol. 366, pp. 62–80, 2016.
- [31] S. F. Masri and T. K. Caughney, "On the Stability of tie Impact Pamper," *J. Appl.*

- Mech.*, vol. 33, no. 3, pp. 586–592, 1966.
- [32] S. F. Masri, "Forced vibration of a class of non-linear two-degree-of-freedom oscillators," *Int. J. Non. Linear. Mech.*, vol. 7, no. 6, pp. 663–674, 1972.
- [33] M. Saeki, "Analytical study of multi-particle damping," *J. Sound Vib.*, vol. 281, no. 3–5, pp. 1133–1144, 2005.
- [34] Z. Xu, M. Y. Wang, and T. Chen, "Particle damping for passive vibration suppression: Numerical modelling and experimental investigation," *J. Sound Vib.*, vol. 279, no. 3–5, pp. 1097–1120, 2005.
- [35] X. M. Bai, B. Shah, L. M. Keer, Q. J. Wang, and R. Q. Snurr, "Particle dynamics simulations of a piston-based particle damper," *Powder Technol.*, vol. 189, no. 1, pp. 115–125, 2009.
- [36] M. Paulick, M. Morgeneyer, and A. Kwade, "Review on the influence of elastic particle properties on DEM simulation results," *Powder Technol.*, vol. 283, pp. 66–76, 2015.
- [37] S. G. Demiryurek, A. Krynkin, and J. Rongong, "Modelling of Nonlinear Dampers Under Low-Amplitude Vibration," in *ACOUSTICS 2020*, 2020, vol. 42.
- [38] B. Darabi and J. A. Rongong, "Polymeric particle dampers under steady-state vertical vibrations," *J. Sound Vib.*, vol. 331, no. 14, pp. 3304–3316, 2012.
- [39] G. Michon, A. Almajid, and G. Aridon, "Soft hollow particle damping identification in honeycomb structures," *J. Sound Vib.*, vol. 332, no. 3, pp. 536–544, 2013.
- [40] G. R. Tomlinson, "Particle Vibration Damper," US006547049B1, 2003.
- [41] I. Yao, "<title>Signal Processing With Acousto-Electric Surface Acoustic Wave (SAW) Devices</title>," *Guid. Wave Opt. Surf. Acoust. Wave Devices Syst. Appl.*, vol. 0239, no. February 1981, pp. 236–244, 1981.
- [42] K. Mao, M. Y. Wang, Z. Xu, and T. Chen, "DEM simulation of particle damping," *Powder Technol.*, vol. 142, no. 2–3, pp. 154–165, 2004.
- [43] S. Simonian, V. Camelo, S. Brennan, N. Abbruzzese, and B. Gualta, "Particle damping applications for shock and acoustic environment attenuation," *Collect. Tech. Pap. - AIAA/ASME/ASCE/AHS/ASC Struct. Struct. Dyn. Mater. Conf.*, no. October, 2008.
- [44] S. S. Simonian, "Particle beam damper," in *Smart Structures and Materials 1995: Passive Damping*, 1995, vol. 2445, no. July, pp. 149–160.
- [45] C. R. Wassgren, C. E. Brennen, and M. L. Hunt, "Vertical vibration of a deep bed of granular material in a container," *J. Appl. Mech. Trans. ASME*, vol. 63, no. 3, pp. 712–719, 1996.
- [46] M. R. Duncan, C. R. Wassgren, and C. M. Krousgrill, "The damping performance of a

- single particle impact damper," *J. Sound Vib.*, vol. 286, no. 1–2, pp. 123–144, 2005.
- [47] R. P. Behringer, D. Howell, L. Kondic, S. Tennakoon, and C. Veje, "Predictability and granular materials," *Phys. D Nonlinear Phenom.*, vol. 133, no. 1–4, pp. 1–17, 1999.
- [48] DEM_Solutions, "EDEM 2.6 Theory Reference Guide," p. 19, 2014.
- [49] S. R. Schwartz, D. C. Richardson, and P. Michel, "An implementation of the soft-sphere discrete element method in a high-performance parallel gravity tree-code," *Granul. Matter*, vol. 14, no. 3, pp. 363–380, 2012.
- [50] N. V. Brilliantov, F. Spahn, J. M. Hertzsch, and T. Pöschel, "Model for collisions in granular gases," *Phys. Rev. E - Stat. Physics, Plasmas, Fluids, Relat. Interdiscip. Top.*, vol. 53, no. 5, pp. 5382–5392, 1996.
- [51] E. Khain, "Bistability and hysteresis in dense shear granular flow," *Epl*, vol. 87, no. 1, 2009.
- [52] F. Goncu, *Mechanics of Granular Materials : Constitutive Behavior and Pattern Transformation*. 2012.
- [53] S. F. Masri, "General Motion of Impact Dampers," *J. Acoust. Soc. Am.*, vol. 47, no. 1B, pp. 229–237, 1970.
- [54] B. L. Fowler, E. M. Flint, and S. E. Olson, "Effectiveness and Predictability of Particle Damping," *Smart Struct. Mater. 2000 Damping Isol.*, vol. 3989, pp. 356–367, 2000.
- [55] J. Rongong, T. Cecil, and D. Webster, "US20060180420A1 - Vibration dampers," pp. 5–8, 2018.
- [56] K. Walton, "The Effective Elastic Moduli of a Random Packing of Spheres," *J. Mech. Phys. Solids*, vol. 35, no. 2, pp. 213–226, 1987.
- [57] Z. Lu, Z. Wang, Y. Zhou, and X. Lu, "Nonlinear dissipative devices in structural vibration control: A review," *J. Sound Vib.*, vol. 423, pp. 18–49, 2018.
- [58] P. Veeramuthuvel, K. Shankar, and K. K. Sairajan, "Application of particle damper on electronic packages for spacecraft," *Acta Astronaut.*, vol. 127, pp. 260–270, 2016.
- [59] S. G. Demiryurek and A. Krynkin, "Low-Frequency Broadband Vibration Damping Using the Nonlinear Damper with Metamaterial Properties," in *DAGA 2021*, 2021, pp. 94–96.
- [60] S. G. Demiryurek and A. Krynkin, "Low-Frequency Broadband Vibration Dampers from Nonlinear Structures with Metamaterial Properties," in *Proceedings of the Institute of Acoustics*, 2021, vol. 43.
- [61] J. A. Rongong and G. R. Tomlinson, "Amplitude Dependent Behaviour in the Application of," no. April, pp. 1–9, 2005.
- [62] B. Darabi and J. A. Rongong, "Amplitude dependent damping from granular

- viscoelastics," *J. Phys. Conf. Ser.*, vol. 382, no. 1, 2012.
- [63] T. Pöschel, T. Schwager, and C. Salueña, "Onset of fluidization in vertically shaken granular material," *Phys. Rev. E - Stat. Physics, Plasmas, Fluids, Relat. Interdiscip. Top.*, vol. 62, no. 1 B, pp. 1361–1367, 2000.
- [64] M. Sánchez and C. Manuel Carlevaro, "Nonlinear dynamic analysis of an optimal particle damper," *J. Sound Vib.*, vol. 332, no. 8, pp. 2070–2080, 2013.
- [65] N. Ahmad, R. Ranganath, and A. Ghosal, "Modeling and experimental study of a honeycomb beam filled with damping particles," *J. Sound Vib.*, vol. 391, pp. 20–34, 2017.
- [66] M. Gharib and S. Ghani, "Free vibration analysis of linear particle chain impact damper," *J. Sound Vib.*, vol. 332, no. 24, pp. 6254–6264, 2013.
- [67] P. Shubham, C. Aggarwal, and S. Joshi, "Optimisation of process Parameter to improve Dynamic Mechanical Properties of 3D Printed ABS Polymer using Taguchi Method," no. 6, pp. 21–28, 2018.
- [68] H. Panossian, "Optimized Non-Obstructive Particle Damping (NOPD) treatment for composite honeycomb structures," in *Collection of Technical Papers - AIAA/ASME/ASCE/AHS/ASC Structures, Structural Dynamics and Materials Conference*, 2006, vol. 10, pp. 7353–7362.
- [69] X. Lei and C. Wu, "Dynamic response prediction of non-obstructive particle damping using principles of gas-solid flows," *J. Vibroengineering*, vol. 18, no. 7, pp. 4692–4704, 2016.
- [70] D. J. Mead, "Wave propagation and natural modes in periodic systems: I. Mono-coupled systems," *J. Sound Vib.*, vol. 40, no. 1, pp. 1–18, 1975.
- [71] D. J. Mead, "Wave propagation and natural modes in periodic systems: II. Multi-coupled systems, with and without damping," *J. Sound Vib.*, vol. 40, no. 1, pp. 19–39, 1975.
- [72] T. Suhara, D. Green, and T. Suhara, "Periodic Structures," *Encycl. Handb. Integr. Opt.*, pp. 272–281, 2019.
- [73] M. BORN, "Wave Propagation in Periodic Structures," *Nature*, vol. 158, no. 4026, pp. 926–926, 1946.
- [74] R. Al Jahdali and Y. Wu, "Coupled Resonators for Sound Trapping and Absorption," *Sci. Rep.*, vol. 8, no. 1, 2018.
- [75] H. Peng and P. Frank Pai, "Acoustic metamaterial plates for elastic wave absorption and structural vibration suppression," *Int. J. Mech. Sci.*, vol. 89, pp. 350–361, 2014.
- [76] A. Nilsson, B. Liu, A. Nilsson, and B. Liu, "Waves in Solids," in *Vibro-Acoustics, Volume 1*, 2015, pp. 67–110.

- [77] E. Deckers, C. Claeys, O. Atak, J. P. Groby, O. Dazel, and W. Desmet, "A wave based method to predict the absorption, reflection and transmission coefficient of two-dimensional rigid frame porous structures with periodic inclusions," *Journal of Computational Physics*, vol. 312, pp. 115–138, 2016.
- [78] A. S. Phani, J. Woodhouse, and N. A. Fleck, "Wave propagation in two-dimensional periodic lattices," *J. Acoust. Soc. Am.*, vol. 119, no. 4, pp. 1995–2005, 2006.
- [79] C. Hakoda, J. Rose, P. Shokouhi, and C. Lissenden, "Using Floquet periodicity to easily calculate dispersion curves and wave structures of homogeneous waveguides," *AIP Conf. Proc.*, vol. 1949, no. April, 2018.
- [80] M. Nouh, O. Aldraihem, and A. Baz, "Wave propagation in metamaterial plates with periodic local resonances," *J. Sound Vib.*, vol. 341, pp. 53–73, 2015.
- [81] M. Nouh, O. Aldraihem, and A. Baz, "Vibration characteristics of metamaterial beams with periodic local resonances," *J. Vib. Acoust. Trans. ASME*, vol. 136, no. 6, pp. 1–12, Dec. 2014.
- [82] L. Raghavan and A. S. Phani, "Local resonance bandgaps in periodic media: Theory and experiment," *J. Acoust. Soc. Am.*, vol. 134, no. 3, pp. 1950–1959, 2013.
- [83] S. S. Deshpande, S. R. Rawat, N. P. Bandewar, and M. Y. Soman, "Consistent and lumped mass matrices in dynamics and their impact on finite element analysis results," *Int. J. Mech. Eng. Technol.*, vol. 7, no. 2, pp. 135–147, 2016.
- [84] U. of Colorado, "Lumped and Consistent Mass Matrices," *Introd. To Finite Elem. Methods*, pp. 31.1-31.23, 2010.
- [85] A. O. O. Krushynska, M. Miniaci, F. Bosia, and N. M. M. Pugno, "Coupling local resonance with Bragg band gaps in single-phase mechanical metamaterials," *Extrem. Mech. Lett.*, vol. 12, pp. 30–36, Apr. 2017.
- [86] M. Applications, "1.1 DEFINITION OF METAMATERIALS (MTMs) AND LEFT-HANDED (LH) MTMs," pp. 1–26, 2000.
- [87] J. Liu, H. Guo, and T. Wang, "A Review of Acoustic Metamaterials and Phononic Crystals," *Crystals*, vol. 10, no. 305, 2020.
- [88] S. Zhang, "Acoustic Metamaterial Design and Applications," p. 189, 2010.
- [89] I.-L. Chang, Z.-X. Liang, H.-W. Kao, S.-H. Chang, and C.-Y. Yang, "The wave attenuation mechanism of the periodic local resonant metamaterial," *J. Sound Vib.*, vol. 412, pp. 349–359, Jan. 2018.
- [90] P. F. Pai, H. Peng, and S. Jiang, "Acoustic metamaterial beams based on multi-frequency vibration absorbers," *Int. J. Mech. Sci.*, vol. 79, pp. 195–205, 2014.
- [91] P. F. Pai, G. Huang, and B. Assouar, "Phononics and Acoustic Metamaterials," in *Theory and Design of Acoustic Metamaterials*, 2015, pp. 207–232.

- [92] G. Palma, H. Mao, L. Burghignoli, P. Göransson, and U. Iemma, "Acoustic Metamaterials in Aeronautics," *Appl. Sci.*, vol. 8, no. 6, p. 971, 2018.
- [93] P. Sheng, "A Step Towards a Seismic Cloak," *Physics (College Park, Md.)*, vol. 7, p. 34, 2014.
- [94] P. T. Gardiner, *Smart Structures and Materials : Implications for Military Aircraft of New Generation*, no. November 1996. 1993.
- [95] M. Rupin, P. Roux, G. Lerosey, and F. Lemoult, "Symmetry issues in the hybridization of multi-mode waves with resonators: an example with Lamb waves metamaterial," *Sci. Rep.*, vol. 5, no. 1, p. 13714, 2015.
- [96] S. Brûlé, E. H. Javelaud, S. Enoch, and S. Guenneau, "Experiments on seismic metamaterials: Molding surface waves," *Phys. Rev. Lett.*, vol. 112, no. 13, pp. 1–5, 2013.
- [97] H. Sun, X. Du, and P. F. Pai, "Theory of metamaterial beams for broadband vibration absorption," *J. Intell. Mater. Syst. Struct.*, vol. 21, no. 11, pp. 1085–1101, 2010.
- [98] S. Brûlé *et al.*, "Experiments on seismic metamaterials: Molding surface waves," *Sci. Rep.*, vol. 7, no. 1, pp. 1–5, 2017.
- [99] C. Claeys, E. Deckers, B. Pluymers, and W. Desmet, "Lightweight NVH Solution Based on Vibro-Acoustic Metamaterials," *ATZextra Worldw.*, vol. 21, no. S1, pp. 50–53, 2016.
- [100] G. Palma, H. Mao, L. Burghignoli, P. Göransson, and U. Iemma, "Acoustic metamaterials in aeronautics," *Appl. Sci.*, vol. 8, no. 6, pp. 1–18, 2018.
- [101] R. Aljahdali, X. Zhang, and Y. Wu, "Effective Medium Theory for Phononic Crystals with Fluid Hosts," in *Theory and Design of Acoustic Metamaterials*, SPIE PRESS, 2015, pp. 315–331.
- [102] U. Iemma, "Theoretical and Numerical Modeling of Acoustic Metamaterials for Aeroacoustic Applications," 2016.
- [103] J. Duran, "Interactions in Granular Media," in *Sands, Powders and Grains: an Introduction to the Physics of Granular Materials*, New York:, and H. E. S. E. Guyon, L. Lam, D. Langevin, Ed. 2000, pp. 19–52.
- [104] Brown, R. L. and J. C. Richards, *Principles of powder mechanics: essays on the packing and flow of powders and bulk solids*, Volume 10. Oxford: Elsevier, 2016.
- [105] C. Güttler, D. Heißelmann, J. Blum, and S. Krijt, "Normal Collisions of Spheres: A Literature Survey on Available Experiments," 2012.
- [106] M. Iwashita K., Oda, "Rolling Resistance At Contacts in Simulation of Shear Band Development by DEM," *Asce*, vol. 124, no. March, pp. 285–292, 1998.
- [107] C. A. Coulomb, "Divers Savants," *Acad. Roy. Sci. Mem. Phys.*, vol. 7, no. 343, 1773.

- [108] B. Darabi, "Dissipation of vibration energy using viscoelastic granular materials," The University of Sheffield, 2013.
- [109] H. Ghaednia, X. Wang, S. Saha, Y. Xu, A. Sharma, and R. L. Jackson, "A Review of Elastic-Plastic Contact Mechanics," *Appl. Mech. Rev.*, vol. 69, no. 6, 2017.
- [110] C. J. Coetzee, "Review: Calibration of the discrete element method," *Powder Technol.*, vol. 310, pp. 104–142, 2017.
- [111] C. J. Coetzee, "Calibration of the discrete element method and the effect of particle shape," in *Proceedings of the 10th South African Conference on Computational and Applied Mechanics, SACAM 2016*, 2016.
- [112] Engineeringtoolbox.com, "Friction and Friction Coefficients," 2021. [Online]. Available: https://www.engineeringtoolbox.com/friction-coefficients-d_778.html. [Accessed: 29-Mar-2021].
- [113] A. Mills, "The coefficient of friction , particularly of ice," *Phys. Eduction*, vol. 43, no. June 2008, pp. 392–395, 2016.
- [114] A. D. Rosato and N. Zhang, "Experiments and simulations on vibration induced densification of bulk solids," *KONA Powder Part. J.*, vol. 24, no. March, pp. 93–103, 2006.
- [115] D. Lippert and J. Spektor, "Rolling Resistance and Industrial Wheels," *Hamilt. Caster*, no. 888, p. 8, 2013.
- [116] Bangs Laboratories, "Material Properties of Polystyrene and Poly(methyl methacrylate) (PMMA) Microspheres," *Bangs Lab. Inc.*, pp. 1–2, 2015.
- [117] K. H. Hunt and F. R. E. Crossley, "Coefficient of Restitution Interpreted As Damping in Vibroimpact," *Am. Soc. Mech. Eng.*, no. 75-APM-H, pp. 440–445, 1975.
- [118] D. B. Hastie, "Experimental measurement of the coefficient of restitution of irregular shaped particles impacting on horizontal surfaces," *Chem. Eng. Sci.*, vol. 101, pp. 828–836, 2013.
- [119] R. E. Stratton and C. M. Wensrich, "Modelling of multiple intra-time step collisions in the hard-sphere discrete element method," *Powder Technol.*, vol. 199, no. 2, pp. 120–130, 2010.
- [120] C. Thornton and Z. Ning, "A theoretical model for the stick/bounce behaviour of adhesive, elastic- plastic spheres," *Powder Technol.*, vol. 99, no. 2, pp. 154–162, 1998.
- [121] R. Sondergaard, K. Chaney, and C. E. Brennen, "Measurements of solid spheres bouncing off flat plates," *Am. Soc. Mech. Eng.*, vol. 112, no. 90, 1990.
- [122] N. Meyer and R. Seifried, "Numerical and experimental investigations in the damping behavior of particle dampers attached to a vibrating structure," *Computers and Structures*, vol. 238. 2020.

- [123] P. F. O. V. Kim; Dunn, "Direct visualization and model validation of microsphere impactand surface capture," *J. Aerosol Sci.*, vol. 39, no. 4, pp. 373–375, 2008.
- [124] X. Li, P. F. Dunn, and R. M. Brach, "Experimental and numerical studies on the normal impact of microspheres with surfaces," *J. Aerosol Sci.*, vol. 30, no. 4, pp. 439–449, 1999.
- [125] J. Duran, "Mixing and Segregation," in *Sands, Powders and Grains: an Introduction to the Physics of Granular Materials*, New York: Springer Berlin Heidelberg, Ed. 2000, pp. 154–183.
- [126] G. T. Nolan, "Computer Simulation of Random Packings of Hard Spheres," *Powder Technol.*, vol. 62, pp. 189–196, 1990.
- [127] H. Iwata and T. Homma, "Distribution of coordination numbers in random packing of homogeneous spheres," *Powder Technol.*, vol. 10, no. 1–2, pp. 79–83, 1974.
- [128] F. Zamponi, "Packings close and loose," *Nature*, vol. 453, no. 7195, pp. 606–607, 2008.
- [129] C. R. Wassgren Jr., "Vibration of Granular Materials," *PhD thesis*. pp. 1–171, 1997.
- [130] H. K. Pak and R. P. Behringer, "Surface waves in vertically vibrated granular materials," *Phys. Rev. Lett.*, vol. 71, no. 12, pp. 1832–1835, 1993.
- [131] W. Liu, G. R. Tomlinson, and J. A. Rongong, "The dynamic characterisation of disk geometry particle dampers," *J. Sound Vib.*, vol. 280, no. 3–5, pp. 849–861, 2005.
- [132] E. R. Nowak, J. B. Knight, E. Ben-Naim, H. M. Jaeger, and S. R. Nagel, "Density fluctuations in vibrated granular materials," *Phys. Rev. E - Stat. Physics, Plasmas, Fluids, Relat. Interdiscip. Top.*, vol. 57, no. 2, pp. 1971–1982, 1998.
- [133] J. Duran, "Fluidization, Decompaction, and Fragmentation," in *Sands, Powders and Grains: an Introduction to the Physics of Granular Materials*, New York: Springer Berlin Heidelberg, Ed. 2000, pp. 54–118.
- [134] H. J. Herrmann, "Physics of granular media," *Chaos, Solitons and Fractals*, vol. 6, no. C, pp. 203–212, 1995.
- [135] K. Hashemnia and S. Pourandi, "Study the effect of vibration frequency and amplitude on the quality of fluidization of a vibrated granular flow using discrete element method," *Powder Technol.*, vol. 327, pp. 335–345, 2018.
- [136] R. Mishra, "Application Of Tuned Mass Damper For Vibration Control Of Frame Structures Under Seismic Excitations," National Institute of Technology, Rourkela, 2011.
- [137] C. Y. Wu, L. Y. Li, and C. Thornton, "Energy dissipation during normal impact of elastic and elastic-plastic spheres," *Int. J. Impact Eng.*, vol. 32, no. 1–4, pp. 593–604, 2005.

- [138] B. Severson, "Nano to Macro Study of Friction and Adhesion in Granular Materials," Northwestern University, 2007.
- [139] J. D. Park, J. S. Myung, and K. H. Ahn, "A review on particle dynamics simulation techniques for colloidal dispersions: Methods and applications," *Korean J. Chem. Eng.*, vol. 33, no. 11, pp. 3069–3078, 2016.
- [140] C. M. Wensrich and A. Katterfeld, "Rolling friction as a technique for modelling particle shape in DEM," *Powder Technol.*, vol. 217, pp. 409–417, 2012.
- [141] R. L. Jackson, H. Ghaednia, H. Lee, A. Rostami, and X. Wang, "Contact mechanics," *Tribol. Sci. Eng. From Basics to Adv. Concepts*, vol. 9781461419, pp. 93–140, 2013.
- [142] EDEM, "EDEM." 2019.
- [143] DEM_Solutions, "EDEM 2 . 4 Theory Reference Guide," p. 19, 2014.
- [144] P. A. Cundall and O. D. L. Strack, "A discrete numerical model for granular assemblies," *Geotechnique*, vol. 29, no. 1, pp. 47–65, 1979.
- [145] Z. Chen, X. Tong, and Z. Li, "Numerical investigation on the sieving performance of elliptical vibrating screen," *Processes*, vol. 8, no. 9, 2020.
- [146] G. R. Tomlinson, D. Pritchard, and R. Wareing, "Damping characteristics of particle dampers," *Proc Instn Mech Engrs*, vol. 215, pp. 253–257, 2001.
- [147] C. X. Wong, A. B. Spencer, and J. A. Rongong, "Effects of enclosure geometry on particle damping performance," *Collect. Tech. Pap. - AIAA/ASME/ASCE/AHS/ASC Struct. Struct. Dyn. Mater. Conf.*, no. May, pp. 1–16, 2009.
- [148] D. N. J. Els, "Damping of rotating beams with particle dampers: Discrete element method analysis," *AIP Conf. Proc.*, vol. 1542, pp. 867–870, 2013.
- [149] Altair Engineering, "EBOOK Applications of EDEM for Powder Handling Processes."
- [150] D. M. Sousani, "What is DEM?," 2019.
- [151] C. Xie, H. Ma, and Y. Zhao, "Investigation of modeling non-spherical particles by using spherical discrete element model with rolling friction," *Eng. Anal. Bound. Elem.*, vol. 105, no. April, pp. 207–220, 2019.
- [152] B. Darabi, J. A. Rongong, and T. Zhang, "Viscoelastic granular dampers under low-amplitude vibration," *JVC/Journal Vib. Control*, vol. 24, no. 4, pp. 708–721, 2018.
- [153] M. Sperl, "Experiments on corn pressure in silo cells - Translation and comment of Janssen's paper from 1895," *Granul. Matter*, vol. 8, no. 2, pp. 59–65, 2006.
- [154] C. W. De Silva, "Experimental modal analysis," *Vib. Monit. Testing, Instrum.*, pp. 237–263, 2007.
- [155] Y. S. Lee, F. Nucera, A. F. Vakakis, D. M. McFarland, and L. A. Bergman, "Periodic

- orbits, damped transitions and targeted energy transfers in oscillators with vibro-impact attachments," *Phys. D Nonlinear Phenom.*, vol. 238, no. 18, pp. 1868–1896, 2009.
- [156] H. H. Huang and C. T. Sun, "Locally resonant acoustic metamaterials with 2D anisotropic effective mass density," *Philos. Mag.*, vol. 91, no. 6, pp. 981–996, 2011.
- [157] P. F. Pai, "Metamaterial-based broadband elastic wave absorber," *J. Intell. Mater. Syst. Struct.*, vol. 21, no. 5, pp. 517–528, 2010.
- [158] M. A. Nough, O. J. Aldraihem, and A. Baz, "Periodic metamaterial plates with smart tunable local resonators," *J. Intell. Mater. Syst. Struct.*, vol. 27, no. 13, pp. 1829–1845, 2016.
- [159] P. Sheng, X. X. Zhang, Z. Liu, and C. T. Chan, "Locally resonant sonic materials," *Phys. B Condens. Matter*, vol. 338, no. 1–4, pp. 201–205, 2003.
- [160] S. S. Rao and P. Griffin, "Mechanical Vibrations Fifth Edition in SI Units," *Mech. Vib.*, p. 62, 2011.
- [161] A. Franck, "Viscoelasticity and dynamic Mechanical Testing," *ANoo4*, pp. 1–6.
- [162] Ultimaker, "Setup to success : 3D printing for engineers," p. 15, 2019.
- [163] D. M. A. Testing and H. A. S. Never, "DMA 25 / DMA 50 DMA desktop series," pp. 50–52.
- [164] PerkinElmer Inc., "Dynamic Mechanical Analysis (DMA) - A Beginner's Guide," *Introd. to DMA*, pp. 1–23, 2008.
- [165] A. Fodor, "DMA tests for 3D printed polymer specimens of fatigue test examination," pp. 129–135, 2017.
- [166] "PLA vs ABS vs Nylon." [Online]. Available: <https://markforged.com/resources/blog/pla-abs-nylon#:~:text=PLA and ABS are both,better plastic for prototyping applications>.
- [167] B. L. Fowler, E. M. Flint, and S. E. Olson, "Design methodology for particle damping," *Proc. SPIE Conf. Smart Struct. Mater. Pap.*, vol. 4331, pp. 4331–20, 2001.
- [168] "polynomial-curve-fitting." [Online]. Available: <https://uk.mathworks.com/help/matlab/math/polynomial-curve-fitting.html>.
- [169] C. C. Claeys, K. Vergote, P. Sas, and W. Desmet, "On the potential of tuned resonators to obtain low-frequency vibrational stop bands in periodic panels," *J. Sound Vib.*, vol. 332, no. 6, pp. 1418–1436, 2013.
- [170] G. Ma, M. Yang, S. Xiao, Z. Yang, and P. Sheng, "Acoustic metasurface with hybrid resonances," *Nat. Mater.*, vol. 13, no. 9, pp. 873–878, 2014.
- [171] V. G. Veselago, "THE ELECTRODYNAMICS OF SUBSTANCES WITH

- SIMULTANEOUSLY NEGATIVE VALUES OF ϵ AND μ ," *Sov. Phys. Uspekhi*, vol. 10, no. 4, pp. 509–514, 1968.
- [172] M. I. Hussein and M. J. Frazier, "Metadamping in dissipative metamaterials," *ASME Int. Mech. Eng. Congr. Expo. Proc.*, vol. 14, pp. 4767–4774, 2013.
- [173] S. Hajarolasvadi and A. E. Elbanna, "Dynamics of metamaterial beams consisting of periodically-coupled parallel flexural elements: A theoretical study," *J. Phys. D: Appl. Phys.*, vol. 52, no. 31, p. 315101, Jul. 2019.
- [174] U. de Giovannini and H. Hübener, "Floquet analysis of excitations in materials," *arXiv*, 2019.
- [175] S. A. Pope and H. Laalej, "A multi-layer active elastic metamaterial with tuneable and simultaneously negative mass and stiffness," *Smart Mater. Struct.*, vol. 23, no. 7, 2014.
- [176] M. R. Ashory, "High Quality Modal Testing Methods," *Vib. Univ. Technol. Cent.*, no. March, p. 272, 1999.
- [177] S. Guenneau, A. Movchan, N. Movchan, S. Guenneau, A. Movchan, and N. Movchan, "Localised bending modes in split ring resonators," vol. 394, no. 2, pp. 141–144, 2007.
- [178] Y. Achaoui, B. Ungureanu, S. Enoch, S. Brûlé, and S. Guenneau, "Seismic waves damping with arrays of inertial resonators," *Extrem. Mech. Lett.*, vol. 8, pp. 30–37, 2016.
- [179] P. F. Pai, G. Huang, and P. F. Pai, "Design of Wide- and Multistopband Acoustic Metamaterials," *Theory Des. Acoust. Metamaterials*, pp. 137–172, 2015.
- [180] J. He and Z.-F. Fu, "Basic vibration theory," *Modal Anal.*, pp. 49–78, 2001.
- [181] B. Balachandran and E. B. Magrab, *Vibrations*, Second. Cengage Learning, 2009.
- [182] H. Sun, X. Du, and P. F. Pai, "Theory of metamaterial beams for broadband vibration absorption," *J. Intell. Mater. Syst. Struct.*, vol. 21, no. 11, pp. 1085–1101, 2010.
- [183] M. Carfagni, E. Lenzi, and M. Pierini, "Loss factor as a measure of mechanical damping," *Proc. Int. Modal Anal. Conf. - IMAC*, vol. 1, pp. 580–584, 1998.
- [184] S. S. Jung, B. S. Jeon, J. Jin, and Y. B. Lee, "Measurement of the loss factor and the Young's modulus in acrylonitrile butadiene styrene and Polymethyl Methacrylate by using an acoustic wave generator," *Int. J. Precis. Eng. Manuf.*, vol. 15, no. 12, pp. 2493–2497, 2014.
- [185] A. N. Norris and Z. Wang, "Low frequency bending waves in periodic plates," *J. Sound Vib.*, vol. 169, no. 4, pp. 485–502, 1994.
- [186] D. Bigoni, S. Guenneau, A. B. Movchan, and M. Brun, "Elastic metamaterials with inertial locally resonant structures: Application to lensing and localization," *Phys. Rev. B - Condens. Matter Mater. Phys.*, vol. 87, no. 17, pp. 1–6, 2013.

- [187] C. Boutin and P. Roussillon, "Wave propagation in presence of oscillators on the free surface," *Int. J. Eng. Sci.*, vol. 44, no. 3–4, pp. 180–204, 2006.
- [188] A. Maurel, J. J. Marigo, K. Pham, and S. Guenneau, "Conversion of Love waves in a forest of trees," *Phys. Rev. B*, vol. 98, no. 13, pp. 1–5, 2018.
- [189] A. Colombi, D. Colquitt, P. Roux, S. Guenneau, and R. V. Craster, "A seismic metamaterial: The resonant metawedge," *Sci. Rep.*, vol. 6, no. Umr 7249, pp. 1–6, 2016.
- [190] Z. Lu, X. Lu, W. Lu, and S. F. Masri, "Experimental studies of the effects of buffered particle dampers attached to a multi-degree-of-freedom system under dynamic loads," *J. Sound Vib.*, vol. 331, no. 9, pp. 2007–2022, 2012.
- [191] Y. Wang, B. Liu, A. Tian, and W. Tang, "Experimental and numerical investigations on the performance of particle dampers attached to a primary structure undergoing free vibration in the horizontal and vertical directions," *J. Sound Vib.*, vol. 371, pp. 35–55, 2016.
- [192] Z. Lu, X. Lu, and S. F. Masri, "Studies of the performance of particle dampers under dynamic loads," *J. Sound Vib.*, vol. 329, no. 26, pp. 5415–5433, 2010.
- [193] J. Hong, L. L. Chen, Y. Ma, G. R. Tomlinson, and J. A. Rongong, "Hysteretic properties of metal rubber particles," *Proc. Inst. Mech. Eng. Part C J. Mech. Eng. Sci.*, vol. 227, no. 4, pp. 693–702, 2013.
- [194] D. J. Ewins, *Modal Testing : Theory , Practice and Application*, Second Edi. Hertfordshire, England: Research Studies Press LTD., 2000.

Appendices

Chapter 3-Appendix

Appendix 3.1

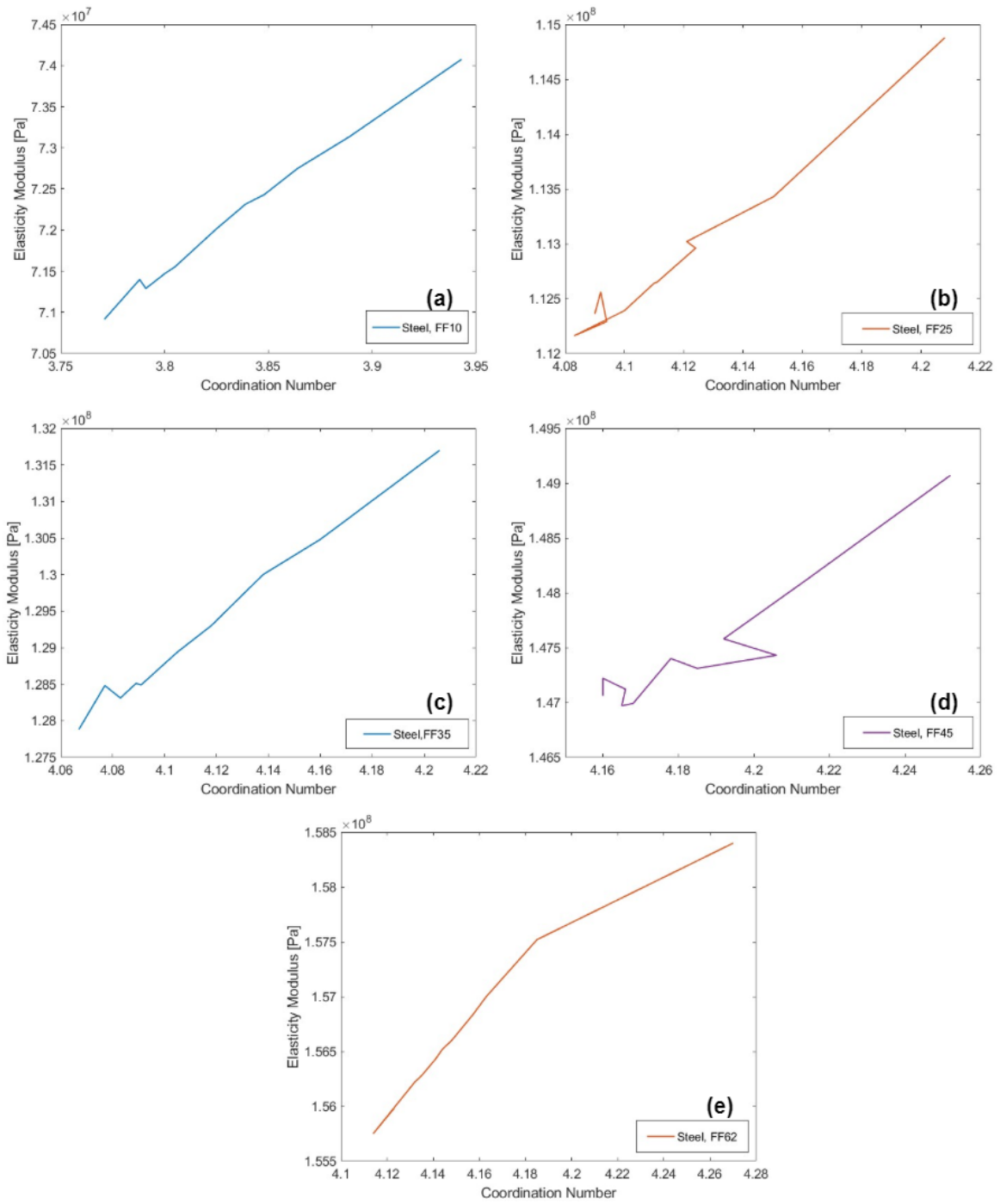


Figure A3. 1: Equivalent Young's Modulus vs Coordination Number Evaluation for Metal Particle Filling

Appendix 3.2

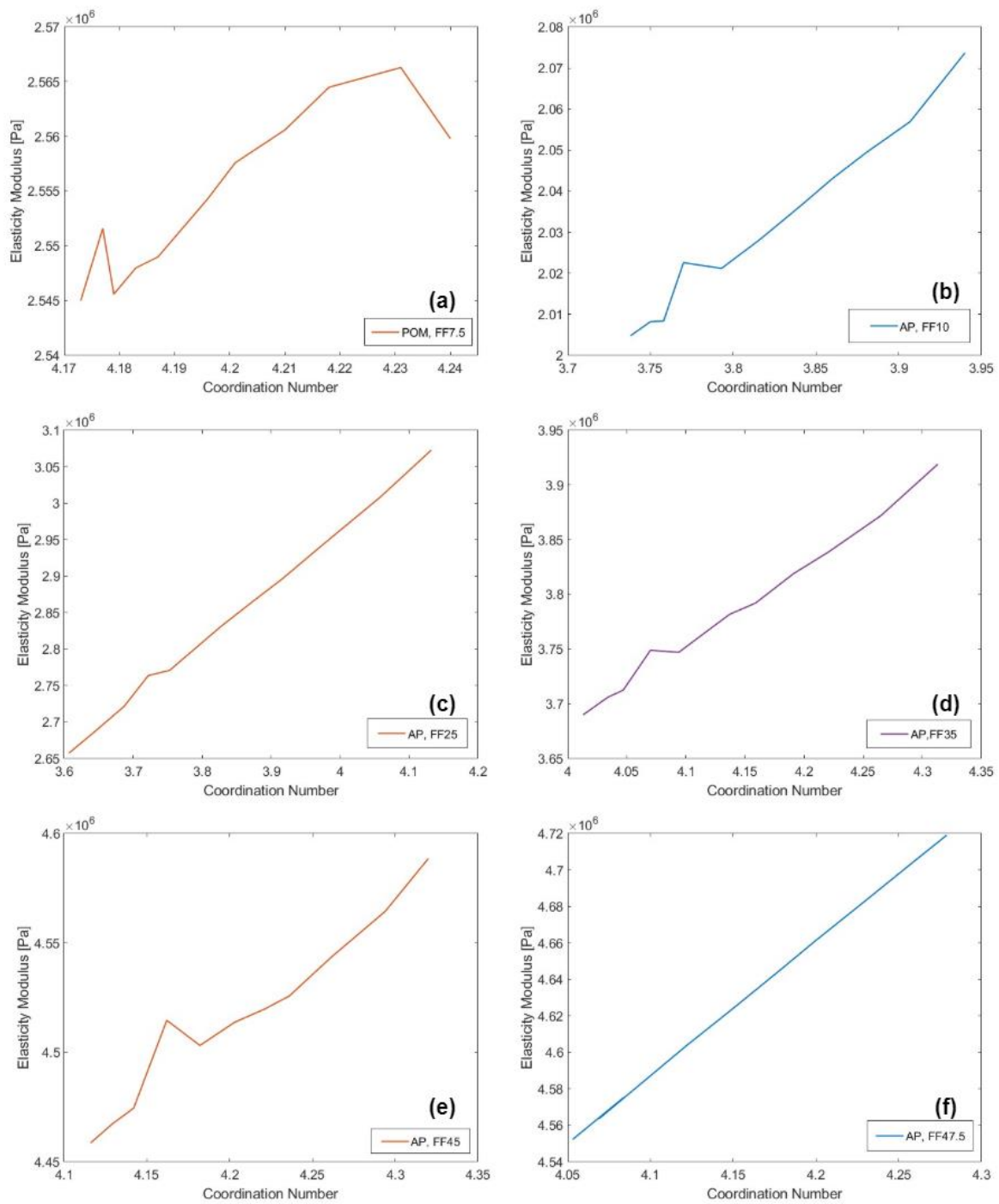


Figure A3. 2: Equivalent Young's Modulus vs Coordination Number Evaluation for Viscoelastic Particle Filling

Chapter 4-Appendix

Appendix 4.1

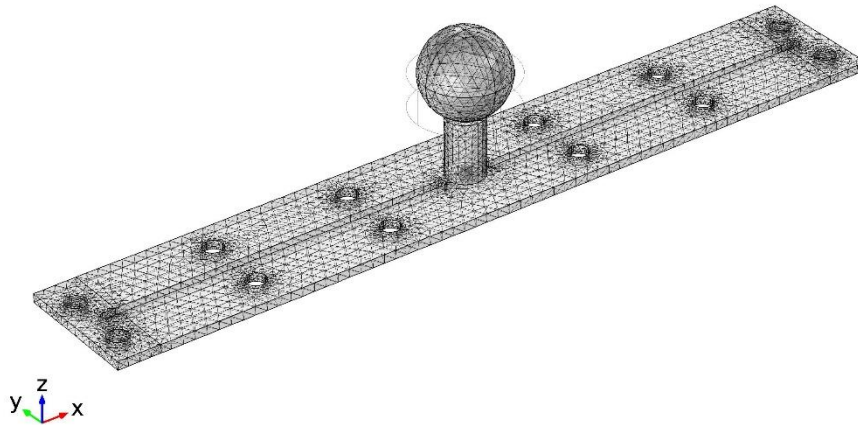


Figure A4. 1: Meshed solid structures

Table A4. 1: Mesh details of the solid geometries

Mesh Details	
Number of Tetrahedral Elements	35330
Number of Triangular Elements	13565
Number of Edge Elements	1783
Number of Vertex Elements	187
Domain Element Statistics	
Number of Elements	35330
Minimum Element Quality	2.38E-7
Average Element Quality	0.6758
Element Volume Ratio	3.79E-6
Mesh Volume	207900.0 mm ³
Maximum Growth Rate	5.342
Average Growth Rate	1.895

Table A4. 2: Material properties of the solid geometries

	Material Properties of the Beam	Material Properties of the Resonator
Young's Modulus [Pa]	200E9	1.45E9
Density [kg/m ³]	7850	950
Poisson's Ratio [-]	0.33	0.35

Appendix 4.2

Table A4. 3: DMTA test results for ABS at 25°C

E [Pa]	E' [Pa]	E'' [Pa]
1.42E+09	1.42E+09	2.40E+07
1.41E+09	1.41E+09	2.58E+07
1.42E+09	1.42E+09	2.74E+07
1.43E+09	1.43E+09	2.86E+07
1.43E+09	1.43E+09	2.80E+07
1.44E+09	1.44E+09	2.98E+07
1.44E+09	1.44E+09	2.82E+07
1.44E+09	1.44E+09	3.00E+07
1.45E+09	1.45E+09	3.04E+07
1.45E+09	1.45E+09	3.13E+07
1.45E+09	1.45E+09	3.27E+07
1.45E+09	1.45E+09	3.42E+07
1.46E+09	1.46E+09	3.33E+07
1.46E+09	1.46E+09	3.48E+07
1.46E+09	1.46E+09	3.69E+07
1.46E+09	1.46E+09	3.78E+07
1.46E+09	1.46E+09	3.60E+07
1.46E+09	1.46E+09	3.69E+07
1.46E+09	1.46E+09	3.75E+07
1.46E+09	1.46E+09	2.57E+07

Table A4. 4: DMTA test results for PLA at 25°C

E [Pa]	E' [Pa]	E'' [Pa]
1.28E+09	1.28E+09	1.74E+07
1.28E+09	1.28E+09	1.80E+07
1.28E+09	1.28E+09	1.92E+07
1.28E+09	1.28E+09	1.93E+07
1.29E+09	1.29E+09	2.03E+07
1.29E+09	1.29E+09	2.00E+07
1.29E+09	1.29E+09	2.22E+07
1.29E+09	1.29E+09	2.26E+07
1.30E+09	1.29E+09	2.46E+07
1.30E+09	1.30E+09	2.46E+07
1.30E+09	1.30E+09	2.72E+07
1.30E+09	1.30E+09	2.69E+07
1.30E+09	1.30E+09	2.46E+07
1.30E+09	1.30E+09	2.67E+07
1.30E+09	1.30E+09	2.63E+07
1.30E+09	1.30E+09	2.76E+07
1.31E+09	1.31E+09	2.86E+07

1.31E+09	1.31E+09	2.94E+07
1.31E+09	1.31E+09	2.86E+07
1.32E+09	1.32E+09	2.21E+07

Appendix 4.3

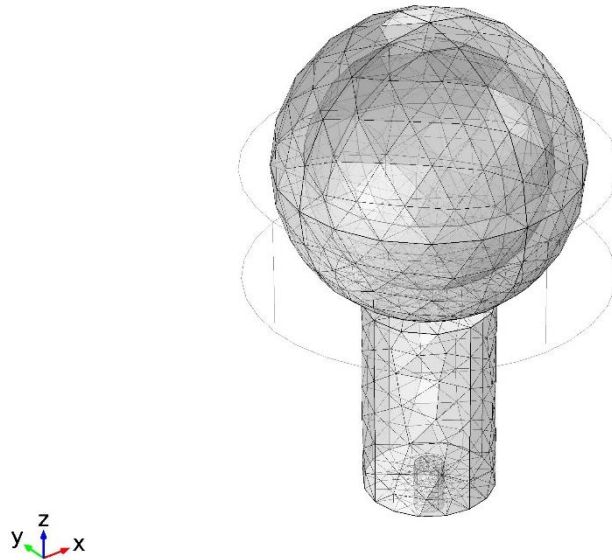


Figure A4. 2: Meshed Resonator

Table A4. 5: Mesh Properties of the Resonator

Mesh Details	
Number of Tetrahedral Elements	5730
Number of Triangular Elements	2006
Number of Edge Elements	297
Number of Vertex Elements	40
Domain Element Statistics	
Number of Elements	5732
Minimum Element Quality	1.33E-7
Average Element Quality	0.655
Element Volume Ratio	1.69E-5
Mesh Volume	44380 mm ³
Maximum Growth Rate	6.284
Average Growth Rate	2.0

Table A4. 6: Material Properties of the Resonator

	Material Properties of the Resonator
Young's Modulus [Pa]	1.45E9
Density [kg/m ³]	950
Poisson's Ratio [-]	0.35

Appendix 4.4: Height Calculation-MATLAB Code

```
clear
close all
clc

r=25
% h is the radius=half length of the spherical cap in contact area
% h=(0.25:0.25:5.5); %for R5.5
% h=(0.25:0.25:11); %for R11
h=(0.5:0.5:25); %for R25
% h=(0.5:0.5:33); %for R33
x1=(2*r+sqrt((2*r)^2-4*h.^2))/2;
x1=x1';
x2=(2*r-sqrt((2*r)^2-4*h.^2))/2;
x2=x2';
writematrix(x1, 'x1_lengthdata_R25.txt');
writematrix(x2, 'x2_lengthdata_R25.txt');
```

Appendix 4.5: Contact Fit Calculation-MATLAB Code

```
clear
close all
clc

% length=load('D:\Education in the UK\1- PhD_University of Sheffield\1- PhD
Project\16- Results\COMSOL Multiphysics_Results\Finite Structure
Analysis\7- Contact Area of Resonator\x2_lengthdata_R5.5.txt');
% length=load('D:\Education in the UK\1- PhD_University of Sheffield\1- PhD
Project\16- Results\COMSOL Multiphysics_Results\Finite Structure
Analysis\7- Contact Area of Resonator\x2_lengthdata_R11.txt');
% length=load('D:\Education in the UK\1- PhD_University of Sheffield\1- PhD
Project\16- Results\COMSOL Multiphysics_Results\Finite Structure
Analysis\7- Contact Area of Resonator\x2_lengthdata_R25.txt');
length=load('D:\Education in the UK\1- PhD_University of Sheffield\1- PhD
Project\16- Results\COMSOL Multiphysics_Results\Finite Structure
Analysis\7- Contact Area of Resonator\x2_lengthdata_R33.txt');

% EigFreq=load('D:\Education in the UK\1- PhD_University of Sheffield\1-
PhD Project\16- Results\COMSOL Multiphysics_Results\Finite Structure
Analysis\7- Contact Area of Resonator\eigfreq_R5.5.txt');
% EigFreq=load('D:\Education in the UK\1- PhD_University of Sheffield\1-
PhD Project\16- Results\COMSOL Multiphysics_Results\Finite Structure
Analysis\7- Contact Area of Resonator\eigfreq_R11.txt');
% EigFreq=load('D:\Education in the UK\1- PhD_University of Sheffield\1-
PhD Project\16- Results\COMSOL Multiphysics_Results\Finite Structure
Analysis\7- Contact Area of Resonator\eigfreq_R25.txt');
EigFreq=load('D:\Education in the UK\1- PhD_University of Sheffield\1- PhD
Project\16- Results\COMSOL Multiphysics_Results\Finite Structure
Analysis\7- Contact Area of Resonator\eigfreq_R33.txt');

% R is the radius of the sphere in mm
R = 25;
x = length;
% x=x(1:1:11); %for R5.5
% x=x(1:1:29); %for R11
```

```

z = EigFreq;
% z=z(1:1:11); %for R5.5
% z=z(1:1:29); %for R11

% h is the radius=half length of the spherical cap in contact area
% h=(0.25:0.25:5.5); %for R5.5
% h=(0.25:0.25:11); %for R11
% h=(0.5:0.5:25); %for R25
h=(0.5:0.5:33); %for R33

a= h./R;
% a=a(1:1:11); %for R5.5
% a=a(1:1:29); %for R11
p3=polyfit(a,z,5);
%2 in polyfit corresponds to the second degree of polynomial
a1=a;
z1=polyval(p3,a1);
p3_eq=poly2sym(p3);

figure
% semilogy(a,z,'o',a1,z1);
plot(a,z,'o',a1,z1);
legend('Eigenfrequency data-3','Polynomial fit');
xlabel('Dimensionless Ratio of Area [-]');
ylabel('Eigenfrequency Level[Hz]');
% xlim([0.45,2.85]);

```

Appendix 4.6

Table A4. 7: Polynomial Fit Calculated Values

<i>Polynomial Fit Data of D=11 mm</i>	<i>Polynomial Fit Data of D=22 mm</i>
54625.200	73252.141
-117577.810	-154418.969
90876.073	122213.138
-33872.992	-45861.942
7317.146	10029.667
523.749	533.119
<i>Polynomial Fit Data of D=50 mm</i>	<i>Polynomial Fit Data of D=66 mm</i>
10780.124	-361.466
-31543.720	-11613.972
36803.083	27041.215
-22160.723	-21747.215
7796.756	7533.433
718.103	756.064

Chapter 5-Appendix

Appendix 5.1

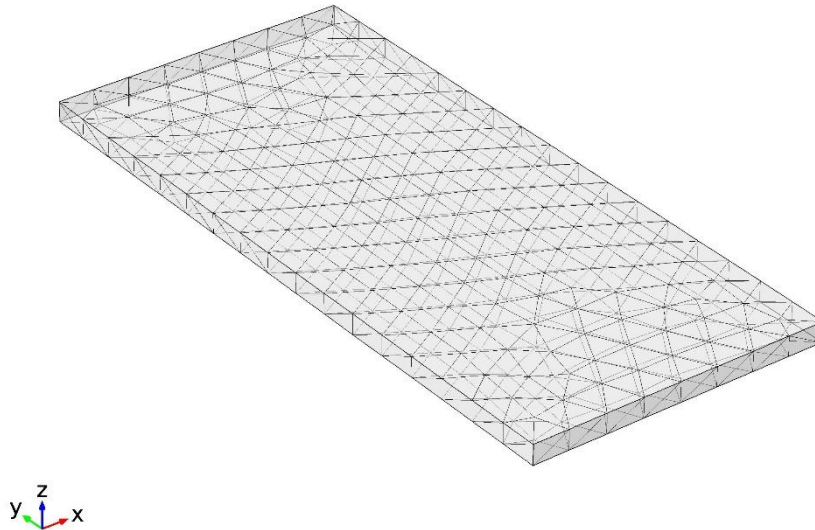


Figure A5. 1: Meshed unit cell (L=170 mm)

Table A5. 1: Mesh properties of the unit cell (L=170 mm)

Mesh Details	
Number of Tetrahedral Elements	980
Number of Triangular Elements	740
Number of Edge Elements	104
Number of Vertex Elements	8
Domain Element Statistics	
Number of Elements	980
Minimum Element Quality	0.1342
Average Element Quality	0.577
Element Volume Ratio	0.229
Mesh Volume	63750.0 mm ³
Maximum Growth Rate	1.951
Average Growth Rate	1.895

Appendix 5.2

Table A5. 2: Material Properties of the Unit Cell (L=170 mm)

	Material Properties of the Unit Cell
Young's Modulus [Pa]	200E9
Density [kg/m ³]	7850
Poisson's Ratio [-]	0.33

Appendix 5.3

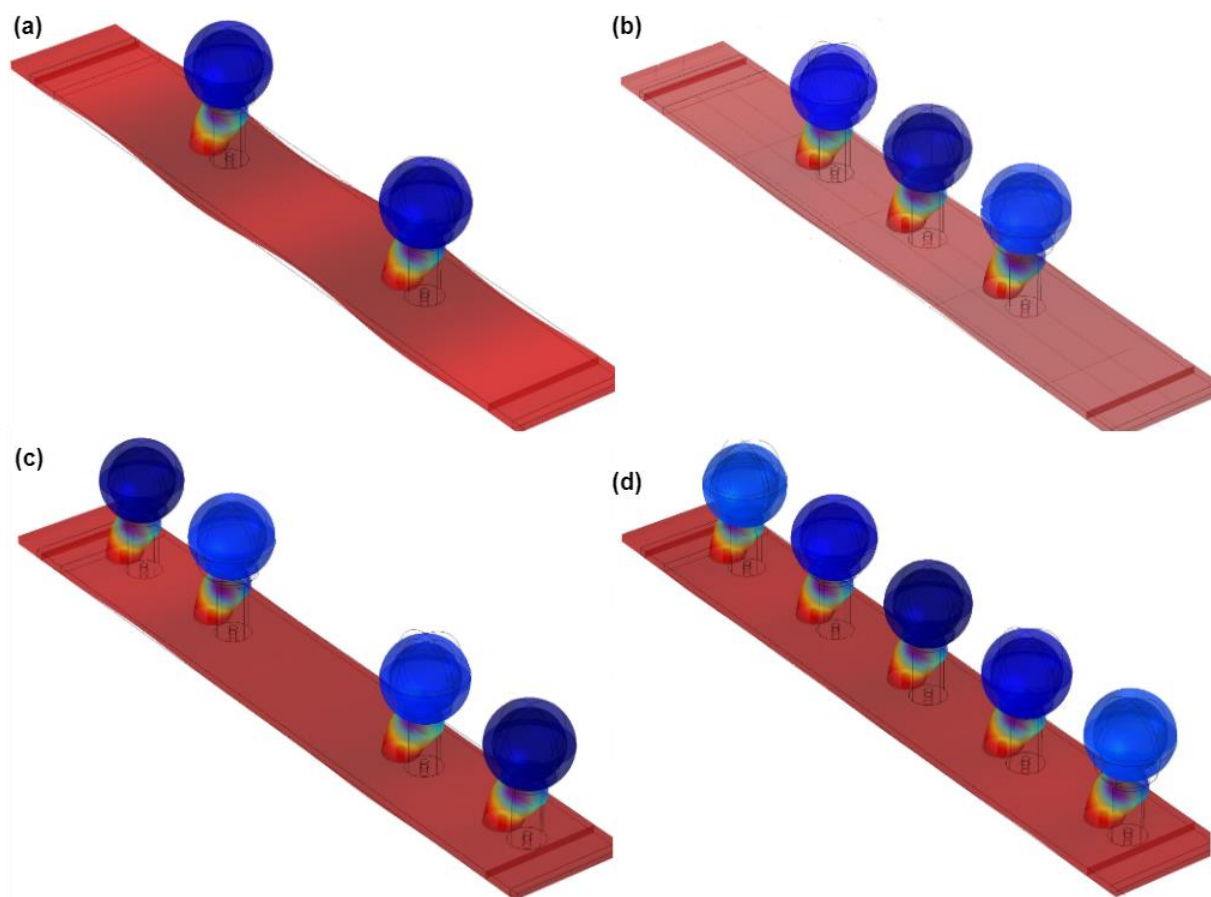


Figure A5. 2: Multiple resonator arrangement (L=90 mm) in the thickness mode : (a) two-resonator, (b) three-resonator, (c) four-resonator, (d) five-resonator arrangement

Chapter 7-Appendix

Appendix 7.1

Table A7. 1: 10% Steel filling equivalent isotropic solid medium Young's Modulus

Frequency [Hz]	Equivalent Young's Modulus [Pa]
50	7.4076E+07
150	7.3135E+07
250	7.2748E+07
350	7.2431E+07
450	7.2315E+07
550	7.2015E+07
650	7.1552E+07
750	7.1468E+07
850	7.1290E+07
950	7.1398E+07
1050	7.0914E+07

Table A7. 2: 25% Steel filling equivalent isotropic solid medium Young's Modulus

Frequency [Hz]	Equivalent Young's Modulus [Pa]
50	1.1488E+08
150	1.1343E+08
250	1.1302E+08
350	1.1296E+08
450	1.1265E+08
550	1.1264E+08
650	1.1239E+08
750	1.1216E+08
850	1.1229E+08
950	1.1256E+08
1050	1.1236E+08

Table A7. 3: 35% Steel filling equivalent isotropic solid medium Young's Modulus

Frequency [Hz]	Equivalent Young's Modulus [Pa]
50	1.3170E+08
150	1.3048E+08
250	1.3000E+08
350	1.2930E+08
450	1.2894E+08
550	1.2878E+08
650	1.2849E+08
750	1.2851E+08
850	1.2831E+08
950	1.2848E+08

1050	1.2788E+08
------	------------

Table A7. 4: 45% Steel filling equivalent isotropic solid medium Young's Modulus

Frequency [Hz]	Equivalent Young's Modulus [Pa]
50	1.4907E+08
150	1.4812E+08
250	1.4758E+08
350	1.4743E+08
450	1.4731E+08
550	1.4740E+08
650	1.4699E+08
750	1.4697E+08
850	1.4712E+08
950	1.4722E+08
1050	1.4706E+08

Appendix 7.2

Table A7. 5: 10% AP filling equivalent isotropic solid medium Young's Modulus

Frequency [Hz]	Equivalent Young's Modulus [Pa]
50	2.0737E+06
150	2.0570E+06
250	2.0493E+06
350	2.0431E+06
450	2.0362E+06
550	2.0282E+06
650	2.0212E+06
750	2.0226E+06
850	2.0084E+06
950	2.0082E+06
1050	2.0048E+06

Table A7. 6: 25% AP filling equivalent isotropic solid medium Young's Modulus

Frequency [Hz]	Equivalent Young's Modulus [Pa]
50	3.0727E+06
150	3.0082E+06
250	2.9441E+06
350	2.8963E+06
450	2.8680E+06
550	2.8310E+06
650	2.7711E+06
750	2.7639E+06
850	2.7218E+06

950	2.6852E+06
1050	2.6577E+06

Table A7. 7: 35% AP filling equivalent isotropic solid medium Young's Modulus

Frequency [Hz]	Equivalent Young's Modulus [Pa]
50	3.9190E+06
150	3.8721E+06
250	3.8391E+06
350	3.8190E+06
450	3.7922E+06
550	3.7819E+06
650	3.7472E+06
750	3.7490E+06
850	3.7126E+06
950	3.7061E+06
1050	3.6900E+06

Table A7. 8: 45% AP filling equivalent isotropic solid medium Young's Modulus

Frequency [Hz]	Equivalent Young's Modulus [Pa]
50	4.5886E+06
150	4.5645E+06
250	4.5433E+06
350	4.5258E+06
450	4.5198E+06
550	4.5138E+06
650	4.5032E+06
750	4.5147E+06
850	4.4746E+06
950	4.4673E+06
1050	4.4587E+06

Appendix 7.3: Loss Factor Calculation Methodology-MATLAB Code

```

dt=0.001; %time interval
f=655.89; %frequency
wf=2*pi*f;

%load the velocity data from EDEM;
A1=readtable('D:\Education in the UK\1- PhD_University of Sheffield\1- PhD
Project\16- Results\COMSOL Multiphysics_Results\2020_November_1st
Week\Velocity_11.csv');
t=A1(:,1);
t=table2array(t);
v1=A1(:,2);
V1=table2array(v1);
V1=V1(39226:end);

```

```

%load the velocity data from EDEM;
A1=readtable('D:\Education in the UK\1- PhD_University of Sheffield\1- PhD
Project\16- Results\COMSOL Multiphysics_Results\2020_November_1st
Week\Velocity x_11.csv');
v1x=A1(:,2);
V1x=table2array(v1x);
V1x=V1x(39226:end);
%load the velocity data from EDEM;
A1=readtable('D:\Education in the UK\1- PhD_University of Sheffield\1- PhD
Project\16- Results\COMSOL Multiphysics_Results\2020_November_1st
Week\Velocity avg_11.csv');
v1_avg=A1(:,2);
V1_avg=table2array(v1_avg);
V1_avg=V1_avg(39226:end);
%load the velocity data from EDEM;
A1=readtable('D:\Education in the UK\1- PhD_University of Sheffield\1- PhD
Project\16- Results\COMSOL Multiphysics_Results\2020_November_1st
Week\Velocity x avg_11.csv');
v1x_avg=A1(:,2);
V1x_avg=table2array(v1x_avg);
V1x_avg=V1x_avg(39226:end);
%load the force data from EDEM;
A1=readtable('D:\Education in the UK\1- PhD_University of Sheffield\1- PhD
Project\16- Results\COMSOL Multiphysics_Results\2020_November_1st Week\Tot
Force_11.csv');
f1=A1(:,2);
F=table2array(f1);
FF=F(392326:end);
%load the force data from EDEM;
A1=readtable('D:\Education in the UK\1- PhD_University of Sheffield\1- PhD
Project\16- Results\COMSOL Multiphysics_Results\2020_November_1st Week\Tot
Force x_11.csv');
f1x=A1(:,2);
Fx=table2array(f1x);
Fx_=Fx(39226:end);
%load the force data from EDEM;
A1=readtable('D:\Education in the UK\1- PhD_University of Sheffield\1- PhD
Project\16- Results\COMSOL Multiphysics_Results\2020_November_1st Week\Tot
Force avg_11.csv');
f1_avg=A1(:,2);
F_avg=table2array(f1_avg);
Favg=F_avg(39226:end);
%load the force data from EDEM;
A1=readtable('D:\Education in the UK\1- PhD_University of Sheffield\1- PhD
Project\16- Results\COMSOL Multiphysics_Results\2020_November_1st Week\Tot
Force x avg_11.csv');
f1x_avg=A1(:,2);
Fx_avg=table2array(f1x_avg);
Fxavg_=Fx_avg(39226:end);
for n=39226
    T1=t1(n:n+153);
    T2=t1(n+154:n+154*2-1);
    T3=t1(n+154*2:n+154*3-1);
    T4=t1(n+154*3:n+154*4-1);
    T5=t1(n+154*4:n+154*5-1);
    T1_=[T1 T2 T3 T4 T5];
    T_eng=mean(T1_,2);

    T01=t01(n:n+153);
    T02=t01(n+154:n+154*2-1);
    T03=t01(n+154*2:n+154*3-1);

```

```

    T04=t01(n+154*3:n+154*4-1);
    T05=t01(n+154*4:n+154*5-1);
    T01_=[T01 T02 T03 T04 T05];
    T0_eng=mean(T01_,2);
end
x1=detrend(cumtrapz(T,V1));
x1avg=detrend(cumtrapz(T,V1_avg));

xx1=detrend(cumtrapz(T,V1x));
xx1_avg=detrend(cumtrapz(T,V1x_avg));
for n=1;

    X1=x1(n:n+153);
    X2=x1(n+154:n+154*2-1);
    X3=x1(n+154*2:n+154*3-1);
    X4=x1(n+154*3:n+154*4-1);
    X5=x1(n+154*4:n+154*5-1);
    X_1=[X1 X2 X3 X4 X5];
    X_eng=mean(X_1,2);

    XX1_avg=x1avg(n:n+153);
    XX2_avg=x1avg(n+154:n+154*2-1);
    XX3_avg=x1avg(n+154*2:n+154*3-1);
    XX4_avg=x1avg(n+154*3:n+154*4-1);
    XX5_avg=x1avg(n+154*4:n+154*5-1);
    XXavg_1=[XX1_avg XX2_avg XX3_avg XX4_avg XX5_avg];
    XX_mean_eng=mean(XXavg_1,2);
end
for n=1;

    XX1=xx1(n:n+153);
    XX2=xx1(n+154:n+154*2-1);
    XX3=xx1(n+154*2:n+154*3-1);
    XX4=xx1(n+154*3:n+154*4-1);
    XX5=xx1(n+154*4:n+154*5-1);
    XX_1=[XX1 XX2 XX3 XX4 XX5];
    XX_eng=mean(XX_1,2);

    XX1_avg=xx1_avg(n:n+153);
    XX2_avg=xx1_avg(n+154:n+154*2-1);
    XX3_avg=xx1_avg(n+154*2:n+154*3-1);
    XX4_avg=xx1_avg(n+154*3:n+154*4-1);
    XX5_avg=xx1_avg(n+154*4:n+154*5-1);
    XXavg_1=[XX1_avg XX2_avg XX3_avg XX4_avg XX5_avg];
    XX_mean_eng=mean(XXavg_1,2);
end

for n=39226;

    F1=F(n:n+153);
    F2=F(n+154:n+154*2-1);
    F3=F(n+154*2:n+154*3-1);
    F4=F(n+154*3:n+154*4-1);
    F5=F(n+154*4:n+154*5-1);
    F1_=[F1 F2 F3 F4 F5];
    F_eng=mean(F1_,2);

    F1_avg=F_avg(n:n+153);
    F2_avg=F_avg(n+154:n+154*2-1);
    F3_avg=F_avg(n+154*2:n+154*3-1);

```

```

    F4_avg=F_avg(n+154*3:n+154*4-1);
    F5_avg=F_avg(n+154*4:n+154*5-1);
    Favg_1=[F1_avg F2_avg F3_avg F4_avg F5_avg];
    F_mean_eng=mean(Favg_1,2);
end

for n=39226;

    F1x=Fx(n:n+153);
    F2x=Fx(n+154:n+154*2-1);
    F3x=Fx(n+154*2:n+154*3-1);
    F4x=Fx(n+154*3:n+154*4-1);
    F5x=Fx(n+154*4:n+154*5-1);
    F1x_=[F1x F2x F3x F4x F5x];
    Fx_eng=mean(F1x_,2);

    F1x_avg=Fx_avg(n:n+153);
    F2x_avg=Fx_avg(n+154:n+154*2-1);
    F3x_avg=Fx_avg(n+154*2:n+154*3-1);
    F4x_avg=Fx_avg(n+154*3:n+154*4-1);
    F5x_avg=Fx_avg(n+154*4:n+154*5-1);
    Favgx_1=[F1x_avg F2x_avg F3x_avg F4x_avg F5x_avg];
    Fx_mean_eng=mean(Favgx_1,2);
end

%max and min points on the hysteresis loop
[cmin,cxix] = (min(XX_mean_eng))
[cmax,cnix] = (max(XX_mean_eng))
[fmin,fxix] = (min(Fx_mean_eng))
[fmax,fnix] = (max(Fx_mean_eng))
figure(1)
plot(XX_mean_eng, Fx_mean_eng)
hold on
plot([cmin cmax], [fmin fmax], 'or', 'MarkerSize', 5, 'LineWidth',1.5)
hold off
xlabel('Displacement [m]');
ylabel('Force [N]');
title('Hysteresis Cycle Using Average Data');
grid
%slope of the hysteresis loop
k_slope = (fmax-fmin)./(cmax-cmin);
%the damping force
Fd = fmax-k_slope*cmax;
%the damping constant
c = Fd/V1x_avg(end);
%energy dissipated per cycle
w = pi*c*2*pi*f*cmax^2;
figure
plot(XX_eng,Fx_eng);
xlabel('Displacement [m]');
ylabel('Force [N]');
title('Hysteresis Cycle Mean Using Total Data');

%calculate max strain energy
Umax_4=0.5*max(xx1)*max(Fx_);
%calculate loss factor
eta = w./(2*pi*Umax_4);

```